SHARED APERTURE ARRAY ANTENNAS COMPOSED OF DIFFERENTLY SIZED ELEMENTS ARRANGED IN SPARSE SUB-ARRAYS

SHARED APERTURE ARRAY ANTENNAS COMPOSED OF DIFFERENTLY SIZED ELEMENTS ARRANGED IN SPARSE SUB-ARRAYS

PROEFSCHRIFT

ter verkrijging van de graad van doctor
aan de Technische Universiteit Delft,
op gezag van de Rector Magnificus prof. dr. ir. J.T. Fokkema,
voorzitter van het College voor Promoties,
in het openbaar te verdedigen op maandag 23 januari 2006 om 13.00 uur

door

Cristian Ioan COMAN

inginer, Academia Tehnică Militară – Bucureşti
geboren te Tîrnăveni, Roemenië

Dit proefschrift is goedgekeurd door de promotor:
Prof.dr.ir. L.P. Ligthart

Samenstelling promotiecommissie:

Rector Magnificus,	voorzitter
Prof.dr.ir. L.P. Ligthart,	Technische Universiteit Delft, promotor
Prof.ir. P. van Genderen	Technische Universiteit Delft
Prof.dr.ing. R. Sorrentino,	Università degli Studi di Perugia, Italië
Prof.dr. A.G. Tijhuis,	Technische Universiteit Eindhoven
Prof.dr.ir. G. Vandenbosch,	Katholieke Universiteit Leuven, België
Dr.ing. I.E. Lager,	Technische Universiteit Delft,
Col.dr.ing. Ş. Cantaragiu,	Ministry of National Defence, Roemenië
Prof.dr.ir. P.M. van den Berg,	Technische Universiteit Delft, reservelid

Shared Aperture Array Antennas Composed of Differently Sized Elements Arranged in Sparse Sub-Arrays
Cristian Ioan Coman.

Thesis Delft University of Technology.
With references and with summary in Dutch.

ISBN 90–76928–09–6

Subject headings: shared aperture antenna; sparse array antenna; cavity-backed, stacked-patch antenna; mode matching method.

Printed in The Netherlands

The work presented in this thesis was financially supported by the Ministry of Defence in The Netherlands.

To Valentina, Radu and Tudor

Contents

Chapter 1

Introduction

Since the first radio experiment in 1900, the field of antenna design has known a continuously growing interest. The advantages of wireless communication, remote sensing and other radio applications have become more and more appreciated by a larger part of the society. Having this social support, a significant amount of work has been put in the development of new, high quality antennas.

At this moment, the state of the art in the antenna field is primarily related to array antennas. Particularly, *active phased array antennas* are complex structures involving not only radiating elements but feeding networks, phase shifters and transmit/receive modules, as well. It is worth noting that the cost of a large array, that has electronic scanning capabilities, is rather high and practical developments were mainly reported for military applications. Apart from the cost, there are still some technical and technological aspects that are of concern for the array antenna community, especially in relation to challenging *system requirements* such as:

- transmitting/receiving signals with a large instantaneous bandwidth;
- good active impedance matching at wide scanning angles;
- low profile architectures (desired for mobile platforms);

From a theoretical perspective, antenna arrays have been given a particular attention due to the complex phenomena associated with the radiation of electromagnetic waves by closely spaced sources. The mutual coupling between array elements affects detrimentally antenna performances (e.g. side lobe level, axial ratio, array scan blindness, etc.). It is known that, by increasing the distances between elements, the coupling effect in array architectures can be reduced. Since 1960 different algorithms have been proposed for designing *sparse* array antennas having non-uniformly spaced elements [137]). With possible large distances between elements, these configurations

are the most straightforward solutions in an attempt to reduce the effect of the mutual coupling. They have also the advantage of controlling the antenna radiation pattern without tapering the amplitudes of the elements.

Wide band array antennas have been developed in the past few decades by different countries within large research programs. In the book of FOURIKIS [45] the most notable realizations are presented in a concise form. These wide band antennas opened new possibilities of integrating different system functions on the same aperture. It is worth mentioning that there are still challenging aspects to be solved in wide band array antennas, as for example controlling the array side lobe level (e.g. grating lobes) at large scanning angles, and reducing the size, the complexity and the cost.

In 2004 the International Research Centre for Telecommunications-transmission and Radar (IRCTR) of Delft University of Technology initiated a major research programme in the antenna field. The project is called "Wide Band Sparse Element Array Antennas - WiSE" and it is supported by different governmental and industrial organizations in The Netherlands, Romania and Turkey. The close cooperation between the Romanian Ministry of National Defence (MoD) and the Dutch Ministry of Defence, within the NATO Partnership for Peace framework, has provided a substantial support to the WiSE project. In particular, it is acknowledged that the Dutch MoD has fully supported financially a Ph.D. position filled by a researcher of Romanian MoD, this collaboration resulting in the present dissertation. The aim of the WiSE project is to investigate the theoretical and technological possibilities of realizing wide band array antennas by using sparse configurations. The results reported in this thesis have been achieved in the frame of the WiSE project, during the preparatory phase from 2001 to 2004 and in the first quarter of the project from 2004 to 2005.

1.1 Wide band array antennas – a survey

The demands for highly accurate sensors and for communication systems capable of transferring large amount of information have led the researchers to the potential offered by wide band signals. It is known that the quantity of information transmitted or collected (remote sensing) with a radio signal is mainly dependent on the signal's bandwidth. In the past few decades technological achievements have been reported in connection with the physical generation and processing of signals having a relative bandwidth higher than 50%. Simple frequency independent antennas, as for example spirals or modified dipoles, have been extensively investigated for transmitting wide and ultra- wide band signals. However, the radiation properties of these radiators are rather poor, with large beamwidth (no angular resolution) and high side lobe level. Array antenna configurations seem to be the most adequate choice for addressing in a favorable manner all these radiation properties.

In designing wide band array antennas two distinct solutions have been

mainly adopted by antenna engineers:

- arranging wide band radiators in a lattice configuration;
- deploying elements operating at different bandwidths on a common aperture.

The first approach is straightforward and benefits from the developments achieved in designing wide and ultra-wide band elementary antennas. The array antenna community has shown a particular interest to an ultra-wide band radiating element known as the tapered notch or the Vivaldi antenna [65, 51]. Some of the attractive features of this radiator are: wide bandwidth ($> 50\%$), it is usually fabricated using printed circuit processing, and the size of the radiating aperture is (relatively) small. Practical realizations reported in [7, 59, 60, 61] have demonstrated the basic characteristics of array configurations operating over a large frequency range. However, the frequency independent antennas have large dimensions, and therefore they are not suitable for low profile array antennas. For example, the Vivaldi antenna has been easily integrated in array configurations due to its small dimensions of the radiating aperture but its length is still large. Since the aperture's dimensions of an array antenna are usually imposed by the system specifications (antenna beamwidth) and is not amenable to minimization, the remaining dimension, the height of the antenna, is mainly addressed when size is to be reduced.

The second solution has its origin in the work done for obtaining *shared aperture antennas* in which different arrays, supporting system functions at separated bandwidths, are deployed on a common panel. Broad band elements [46, 84] as well as narrow band radiators [98, 112] were used for designing multi band array antennas. Due to the grating lobes condition, the maximum distance between uniformly distributed elements is limited by the highest frequency in the antenna operational bandwidth. Therefore, interleaving radiators operating at different frequencies is a difficult task and the published solutions have either widely separated bandwidths, limited scan angle (if any), thick structures, or are technologically complicated.

1.2 Research objective

The central problem, which is investigated in this thesis, refers to the **design of wide band (multi-band) array antennas**. The primary focus is on the solution to interleaving sub-arrays operating at separate frequencies. For being able to deploy distinctive sub-arrays on a common aperture, without elements overlapping, sparse configurations are aimed at. Sparse array antennas offer two major advantages, namely: they have non-uniformly distributed elements, with possibly large distances between elements, and they do not exhibit grating lobes. Therefore, a straightforward idea would be to

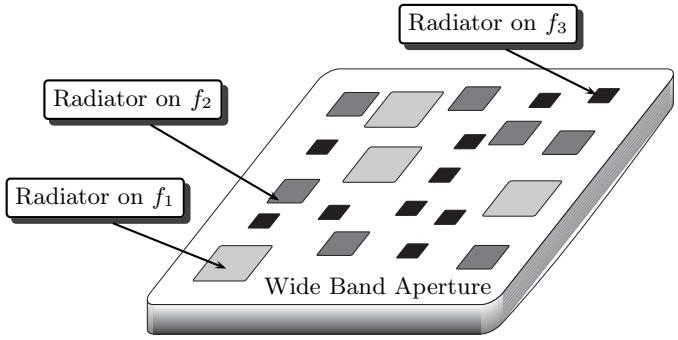

Figure 1.1: Wide band array antenna consisting of interleaved *sparse* sub-arrays operating at different frequency

fill the empty space in an a-periodic array antenna with elements operating at adjacent frequency bandwidths, which are arranged in sparse configurations, as well. A graphical sketch of this novel approach is depicted in Fig. 1.1, in which three types of elements (operating at frequencies f_1, f_2 and f_3) are arranged on a common aperture in distinctive sparse sub-arrays.

1.3 Research lines

Array antennas are complex systems with multiple features to be investigated before a practical realization can be initiated. In this work, attention has been paid to a number of aspects which make a trade off between manufacturing an experimental model and demonstrating the viability of the new concept. A graphical illustration of the major topics investigated is provided in Fig. 1.2. The main goal of the WiSE project is to investigate the features of wide band array antennas assembled using moderate band radiators arranged in sparse configurations. Since an experimental demonstrator is aimed at for the final assessment of the new concept, attention has been given concurrently to the designs of the elementary radiator and of the array architecture.

Moderate bandwidth antennas have received special attention due to the attractive compromise realized between *bandwidth* and *size*. Conventionally, the design of these antennas starts from a known geometry and search for the optimum dimensions that will fit the antenna specifications. It should be noted that, since they have a complex geometry, there are no straightforward design relations and antenna engineers have to make use of the electromagnetic numerical analysis tools. Having in mind the idea of a systematic, repetitive design, the elementary radiators were taken to be composed of three distinctive functional parts: radiating part, matching

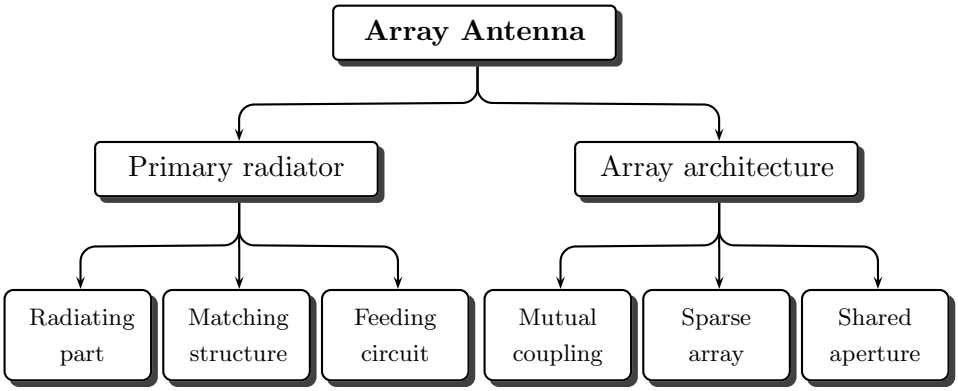

Figure 1.2: Research tree

structure, and feeding circuit. A similar functional interpretation can be adopted for a large category of antennas and it gives a notable flexibility in generating new topologies by simply combining different models.

Regarding the array architecture, three research directions were identified as relevant for evaluating the potential of the new approach to design wide band array antennas. Commonly, in uniform array antennas the mutual coupling effect is considered indirectly, by imposing periodic boundary conditions to the elementary radiators. However, when a-periodic arrays are to be investigated, an important step is to evaluate the electromagnetic interaction between array elements. Since the first work of UNZ in 1960 many algorithms have been proposed for constructing sparse array configuration with no grating lobes [137]. After a careful investigation it appears that most of these procedures have their origin in the *mathematical optimization* field. Therefore, the possibility to work with integer or real numbers and to solve problems with tens or thousands of variables are efficient criteria to choose for one method or another. A less investigated problem, which is highly relevant for the WiSE project, is the possibility of interleaving sparse sub-arrays. Upon giving up the assumption that the elementary antennas are point radiators, a difficult constraint, namely that the elements should not overlap, must be considered during the design of shared aperture array antennas.

1.4 Novelties and main results

The new approach to designing wide band array antennas has raised a couple of research incentives that have been addressed in an original manner. The most relevant novelties presented in this thesis are as follows:

- reduction of the order of integration in the calculation of the mutual coupling admittances between different aperture antennas (Chapter 3, Section 3.2.3);
- fast approximation of the mutual coupling in array antennas (Chapter 3, Section 3.4);
- modular design of dielectric filled waveguide antennas and of cavity-backed stacked-patch antennas (Chapter 4);
- design of arbitrary, linear array antennas by also taking into account the effect of the mutual coupling (Chapter 5, Section 5.5.1);
- sparse Synthetic Aperture Radar (SAR) processing in ground penetrating radar applications (Chapter 5, Section 5.5.2);
- numerical demonstration of the capabilities of sparse array antennas in applications requiring wide angle impedance matching (Chapter 5, Section 5.5.3);
- interleaving methods for designing shared apertures (Chapter 6, Sections 6.1.2 and 6.1.3);
- the concept of wide-band, multifunction array antennas consisting of interleaving sparse sub-arrays (Chapter 6, Section 6.2).

Consequently, the following results are to be mentioned as the main achievements of this work:

- implementation of the Boundary Integral Resonant Mode Expansion (BI-RME) for the fast evaluation of the modes of non canonical, hollow waveguides (Chapter 2, Section 2.2.8);
- implementation of the polynomial approximation of the coupling admittance between rectangular apertures, by also accounting for the effect of the higher order modes (Chapter 3, Section 3.4);
- design procedure for elementary antennas based on the circuits theory and the lumped elements representation (Chapter 4, Section 4.2.2); ;
- development of full-wave software tools for the analysis of elementary antennas operating in sparse, finite arrays and in shared aperture array configurations (Chapter 5, Section 5.5.3 and Chapter 6, Section 6.2);
- evaluation of the performances of large, sparse array antennas by means of synthetic aperture radar measurements(Chapter 5, Section 5.5.2);
- experimental study of cavity-backed, stacked patch antennas operating in isolated mode and in planar, sparse array configurations (Chapter 4, Section 4.4 and Chapter 5, Section 5.5.3).

- experimental demonstration of the concept of wide-band, multifunction array antennas consisting of interleaving sparse sub-arrays (Chapter 6, Section 6.2).

It is worth mentioning that the numerical implementation of the full wave analysis involved intricate mathematical problems, such as numerical integration, treatment of singularities and limits of discontinuous functions, which were solved in an original manner. These achievements are not singled out in this introductory chapter but they will be underlined in the following chapters as they appear.

1.5 Outline of the thesis

The dissertation is organized in three parts, covering the main aspects associated with the design of array antennas. In the first part, the theoretical formulation of the electromagnetic problem will be presented. Variants of the Mode Matching Method (MMM) have been developed for the full wave investigation of the elementary radiators and of the array configurations. The second part of the thesis will be dedicated to the analysis and design of elementary antennas. Moreover, the impact of the technological aspects on the antenna performances will be discussed and formulated in terms of design constraints. The third part covers the aspects related to sparse array antennas. Shared apertures, consisting of interleaved sparse subarrays are given a special attention in particular for wide band applications.

Hereafter, a description of the account to follow is provided:

- **Chapter 2** - The *modal analysis of waveguide structures*, which is at the core of the electromagnetic investigation performed in this thesis, is presented in this chapter. It starts with the definition of the *modes* inside hollow waveguides and proceeds with the formulation of the analysis of some simple planar discontinuities. These aspects are considered necessary since they will be often called upon in the analysis of the antennas. A last section in this chapter is dedicated to the Boundary Integral - Resonant Mode Expansion (BI-RME) method used for the calculation of the modes of waveguide segments with arbitrary cross sections. The computer implementation, including numerical validations, is presented for the case of rectangular waveguides perturbed by cylindrical conductors.

- **Chapter 3** - This chapter deals with the *modal analysis* of the phenomena related to the *radiation* from rectangular apertures in metallic flanges. The problem is formulated and solved for the general case of arbitrary array antennas consisting of differently sized apertures. Two techniques, namely, the Fourier approach and the solution based on

the Green's function are presented in detail. Computer implementations of these methods are discussed subsequently. The chapter is concluded by discussing a new approach to reducing the computational time necessary for the evaluation of the mutual coupling effect in finite (a-periodic) array antennas.

- **Chapter 4** - The procedure adopted for the analysis of elementary antennas is described in this chapter. Starting with a discussion on the requirements to be met by the elementary radiators employed in array configurations, the study proceeds with the formulation of the *electromagnetic analysis* of a few particular antenna configurations. Some design strategies adopted for dimensioning the elementary antennas are also presented in this chapter. Scattering parameters, as well as admittance parameters, are used in optimization loops for *automatic antenna design*. For gaining insight on the operation of the elementary antennas, a study of these parameters is performed and the influence of the critical dimensions is examined. In the end the attention focuses on the *manufacturing* and the measurement of elementary antennas. Some technological aspects are investigated from de perspectives of accurate computer simulations and low cost manufacturing. Measurements performed on cavity backed, stacked patches, probe fed antennas are compared against the simulation results.

- **Chapter 5** - The topics discussed here are related to *sparse array antennas*. Representative design techniques are discussed on the basis of numerical simulations. A new formulation of the problem is proposed for designing array configurations consisting of elements that are arbitrarily deployed on the aperture. The approach takes into consideration the physical size of the radiators and the mutual coupling effect. To substantiate the performance of sparse array antennas, measurement results are included, as well. A procedure for using the synthetic aperture radar measurements in the evaluation of the performance of large sparse array antenna is also introduced.

- **Chapter 6** - In this chapter an advanced array antenna concept, namely, *shared apertures*, is addressed. Some methods for interleaving sparse sub-arrays are proposed and discussed. The experimental investigation of the new proposal for increasing the bandwidth of an array antenna is presented in. The mutual coupling effect is a key issue to be investigated in an array consisting of radiators operating at different frequency. Measurements of the matching properties and the radiation patterns of the individual radiators in the shared aperture configuration are presented in comparison with simulations results.

- **Chapter 7** - This chapter provides the conclusions and discusses some of the open problems identified at the completion of this Ph.D. study.

Chapter 2

Modal analysis of waveguide structures

The chapter explains the modal formalism used to represent the electromagnetic field quantities inside waveguide transmission lines.

In the first part, the derivation of the *modes* is explained, starting from the Maxwell's equations. Subsequently, the properties of the modes are also introduced in connection with particular aspects linked to the mode matching method. It is worth noting that the modes of a rectangular waveguide are the most extensively used expansion functions in this work. Therefore, for this particular transmission line, the mathematical expressions of the modes are given. The chapter proceeds with the presentation of the Boundary Integral - Resonant Mode Expansion (BI-RME) method. The BI-RME method is used for the evaluation of the modes of uniform waveguide segments with arbitrary cross-section. Some particular aspects of this method, which have received less attention in the literature, are discussed as well. The mode matching analysis of waveguide discontinuities is introduced in the last part of the chapter.

2.1 Electromagnetic field expansion in hollow waveguides

The propagation of the electromagnetic filed inside hollow waveguides has been extensively investigated by many authors since the introduction of this type of transmission line in the microwave applications. At this moment the theory of common waveguides (rectangular, circular, coaxial) is well established and reported in many books (see, for example, [91, 26, 56]). In this dissertation the basic formulation will be summarized and some aspects, which will be later used as foundation for the explanations given in other

parts of this manuscript, will be outlined.

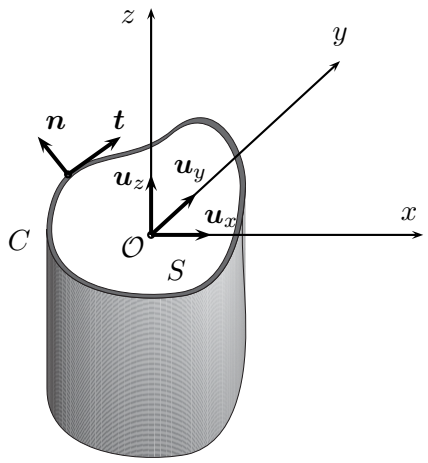

Figure 2.1: Uniform waveguide segment of arbitrary cross-section.

The geometry of a generic waveguide configuration is depicted in Fig. 2.1. It consists of a metallic cylinder oriented along the $\mathcal{O}z$ axis. The interior region is considered as being filled with an isotropic and uniform dielectric material characterized by the dielectric permittivity ε and the magnetic permeability μ.

The electromagnetic field in a macroscopic domain is governed by the classical field equations of Maxwell. In differential form these are [26, p. 2]

$$\nabla \times \boldsymbol{E} = -\frac{\partial \boldsymbol{B}}{\partial t}, \tag{2.1}$$

$$\nabla \times \boldsymbol{H} = \frac{\partial \boldsymbol{D}}{\partial t} + \boldsymbol{J}, \tag{2.2}$$

$$\nabla \cdot \boldsymbol{D} = \rho, \tag{2.3}$$

$$\nabla \cdot \boldsymbol{B} = 0, \tag{2.4}$$

$$\nabla \cdot \boldsymbol{J} = -\frac{\partial \rho}{\partial t}, \tag{2.5}$$

where:

$\boldsymbol{E} = \boldsymbol{E}(\boldsymbol{r}, t)$ is the electric field strength;

$\boldsymbol{B} = \boldsymbol{B}(\boldsymbol{r}, t)$ is the magnetic flux density;

$\boldsymbol{H} = \boldsymbol{H}(\boldsymbol{r}, t)$ is the magnetic field strength;

$\boldsymbol{D} = \boldsymbol{D}(\boldsymbol{r}, t)$ is the electric flux density;

$\boldsymbol{J} = \boldsymbol{J}(\boldsymbol{r}, t)$ is the electric current density;

$\rho = \rho(\boldsymbol{r}, t)$ is the charge density;

$\boldsymbol{r}$ is the position vector and t is the time coordinate.

Note that the electromagnetic field is taken in this work to be of harmonic nature, with a constant radian frequency ω. The time variation of the field quantities are assumed to be $\exp(+j\omega t)$. At the same time it is pointed out that the dielectric materials are assumed to be homogeneous, isotropic and lossless media whereas the metal ones are considered perfect conductors.

In the study of waveguide structures, it is efficient to express the electromagnetic field in the interior domain as a superposition of an infinite number of *modes* [91, p. 2]. The advantage of this approach is that the electric and magnetic field quantities of a waveguide mode can be factored into a form component and a propagation component. The form component is the one related to the shape of the transversal section while the propagation component can be seen as an amplitude modulation of the form part in the longitudinal direction. Once the two dimensional distribution of the mode in the transversal section is known at a certain point on the longitudinal axis, the field quantities at any other transversal section can be easily derived by a simple scaling operation. Therefore, by eliminating the longitudinal component of the field, the Maxwell equations can be reduced to a transversal vectorial form [91, p. 3]:

$$\frac{\partial \boldsymbol{E}_t}{\partial z} = -jk\eta(\overline{\mathbf{I}} + \frac{1}{k^2}\boldsymbol{\nabla}_t\boldsymbol{\nabla}_t) \cdot (\boldsymbol{H}_t \times \boldsymbol{u}_z), \tag{2.6}$$

$$\frac{\partial \boldsymbol{H}_t}{\partial z} = -\frac{jk}{\eta}(\overline{\mathbf{I}} + \frac{1}{k^2}\boldsymbol{\nabla}_t\boldsymbol{\nabla}_t) \cdot (\boldsymbol{u}_z \times \boldsymbol{E}_t), \tag{2.7}$$

where:

$\boldsymbol{E}_t$ is the root mean square value of the electric field intensity transverse to the z-axis;

$\boldsymbol{H}_t$ is the root mean square value of the magnetic field intensity transverse to the z-axis;

$k = \omega\sqrt{\mu\epsilon} = 2\pi/\lambda$ is the propagation constant in the medium;

$\eta = \sqrt{\mu/\epsilon}$ is the intrinsic impedance of the medium inside the waveguide

$\overline{\mathbf{I}}$ is unit dyadic defined such that $\overline{\mathbf{I}} \cdot \boldsymbol{A} = \boldsymbol{A} \cdot \overline{\mathbf{I}} = \boldsymbol{A}$ with $\boldsymbol{A}$ being a vector;

$\boldsymbol{\nabla}_t = \boldsymbol{u}_x \frac{\partial}{\partial x} + \boldsymbol{u}_y \frac{\partial}{\partial y}$ is the gradient operator transverse to the z-axis.

The longitudinal components of the electric and magnetic field can be derived from the transversal quantities by using the relations [91]:

$$\frac{jk}{\eta} E_z = \boldsymbol{\nabla}_t \cdot (\boldsymbol{H}_t \times \boldsymbol{u}_z), \tag{2.8}$$

$$jk\eta H_z = \boldsymbol{\nabla}_t \cdot (\boldsymbol{u}_z \times \boldsymbol{E}_t). \tag{2.9}$$

In general, the electric and magnetic field intensities are the unknowns to be determined from Maxwell equations. When these quantities must be evaluated inside a waveguide transmission line it is appropriate to express them in terms of modal field quantities [36, p. 2]:

Transversal components

$$\boldsymbol{E}_t(x,y,z) = \sum_{m=1}^{\infty} \boldsymbol{E}_{t,m}(x,y,z), \tag{2.10}$$

$$\boldsymbol{H}_t(x,y,z) = \sum_{m=1}^{\infty} \boldsymbol{H}_{t,m}(x,y,z), \tag{2.11}$$

Longitudinal components

$$E_z(x,y,z) = \sum_{m=1}^{\infty} E_{z,m}(x,y,z), \tag{2.12}$$

$$H_z(x,y,z) = \sum_{m=1}^{\infty} H_{z,m}(x,y,z). \tag{2.13}$$

The terms $\boldsymbol{E}_{t,m}$,$\boldsymbol{H}_{t,m}$, $m = 1, \cdots, \infty$, represent the modal electric and magnetic field quantities transversal to the waveguide axis, and $E_{z,m}$, $H_{z,m}$ are the longitudinal modal components (the index m denotes the mode order). As it was already discussed, these modes can be factorized in two parts, one describing the variation in the transversal section and the other one the evolution along the longitudinal axis. For the transversal modes the following relations are introduced [36, p. 2]

$$\boldsymbol{E}_{t,m}(x,y,z) = V_m(z)\boldsymbol{e}_{t,m}(x,y), \tag{2.14}$$

$$\boldsymbol{H}_{t,m}(x,y,z) = I_m(z)\boldsymbol{h}_{t,m}(x,y), \tag{2.15}$$

where $\boldsymbol{e}_{t,m}$ and $\boldsymbol{h}_{t,m}$ are vector functions that form the modal set. They can be of three basic types:

- Transverse Electric (TE) with $E_z = 0$,

- Transverse Magnetic (TM) with $H_z = 0$ and
- Transverse Electromagnetic (TEM) with $E_z = 0$ and $H_z = 0$.

The modal amplitudes V_m and I_m, $m = 1, \cdots, \infty$, can be taken as being the *equivalent voltage* and *current* of the m^{th} waveguide mode.

An important property of the equivalent voltages and currents is that they satisfy the *telegraphists equation* [36, p. 2]:

$$V_m(z) = V_m^+ e^{-j\beta_m z} + V_m^- e^{j\beta_m z}, \tag{2.16}$$

$$I_m(z) = I_m^+ e^{-j\beta_m z} + I_m^- e^{j\beta_m z}, \tag{2.17}$$

with V_m^+ and I_m^+ denoting the amplitudes of the *direct* modal waves (propagating in the positive direction of the z-axis) and V_m^- and I_m^- representing the amplitudes of the *inverse* waves, respectively. The phase constant β_m of the mode m characterizes the propagation inside the transmission line and it is frequency dependant. The link between the modal equivalent voltages and currents is controlled by the *characteristic impedance* [36, p. 3]

$$Z_{c,m} = \frac{V_m^+}{I_m^+} = -\frac{V_m^-}{I_m^-}. \tag{2.18}$$

Similar representations can be easily derived for the longitudinal modal components by making use of the transversal quantities (relations (2.14) to (2.17)) in (2.8) and (2.9). Explicit formulas for the E_z and H_z components will be given in the following sections in relation to the definition of the TE and the TM modes.

2.1.1 TE, TM and TEM modes

The elementary functions used to describe the waveguide modes can be obtained by solving a certain differential equation on the waveguide cross-section S (see Fig.2.1). The separation between TE, TM and TEM modes emerges from imposing different boundary conditions on the contour C of the domain S.

TE modes

The modal functions used in the definition of the TE modes can be selected from the solutions of an eigenvalue problem defined on the waveguide cross-section S, with Neumann boundary conditions on contour C [36, p. 3]:

$$\boldsymbol{\nabla}_t \boldsymbol{\nabla}_t \Phi_m + k_{c,m}^2 \Phi_m = 0, \tag{2.19}$$

$$\frac{\partial \Phi_m}{\partial n} = \boldsymbol{n} \cdot \boldsymbol{\nabla}_t \Phi_m = 0 \text{ on } C, \tag{2.20}$$

where $\partial/\partial n$ denotes the derivative along the outwardly directed normal to the contour C and $k_{c,m}^2$ and Φ_m represent the eigenvalue and the eigenfunction associated to the m^{th} waveguide mode, respectively. The quantity $k_{c,m}$ is also known as the cutoff wave number associated to the m^{th} mode. Having the scalar eigenfunction Φ_m calculated, the modal field components read

$$\boldsymbol{e}_{t,m} = \boldsymbol{u}_z \times \boldsymbol{\nabla}_t \Phi_m, \tag{2.21}$$

$$\boldsymbol{h}_{t,m} = \frac{Z_{c,m}}{\eta_m} \boldsymbol{u}_z \times \boldsymbol{e}_{t,m}, \tag{2.22}$$

$$h_{z,m} = \frac{k_{c,m}^2}{k} \Phi_m, \tag{2.23}$$

where:

$k = \omega\sqrt{\mu\epsilon}$ represents the wave number of the medium;

$\eta_m = \omega\mu/\beta_m$ is the wave impedance of the m^{th} TE mode and;

$\beta_m = \sqrt{\omega^2\mu\epsilon - k_{c,m}^2}$ is the modal phase constant.

In the definition of the β_m the quantity $\omega^2\mu\epsilon - k_{c,m}^2$ has real values in case of lossless materials and complex values for the lossy ones.Therefore, in isotropic, loss-less materials (the only ones considered in this work), the propagation constant of the waveguide modes can be real value or imaginary value depending on the frequency of analysis. Attention must be paid to the fact that the square root operator used to define the phase constant β_m will provide multiple solutions. These solutions can be associated to the evanescent and to the propagating waves related to the transmission line. The wave impedance η_m can also take real, imaginary or complex values depending on the frequency of analysis and the type of the material (lossless or lossy). It is worth noting that the inclusion of the dielectric losses in the modal analysis is straightforward, by simply expressing the dielectric permittivity as a complex number. The losses in the waveguide walls can be considered in the study of the waveguide transmission lines as well, a detailed discussion on this topic being provided in [26, p. 340].

From the definition of the TE modes, it is evident that the longitudinal magnetic field inside the waveguide is described by TE quantities, only. If the characteristic admittance $Z_{c,m}$, which is an arbitrary constant, is taken to be equal with the wave impedance η_m the magnetic field component oriented along the z-axis yields [36, p. 4]

$$H_z(x,y,z) = -\frac{j}{\eta} \sum_{m=1}^{\infty} V_m(z) h_{z,m}(x,y). \tag{2.24}$$

TM modes

The TM modes are derived from the solutions of a differential equation identical with that for the TE modes (2.19), except for that in this case the boundary conditions are of Dirichlet type [36, p. 3]:

$$\boldsymbol{\nabla}_t \boldsymbol{\nabla}_t \Phi_m + k_{c,m}^2 \Phi_m = 0, \tag{2.25}$$

$$\Phi_m = 0 \text{ on } C. \tag{2.26}$$

The TM modal field components can be evaluated from the scalar eigenfunction Φ_m using the relations:

$$\boldsymbol{e}_{t,m} = -\boldsymbol{\nabla}_t \Phi_m, \tag{2.27}$$

$$\boldsymbol{h}_{t,m} = \frac{Z_{c,m}}{\eta_m} \boldsymbol{u}_z \times \boldsymbol{e}_{t,m}, \tag{2.28}$$

$$e_{z,m} = \frac{k_{c,m}^2}{k} \Phi_m, \tag{2.29}$$

where the characteristic impedance of TM modes is defined as:

$$\eta_m = \frac{\beta_m}{\omega \epsilon}. \tag{2.30}$$

The TM modes are used to describe the electric field component oriented along the longitudinal axis of the waveguide. With the usual assumption that the characteristic impedance equals the wave impedance, the expression of the electric component along the z-axis reads [36, p. 4]:

$$E_z(x, y, z) = -j\eta \sum_{m=1}^{\infty} I_m(z) e_{z,m}(x, y). \tag{2.31}$$

TEM modes

In the case when the cross-section of the waveguide represents a multiply connected domain (there are more than one separated, metallic areas), TEM modes should also be used in the representation of the electromagnetic field. Such modes are characterized by both E_z and H_z being zero. It is known [91] that the number of TEM modes that can be defined in an arbitrary waveguide equals the number of separated metallic areas that exist inside the external contour of the waveguide.

The TEM modes can be easily derived from the expression of the TM modes with the observation that E_z in (2.29) must be zero. The $E_z = 0$

condition is satisfied by all scalar function Φ_m corresponding to zero eigenvalues $k_{c,m}^2$. Therefore, the differential equation to be solved for the TEM modes reads [36, p. 5]

$$\boldsymbol{\nabla}_t \boldsymbol{\nabla}_t \Phi_m = 0, \tag{2.32}$$

$$\frac{\partial \Phi_m}{\partial \boldsymbol{t}} = \boldsymbol{t} \cdot \boldsymbol{\nabla}_t \Phi_m = 0 \text{ on } C, \tag{2.33}$$

where $\partial/\partial \boldsymbol{t}$ denotes the derivative along the tangent $\boldsymbol{t}$ to the contour C. The boundary condition (2.33) implies that the potential Φ_m on each separated line defining the contour of the waveguide section is constant. The electric and magnetic modal vectors are expressed by

$$\boldsymbol{e}_{t,m} = -\boldsymbol{\nabla}_t \Phi_m, \tag{2.34}$$

$$\boldsymbol{h}_{t,m} = \frac{Z_{c,m}}{\eta_m} \boldsymbol{u}_z \times \boldsymbol{e}_{t,m}. \tag{2.35}$$

The propagation constant β_m and the wave impedance η_m can be derived from those introduced for the TE and TM modes with the condition $k_{c,m}^2 = 0$

$$\beta_m = \sqrt{\omega^2 \mu\epsilon - k_{c,m}^2} = \omega\sqrt{\mu\epsilon}, \tag{2.36}$$

$$\eta_m = \frac{\beta_m}{\omega\epsilon} = \frac{\omega\sqrt{\mu\epsilon}}{\omega\epsilon} = \sqrt{\frac{\mu}{\epsilon}}. \tag{2.37}$$

A wave is considered of *propagating* type if its $\beta_m \in \mathbb{R}$. When the phase constant is a negative imaginary number the corresponding wave is of *evanescent* type in the positive direction of the longitudinal axis. A wave can change its character from propagating to evanescent and vice-versa if the operational frequency increases over or decreases below the mode's *cut-off frequency*. The modal cut-off frequency $f_{c,m}$ is defined as the frequency at which the propagation constant β_m becomes zero

$$f_{c,m} = \frac{k_{c,m}}{2\pi\sqrt{\mu\epsilon}}. \tag{2.38}$$

It is evident that the TEM modes, which are characterized by $k_{c,m} = 0$, have the cut-off frequency equal to zero. As a consequence these modes can be used to transfer alternating current energy and direct current energy, as well.

2.1.2 Properties of modal vectors

So far we have discussed the modal expansion of the electromagnetic field inside a waveguide transmission line. In this section some of the relevant properties of the modal functions are presented.

One of the most important properties of the modal vectors $\boldsymbol{e}_{t,m}$ and $\boldsymbol{h}_{t,m}$ is that they form an orthogonal basis [91, p. 5]

$$\int_S \boldsymbol{e}_{t,m} \times \boldsymbol{h}_{t,n} \cdot \boldsymbol{u}_z dS = \begin{cases} 0 & \text{for } m \neq n \\ 1 & \text{for } m = n \end{cases}, \tag{2.39}$$

The normalization property in (2.39) is derived from a meaningful equivalence between the waveguide modes and transmission line models. In particular, the *power* flow associated with modal field must be equal to that transferred by an equivalent transmission line. Other useful relations can be derived from (2.39) by considering the relation between the magnetic and electric modal vectors ($\boldsymbol{h}_{t,m} = Z_{c,m}/\eta_m \boldsymbol{u}_z \times \boldsymbol{e}_{t,m}$):

$$\int_S \boldsymbol{e}_{t,m} \cdot \boldsymbol{e}_{t,n} dS = \begin{cases} 0 & \text{for } m \neq n \\ \frac{\eta_m}{Z_{c,m}} & \text{for } m = n \end{cases}, \tag{2.40}$$

$$\int_S \boldsymbol{h}_{t,m} \cdot \boldsymbol{h}_{t,n} dS = \begin{cases} 0 & \text{for } m \neq n \\ \frac{Z_{c,m}}{\eta_m} & \text{for } m = n \end{cases}. \tag{2.41}$$

From Green's first identity [26, p. 789] applied to the scalar eigenfunction Φ_m and its conjugate Φ_m^*, one can obtain

$$k_{c,m}^2 \int_S |\Phi_m|^2 dS = \int_S |\boldsymbol{\nabla}_t \Phi_m|^2. \tag{2.42}$$

By observing that the two surface integrals in (2.42) are positive quantities it is obvious that the eigenvalue $k_{c,m}^2$ should be greater or equal to zero. Therefore, the cutoff wavenumber $k_{c,m}$ is always a real number. The normalization condition can be written for the scalar eigenfunction by substituting the expression of the electric modal vector (2.21), (2.27) or (2.34) in (2.40), and equating in (2.42)

$$\int_S \Phi_m^2 dS = \frac{\eta_m}{Z_{c,m} k_{c,m}^2}. \tag{2.43}$$

As a consequence of $k_{c,m} \in \mathbb{R}$, the scalar eigenfunction and the modal eigenvectors can be taken as real quantities [36, p. 6]. Furthermore, for assuring the physical significance of the expressions (2.40) and (2.41), the ratio between $Z_{c,m}$ and η_m should be real and positive. Since the wave impedance is a complex number below the cutoff frequency and real above this frequency, the same should hold for the characteristic impedance. By choosing $Z_{c,m} = \eta_m$ the above condition is ensured and, unless otherwise specified, it will be adopted from now on.

The power flowing through a waveguide cross-section can also be evaluated in view of the modal representation of the electric and magnetic field quantities. By integrating the Poynting vector on the transversal section of the waveguide the active transferred power reads:

$$P = \frac{1}{2}\int_S \boldsymbol{E}_t \times \boldsymbol{H}_t^* dS = \frac{1}{2}\sum_{m=1}^{\infty} V_m(z) I_m^*(z), \tag{2.44}$$

where the orthogonality relation between the modes was used. As a consequence, one can clearly observe that the power in uniform waveguides is independently carried by each mode. The modes exchange energy at discontinuities, only.

2.1.3 Modes of rectangular waveguides

For some waveguides having canonical transversal sections the modes can be expressed by using analytical formulas. This is also the case for rectangular waveguides with a geometry as depicted in Fig. 2.2.

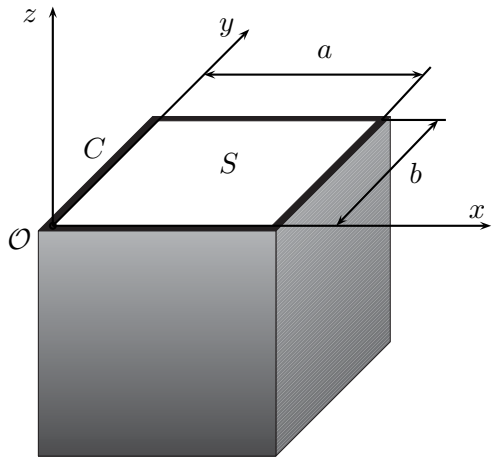

Figure 2.2: Geometry of the involved rectangular waveguide.

The scalar functions of the TE and TM modes are given by [36, p. 7]

$$\Phi_{m,n} = \begin{cases} A_{m,n}\cos\left(\frac{m\pi x}{a}\right)\cos\left(\frac{n\pi y}{b}\right), & TE \text{ modes}, \quad m,n = 0,1,2,\ldots \\ A_{m,n}\sin\left(\frac{m\pi x}{a}\right)\sin\left(\frac{n\pi y}{b}\right), & TM \text{ modes}, \quad m,n = 1,2,3,\ldots \end{cases}, \tag{2.45}$$

where a, b are the waveguide dimensions as indicated in Fig. 2.2 and the pair m, n has been used for designating a certain waveguide mode. The indexes

m and n can have zero values (but not simultaneously) for the TE modes and are always different from zero in the case of TM modes. The constant $A_{m,n}$ sets the amplitude of the modal wave. A convenient choice for $A_{m,n}$ is such that the normalization condition (2.43) is satisfied.

$$A_{m,n} = \frac{1}{k_{c,m,n}} \sqrt{\frac{\alpha_m \alpha_n}{ab}}, \tag{2.46}$$

where:

$$\alpha_i = \begin{cases} 1, & i = 0 \\ 2, & i \neq 0 \end{cases} . \tag{2.47}$$

The cutoff wavenumbers have a simple, analytical expression in the case of a rectangular domain

$$k_{c,m,n} = \sqrt{\left(\frac{m\pi}{a}\right)^2 + \left(\frac{n\pi}{b}\right)^2}. \tag{2.48}$$

The detailed expressions of the modal field quantities pertaining to a rectangular waveguide are given in Table 2.1.

Common, rectangular waveguides are used as uni-modal transmission lines. This means that the size of the transversal section is designed such that only one mode has its cut-off frequency below the operational band. However, the higher order modes, discussed in this section, are useful in characterizing the electromagnetic field at discontinuities of the transmission lines. The two dimensional functions describing the distribution of the modal quantities in the cross-section of a rectangular domain (with specific boundary conditions) can be also used as a decomposition basis in the representation of unknown or complex functions. An example in this sense will be introduced in the next section, where the modes of a rectangular domain are used in the series representation of the Green's functions.

2.2 Boundary Integral - Resonant Mode Expansion (BI-RME) method

Evaluation of the modal components of a uniform, hollow metallic waveguide and their corresponding cutoff wavenumbers can be seen as the calculation of the resonance frequencies and resonance modes of a two dimensional domain. For some simple geometry like cylindrical waveguides with rectangular, circular, coaxial or elliptical cross section, the modal quantities are known in analytical form (or series representation). In the case of arbitrary cross-sections the evaluation of the modal quantities is done using numerical techniques. A concise enumeration of these methods, developed before 1974, is presented in [104]. Currently, the most popular solutions can be divided

Table 2.1: Expressions of the TE and TM modes of a rectangular waveguide.

Quantity	TE modes	TM modes
$\Phi(x,y)$	$A_{m,n}\cos\left(\frac{m\pi x}{a}\right)\cos\left(\frac{n\pi y}{b}\right)$	$A_{m,n}\sin\left(\frac{m\pi x}{a}\right)\sin\left(\frac{n\pi y}{b}\right)$
$e_x(x,y)$	$-A_{m,n}\frac{n\pi}{b}\cos\left(\frac{m\pi x}{a}\right)\sin\left(\frac{n\pi y}{b}\right)$	$-A_{m,n}\frac{m\pi}{a}\cos\left(\frac{m\pi x}{a}\right)\sin\left(\frac{n\pi y}{b}\right)$
$e_y(x,y)$	$A_{m,n}\frac{m\pi}{a}\sin\left(\frac{m\pi x}{a}\right)\cos\left(\frac{n\pi y}{b}\right)$	$-A_{m,n}\frac{n\pi}{b}\sin\left(\frac{m\pi x}{a}\right)\cos\left(\frac{n\pi y}{b}\right)$
$e_zx(x,y)$	0	$A_{m,n}\frac{k_{c,m,n}^2}{k}\sin\left(\frac{m\pi x}{a}\right)\sin\left(\frac{n\pi y}{b}\right)$
$h_x(x,y)$	$-A_{m,n}\frac{m\pi}{a}\sin\left(\frac{m\pi x}{a}\right)\cos\left(\frac{n\pi y}{b}\right)$	$A_{m,n}\frac{n\pi}{b}\sin\left(\frac{m\pi x}{a}\right)\cos\left(\frac{n\pi y}{b}\right)$
$h_y(x,y)$	$-A_{m,n}\frac{n\pi}{b}\cos\left(\frac{m\pi x}{a}\right)\sin\left(\frac{n\pi y}{b}\right)$	$-A_{m,n}\frac{m\pi}{a}\cos\left(\frac{m\pi x}{a}\right)\sin\left(\frac{n\pi y}{b}\right)$
$h_z(x,y)$	$A_{m,n}\frac{k_{c,m,n}^2}{k}\cos\left(\frac{m\pi x}{a}\right)\cos\left(\frac{n\pi y}{b}\right)$	0

into two categories: one based on finite elements [116](Chapter 6), finite difference [116](Chapter 3) or transmission line matrix method [116](Chapter 7) and the other one based on the solution of integral equations by algorithms such as the method of moment [116](Chapter 5) or the mode matching method [36]. On the one hand the characteristics of the former class are:

- they require meshing of the cross-section. The accuracy of the solution is therefore directly related to the capabilities of defining an appropriate mesh or to the use of complex procedures such as, for example, the sub-meshing or the conformal meshing [116];
- when irregular or pointed boundaries are involved, a fine mesh is required even for the calculation of modes having a low cut-off frequency;
- fine meshing leads to a large-size standard eigenvalue matrix problem or require a multi-step iterative solution;

- computer implementations involve time-consuming procedures and/or availability of large computer memories;
- finite element methods can be used to solve complex structures characterized by complicated geometry and different materials;
- time domain methods are well recognized for their fast analysis over a wide frequency range.

On the other hand, the algorithms adopted for solving integral equation problems have the following properties:

- the meshing requirements are less complicated and simple procedures can be used to discretize the geometry under investigation [36, p. 136];
- they make use of Green's functions for the calculation of the field, which are not always easy to find for complex topologies;
- in general singular integrals have to be solved with a good accuracy;
- storage requirements are strongly reduced for the methods in this class;
- they lead to small size, non-algebraic eigenvalue problems;
- the computing time is still fairly long when many higher order modes have to be computed due to the transcendental frequency dependence of the matrix elements;
- the wide band analysis involves a frequency loop, which is more often than not a time-consuming operation.

From these characteristics it is evident that in case of waveguide structures, with simple geometry, the methods based on solving integral equation problems are the most preferred ones.

The Boundary Integral - Resonant Mode Expansion (BI-RME) method was proposed more than twenty years ago by Conciauro *et al.* [35] for the calculation of the modes of arbitrarily shaped waveguides. The methods belongs to the class of integral equations based algorithms and it leads to a *small-size, linear eigenvector problem.* As a result, the necessary time for finding the modal cut-off frequencies, often a time consuming procedure in integral equation based methods, can be reduced. Its originality resides in the fact that instead of using the common free-space Green's function it makes use of a dyadic Green's function defined inside a rectangular or circular domain.

The detailed formulation of this numerical technique is presented in [36]. In this section, the basic relations of the BI-RME method will be given with some detailed exemplification concerning the case of modal analysis of rectangular waveguides perturbed by axial circular conductors.

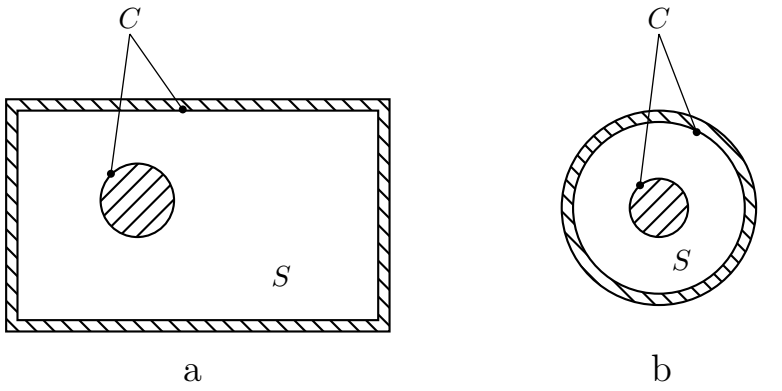

Figure 2.3: Examples of waveguide geometries employed in antenna applications. (a) - arbitrary cross-section; (b) canonical cross-section.

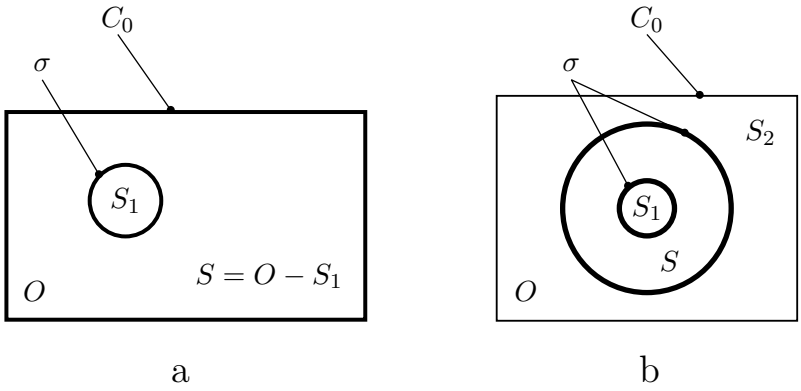

Figure 2.4: Calculation domains involved in the BI-RME method for the waveguide cross-sections presented in Fig. 2.3. (a) - arbitrary cross- section where the BI-RME box (C_0) coincides with the waveguide contour; (b) - canonical cross-section where the BI-RME box (C_0) differs from the waveguide contour.

2.2.1 Modes of waveguides having arbitrary cross-sections

The electromagnetic field quantities inside of waveguide segments, having arbitrary or canonical cross-section as the ones depicted in Fig. 2.3, can be represented by using TE, TM and TEM modes. The modes of the canonical geometries are known analytically whereas these of the arbitrary waveguides can be estimated by using the BI-RME method. As was already mentioned, at the core of this method is the use of resonant mode expansions

of the Green's functions, by means of modes defined in rectangular or circular domains. Therefore, when the arbitrary section under investigation does not have such a particular contour the problem will be extended by embedding the domain of interest S into a rectangular or circular domain O. The computational domains chosen for the two waveguide sections presented in Fig. 2.3 are depicted in Fig. 2.4. The simple case of the coaxial cable has been used here to illustrate the extension to a rectangular domain.

The internal contour σ (associated to the boundaries of the metal insertions in the waveguide) is supposed to be described by a parametric equation

$$\boldsymbol{s} = \boldsymbol{s}(l), \tag{2.49}$$

where s denotes a point on σ and l represent the length along the curve σ taken with respect to a reference point. As discussed in [35], the electric field inside the domain O, perturbed by the metallic contour σ, can be written as [35]

$$\boldsymbol{E}(\boldsymbol{r}) = -j\eta k \fint_{\sigma} \overline{\boldsymbol{G}}_e(\boldsymbol{r}, \boldsymbol{s}', k) \cdot \boldsymbol{J}_\sigma(l')\, dl', \tag{2.50}$$

where:

$\boldsymbol{r}$ represents a generic point inside of the domain O;

$\eta = \sqrt{\frac{\mu}{\varepsilon}}$ is the medium impedance;

$k = \omega\sqrt{\mu\varepsilon}$ denotes the wavenumber;

$\overline{\boldsymbol{G}}_e$ is the two-dimensional Green's function of electric type pertaining to the domain O (either rectangular or circular);

$\boldsymbol{J}_\sigma$ designates the current density on the metallic sheet σ;

$\boldsymbol{s}' = \boldsymbol{s}(l')$ indicates a source point on σ.

The dyadic Green's function has a singular behavior when the observation point $\boldsymbol{r}$ lies on the source points located on σ. Therefore, the integral in the equation 2.50 is taken in the sense of *principal value* (indicated with the dash symbol in the integral sign). The boundary conditions on the external contour C_O are satisfied due to the nature of $\overline{\boldsymbol{G}}_e$. By imposing the condition that the tangential component of the electric field $\boldsymbol{E}$ must vanish on σ, it is possible to derive an integral equation where the unknown is the current density $\boldsymbol{J}_\sigma$. This equation has nontrivial solutions, characterized by different k's that represent the cut-off wavenumbers of the modes of the canonic (rectangular or circular) waveguide perturbed by the metallic contour σ.

When separated regions exist inside the canonic contour C_o (such as S,S_1 and S_2 in Fig. 2.4) the method yields simultaneously the cutoff-frequencies and the modes pertaining to each of these closed domains. Separation between modes belonging to different regions can be done relatively

easily, by using the observation that the mode distribution is approximately zero outside the pertinent domain.

The expression of the dyadic $\overline{\boldsymbol{G}}_e$, defined on rectangular or circular domains, can be written as a sum of a transversal component $\overline{\boldsymbol{G}}_{et}$ and a longitudinal component G_{ezz} [35]

$$\overline{\boldsymbol{G}}_e(\boldsymbol{r},\boldsymbol{s}',k) = \overline{\boldsymbol{G}}_{et}(\boldsymbol{r},\boldsymbol{s}',k) + \boldsymbol{u}_z\boldsymbol{u}_z G_{ezz}(\boldsymbol{r},\boldsymbol{s}',k), \tag{2.51}$$

where $\boldsymbol{u}_z$ denotes the unit vector along the longitudinal axis of the waveguide. The dyadic components have the expressions

$$\begin{aligned}\overline{\boldsymbol{G}}_{et}(\boldsymbol{r},\boldsymbol{s}',k) &= -\frac{1}{k^2}\boldsymbol{\nabla}_t\boldsymbol{\nabla}'_t g(\boldsymbol{r},\boldsymbol{s}') + \overline{\boldsymbol{G}}_{st}(\boldsymbol{r},\boldsymbol{s}') \\ &\quad + \sum_m \frac{k^2}{k_m^2(k_m^2-k^2)}\boldsymbol{e}_m(\boldsymbol{r})\boldsymbol{e}_m(\boldsymbol{s}'), \end{aligned}\tag{2.52}$$

$$G_{ezz}(\boldsymbol{r},\boldsymbol{s}',k) = g(\boldsymbol{r},\boldsymbol{s}') + \sum_m \frac{k^2}{{k'_m}^2({k'_m}^2-k^2)}\psi_m(\boldsymbol{r})\psi_m(\boldsymbol{s}'), \tag{2.53}$$

where:

$\boldsymbol{\nabla}'_t$ is the gradient operator transverse to the z-axis at the source point;

g denotes a scalar two-dimensional Green's function;

$\overline{\boldsymbol{G}}_{et}$ is a solenoidal dyadic function normal to the boundary C_o;

k_m and k'_m are the cut-off wavenumbers of the TE and TM modes, respectively, of the rectangular (or circular) waveguide;

$\boldsymbol{e}_m$ is the electric field transverse vector of the m^{th} TE mode in the O domain;

ψ_m is the scalar function of the m^{th} TM mode in the O domain.

The Green's function g satisfies the Poisson equation in the domain O

$$\begin{aligned}\boldsymbol{\nabla}_t\boldsymbol{\nabla}_t\, g(\boldsymbol{r},\boldsymbol{s}') &= -\delta(\boldsymbol{r}-\boldsymbol{s}') \qquad \boldsymbol{r},\boldsymbol{s}' \in O \\ g(\boldsymbol{r},\boldsymbol{s}') &= 0 \qquad\qquad\quad \boldsymbol{r} \in C_\mathrm{o}\end{aligned}\ , \tag{2.54}$$

with $\delta(\boldsymbol{r}-\boldsymbol{s}')$ representing the two dimensional delta function. The relation between solenoidal dyadic $\overline{\boldsymbol{G}}_{st}$ and the scalar function g is given by the following relation [36, p. 320]

$$\boldsymbol{\nabla}_t \times \boldsymbol{\nabla}_t \times \overline{\boldsymbol{G}}_{st}(\boldsymbol{r},\boldsymbol{s}') = \overline{I}\delta(\boldsymbol{r}-\boldsymbol{s}') + \boldsymbol{\nabla}_t\boldsymbol{\nabla}'_t\, g(\boldsymbol{r},\boldsymbol{s}'). \tag{2.55}$$

The expressions of the g and $\overline{\boldsymbol{G}}_{st}$ are known in closed form for a circular domain. In the case when these quantities should be evaluated in a rectangular cross-section they can be expressed in the form of a rapidly converging one-index series. For the reader's convenience, the exact expressions of g and $\overline{\boldsymbol{G}}_{st}$ are given in Appendix A. From those relations it can be noted that they exhibit a logarithmic singularity when the observation and the source points coincides. The expressions of the modal vectors $\boldsymbol{e}_m$ are similar to those presented in Table 2.1. A deviation is noted in the definition of the scalar function of the TM modes ψ_m of the rectangular waveguide, in the sense that the expression in Table 2.1 is scaled (multiplied) with the cut-off wavenumber, in order to satisfy the normalization condition

$$\int_O \psi_m^2 dS = 1. \tag{2.56}$$

The unknown current density $\boldsymbol{J}_\sigma$ can be also split in transversal and longitudinal components [36, p. 320]

$$\boldsymbol{J}_\sigma(l') = J_t(l')\boldsymbol{t}(l') + J_l(l')\boldsymbol{u}_z, \tag{2.57}$$

with $\boldsymbol{t}(l')$ denoting the unit vector tangent to σ in the l' point. By substituting (2.51), (2.52) and (2.57) in (2.50) the transversal and longitudinal components of the electric field inside the domain O can be expressed by separated equations [36, p. 320]

$$\begin{aligned}
\boldsymbol{E}_t(\boldsymbol{r}) &= j\frac{\eta}{k}\int_\sigma \boldsymbol{\nabla}\frac{\partial g(\boldsymbol{r},\boldsymbol{s}')}{\partial l'} J_t(l')\, dl' - j\eta k \int_\sigma \overline{\boldsymbol{G}}_{st}(\boldsymbol{r},\boldsymbol{s}')\cdot\boldsymbol{t}(l')J_t(l')\, dl' \\
&\quad -j\eta k^3 \sum_m \frac{\boldsymbol{e}_m(r)}{k_m^2(k_m^2-k^2)}\int_\sigma \boldsymbol{e}_m(\boldsymbol{s}')\cdot\boldsymbol{t}(l')J_t(l')\, dl', \qquad (2.58) \\
E_z(\boldsymbol{r}) &= -j\eta k \int_\sigma g(\boldsymbol{r},\boldsymbol{s}')J_z(l')\, dl' \\
&\quad -j\eta k^3 \sum_m \frac{\psi_m(\boldsymbol{r})}{{k'_m}^2({k'_m}^2-k^2)}\int_\sigma \psi_m(\boldsymbol{s}')J_z(l')\, dl'. \qquad (2.59)
\end{aligned}$$

The logarithmic singularities of the two terms of the Green's function are integrable after multiplication by the current density. However, upon differentiating the scalar term g, the singularity changes its nature and it will result in a non-integrable singularity. This explains why the principal value symbol has been retained only in the first integral in (2.58). By employing the following identity [35]

$$\int_\sigma \frac{\partial g(\boldsymbol{r},\boldsymbol{s}')}{\partial l'}\, dl' = -\int_\sigma g(\boldsymbol{r},\boldsymbol{s}')\frac{\partial J_t(l')}{\partial l'}\, dl', \tag{2.60}$$

it is possible to eliminate the principal value integration in (2.57). The relation (2.60) was obtained from integrating by parts, observing that the

singularity of g is integrable and accounting for the following properties of g and J_t: g is zero at any point of σ lying on the external contour C_o and J_t vanishes at extremes of σ (in the case of open curves). It is once again pointed out that TE modes have no longitudinal electric field component. This axial component is given by the TM modes, only. Therefore, equation (2.58) can be used to estimate the cut-off wavenumbers of TE modes while equation (2.59) will be employed for finding the TM modes. By imposing the boundary conditions on the metallic contour σ

$$\boldsymbol{E}_t(\boldsymbol{r}) \cdot \boldsymbol{t}(\boldsymbol{r}) = 0 \qquad \boldsymbol{r} \in \sigma, \tag{2.61}$$

$$E_z(\boldsymbol{r}) = 0 \qquad \boldsymbol{r} \in \sigma, \tag{2.62}$$

the following integral equations can be obtained [36, p. 321]:

TE modes

$$\frac{1}{k^2}\frac{\partial}{\partial l}\int_\sigma g(\boldsymbol{r},\boldsymbol{s}')\frac{\partial J_t(l')}{\partial l'}\,dl' + \int_\sigma \boldsymbol{t}(l')\cdot\overline{\boldsymbol{G}}_{st}(\boldsymbol{r},\boldsymbol{s}')\cdot\boldsymbol{t}(l')J_t(l')\,dl' + \sum_m \frac{\boldsymbol{t}(l)\boldsymbol{e}_m(\boldsymbol{r})}{k_m^2}a_m = 0, \tag{2.63}$$

with the notation

$$a_m = \frac{k^2}{k_m^2 - k^2}\int_\sigma \boldsymbol{e}_m(\boldsymbol{s}')\cdot\boldsymbol{t}(l')J_t(l')\,dl', \tag{2.64}$$

TM modes

$$\int_\sigma g(\boldsymbol{r},\boldsymbol{s}')J_z(l')\,dl' + \sum_m \frac{\psi_m(\boldsymbol{r})}{{k'_m}^2}a'_m = 0, \tag{2.65}$$

with a'_m denoting

$$a'_m = \frac{k^2}{{k'_m}^2 - k^2}\int_\sigma \psi_m(\boldsymbol{s}')J_z(l')\,dl'. \tag{2.66}$$

After setting up separated equations for the TE and TM modes it is appropriate to treat them apart, in a more specific manner. In the followings the procedures adopted in this work for solving the modal distribution on waveguide segments with arbitrary cross-sections are discussed in detail.

2.2.2 Calculation of TE modes

To find the TE modes of a waveguide with arbitrary cross-section one has to solve the integral equation 2.63. A first problem is to choose an analytical representation of the unknown current density J_z. By taking into

account that its variation along the contour σ is relatively smooth (except at edges and corners, a case that will be treated separately), the following representation is adopted [36, p. 322]:

$$J_z(l') = \sum_{n=1}^{N} b_n w_n(l'), \tag{2.67}$$

with $b_n, n = 1, \cdots, N$ denoting the coefficients of the w_n base function defined on σ.

Commonly there are two approaches in defining the base functions:

- one solution is to consider that w_n have non-vanishing values on the entire domain σ (also referred to as the entire domain expansion); this is useful for simple structures, when the current distribution can be approximated with a reduced number of base functions.
- a second choice is to have base functions that have (possibly) non-zero values on a restricted domain included in σ only (often referred to as the sub-sectional expansion); the advantage of this approach is that complicated structures can be easily dealt with.

In this work piece-wise, parabolic base functions, as those presented in Fig. 2.5, will be used. The contour σ is divided into N segments, which need not necessarily be equal. As can be seen in Fig. 2.5, the functions w_n are defined on three consecutive segments and some of them are partially overlapped. The series appearing in 2.63 is regular inside the domain O and

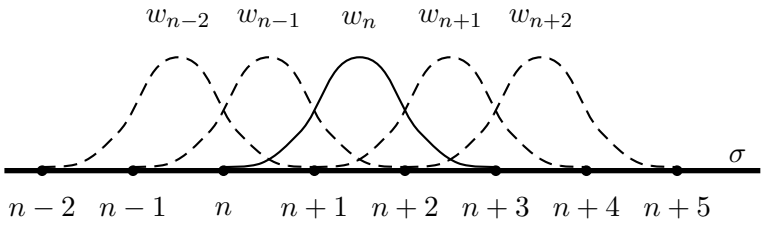

Figure 2.5: Piece-wise parabolic base functions used to represent the transversal current on the inner metallic sheet.

converge rapidly since its terms drop to zero as k_m^{-4}. Therefore, the infinite summation can be truncated up to the M^{th} term with a good approximation in the case when k is sufficiently smaller than k_m.

By substituting (2.67) in (2.63) and (2.63) and by applying the Galerkin's

procedure [56], the following algebraic equation is obtained [36, p. 322]

$$\left\{ \begin{bmatrix} \boldsymbol{U} & \boldsymbol{O}^T \\ \boldsymbol{O} & \boldsymbol{C} \end{bmatrix} - k^2 \begin{bmatrix} \boldsymbol{D} & \boldsymbol{R}^T \\ \boldsymbol{R} & \boldsymbol{L} \end{bmatrix} \right\} \begin{bmatrix} \boldsymbol{a} \\ \boldsymbol{b} \end{bmatrix} = 0, \tag{2.68}$$

where:

$\boldsymbol{a} = [a_1, a_2, \cdots, a_M]^T$ is a column vector with a_i defined in (2.64)(the superscript ^{T} denotes the matrix transpose);

$\boldsymbol{b} = [b_1, b_2, \cdots, b_N]^T$ is a vector of coefficients assigned to the base functions;

$\boldsymbol{U}$ is the identity matrix of order M;

$\boldsymbol{O}$ is the zero matrix of order $N \times M$;

$\boldsymbol{D} = \text{diag}(k_1^{-2}, k_2^{-2}, \cdots, k_M^{-2})$ is a diagonal matrix;

and the entries in the matrix $\boldsymbol{C}$, $\boldsymbol{L}$ and $\boldsymbol{R}$ are given by:

$$C_{ij} = \int_\sigma \int_\sigma g(\boldsymbol{s}, \boldsymbol{s}') \frac{\partial w_i(l)}{\partial l} \frac{\partial w_j(l')}{\partial l'} \, dl dl', \tag{2.69}$$

$$L_{ij} = \int_\sigma \int_\sigma w_i(l) w_j(l') \boldsymbol{t}(l) \cdot \overline{\boldsymbol{G}}_{st}(\boldsymbol{s}, \boldsymbol{s}') \cdot \boldsymbol{t}(l') \, dl dl', \tag{2.70}$$

$$R_{im} = \frac{1}{k_m^2} \int_\sigma w_i(l) \boldsymbol{t}(l) \cdot \boldsymbol{e}_m(\boldsymbol{s}) \, dl, \tag{2.71}$$

$$\text{with} \qquad i, j = 1, 2, \cdots, N; \quad m = 1, 2, \cdots, M.$$

At this point it is worth noting some useful properties of the matrices involved in equation (2.68). The matrices $\boldsymbol{C}$ and $\boldsymbol{L}$ are symmetric because the reciprocity of the Green's functions g and $\overline{\boldsymbol{G}}_{st}$. Moreover, the $\boldsymbol{L}$ matrix is always positive definite while the $\boldsymbol{C}$ matrix is positive definite only in the case when the inner sheet σ does not include closed loops. In the case when the contour σ has delimited P closed areas inside the computational domain O, the matrix $\boldsymbol{C}$ is semi-positive definite and its rank is $R = N - P$. In this case P vectors $\boldsymbol{b}$ exist such that $\boldsymbol{C}\boldsymbol{b} = 0$. Consequently, equation (2.68) is satisfied for $\boldsymbol{a}$ a null vector and $k = 0$ and one can denote these solution as trivial and neglect them. The linear matrix eigenproblem in equation (2.68) may be solved using standard algorithms like the one presented in [48]. The solution of this problem consist in $M+R$ positive eigenvalues k^2 and the corresponding eigenvectors $[\boldsymbol{a}\ \boldsymbol{b}]^T$. The square root of one of these eigenvalue identifies the cut-off wavenumber of a TE mode pertaining to one of the closed domain included in O. The eigenvector associated to this eigenvalue contains the coefficients that should be used for calculating the modal field

quantities associated to the TE mode. For example, the transverse, modal, electric vector reads

$$\begin{aligned}\boldsymbol{E}_t(\boldsymbol{r}) &= -j\eta\left\{\sum_{n=1}^{N} b_n\left[\frac{1}{k}\boldsymbol{\nabla}\int_\sigma g(\boldsymbol{r},\boldsymbol{s}')\frac{\partial w_n(l')}{\partial l'}\,dl'\right.\right.\\ &\left.\left.+k\int_\sigma \overline{\boldsymbol{G}}_{st}(\boldsymbol{r},\boldsymbol{s}')\cdot\boldsymbol{t}(l')w_n(l')\,dl'\right]+k\sum_{m=1}^{M}\frac{a_m\boldsymbol{e}_m(\boldsymbol{r})}{k_m^2}\right\}. \quad (2.72)\end{aligned}$$

In the situation when σ divides O in separated domains, the value of the modal electric field quantity calculated at different points within these closed regions are strongly unbalanced. By observing that the field distribution of a mode differs from zero inside the pertinent domain and is zero outside it is possible to attach the mode to a certain region. Another useful observation, for the problem of modes selection, is that the value of the cut-off wavenumber is directly related to the size of the pertaining domain. Therefore, when the region of interest is much larger than the other zones in the computation domain, it is expected that the lower eigenvalues are the desired ones.

2.2.3 Calculation of TM modes

For evaluating the TM modes the integral equation (2.65) has to be solved. A procedure, similar to that presented for the TE modes in the Section 2.2.2, will be adopted in this sense. The longitudinal current density can be expressed as a weighted sum of base functions [36, p. 322]

$$J_z(l') = \sum_{n=1}^{N} b'_n w_n(l'), \quad (2.73)$$

where b'_n are unknown coefficients and w_n represent base functions defined on σ. Piece-wise parabolic functions as depicted in Fig. 2.5 may be also adopted as base functions. After introducing (2.73) in (2.65) and applying the Galerkin's method, the integral equation problem can be written in a matrix form [36, p. 324]

$$\left\{\begin{bmatrix}\boldsymbol{U} & \boldsymbol{O}^T\\ \boldsymbol{O} & \boldsymbol{O}'\end{bmatrix}-k^2\begin{bmatrix}\boldsymbol{D}' & \boldsymbol{R}'^T\\ \boldsymbol{R}' & \boldsymbol{L}'\end{bmatrix}\right\}\begin{bmatrix}\boldsymbol{a}'\\ \boldsymbol{b}'\end{bmatrix}=0, \quad (2.74)$$

where:

$\boldsymbol{a}' = [a'_1, a'_2, \cdots, a'_M]^T$ is a column vector with a'_i defined in (2.66);

$\boldsymbol{b} = [b'_1, b'_2, \cdots, b'_N]^T$ is a vector of coefficients assigned to the base functions;

$\boldsymbol{U}$ is the identity matrix of order M;

O is the zero matrix of order $N \times M$ and O' is the null matrix of the size $N \times N$;

$\boldsymbol{D'} = \mathrm{diag}({k'_1}^{-2}, {k'_2}^{-2}, \cdots, {k'_M}^{-2})$ is a diagonal matrix;

and the entries in the matrix $\boldsymbol{L'}$ and $\boldsymbol{R'}$ are given by:

$$L'_{ij} = \int_\sigma \int_\sigma w_i(l) g(\boldsymbol{s}, \boldsymbol{s'}) w_j(l') \, dl dl', \tag{2.75}$$

$$R'_{im} = \frac{1}{k'^2_m} \int_\sigma w_i(l) \psi_m(\boldsymbol{s}) \, dl, \tag{2.76}$$

$$\text{with} \qquad i, j = 1, 2, \cdots, N; \quad m = 1, 2, \cdots, M.$$

In (2.74) the last N equations admit trivial solutions with $k = 0$, $\boldsymbol{a'} \neq 0$, $\boldsymbol{b'} \neq 0$. These solutions have no physical relevance (the zero cut-off wavenumbers correspond to TEM modes) and therefore they must be ignored. After eliminating the k^2 in these equations it is possible to express the unknown vector $\boldsymbol{b'}$ as function of $\boldsymbol{a'}$ [36, p. 324]

$$\boldsymbol{b'} = -{\boldsymbol{L'}}^{-1} \boldsymbol{R'} \boldsymbol{a'}, \tag{2.77}$$

The inverse of the matrix $\boldsymbol{L}$, can be easily estimated since the matrix is always non-singular [35, Appendix II]. Further, by replacing $\boldsymbol{b'}$ in the remaining equations of (2.74) it is possible to cast the eigenproblem into a standard formulation

$$(\boldsymbol{D'} - {\boldsymbol{R'}}^T {\boldsymbol{L'}}^{-1} \boldsymbol{R'}) \boldsymbol{a'} = k^{-2} \boldsymbol{a'}, \tag{2.78}$$

This simplified problem admits M eigenvalues and eigenvectors that correspond to the TM modes of the closed domains included in O. Analogue to the case of TE modes, the selection of the modes pertaining to the region of interest can be done by evaluating the modal field quantity at points inside and outside of this region. The expression of the longitudinal electric field reads

$$E_z(\boldsymbol{r}) = -j\eta k \left[\sum_{n=1}^{N} b'_n \int_\sigma g(\boldsymbol{r}, \boldsymbol{s'}) w_n(l') \, dl' + \sum_{m=1}^{M} \frac{{a'_m}^2}{k'_m} \psi_m(\boldsymbol{r}) \right]. \tag{2.79}$$

It is noted that, when there is a large difference between the area of the domain of interest and the areas of the other closed domains included in O, the cut-off wavenumbers can be used to make a preliminary selection of the relevant modes.

2.2.4 Calculation of TEM modes

As already discussed in the Section 2.1.1, the TEM modes of hollowed waveguides have the cut-off wavenumber zero. Therefore, the task in this case is to evaluate the modal field quantities, only. These quantities can be effortlessly determined as the gradient of a scalar potential $\Phi(\boldsymbol{r})$, which is generated by a surface charge density ρ_σ on σ [36, p. 324].

$$\Phi(\boldsymbol{r}) = \int_\sigma g(\boldsymbol{r}, \boldsymbol{s}')\rho_\sigma(l')\, dl', \tag{2.80}$$

In (2.80) g denotes the scalar Green's function that was introduced for the evaluation of the TE and TEM modes. In the general case, when σ consists of Q separated lines $\sigma_1, \sigma_2, \cdots, \sigma_Q$ and none is in contact with the boundary of the computational domain S_o, there are Q TEM modes to be determined. As stated in [26, p. 124], the modal potential $\Phi(\boldsymbol{r})$ of these modes is uniquely determined by assigning the potentials $\Phi_1, \Phi_2, \cdots, \Phi_Q$ at the inner conductors. The unknown charge density ρ_σ can be represented as a finite summation of N piece-wise base functions weighted with scalar coefficients yet to be determined

$$\rho_\sigma(l') = \sum_{n=1}^{N_1} b_n'' w_n(l') + \sum_{n=N_1+1}^{N_1+N_2} b_n'' w_n(l') + \cdots + \sum_{n=N-N_Q+1}^{N} b_n'' w_n(l'), \tag{2.81}$$

where distinctive summations represent the charge density on the separated lines $\sigma_1, \sigma_2, \cdots, \sigma_q$ of σ, and $N_1, N_2, \cdots, N_Q$ are the numbers of base functions associated to these separated contours. Equating the general expression of $\Phi(\boldsymbol{r})$ to the (assigned) values of the potential on the inner conductors and by making use of the orthogonality properties of the base functions the following simple equation results [36, p. 325]

$$\boldsymbol{L}'\boldsymbol{b}'' = \boldsymbol{f}, \tag{2.82}$$

where $\boldsymbol{b}'' = [b_1'', b_2'', \cdots, b_Q'']^T$, $\boldsymbol{L}'$ is identical with the matrix introduced in (2.74) and $\boldsymbol{f} = [f_1, f_2, \cdots, f_N]^T$ is an N dimensional vector with

$$f_n = \Phi_q \int_{\sigma_q} w_n(l')\, dl', \tag{2.83}$$

for $N_1 + N_2 + \cdots + N_{q-1} < n \leq N_1 + N_2 + \cdots + N_q$ and $q = 2, \cdots, Q$. The unknown coefficients $\boldsymbol{b}_n{}''$ can now be easily evaluated from (2.82) by multiplying the inverse of the (non-singular) matrix $\boldsymbol{L}'$ with the vector $\boldsymbol{f}$. Therefore, for a given distribution of the potentials on the internal conductors the electrostatic potential $\Phi(\boldsymbol{r})$ yields [36, p. 325]

$$\Phi(\boldsymbol{r}) = \sum_{n=1}^{N} b_n{}'' \int_\sigma g(\boldsymbol{r}, \boldsymbol{s}')w_n(l')\, dl'. \tag{2.84}$$

When the cross-section of the waveguide supports multiple TEM modes, equation (2.84) gives the distribution of the potential for a specific mode or a combination of modes. A simple procedure for selecting the TEM modes belonging to the region of interest is to choose the potential of the inner conductors such that all other modes are zero.

The numerical evaluation of the TE, TM and TEM BI-RME modes requires the calculation of a number of improper integrals involving the static and the dyadic Green's functions. A detailed description of the procedure adopted in the numerical computation of these entries (the elements of the $\boldsymbol{C}$, $\boldsymbol{L}$, $\boldsymbol{R}$, $\boldsymbol{L}'$ and $\boldsymbol{R}'$ matrices) is presented in Appendix B.

After computing all matrices in the equations (2.68), (2.74) and (2.82) an eigenproblem solver can be used to determine the cutoff wavenumbers and the spatial distribution of the waveguide modes.

2.2.5 Field representation

From an practical point of view, the representation of the modal quantities inside a transmission line can be very useful. In this thesis the spatial behavior of the modal functions are used as an first validation test of the BI-RME method.

TE modes

In the derivation of the eigenfunction corresponding to the TE modes calculated with BI-RME, we have used as an initial point the expression of the modal electric field given in (2.72). By making use of the basic relations between the field quantities and eigenfunctions and the properties of these functions it is possible to put forth the following expression of the TE eigenfunctions

$$\phi_q(\boldsymbol{r}) = \sum_{m=1}^{M^{TE}} a_{m,q}\phi_m(\boldsymbol{r}) - \sum_{n=1}^{N} b_{n,q}\left[\int_\sigma \nabla' F_0(\boldsymbol{r},\boldsymbol{s}')\cdot\boldsymbol{n}w_n(l')\,dl'\right], \quad (2.85)$$

where:

$q = 1, 2, \cdots, Q^{TE}$ represents the index of the TE mode of the arbitrary waveguide and Q^{TE} is the rank of the TE eigenproblem;

M^{TE} is the number of TE modes of the rectangular waveguide used as frame in BI-RME;

ϕ_m is the m^{th} TE eigenfunction of the rectangular waveguide;

$[a_q\ b_q]^T$ is the q^{th} eigenvector of the TE problem;

F_0 is the Green's function given in the Appendix A.1.

TM modes

The eigenfunction of the non-canonical waveguide sections are written in the case of TM modes as [36, p. 124]

$$\psi_q(\boldsymbol{r}) = \chi'_q \left\{ \sum_{m=1}^{M^{TM}} \frac{a'_{m,q}}{{k'_m}^2} \psi_m(\boldsymbol{r}) + \sum_{n=1}^{N} b'_{n,q} \left[\int_\sigma g(\boldsymbol{r}, \boldsymbol{s}') w_n(l')\, dl' \right] \right\}, \quad (2.86)$$

where $q = 1, 2, \cdots, Q^{TM}$ represents the index of the TM mode of the arbitrary waveguide and $Q^{TM} = M^{TM} + N$ is the rank of the TM eigenproblem. Note that (2.86) deviates slightly from the expression given in [36, p. 124], in the sense that the expansion was multiplied by the eigenvalue χ'_q in view of complying to the normalization condition.

TEM modes

The electrostatic potential corresponding to the TEM modes reads [36, p. 325]

$$\phi_q^{TEM}(\boldsymbol{r}) = \sum_{n=1}^{N} b''_{n,q} \left[\int_\sigma g(\boldsymbol{r}, \boldsymbol{s}') w_n(l')\, dl' \right], \quad (2.87)$$

with $b_{n,q}$ denoting the elements of the solution satisfying equation (2.82) for a certain distribution of the potentials on the N internal conductors.

The eigenfunctions (2.85) and (2.86) must comply with the normalization conditions given by

$$\int_O |\phi_q|^2 = 1; \quad \int_O |\psi_q|^2 = 1. \quad (2.88)$$

In this sense, the eigenvectors used in the representation of these scalar potentials are required to satisfy the following relations:

$$[a]_q^T [a]_q + [b]_q^T C [b]_q = \chi_q^2, \quad TE \quad \text{modes}, \quad (2.89)$$

$$[a']_q^T [a']_q = {\chi'_q}^2, \quad TM \quad \text{modes}. \quad (2.90)$$

Note that two approximation models are available for the Green's functions used in the definition of the modal quantities (2.85), (2.86), and (2.87) (see Appendix A):

- one that employs (rapidly converging) series involving logarithmic functions that incorporate implicitly the Green's functions' singular behavior (referred to as the "RCs variant") and

- one in terms of series of eigenfunctions of the rectangular computation domain (referred to as the "resonant mode expansion").

The RCs variant is highly recommended in the representation of the field quantities in the vicinity of singular points. The resonant mode expansion can also be employed in the representation of the field but with this variant is quite difficult to put in evidence the singular behavior. In later sections it will be demonstrated that the slow converging form turns out to be very efficient in evaluating the coupling coefficients between modes at planar discontinuities.

In representing the field quantities by means of logarithmic forms of the Green's functions one has to evaluate some singular integrals. These integrals can be solved in a manner that is similar to that presented in Appendix B.

2.2.6 Selection of the modes

A particularity of the BI-RME method is that when the computation domain O includes closed regions (for example in Fig. 2.4, the sub-domains S, S_1 and S_2) the solutions of the eigenvector problems incorporate the modes of all closed areas. However, from a practical perspective, it is necessary to assign these modes to the relevant regions. A criterion for distinguishing between modes of interest (hereafter denoted as *internal*) and modes that should be ignored (denoted as *external*) can be derived from the observation that the modal eigenfunctions are different from zero in the related domain, only [36, p. 140]. Actually, due to the approximation method the modes are not exactly zero outside the considered domain. In any case, a mode can be allotted to the domain S by comparing its magnitude inside and outside of S, and taking into account that values inside the domain should be much larger than the values in the complementary regions.

A simple and easily automatic procedure for selecting the internal modes was proposed in [36, 34, 5]. The procedure is based on the comparison of the quantities h_q^- and h_q^+ given by:

TE modes

$$h_q^- = \int_{\sigma^*} \left(\phi_q^-\right)^2 \, dl, \qquad h_q^+ = \int_{\sigma^*} \left(\psi_q^+\right)^2 \, dl, \tag{2.91}$$

TM modes

$$h_q^- = \int_{\sigma^*} \left(\frac{\partial \psi_q^-}{\partial \boldsymbol{n}}\right)^2 \, dl, \qquad h_q^+ = \int_{\sigma^*} \left(\frac{\partial \psi_q^+}{\partial \boldsymbol{n}}\right)^2 \, dl, \tag{2.92}$$

where σ^* denotes the closed contour from σ delimiting the domain of interest. The superscripts $^-$ and $^+$ indicate that the quantities are taken closed to the curve σ^* inside and outside of this boundary, respectively.

Difficulties in identifying the internal modes are expected in the case when some internal and external eigenfunctions are "quasi-degenerate" [36, p. 140]. These quasi-degenerate modes seem to be the result of a numerical effect and they are characterized by:

- closely spaced eigenvalues,
- comparable amplitudes inside and outside S and
- a representation of a linear combination of internal and external eigenfunctions

In treating these modes one has to search for a linear combination of a group of them, which maximize the difference between the amplitudes inside and outside of the domain of interest. As suggested in [36, p. 141], this procedure can be implemented by replacing a group of degenerated eigenvectors with a set of new vectors, constructed by means of a rotation of the quasi-degenerate ones. In the followings, a method to find the optimum rotation angle will be presented. Let $[x]_a = [x'_{1a}\ x'_{2a}\ \cdots\ x'_{Ma}]^T$ and $[x]_b = [x'_{1b}\ x'_{2b}\ \cdots\ x'_{Mb}]^T$ be two quasi-degenerate eigenfunctions that are transformed into a new pair $[x]'_a$ and $[x]'_b$ in accordance with

$$\begin{bmatrix} [x]'_a \\ [x]'_b \end{bmatrix} = \begin{pmatrix} \cos\Theta & -\sin\Theta \\ \sin\Theta & \cos\Theta \end{pmatrix} \begin{bmatrix} [x]_a \\ [x]_b \end{bmatrix}, \tag{2.93}$$

where Θ represents the rotation angle to be found. In a generalized form, the quantities h_j^+ and h_j^- attached to an eigenvector $[x]_j$ can be approximated by

$$h_j^+ = \alpha \sum_{i=1}^{N_s} \left(\Phi_{ji}^+\right)^2, \tag{2.94}$$

$$h_j^- = \alpha \sum_{i=1}^{N_s} \left(\Phi_{ji}^-\right)^2, \tag{2.95}$$

where:

N_s represents the number of equal segments of σ^* used in the numerical integration;

α denotes an integration constant;

$\Phi_{ji}^{\pm} = [x]_j[M]_i^{\pm}$ is the value of the j^{th} eigenfunction $\psi_j^{\pm}$ or $\partial\phi_j^{\pm}/\partial\boldsymbol{n}$ at the middle of the i^{th} segment of σ^*; $[M]_i^{\pm}$ is a column vector that can be derived from (2.85) or (2.86).

By combining (2.93) and (2.95) the quantities h'^{+}_{a} and h'^{-}_{a} corresponding to the rotated vector $[x]'_a$ read

$$h'^{\pm}_{a} = h^{\pm}_{a}\cos^2\Theta + h^{\pm}_{b}\sin^2\Theta - \beta^{\pm}\sin 2\Theta, \tag{2.96}$$

with the notation

$$\beta^{\pm} = \alpha\sum_{i=1}^{N_s}\Phi^{\pm}_{ai}\Phi^{\pm}_{bi}. \tag{2.97}$$

Further, a cost function F_{cost} is defined in order to solve the optimization problem in Θ. Initially the objective function was defined as

$$F_{cost} = h'^{+}_{a} - h'^{-}_{a}. \tag{2.98}$$

After some tests it was concluded that this function has a low sensitivity with respect to the extreme points and, therefore, a new relation was proposed

$$F_{cost} = \frac{h'^{+}_{a}}{h'^{-}_{a}}. \tag{2.99}$$

The maxima and minima of this new cost function are searched among the extreme points of the numerator and denominator quantitates in (2.99). These points can be easily calculated by simply equating to zero the first derivative of $h'^{\pm}_{a}$ and finding the angles that satisfy this equation:

$$\Theta = \frac{1}{2}\arctan\frac{2\beta^{\pm}}{h'^{\pm}_{b} - h'^{\pm}_{a}}. \tag{2.100}$$

If the cost function F_{cost} increases/ decreases significantly, the $[x]'_a$ is allotted to the internal/ external region. Otherwise, if the h'^{+}_{a} and h'^{-}_{a} quantities remain comparable, the eigenvector $[x]'_a$ will be omitted from the field representation. Similar discussion holds for the $[x]'_b$ vector. The complete procedure adopted for the selection of the internal modes can be summarized in the following steps.

1. Evaluate the h^{+}_{q} and h^{-}_{q} quantities for all computed modes of the arbitrary section.

2. The eigenvectors satisfying $\gamma h^{-}_{q} > h^{+}_{q}$, with a pre-defined threshold γ, are included in the I-set of the internal modes and all those fulfilling the condition $\gamma h^{+}_{q} > h^{-}_{q}$ are denoted as external modes (constituting the E-set). The remaining modes that were not included in I-set or E-set are considered inaccurate and they have to be assigned to I-set, E-set or ignored, after a further examination. The γ threshold is a number smaller than 1 (in this work $\gamma = 0.05$ was used).

3. Treat sequentially the inaccurate modes. A quasi-degenerated mode is considered as possibly corrupted by the numerical coupling with another quasi-degenerated mode if such vectors exist with a small difference between their wavenumbers (e.g. 5%). For these vectors, the de-coupling algorithm presented above in this section is applied and the modes are allotted to the I-set, E-set or if the amplitudes inside and outside of σ^* remain comparable, the modes are ignored. Moreover, the quasi-degenerated modes that have isolated wavenumbers are disregarded, as well.

Conclusions related to the performance of the above selection algorithm will be presented later in the Section 2.2.8 dedicated to the computer implementation of the BI-RME method.

2.2.7 Quasi-orthogonality of the eigenfunctions

The Mode Matching Method requires that the expansion functions used in the waveguide sections are orthogonal. Due to the truncations of the Green's series in the BI-RME method the modal quantities calculated with this algorithm turn out to be quasi-orthogonal. A detailed analysis was carried out, in order to identify the parameters that control the orthogonality of the BI-RME modes. The discussion is presented for the TM modes[1] with the observation that a similar formulation can be derived for the TE modes. The TM eigenfunctions given in (2.86) can be rewritten as:

$$\psi_q(\boldsymbol{r}) = \chi'_q \left\{ [\psi(\boldsymbol{r})]^T \boldsymbol{D'} [a']_q + \sum_{n=1}^{N} b'_{n,q} \left[\int_\sigma g(\boldsymbol{r}, \boldsymbol{s'}) w_n(l')\, dl' \right] \right\}, \qquad (2.101)$$

where $[\psi(\boldsymbol{r})] = [\psi_1(\boldsymbol{r}), \psi_2(\boldsymbol{r}), \cdots, \psi_{M^{TM}}(\boldsymbol{r})]$ and $\boldsymbol{D'}$ is the diagonal matrix introduced in (2.74). By substituting the scalar Green's function g with its resonant series expansion, the integral term in (2.101) yields

$$\int_\sigma g(\boldsymbol{r}, \boldsymbol{s'}) w_n(l')\, dl' = \sum_{i=1}^{\infty} \frac{\psi_i^{TM}(\boldsymbol{r})}{k_i'^2} \int_\sigma \psi_i^{TM}(\boldsymbol{s'}) w_n(l')\, dl'. \qquad (2.102)$$

From (2.77) and (2.78) one can obtain

$$\boldsymbol{D'} [a']_q = \chi'^{-2}_q [a']_q - \boldsymbol{R'}^T [b']_q \qquad (2.103)$$

with $[b']_q = [b'_{1,q}, b'_{n,q}, \cdots, b'_{N,q}]^T$ being a column vector.

[1] The formulation was suggested to the author by Professor Giuseppe Conciauro (personal correspondence).

By introducing (2.103) in (2.101) and by recalling the definition (2.76) of the elements in $\boldsymbol{R}'$, the TM eigenfunctions become

$$\psi_q(\boldsymbol{r}) = \chi'_q \left\{ [\psi(\boldsymbol{r})]^T {\chi'}_q^{-2} [a']_q + [\epsilon(\boldsymbol{r})][b']_q \right\}, \tag{2.104}$$

where $[\epsilon(\boldsymbol{r})] = [\epsilon_1(\boldsymbol{r}), \epsilon_2(\boldsymbol{r}), \cdots, \epsilon_N(\boldsymbol{r})]^T$ with

$$\begin{aligned} \epsilon_n(\boldsymbol{r}) &= \int_\sigma g(\boldsymbol{r}, \boldsymbol{s}') w_n(l')\, dl' - \sum_{i=1}^{M^{TM}} \frac{\psi_i^{TM}(\boldsymbol{r})}{{k'_i}^2} \int_\sigma \psi_i^{TM}(\boldsymbol{s}') w_n(l')\, dl' = \\ &= \sum_{i=M^{TM}+1}^{\infty} \frac{\psi_i^{TM}(\boldsymbol{r})}{{k'_i}^2} \int_\sigma \psi_i^{TM}(\boldsymbol{s}') w_n(l')\, dl'. \end{aligned} \tag{2.105}$$

Observing that the eigenfunctions of the frame domain are orthonormal

$$\langle \psi_i^{TM}, \psi_j^{TM} \rangle = \begin{cases} 1 & \text{for} \quad i = j \\ 0 & \text{for} \quad i \neq j \end{cases}, \tag{2.106}$$

the inner product of the modes pertaining to an arbitrary domain reads

$$\langle \psi_p, \psi_q \rangle = (\chi_p \chi_q)^{-1} [a']_p [a']_q + (\chi_p \chi_q) [b']_p^T [\epsilon] [\epsilon]^T [b']_q. \tag{2.107}$$

Due to the normalization condition (2.90) and the orthogonality of the eigenvectors $[a']_q$ we finally obtain

$$\langle \psi_p, \psi_q \rangle = \delta_{pq} + E_{pq} \tag{2.108}$$

where δ_{pq} denotes the Kronecker delta function and

$$E_{pq} = (\chi_p \chi_q) [b']_p^T [\epsilon] [\epsilon]^T [b']_q, \tag{2.109}$$

represents the deviation from orthogonality of the inner product of the eigenvectors of the arbitrary section. It is evident from (2.105) that this error decreases and tends to zero with increasing number of the expansion functions of the rectangular frame.

$$\lim_{M^{TM} \to \infty} E_{pq} = 0. \tag{2.110}$$

In conclusion the TM modes, evaluated by the BI-RME method, are quasi-orthogonal on the enlarged domain O. The orthogonality of these functions is attained only in the ideal case, when the numbers of terms in the resonant mode expansion is infinite. In all the practical situations, a sufficient degree of orthogonality can be achieved with a relatively large number of modes of the rectangular box (typically hundreds to thousands).

2.2.8 Computer implementation and numerical validation

The BI-RME algorithm described in the previous sections was implemented in a MATLAB® computer code. The integrals involved by the evaluation of the entries in the eigenproblems (2.68) and (2.74) were computed numerically by using a three points Gauss scheme and singularities of these integrals were treated analytically. The eigenvector problems were solved using the functions available in the MATLAB environment (in fact MATLAB uses LAPACK routines to compute eigenvalues and eigenvectors [2]). Two basic functions were implemented for the evaluation of the modes of rectangular coaxial waveguides (Fig. 2.3.a) and the modes of the coaxial cables (Fig. 2.3.b), respectively. For gaining confidence in the software implementation,

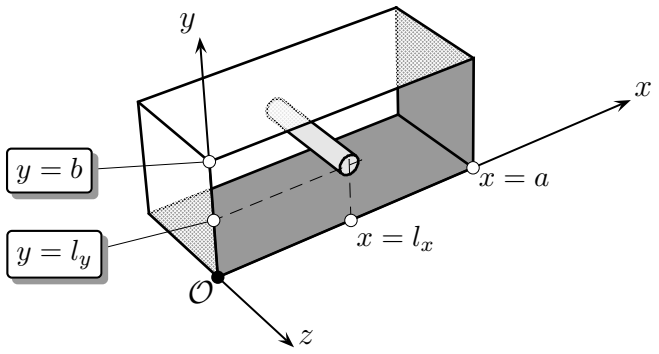

Figure 2.6: Segment of a rectangular waveguide containing an inner cylindrical conductor; the diameter of the conductor is taken to be $2\,\rho$.

extended computer simulations were carried out using the generated MATLAB codes. This dissertation only includes the most relevant results related to the numerical integration and the correctness of the waveguide modes.

Numerical integration

Firstly, attention has been given to the evaluation of the elements of the matrix $\boldsymbol{R}$,$\boldsymbol{L}$,$\boldsymbol{C}$,$\boldsymbol{R}'$ and $\boldsymbol{L}'$, which involve numerical integration. The numerical experiments were carried out for a hollow, square waveguide of dimensions $a = b = 20\,\text{mm}$ and having a *centered* inner conductor of diameter $2\,\rho = 0.64\,\text{mm}$ (see Fig. 2.6 for the significance of these dimensions). Note that the diameter of the inner pin was chosen in accordance with that of a sub-miniature version A (SMA) connector. The results produced with the proposed integration scheme were compared against those obtained using a general purpose integration function available in MATLAB. The MATLAB built-in function implements a low order method using an adaptive recursive Simpson's rule. Some relevant results of this comparison study are presented in Table 2.2. In this table, the Gauss column represents the computation

Table 2.2: Performances of different numerical integration schemes.

Quantity	Matrix size	Computation time [s]		Ratio	Rel. dev. [%]
		Gauss	Simpson		
$\boldsymbol{R}$	9×334	0.25	30.51	122	0.42
$\boldsymbol{R}$'	9×294	0.26	26.92	101	0.46
$\boldsymbol{C}$	9×9	0.30	156.21	517	0.63
$\boldsymbol{L}$	9×9	0.09	49.53	516	0.09
$\boldsymbol{L}$'	9×9	0.10	52.60	517	0.09

times when the singularities were solved analytically and the times in the Simpson column are given for the case when the singularities where solved numerically (no special treatment).

Note that the precision in the adaptive Simpson's procedure was set to a relatively low level 10^{-4}. Clearly, from the Table 2.2 is evident that the time spend to develop specific integration schemes for calculating the elements of the eigenvector problems in BI-RME turned out to be extremely beneficial. By treating analytically the singularities it was possible to achieve very low computation times whereas the relative deviation (Rel. dev.) between the two solutions was less than 1%.

Validation of the BI-RME modes

A natural question that emerges after the calculation of the waveguide modes is "*Are these results correct?*". To sort out this interrogative problem three waveguide configurations have been used as benchmark. The configurations are:

- a cylindrical waveguide with radius $\rho = 8\,\text{mm}$ embedded into a square waveguide with $a = b = 20\,\text{mm}$. This model is denoted as the *C model*;
- a coaxial cable with the dimensions replicating a SMA connector ($r_{in} = 0.64\,\text{mm}$, $r_{out} = 2.05$ $\varepsilon_r = 1.951$) placed inside a square waveguide ($a = b = 20\,\text{mm}$). The configuration is referred to as the *CC model*.
- a square waveguide of dimensions $a = b = 20\,\text{mm}$ perturbed by a centered inner conductor of radius $\rho = 0.64\,\text{mm}$, hereafter denoted as the *CR model*

The *C model* offers the possibility to compare the results calculated with BI-RME with analytical solutions readily available in the literature for the circular waveguides. In the case of BI-RME, the internal domain was taken to be the cross-section of the inner conductor. The performances of the mode

selection algorithm (discussed in Section 2.2.6) are depicted in Fig.2.7. In this figure "1" indicates a mode pertaining to the internal domain and zero a mode of the external region or a inaccurate mode. Since the internal and external regions have comparable areas, the cut-off frequencies for the two domains are in the same frequency range. Therefore, searching for the modes of interest is a necessary step before using the results in further analysis. The accuracy of the cutoff frequencies is tested by comparison with the analytical values. The results of this test are depicted in Fig. 2.8 and Fig. 2.9. It is noticed that the error between the two sets of solutions is less than 0.15%. Also, the representation of the eigenfunctions in Fig. 2.10 validate the BI-RME implementation.

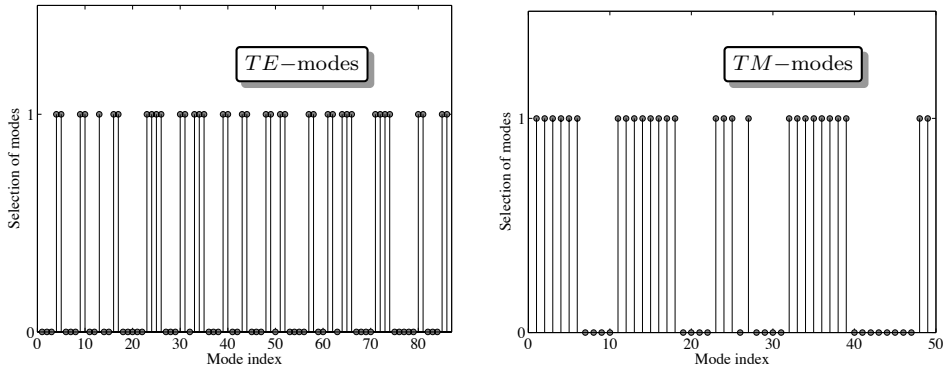

Figure 2.7: Selection of the *internal* modes

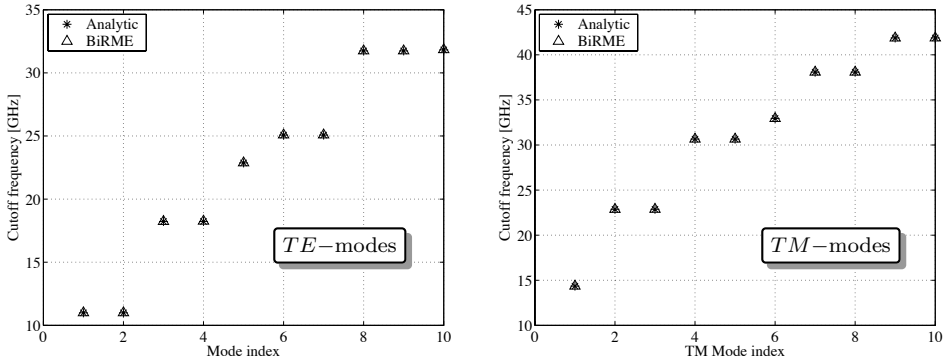

Figure 2.8: The cutoff frequencies of the modal eigenfunctions in the case of the *C model*; computations using BI-RME and analytical formulas

The study of the *CC model* further confirmed the robustness of the modes selection algorithm. A comparative investigation of the cutoff frequencies is presented in Table 2.3. The relative error in this case is lower than 0.26%. In Fig.2.11 some of the patterns of the coaxial cable eigen-

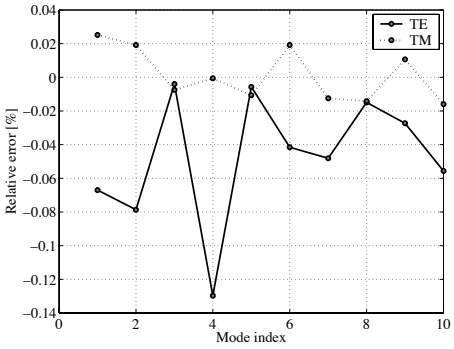

Figure 2.9: The relative deviation between the computed cutoff frequencies of the modal eigenfunctions in the case of the *C model*.

Table 2.3: Cutoff frequencies of the coaxial cable *CC model*.

Mode	Symmetry	BI-RME [GHz]	Analytic [GHz]	Relative Error [%]
TE_{11}	Cos	26.151	26.109	0.16
TE_{11}	Sin	26.151	26.109	0.16
TE_{21}	Cos	49.383	49.258	0.25
TE_{21}	Sin	49.387	49.258	0.25

function are plotted, in order to verify if the selected modes have a correct behavior inside the domain of interest.

The modal quantities of the non-canonical waveguide represented by the *CR model* can not be expressed in closed forms. Therefore, an all-purpose FEM module for solving Partial Differential Equations (PDE's) was used to generate reference results. The cutoff frequencies of the modal eigenfunctions obtained by using BI-RME were compared against those computed with FEM runs with increasingly denser meshes. The results of this comparison are given in Fig. 2.12. Both plots clearly demonstrate the fact that the cutoff frequencies computed by means of the FEM module converge (quite rapidly) to the BI-RME solution. This aspect is further emphasized by the plot of the relative deviation between the cutoff frequencies computed using BI-RME, on one hand, and with FEM in the case of the finest mesh (mesh "FEM3" in Fig. 2.12), on the other hand, that is presented in Fig. 2.13.

The spatial distribution of the first 4 TE- and 4 TM- eigenfunctions generated by BI-RME and FEM modules are depicted in Figs. 2.14 and 2.15, respectively. Note that some of the plots generated on the basis of the FEM data have been rotated. This rotation is intrinsic to the employed module and cannot be controlled by the user. Apart from this rotation, the plots

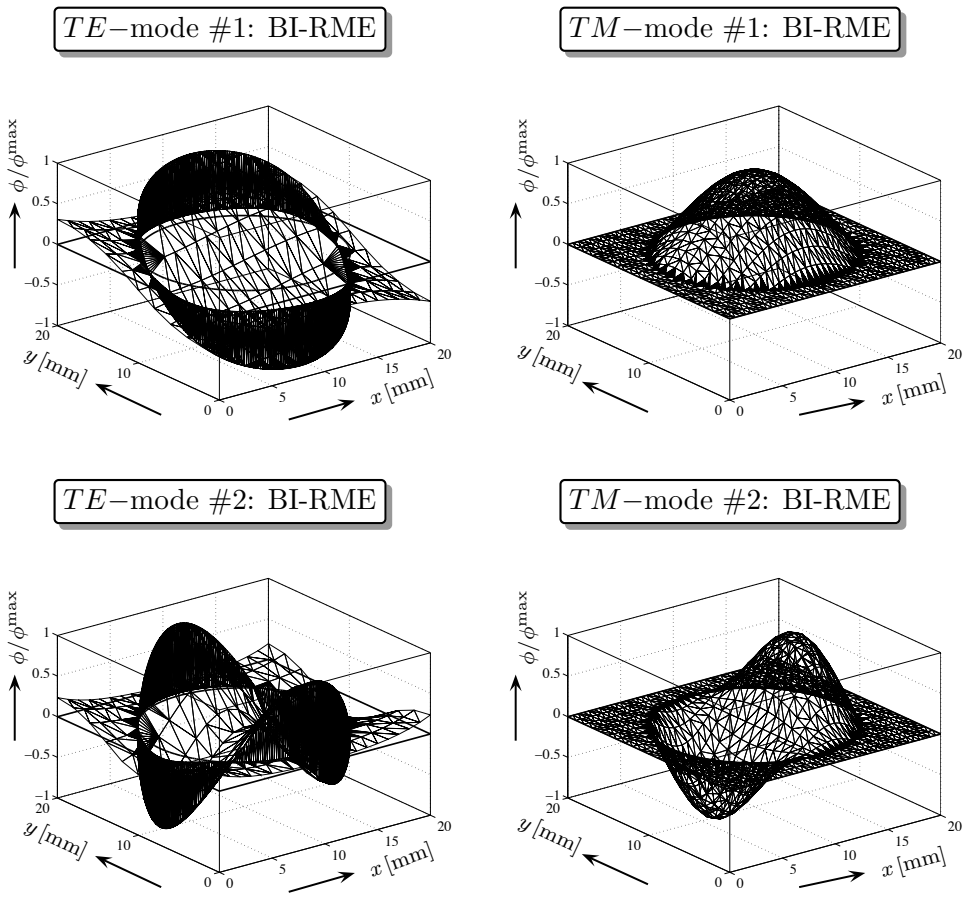

Figure 2.10: The spatial distribution of modal eigenfunctions in the case of the *C model*: the first 2 $TE-$ and $TM-$ modes.

in Figs. 2.14 and 2.15 illustrate very well the correctness of the BI-RME computations. The same conclusion follows from examining Fig. 2.16 that concerns the $TEM-$mode

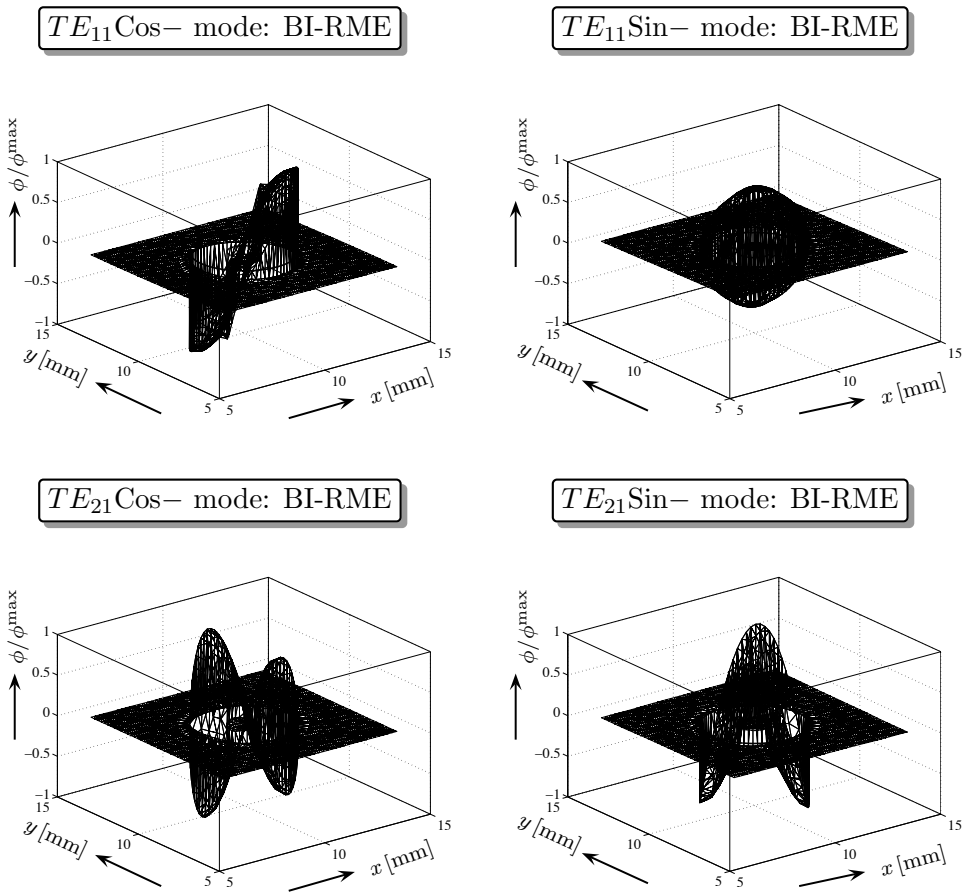

Figure 2.11: The spatial distribution of modal eigenfunctions in the case of the *C model*: the first 2 $TE-$ and $TM-$ modes.

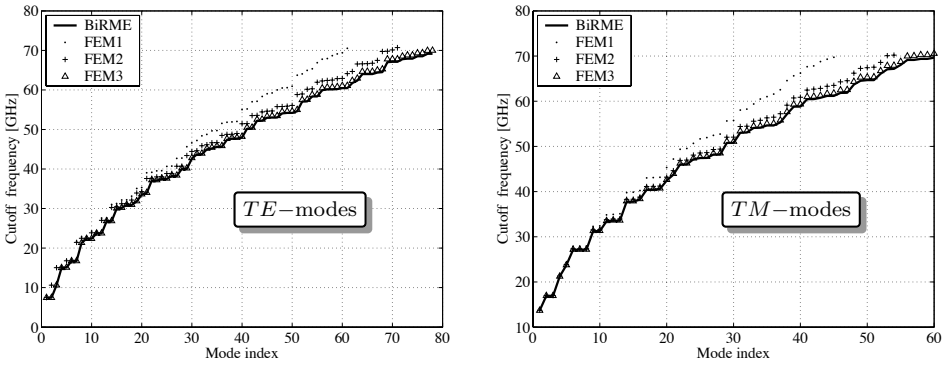

Figure 2.12: The cutoff frequencies of the modal eigenfunctions in the case of the *CR model*; computations using BI-RME and FEM with increasingly dense meshes (FEM1- coarse mesh, FEM3 -finest mesh).

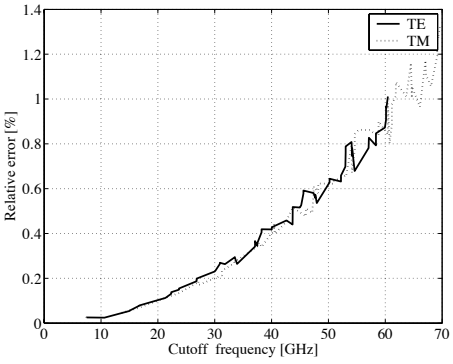

Figure 2.13: The relative deviation between the computed cutoff frequencies of the modal eigenfunctions in the case of the *CR model*; computations using BI- RME and FEM with the finest mesh (mesh "FEM3" in Fig. 2.12).

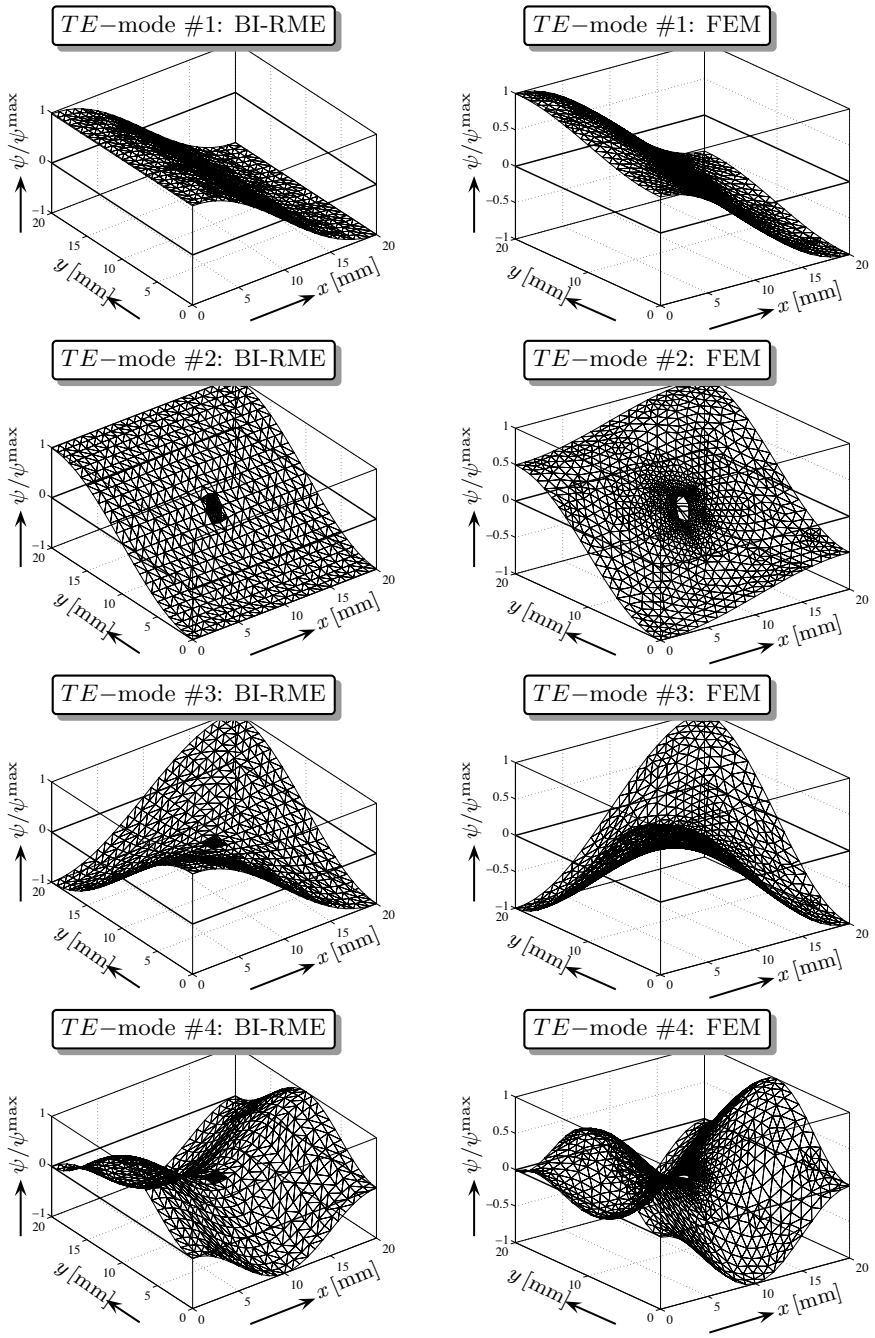

Figure 2.14: The spatial distribution of the modal eigenfunctions in the case of the *CR model*: the first 4 $TE-$modes.

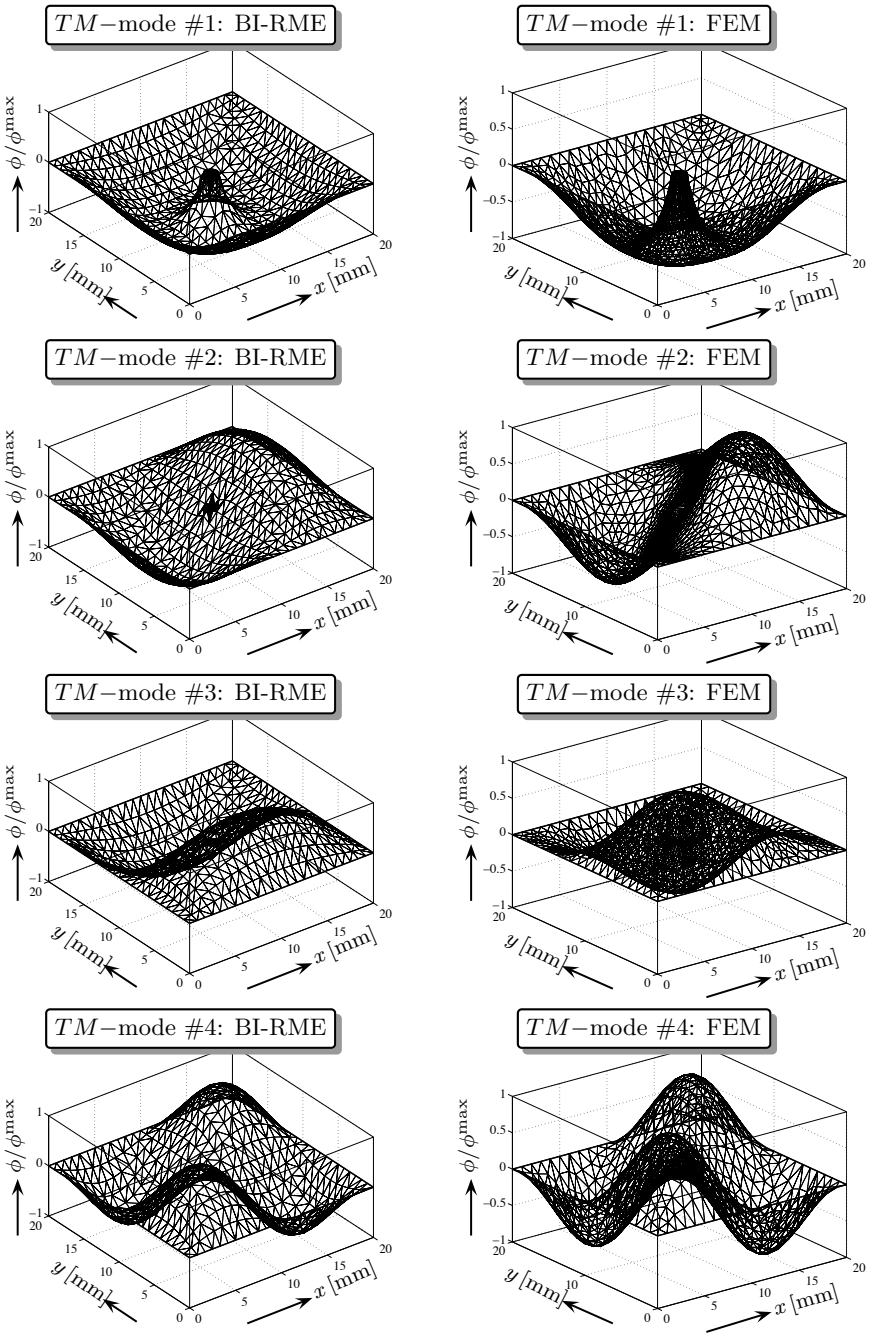

Figure 2.15: The spatial distribution of the modal eigenfunctions in the case of the *CR model*: the first 4 $TM-$modes.

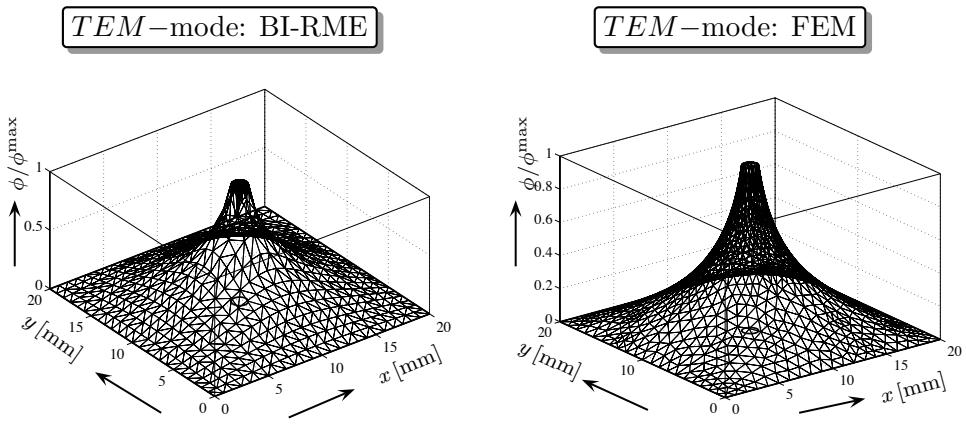

Figure 2.16: The spatial distribution of modal eigenfunctions in the case of the *CR model*: the $TEM-$mode.

The relevance of the three case studies included in this section is further outlined in the followings:

- The analysis of the *C model* demonstrated that the modal cutoff frequencies provided by BI-RME are very accurate. The mode selection procedure had to deal with internal and external modes having cutoff frequencies in the same range. Representation of the eigenfunction patterns is illustrative for the correctness of the BI-RME modes. Suspicious behavior is noted in the case of TE modes, which are not exactly zero outside the relevant domain.

- By analyzing the coaxial cable model, the accuracy of the BI-RME calculations was furthermore substantiated. The representation of the modal quantities revealed the fact that, by increasing the distance between the contour of the internal domain and the rectangular frame, the quality of the BI-RME TE modes is improved. This is a model that will often be used in the antenna design procedure and, therefore, is recommended to have it very well analyzed.

- The arbitrary waveguide cross-section proposed in the *CR model* required the use of a numerical method to generate reference results. It is noticed that the mode selection algorithm could not be tested on this model due to the fact that the cutoff frequencies of the "external" domain (the circular waveguide represented by the inner pin) are much higher than the maximum frequency in the analysis. Therefore, all the computed modes are either internal or inaccurate.

Additional to the validation tests presented in this section there were other necessary numerical investigations performed during the implementa-

tion process. For example, some peculiar aspects of the BI-RME method were investigated in [75] by means of numerical implementation described in this section.

For uniform waveguides, the modes defined on the transversal section can be evaluated at any point along the transmission line by simply applying a multiplication with a known coefficient. In the case when the configuration under investigation comprises junctions of waveguide segments having different cross-sections it is necessary to evaluate the coupling between the modes exited at the discontinuity.

2.3 Mode Matching analysis of planar discontinuities

The Mode Matching Method is probably the most adequate approach to the full wave analysis of guided structures. The theoretical formulations of this technique can be traced back to the fifties [90, 79], when the *single mode equivalent networks* were proposed for representing complex waveguide discontinuities in terms of lumped circuit elements. Currently, there are many variants of this method, which take into account also higher order modes excited at discontinuities [36]. In this section, the basic formulation of this method is introduced in order to have a consistent definition of the terminology that will be later used in the design of antenna elements.

2.3.1 Network formalism of waveguide discontinuities

The modal decomposition of the electromagnetic field inside guided structures allows for a simplified representation of waveguide discontinuities as a *multi-port* circuit. A schematic description of this concept is presented in Fig. 2.17.

When the waveguide discontinuity refers to a sharp transition from one arbitrary section to a different waveguide section (with the non-overlapping areas metalized) the electromagnetic field at this jump can be approximated as a superposition of a finite number of waveguide modes. The modes at each side of the discontinuity are selected from those corresponding to the pertinent waveguide.

Let N_1 and N_2 being the number of modes retained in the approximation of field quantities inside the two connected waveguides. For each of these modes it is possible to define an equivalent modal voltage and current (see Section 2.1). The link between these circuit parameters is described by the so-called microwave network formalism [36, p. 57]. The system of linear equations derived from the Maxwell's equations, which relates the $N_1 + N_2$

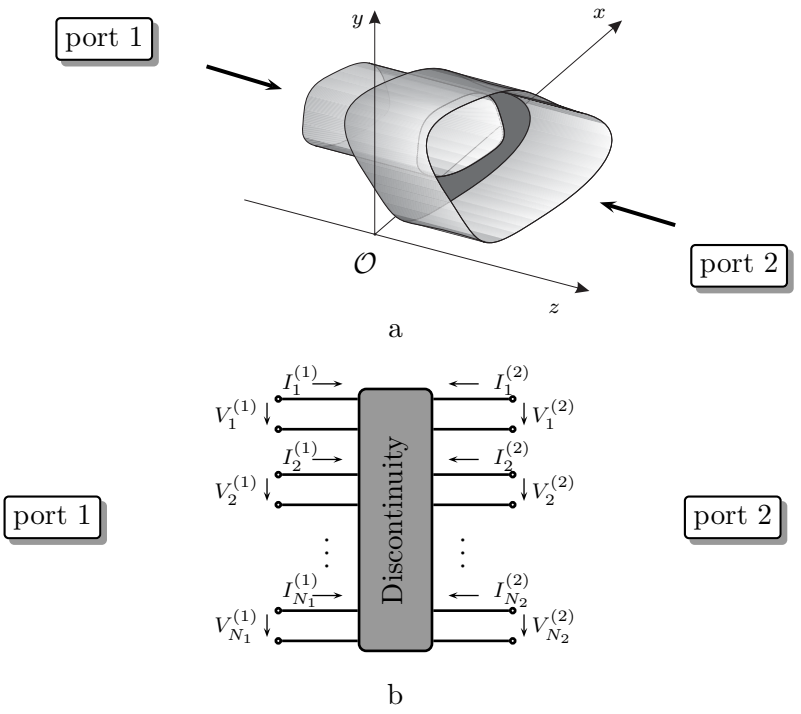

Figure 2.17: Microwave network formalism of waveguide discontinuities. (a) - arbitrary waveguide step junction; (b) - multiport description.

voltages to the $N_1 + N_2$ modal currents reads

$$[I] = [Y] \cdot [V], \tag{2.111}$$

where $[I] = [I_1^1, I_2^1, ...I_{N_1}^1, I_1^2, I_2^2, ...I_{N_2}^2]^T$ is a column vector of the currents, $[V] = [V_1^1, V_2^1, ...V_{N_1}^1, V_1^2, V_2^2, ...V_{N_2}^2]^T$ is that of the voltages and $[Y]$ is a $(N_1 + N_2) \times (N_1 + N_2)$ matrix of coupling admittances between all modes.

In most practical cases the interconnected waveguides are uni-modal transmission lines. This means that only one mode satisfies the propagation condition, all the other modes excited at the discontinuity being of evanescent nature. However, the non-propagating modes should be considered in the mechanism of transferring the energy when discontinuities are closely positioned. By incorporating the higher order modes in the circuit description of the discontinuity the concept of admittance is generalized and therefore the $[Y]$ matrix is usually referred to as a Generalized Admittance Matrix (GAM). Rearranging the linear equations in the system (2.111) it is possible to define a Generalized Impedance Matrix (GIM), which satisfy the relation:

$$[V] = [Z] \cdot [I]. \tag{2.112}$$

By expressing the modal quantities in terms of direct $[a]$ and reflected $[b]$ wave vectors a Generalized Scattering Matrix (GSM) can be introduced to describe the transition between the two waveguide sections

$$[b] = [S] \cdot [a]. \tag{2.113}$$

The direct and reflected waves can be defined in terms of equivalent voltage and current amplitudes according:

$$a_m^{(i)} = \frac{V_m^{(i)} + Z_{c,m}^{(i)} I_m^{(i)}}{2\sqrt{Z_{c,m}^{(i)}}}, \tag{2.114}$$

$$b_m^{(i)} = \frac{V_m^{(i)} - Z_{c,m}^{(i)} I_m^{(i)}}{2\sqrt{Z_{c,m}^{(i)}}}. \tag{2.115}$$

Consequently, the following relations hold

$$V_m^{(i)} = \sqrt{Z_{c,m}^{(i)}} \left(a_m^{(i)} + b_m^{(i)} \right), \tag{2.116}$$

$$I_m^{(i)} = \sqrt{Y_{c,m}^{(i)}} \left(a_m^{(i)} - b_m^{(i)} \right). \tag{2.117}$$

In practice, often it is necessary to convert one set of parameters into another one. Therefore, the interrelations among the above generalized matrix descriptions are provided in the followings

$$[\tilde{Y}] = [\tilde{Z}]^{-1} = ([\mathrm{U}] + [S])^{-1} \cdot ([\mathrm{U}] - [S]), \tag{2.118}$$

$$[\tilde{Z}] = [\tilde{Y}]^{-1} = ([\mathrm{U}] + [S]) \cdot ([\mathrm{U}] - [S])^{-1}, \tag{2.119}$$

$$[S] = \left([\tilde{Z}] - [\mathrm{U}] \right) \cdot \left([\tilde{Z}] + [\mathrm{U}] \right)^{-1} \tag{2.120}$$

$$= \left([\mathrm{U}] + [\tilde{Y}] \right)^{-1} \cdot \left([\mathrm{U}] + [\tilde{Y}] \right), \tag{2.121}$$

where [U] denotes the identity matrix and the tilde was used to indicate that the entries in the generalized admittance and impedance matrices are normalized according to the following expressions

$$\tilde{Y}_{m,n}^{(i,j)} = \frac{Y_{m,n}^{(i,j)}}{\sqrt{Y_{c,m}^{(i)}}\sqrt{Y_{c,n}^{(j)}}} \tag{2.122}$$

$$\tilde{Z}_{m,n}^{(i,j)} = \frac{Z_{m,n}^{(i,j)}}{\sqrt{Z_{c,m}^{(i)}}\sqrt{Z_{c,n}^{(j)}}} \tag{2.123}$$

Note that the characteristic admittances and impedances ($Z_{c,m}$ and $Y_{c,m}$) have real or complex values depending on the analysis frequency (similar to the wave admittance). Therefore, attention must be given when taking the square root from complex quantities (for example to avoid simplifications like $\sqrt{Z_{c,m}^{(i)}}\sqrt{Z_{c,m}^{(j)}} = \sqrt{Z_{c,m}^{(i)} Z_{c,m}^{(j)}}$).

2.3.2 Analysis of a step junction

Complicated, colinear waveguide structures can be studied by splitting the configuration in segments of uniform waveguide and simple transitions among different cross-sections. The network parameters of a uniform waveguide segment are evaluated using elementary trigonometric functions PageciteConciauro61. More elaborated procedures are required for the characterization of the step junctions between waveguide segments. These formulations are either based on the power conservation principle or on the continuity properties of electromagnetic field quantities. In the followings the methodology based on the field continuity is summarized.

We consider a transition from a waveguide with a small cross-section (S_1) to a waveguide having a larger cross-section (S_2), as illustrated in Fig. 2.17. The junction is located at $z = 0$ and consists of a $S_a = S_1 \cap S_2$ open aperture and a metallic area $S_c = S_2 - S_1$. In the plan of the junction the boundary conditions impose the continuity of the tangential electric and magnetic fields on the aperture S_a and the vanishing of the tangential electric field on the metal. By denoting with $E_t^{(i)}$ and $H_t^{(i)}$ the transversal electric and magnetic field components at the ports $i = 1, 2$ the following relations hold

$$\boldsymbol{E}_t^{(2)} = \begin{cases} \boldsymbol{E}_t^{(1)} & \text{on} \quad S_a \\ 0 & \text{on} \quad S_c \end{cases}, \tag{2.124}$$

$$\boldsymbol{H}_t^{(2)} = \boldsymbol{H}_t^{(1)} \quad \text{on} \quad S_a \ . \tag{2.125}$$

By expressing the field quantities as a finite summation of modal components the continuity relations (2.124) and (2.125) can be put in matrix form ([36, p. 64]):

$$[V_2] = [W] \cdot [V_1], \tag{2.126}$$

$$[I_1] = -[W]^T \cdot [I_2]. \tag{2.127}$$

The minus sign in (2.127) was introduced to indicate that the currents at all ports enter the discontinuity. The elements of the coupling matrix $[W]$ are given by:

$$w_{m,n} = \int_{S_1} \boldsymbol{e}_m^{(2)} \cdot \boldsymbol{e}_n^{(1)} \, dS = \int_{S_1} \boldsymbol{h}_m^{(2)} \cdot \boldsymbol{h}_n^{(1)} \, dS, \tag{2.128}$$

where $\boldsymbol{e}_p^{(i)}$ and $\boldsymbol{h}_p^{(i)}$ represent the p^{th} electric and magnetic modal eigenvectors at port $i = 1, 2$.

The coupling matrix $[W]$ describes the discontinuity as a function of geometry and materials, in the absence of sources. To evaluate the electromagnetic field quantities, it is necessary to specify the source in terms of some modal currents or voltages, which can be used in (2.126) and (2.127) to find all the other modal unknowns. Other descriptions, such as the generalized scattering matrix or the generalized admittance matrix, can be easily derived from the coupling matrix $[W]$.

2.3.3 The coupling matrix between different waveguides sections

For analyzing the waveguide discontinuities one should start with the evaluation of the entries in the coupling matrix $[W]$, given by the relation 2.128. In practice, there is a clear distinction between the step junctions involving canonical waveguides (for example rectangular or circular) and waveguides with arbitrary sections. The difference is that in the first case the modes are known in analytical form, which improves the accuracy and the speed of evaluating the $w_{m,n}$ elements, whereas the modes of arbitrary waveguides are only approximated by means of numerical methods, with a certain precision limited by the computational feasibility.

Coupling between rectangular waveguides

Firstly, let us consider the case of a transition between two rectangular waveguide as depicted in Fig. 2.18. Taking into account the fact that the field at each side of the discontinuity is expressed using TE and TM modes, one can distinguish among four situations given by the combinations of these types of modes.

If the double index (i, j) is used to designate the modes of the small waveguide (having the cross-section S_1) and the pair (u, v) the modes of the large waveguide, the coupling coefficients (2.128) between $TM^{(1)}$ and $TM^{(2)}$ modes read

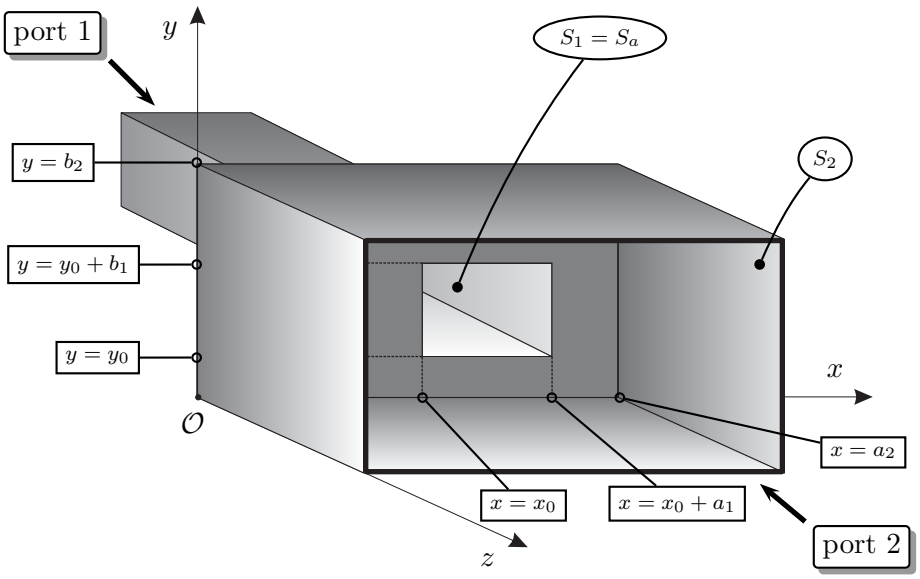

Figure 2.18: Step dicontinuity between colinear, rectangular waveguides.

$$
\begin{aligned}
w_{i,j,u,v}^{TM^{(1)}TM^{(2)}} \;=\;& \pi^2 A_{i,j}^{(1)} A_{u,v}^{(2)} \cdot \\
& \left[\frac{ui}{a_1 a_2} \int_{x_0}^{x_0+a_1} \cos\left(\frac{u\pi x}{a_2}\right) \cos\left(\frac{i\pi(x-x_0)}{a_1}\right)\, dx \cdot \right. \\
& \int_{y_0}^{y_0+b_1} \sin\left(\frac{v\pi y}{b_2}\right) \sin\left(\frac{j\pi(y-y_0)}{b_1}\right)\, dy + \\
& \frac{vj}{b_1 b_2} \int_{x_0}^{x_0+a_1} \sin\left(\frac{u\pi x}{a_2}\right) \sin\left(\frac{i\pi(x-x_0)}{a_1}\right)\, dx \cdot \\
& \left. \int_{y_0}^{y_0+b_1} \cos\left(\frac{v\pi y}{b_2}\right) \cos\left(\frac{j\pi(y-y_0)}{b_1}\right)\, dy \right] . \qquad (2.129)
\end{aligned}
$$

In writing the relation (2.129) the modal eigenvectors of the rectangular waveguides were substituted with the expressions given in Table 2.1.

By denoting with I_{cx}, I_{sx}, I_{cy} and I_{sy} the line integrals in (2.129), involving the sine and cosine functions along the x and y axis, the coupling coefficients become

$$
w_{i,j,u,v}^{TM^{(1)}TM^{(2)}} = \pi^2 A_{i,j}^{(1)} A_{u,v}^{(2)} \left(\frac{ui}{a_1 a_2} I_{cx} I_{sy} + \frac{vj}{b_1 b_2} I_{sx} I_{cy} \right) . \qquad (2.130)
$$

For the convenience of the reader, the expressions and the analytical solutions of the integrals I_{cx}, I_{sx}, I_{cy} and I_{sy} have been included in the Appendix C.

It is known [36, p. 73] that the coupling between the $TM^{(1)}$ modes of the small waveguide and the $TE^{(2)}$ modes of the large waveguide is always equal to zero (even at steps between arbitrary waveguides).

$$w_{i,j,u,v}^{TM^{(1)}TE^{(2)}} = 0 \tag{2.131}$$

The coupling coefficients between $TE^{(1)}$ and $TM^{(2)}$ modes have the general expression

$$w_{i,j,u,v}^{TE^{(1)}TM^{(2)}} = \pi^2 A_{i,j}^{(1)} A_{u,v}^{(2)} \left(\frac{uj}{a_2 b_1} I_{cx} I_{sy} - \frac{vi}{a_1 b_2} I_{sx} I_{cy} \right), \tag{2.132}$$

and those among $TE^{(1)}$ and $TE^{(2)}$ read

$$w_{i,j,u,v}^{TE^{(1)}TE^{(2)}} = \pi^2 A_{i,j}^{(1)} A_{u,v}^{(2)} \left(\frac{vj}{b_1 b_2} I_{cx} I_{sy} + \frac{mi}{a_1 a_2} I_{sx} I_{cy} \right). \tag{2.133}$$

Since the coupling coefficients between rectangular waveguide sections are known in closed forms (which involve the evaluation of simple trigonometric functions), a large number of coefficients can be calculated with an excellent accuracy in a very short time.

Coupling between BI-RME modes and the resonant modes

An attractive feature of the BI-RME method is that a significant amount of data, calculated during the procedure of estimating the arbitrary waveguide modes, can be utilized in the evaluation of the coupling coefficients between an arbitrary waveguide segment and a rectangular one.

It is simple to demonstrate that, by using the resonant mode expansions of the Green's functions, the modal electric field quantities of the arbitrary waveguide (the BI-RME modes) can be expressed as [4]:

$$\mathcal{E}_q^{TE}(\boldsymbol{r}) = \sum_{i=1}^{\infty} \boldsymbol{e}_i^{TM}(\boldsymbol{r}) A_i^q + \sum_{i=1}^{\infty} \boldsymbol{e}_i^{TE}(\boldsymbol{r}) B_i^q + \sum_{m=1}^{M^{TE}} \boldsymbol{e}_m^{TE}(\boldsymbol{r}) C_m^q, \tag{2.134}$$

$$\mathcal{E}_q^{TM}(\boldsymbol{r}) = \sum_{i=1}^{\infty} \boldsymbol{e}_i^{TM}(\boldsymbol{r}) D_i^q + \sum_{m=1}^{M^{TM}} \boldsymbol{e}_m^{TE}(\boldsymbol{r}) E_m^q, \tag{2.135}$$

$$\mathcal{E}_q^{TEM}(\boldsymbol{r}) = \sum_{i=1}^{\infty} \boldsymbol{e}_i^{TM}(\boldsymbol{r}) F_i^q, \tag{2.136}$$

where $\boldsymbol{e}_p^{TM}$ and $\boldsymbol{e}_p^{TE}$ are the electric modal eigenvectors of TM and TE type pertaining to the BI-RME frame (rectangular waveguide), and the other quantities are given by:

$$A_i^q = -\frac{1}{\chi_q k_i'} \sum_{n=1}^{N} b_n^q \int_\sigma \psi^{TM}(\boldsymbol{s}) \frac{\partial w_n(l)}{\partial l}\, dl, \tag{2.137}$$

$$B_i^q = \frac{\chi_q}{k_i^2} \sum_{n=1}^{N} b_n q \int_\sigma \boldsymbol{e}_i^{TE}(\boldsymbol{s}) \cdot \boldsymbol{t}(l) w_n(l)\, dl, \tag{2.138}$$

$$C_m^q = \chi_q \frac{a_m^q}{k_m^2}, \tag{2.139}$$

$$D_i^q = \frac{1}{k_i'} \sum_{n=1}^{N} b'^q_n \int_\sigma \psi^{TM}(\boldsymbol{s}) w_n(l)\, dl, \tag{2.140}$$

$$E_m^q = \frac{a'^q_m}{k'_m}, \tag{2.141}$$

$$F_i^q = \frac{1}{k_i'} \sum_{n=1}^{N} b''^q_n \int_\sigma \psi^{TM}(\boldsymbol{s}) w_n(l)\, dl. \tag{2.142}$$

Obviously, in numerical implementations the infinite summations in (2.134), (2.135) and (2.136) are truncated to a finite number of frame modes. With this approach it is possible to arrange the elements A_i^q, B_i^q,C_m^q,D_i^q,E_m^q and F_i^q in matrix configurations (with q indicating the row and i or m marking the column) such that the modes of the arbitrary waveguide can be written in a more compact manner

$$\begin{bmatrix} \mathcal{E}^{TE} \\ \mathcal{E}^{TM} \\ \mathcal{E}^{TEM} \end{bmatrix} = \begin{bmatrix} \mathbf{B}+\mathbf{C} & \mathbf{A} \\ \mathbf{0} & \mathbf{D}+\mathbf{E} \\ \mathbf{0} & \mathbf{F} \end{bmatrix} \begin{bmatrix} \boldsymbol{e}^{TE} \\ \boldsymbol{e}^{TM} \end{bmatrix}, \tag{2.143}$$

where, $[\mathcal{E}^{TE}\mathcal{E}^{TM}\mathcal{E}^{TEM}]^T$ is a column vector of the electric eigenvectors considered for the arbitrary waveguide and $[\boldsymbol{e}^{TE}\boldsymbol{e}^{TM}]^T$ is a column vector of the electric modal quantities of the rectangular frame.

The coupling matrix between the modes of an arbitrary waveguide section and those of a rectangular waveguide replicating the BI-RME frame reads:

$$[W] = \int_{S_a} \begin{bmatrix} \boldsymbol{e}^{TE} \\ \boldsymbol{e}^{TM} \end{bmatrix} \cdot \begin{bmatrix} \mathcal{E}^{TE} \\ \mathcal{E}^{TM} \\ \mathcal{E}^{TEM} \end{bmatrix}^T dS. \tag{2.144}$$

By using (2.143) in (2.144) and by noting that, due to the orthogonality the

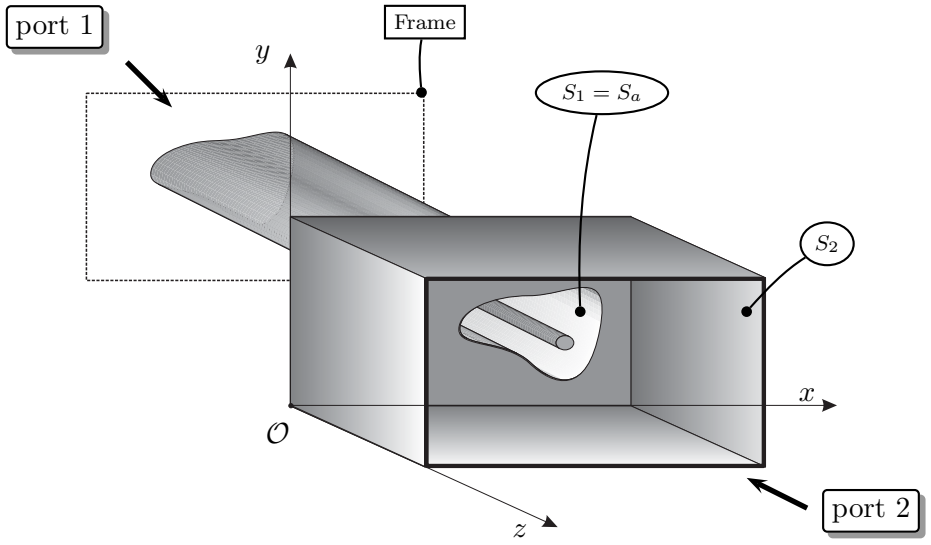

Figure 2.19: Transition from an arbitrary waveguide to a rectangular waveguide replicating the BI-RME frame.

following relation hold (**U** is the identity matrix)

$$\int_{S_a} \begin{bmatrix} \boldsymbol{e}^{TE} \\ \boldsymbol{e}^{TM} \end{bmatrix} \cdot \begin{bmatrix} \boldsymbol{e}^{TE} \\ \boldsymbol{e}^{TM} \end{bmatrix}^T dS = \mathbf{U}, \tag{2.145}$$

it is easy to demonstrate that the coupling matrix (2.144) reduces to:

$$[W] = \begin{bmatrix} \mathbf{B}+\mathbf{C} & \mathbf{A} \\ \mathbf{0} & \mathbf{D}+\mathbf{E} \\ \mathbf{0} & \mathbf{F} \end{bmatrix}^T . \tag{2.146}$$

It is worth observing that coupling matrix (2.146) between the arbitrary modes and the modes of the rectangular frame incorporates only quantities which have already been evaluated for the representation of the non-canonical modes.

Another pertinent remark is that for the calculation of the modes of the arbitrary section it is sufficient to consider a limited number of the frame modes, equal to the number of the modes used to describe the field at discontinuity on the rectangular waveguide side. Due to the orthogonality relation (2.145) it is clear that a better representation of the non-canonical modes (in the sense of increasing the number of resonant modes) does not improve the accuracy in modeling the discontinuity.

Coupling between arbitrary waveguides

The general case of a step junction between waveguides with arbitrary cross section can also be analyzed in a way that is similar to the one presented in the previous paragraph.

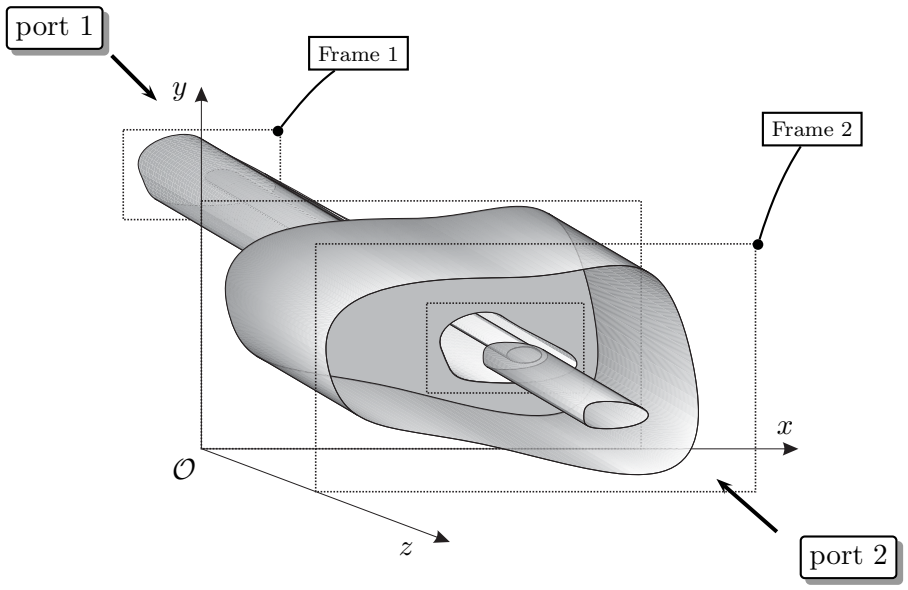

Figure 2.20: Arbitrary to arbitrary waveguide step junction.

Let $[\mathcal{E}^{TE}\mathcal{E}^{TM}\mathcal{E}^{TEM}]_1^T$ and $[\mathcal{E}^{TE}\mathcal{E}^{TM}\mathcal{E}^{TEM}]_2^T$ be two column vectors of BI-RME modes related to the waveguide segments connected at the discontinuity. The coupling matrix between these two sets of modes is evaluated as:

$$[W] = \int_{S_a} \left[\begin{array}{c} \mathcal{E}^{TE} \\ \mathcal{E}^{TM} \\ \mathcal{E}^{TEM} \end{array} \right]_2 \cdot \left[\begin{array}{c} \mathcal{E}^{TE} \\ \mathcal{E}^{TM} \\ \mathcal{E}^{TEM} \end{array} \right]_1^T dS. \tag{2.147}$$

By recalling the relation between the non-canonical modes and the modes of the rectangular frame (2.143), the coupling matrix yields

$$[W] = [W]_{AF2} \left\{ \int_{S_a} \left[\begin{array}{c} \boldsymbol{e}^{TE} \\ \boldsymbol{e}^{TM} \end{array} \right]_2 \cdot \left[\begin{array}{c} \boldsymbol{e}^{TE} \\ \boldsymbol{e}^{TM} \end{array} \right]_1^T dS \right\} [W]_{AF1}^T, \tag{2.148}$$

where $[W]_{AF2}$ and $[W]_{AF1}$ represent the coupling matrices between the BI-RME modes and the modes of the computational rectangular contour, having the general expression given in the equation (2.146).

The modal coupling matrix between the rectangular frames can be written as

$$[W]_{FF} = \int_{S_a} \left[\begin{array}{c} \boldsymbol{e}^{TE} \\ \boldsymbol{e}^{TM} \end{array} \right]_2 \cdot \left[\begin{array}{c} \boldsymbol{e}^{TE} \\ \boldsymbol{e}^{TM} \end{array} \right]_1^T dS \tag{2.149}$$

Note that the entries in the $[W]_{FF}$ matrix are known in analytical forms and, therefore, the calculation of this matrix can be done in a short time.

Finally, the coupling matrix between arbitrary waveguides can be expressed as a product of three known matrices

$$[W] = [W]_{AF2}^T [W]_{FF} [W]_{AF1}. \tag{2.150}$$

It is pointed out that the accuracy in analyzing arbitrary step junctions is, essentially, given by the numbers of canonical modes used to describe the transition among the modes of the two rectangular frames. When the two frames are taken to be identical, the relation (2.150) reduces to the formulas provided in [36, p. 330]. However, the formulation (2.150) becomes advantageous when it is necessary to analyze the transitions among waveguides having cross sectional areas within a large ratio. Another problem that can be favorably addressed by the approach presented in (2.150) is in a design procedure that searches for the optimum offset between two waveguide sections. In this situation it is only necessary to recalculate the $[W]_{FF}$ matrix, which is known in a closed form.

2.4 Conclusions

The formulation of the Mode Matching (MM) method adopted in the analysis of waveguide transmission lines was presented. A particular attention was given to the problem of computing the modes of uniform waveguide segments with arbitrary cross-section. In this respect the Boundary Integral - Resonant Mode Expansion (BI-RME) method was discussed and some particular aspect were extended in an original manner. Numerous mathematical aspects related to the calculation of the BI-RME modes were presented in this chapter and in the appendixes related to it. The computer implementation of the BI-RME analysis was accurately investigated by solving a large number of test problems. The formalism adopted in the calculation of the coupling coefficients between modes of waveguide segments having arbitrary cross sections was discussed, as well.

It is concluded that the modal techniques are the most appropriated full wave methods for the analysis of waveguide structures. These method offer a high and controllable accuracy without requiring expensive computational resources. The modal techniques are also characterized by fast computation times, the performances of the software implementations presented in this section being comparable with those of similar commercial packages.

Elements of novelty

The problem of selecting the modes in the BI-RME method was extended and an analytical solution was proposed for the optimum rotation angle that should be used in the case of processing quasi-degenerate modes. It was demonstrated that the BI-RME modes are quasi-orthogonal and the orthogonality of these modes can be improved by increasing the numbers of canonical modes used in the series representation of the Green's function. It is worth observing the efficiency, in terms of computing times and storage requirements, of the BI-RME computer implementations. This computational performance was achieved by adopting a new matrix formulation of the modal analysis. In this chapter it was also indicated that the modal coupling between arbitrary waveguides, having the area of the transversal sections in a large ratio, can be evaluated in a more efficient way by considering differently sized BI-RME boxes.

Chapter 3

Modal analysis of radiating apertures

The chapter presents the Mode Matching (MM) analysis of the radiation phenomena associated to rectangular aperture antennas operating either in isolated mode or in array configurations. The problem is formulated and solved for the general case of arbitrary array antennas consisting of differently sized apertures. A number of numerical examples are presented in order to demonstrate some of the capabilities of the software implementations of this MM analysis. In the last part of the chapter a solution for the fast evaluation of the mutual coupling effect in arbitrary array antennas is presented

3.1 Aperture antennas

Aperture antennas are among the most widely utilized radiating elements in phased array systems. They are often found in the simple form of open-ended waveguide radiators or the more complex configurations involved by the cavity backed antennas. The electromagnetic investigation of the radiation phenomena associated with an open aperture has been performed by means of both numerical techniques (as the finite element method [57] or finite difference method [107]) and (semi-) analytical ones (as, for example, the mode matching method).

For analyzing large array architectures or in optimization procedures applied to single elements, the use of standard numerical techniques may turn out to be less appropriate. This is mainly due to the use of a discrete representation of the entire computational domain. Large problems (not necessarily concerning complex topologies) lead to a high number of unknowns in the mesh based solvers and this becomes a critical point when limited computational resources are available.

It is then obvious that the methods avoiding any kind of meshing are much better suited for the analysis of large array configurations or for the fast characterization of single elements. From this point of view, the *mode matching method* (MMM) is regarded as an appropriated alternative to the use of purely numerical techniques.

In principle, the MM method aims at finding the mutual coupling between different modes considered on the aperture radiators. In particular, the evaluation of the mutual coupling level between rectangular or circular apertures has received a large attention in the past. A brief literature survey will reveal that, after the initial formulation of the problem [47, 18, 38, 39] where only the dominant mode in the aperture was taken into consideration, several other multi-mode procedures have been published [89, 88, 92, 86, 127, 12].

From the beginning it should be noted that the expansion of the field in the aperture is typically done by either using the modes of the relevant waveguide or by employing (singular) polynomial functions. Restricting the discussion to the solutions that make use of the waveguide modes (the most robust ones) two approaches exist for the evaluation of the mutual coupling effect. A first technique is based on the Fourier representation of the electromagnetic field in the free space. Representative for this approach are the works published in [8, 108]. The second methodology makes use of the Green's function to describe the radiated field. Of relevance for this method are the detailed procedures given in [16, 14, 15].

A common point in all these modal investigations is that the apertures are taken to be deployed on an infinite metallic flange. This hypothesis permits the use of the free-space Green's function, thus considerably alleviating the numerical effort. Another particular aspect is that, often, the aperture is filled with dielectric in order to reduce its size at an extent that accommodates the dimensional constraints imposed in array configurations.

The geometry of the analyzed, single-aperture antenna is depicted in Fig 3.1. The interior of the rectangular waveguide is filled with a homogeneous, isotropic, lossless medium with relative permittivity $\varepsilon_r^{(1)}$ and relative permeability $\mu_r^{(1)}$. The waveguide radiates into the half space ($z > 0$), where the medium is taken to be homogeneous and isotropic and characterized by relative permittivity $\varepsilon_r^{(2)}$ and relative permeability $\mu_r^{(2)}$.

3.2 Evaluating of the mutual coupling between rectangular apertures

The modal analysis of aperture antennas is formulated here, for the general case represented by an array configuration consisting of differently sized

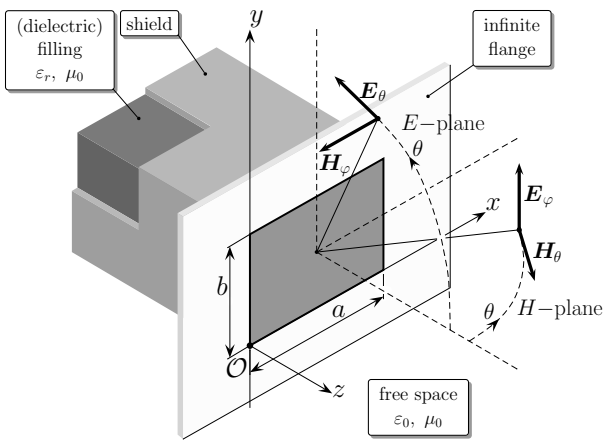

Figure 3.1: Geometry of a rectangular aperture antenna.

elements. As was already suggested, the investigation of a single aperture radiator deployed on an infinite metallic flange (Fig. 3.1) can be seen as a particular array configuration with only one element.

Let us consider an array of N rectangular apertures arranged on a non-uniform rectangular grid. The i and j elements of this array are indicated in Fig. 3.2.

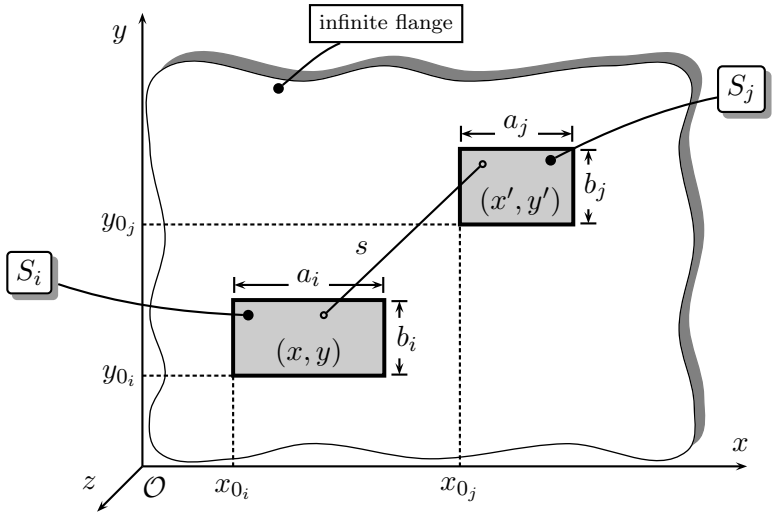

Figure 3.2: Differently sized rectangular apertures in a ground plane.

The kernel of the modal analysis of such an array of apertures is based on the continuity properties of the electromagnetic field components, at the

plane of the metallic flange ($z = 0$). In terms of electric and magnetic field strengths the field continuity can be formulated as:

$$\boldsymbol{E}_t^{(2)} = \begin{cases} \boldsymbol{E}_t^{(1)} & \text{on } S_1 \cup S_2 \cup \cdots S_N \\ 0 & \text{elsewhere} \end{cases} , \tag{3.1}$$

$$\boldsymbol{H}_t^{(2)} = \boldsymbol{H}_t^{(1)} \quad \text{on } S_1 \cup S_2 \cup \cdots S_N \ , \tag{3.2}$$

where the superscript (1) denotes the quantities inside the rectangular waveguides very close to the apertures ($z \uparrow 0$) and the superscript (2) indicates the field components in the free space, in the vicinity of the aperture ($z \downarrow 0$). Note that in 3.1 and 3.2 the field components are those transversal to the propagation along the z direction.

The $\boldsymbol{E}_t^{(1)}$ and $\boldsymbol{H}_t^{(1)}$ quantities can be represented as sums of distinct field components defined on the aperture domains S_1 to S_N. Moreover, the field transverse to the propagation direction in the waveguide i is expressed as a sum of M_i modes (see Chapter 2):

$$\left[\begin{array}{c} \boldsymbol{E} \\ \boldsymbol{H} \end{array} \right]_t^i (x, y, z) = \sum_{p=1}^{M_i} \left[a_p^i e^{-\mathrm{j}\gamma_p z} \pm b_p^i e^{\mathrm{j}\gamma_p z} \right] \cdot \left[\begin{array}{c} \boldsymbol{e} \\ \boldsymbol{h} \end{array} \right]_p^i (x, y) Y_{p,i}^{\mp\frac{1}{2}}, \tag{3.3}$$

where:

$\boldsymbol{e}_p^i$ and $\boldsymbol{h}_p^i$ are the transverse modal vectors satisfying the relation $\boldsymbol{e}_p^i = \boldsymbol{h}_p^i \times \mathbf{u}_z$;

$Y_{p,i}$ is the wave admittance of mode p in the aperture i and equals $Y_0 \gamma_{p,i}/k$ for TE modes and $Y_0 k/\gamma_{p,i}$ for TM modes;

$Y_0 = \sqrt{\frac{\epsilon_0}{\mu_0}} \approx 1/377\,\mathrm{S}$ is the air admittance;

$k = 2\pi/\lambda$ is the air wavenumber, with λ being the wavelength corresponding to the operational frequency f;

$\gamma_{p,i} = \sqrt{k^2 \epsilon_r^{(i)} - k_{c,p,i}^2}$ is the propagation constant of the p^{th} mode in the waveguide i filled with a dielectric having the relative permittivity ϵ_r^i;

a_p^i and b_p^i are the amplitudes of the direct and reflected waves of the p^{th} mode pertaining to the waveguide i.

For rectangular waveguides the modal vectors $\boldsymbol{e}_p^i$ and $\boldsymbol{h}_p^i$ are known in closed forms, as given in the Table 2.1. It is pointed out that the index p used for designating a mode is changed to the pair (m, n) for rectangular waveguides.

To express the radiated field one can either make use of the Fourier transform or the Green's function in the free space. In the followings the analysis of the aperture's array will be discussed separately for the two cases.

3.2.1 Fourier approach

The radiation of a monochromatic wave (harmonic at frequency f) from an aperture mounted on an infinite ground plane can be written as a superposition of plane waves of the form $\boldsymbol{f}(k_x, k_y)e^{-\mathrm{j}\boldsymbol{k}\cdot\boldsymbol{r}}$ ([11, p. 622]) where $\boldsymbol{r} = \boldsymbol{u}_x x + \boldsymbol{u}_y y + \boldsymbol{u}_z z$ represents the position vector of the observation point, and $\boldsymbol{k} = \boldsymbol{u}_x k_x + \boldsymbol{u}_y k_y + \boldsymbol{u}_z k_z$ is the propagation factor (also referred to as the *vector wavenumber*). The function $\boldsymbol{f}(k_x, k_y)$ is the vector amplitude of the wave, and k_x and k_y are the spatial spectral frequencies which extend over the entire spectrum ($-\infty \leq k_x, k_y \leq \infty$) represented by a hemispherical observation domain. Thus the field $\boldsymbol{E}^{(2)}$ can be written as ([11, p. 622])

$$\boldsymbol{E}^{(2)}(x, y, z) = \frac{1}{4\pi^2} \int_{-\infty}^{+\infty} \int_{-\infty}^{+\infty} \boldsymbol{f}(k_x, k_y) e^{-\mathrm{j}\boldsymbol{k}\cdot\boldsymbol{r}}\, dk_x dk_y. \tag{3.4}$$

Consequently, the magnetic component of the radiated field can be expressed as ([11, p. 625])

$$\boldsymbol{H}^{(2)}(x, y, z) = -\frac{1}{4\pi^2 k\eta} \int_{-\infty}^{+\infty} \int_{-\infty}^{+\infty} \boldsymbol{f} \times \boldsymbol{k} e^{-\mathrm{j}\boldsymbol{k}\cdot\boldsymbol{r}}\, dk_x dk_y, \tag{3.5}$$

where $\eta = \sqrt{\mu^{(2)}/\epsilon^{(2)}}$ is the impedance of the medium (for air $\eta = \sqrt{\mu_0/\epsilon_0} \approx 377\,\Omega$).

In general, the vector amplitude $\boldsymbol{f}(k_x, k_y)$ can be written in a Cartesian frame as

$$\boldsymbol{f}(k_x, k_y) = \mathbf{u}_x f_x(k_x, k_y) + \mathbf{u}_y f_y(k_x, k_y) + \mathbf{u}_z f_z(k_x, k_y). \tag{3.6}$$

By using the relation between the propagation constants k_x, k_y, k_z and the wavenumber of the medium $k = 2\pi f\sqrt{\mu^{(2)}\epsilon^{(2)}}$,

$$k^2 = k_x^2 + k_y^2 + k_z^2, \tag{3.7}$$

it can be easily demonstrated that the components f_x, f_y, f_z satisfy

$$f_z = -\frac{f_x k_x + f_y k_y}{k_z} \tag{3.8}$$

All three components of $\boldsymbol{f}$ can be found from the transversal components of the electric field ($E_x^{(2)}$, $E_y^{(2)}$) at $z = 0$, which is the plane of the apertures and ground plane in Fig. 3.2. By considering the continuity equation (3.1) and the fact that there are a number of N distinct apertures on the metallic flange ($z = 0$) one can obtain:

$$\begin{aligned} \begin{bmatrix} f_x \\ f_y \end{bmatrix}(k_x, k_y) &= \sum_{i=1}^{N} \sum_{p=1}^{M_i} \frac{1}{\sqrt{Y_{p,i}}} \left[a_p^i + b_p^i\right] \int_0^{a_i} \int_0^{b_i} \begin{bmatrix} e_x \\ e_y \end{bmatrix}_p^i \\ &\quad e^{+\mathrm{j}(k_x x' + k_y y')}\, dx' dy'. \end{aligned} \tag{3.9}$$

In deriving (3.9) use was made of the modal expression of the electric field at each aperture given by equation (3.3). In a more compact form, the components f_x and f_y read:

$$\left[\begin{array}{c} f_x \\ f_y \end{array} \right](k_x, k_y) = \sum_{i=1}^{N} \sum_{p=1}^{M_i} \frac{1}{\sqrt{Y_{p,i}}} V_p^i \left[\begin{array}{c} C_x \\ C_y \end{array} \right]_p^i (k_x, k_y), \tag{3.10}$$

where $V_p^i = a_p^i + b_p^i$ is the equivalent modal voltage associated to the p mode at the i^{th} aperture and the quantities C_x and C_y are given by

$$\left[\begin{array}{c} C_x \\ C_y \end{array} \right]_p^i (k_x, k_y) = \iint\limits_{S_i} \left[\begin{array}{c} e_x \\ e_y \end{array} \right]_p^i e^{+\mathrm{j}(k_x x' + k_y y')} \, dS'. \tag{3.11}$$

The magnetic field $\boldsymbol{H}_t^{(2)}$ can now be evaluated by introducing (3.9) in (3.5). Subsequently, by imposing the continuity relation (3.2) and by applying the Galerkin procedure on the magnetic, transversal modal vectors on each aperture, a coupling admittance between the mode p at the aperture i and the mode q at the aperture j is obtained:

$$\begin{aligned} Y_{q,p}^{j,i} \;=\; & -\frac{Y_0}{4\pi^2 k \sqrt{Y_q^j}\sqrt{Y_q^j}} \int_{-\infty}^{+\infty} \int_{-\infty}^{+\infty} \left[C_{p,y}^i k_z + k_y \frac{C_{p,x}^i k_x + C_{p,y}^i k_y}{k_z} \right] B_{q,x}^j \\ & - \left[k_x \frac{C_{p,x}^i k_x + C_{p,y}^i k_y}{kz} + C_{p,x}^i k_z \right] B_{q,y}^j \, dk_x dk_y, \end{aligned} \tag{3.12}$$

where $B_{q,x}^j$ and $B_{q,y}^j$ have the expression:

$$\left[\begin{array}{c} B_x \\ B_y \end{array} \right]_q^j = \iint\limits_{S_j} \left[\begin{array}{c} h_x \\ h_y \end{array} \right]_q^j e^{-\mathrm{j}(k_x x + k_y y)} \, dS. \tag{3.13}$$

The integrals in (3.13) can be solved analytically, the solutions being calculated in a similar way as presented in Appendix C. Some difficulties may arise in evaluating the coupling admittance $Y_{q,p}^{j,i}$ (3.12), when $k_x^2 + k_y^2 = k^2$ and the k_z component of the propagation factor becomes zero (this is introducing a singularity in the integral (3.12)). A way to circumvent this impediment will be presented in Section 3.2.3.

3.2.2 Green's function approach

The Green's function formulation of the mutual coupling between different apertures laying on an infinite metallic flange is described in the references

[16],[15] and [97]. The procedure follows similar steps with those presented previously in the Fourier approach and therefore, we restrict ourselves to providing here only the final formula for the coupling admittance between the mode p at the aperture i and the mode q at the aperture j [16]

$$Y_{q,p}^{j,i} = \frac{\mathrm{j}kY_0}{4\pi\sqrt{Y_q^j}\sqrt{Y_q^j}} \iint\limits_{S_i} \iint\limits_{S_j} \boldsymbol{\Psi}_p^i \cdot \boldsymbol{\Psi}_q^j G(x-x', y-y')\, dSdS', \tag{3.14}$$

where G is the free space Green's function given by

$$G(x-x', y-y') = \frac{\exp\left[-\mathrm{j}k\sqrt{(x-x')^2+(y-y')^2}\right]}{\sqrt{(x-x')^2+(y-y')^2}}, \tag{3.15}$$

and the vector function $\boldsymbol{\Psi}_p^i$ incorporates the transverse and axial magnetic field component $\boldsymbol{h}_p^i$ and h_{zp}^i.

$$\boldsymbol{\Psi}_p^i = \boldsymbol{h}_p^i + \mathbf{u}_z \frac{\gamma_{p,i}}{k} h_{z,p}^i. \tag{3.16}$$

By substituting in (3.14) the magnetic modal quantities with the expressions given in Table 2.1 (for the rectangular apertures) one obtains

$$Y_{(m,n),(m',n')}^{i,j} = \frac{\mathrm{j}kY_0}{2\pi\sqrt{Y_{m,n}^i}\sqrt{Y_{m',n'}^j}} A_{m,n}^i A_{m',n'}^j \left(c_x I_x + c_y I_y - c_z I_z\right), \tag{3.17}$$

where

$$\begin{matrix} I_x \\ I_y \\ I_z \end{matrix} = \iint\limits_{S_i} \iint\limits_{S_j} \begin{matrix} \sin \\ \cos \\ \cos \end{matrix} \left(\frac{m\pi x}{a_i}\right) \cdot \begin{matrix} \cos \\ \sin \\ \cos \end{matrix} \left(\frac{n\pi y}{b_i}\right) \cdot \begin{matrix} \sin \\ \cos \\ \cos \end{matrix} \left(\frac{m'\pi x'}{a_j}\right) \cdot \begin{matrix} \cos \\ \sin \\ \cos \end{matrix} \left(\frac{n'\pi y'}{b_j}\right) \cdot G(x-x', y-y')\, dSdS' \tag{3.18}$$

and the coefficients c_x, c_y and c_z being listed in Table 3.1.

The coupling admittances (3.12) or (3.14) can be seen as entries of a Generalized Admittance Matrix $[Y]$ which describes in a compact form the network formalism (introduced in Section 2.3.1) of the aperture discontinuity. Furthermore, a Generalized Scattering Matrix $[S]$ of the array antenna can be derived, yielding:

$$[S] = 2([U] + [Y])^{-1} - [U], \tag{3.19}$$

Table 3.1: Coefficients of the Bird's coupling admittance formula.

Coupling	c_x	c_y	c_z
$TE_{mn} \leftrightarrow TE_{m'n'}$	$\pi^2 \frac{mm'}{a_i a_j}$	$\pi^2 \frac{nn'}{b_i b_j}$	$\left(\frac{k_{c,mn} k_{c,m'n'}}{k}\right)^2$
$TE_{mn} \leftrightarrow TM_{m'n'}$	$-\pi^2 \frac{mn'}{a_i b_j}$	$\pi^2 \frac{nm'}{b_i a_j}$	0
$TM_{mn} \leftrightarrow TE_{m'n'}$	$-\pi^2 \frac{nm'}{b_i a_j}$	$\pi^2 \frac{mn'}{a_i b_j}$	0
$TM_{mn} \leftrightarrow TM_{m'n'}$	$\pi^2 \frac{nn'}{b_i b_j}$	$\pi^2 \frac{mm'}{a_i a_j}$	0

where $[U]$ represents the identity matrix. The scattering matrix $[S]$ satisfies the relation:

$$[b] = [S] \cdot [a], \tag{3.20}$$

with a and b denoting two column vectors of the incident and reflected waves amplitudes on each aperture in the array as defined in (3.3). It is worth noting that the matrices $[Y]$ and $[S]$ describe the mutual coupling effects in the array configuration without any dependency of the elements excitations.

3.2.3 Key mathematical steps in evaluating mutual admittances

The key aspect in the evaluation of the coupling admittances (3.17) is to solve the four-fold integrals I_x, I_y and I_z. The direct numerical integration of these quantities is a very time consuming procedure and should only be considered in case of arbitrary apertures. One of the main problem that involves heavily computer calculations is represented by the singularity of the Green's function G when the observation point overlaps the source point. For rectangular apertures, there are essentially three main approaches that have been adopted to circumvent this difficulty:

- Polynomial approximation of a specific part of the function to be integrated such that the singularity can be integrated out analytically [115].
- Replacement of the Green's function by its Fourier transform [16]
- The Lewin's method for substituting integration variables [79]

By applying these procedures one can also achieve a reduction of the order of integration, which turns out to be beneficial regarding the computation

time.

In the followings, there will be presented the spectral approach and the Lewin's method.

Spectral method

The Green's function (3.15) can be represented in the spectral domain as:

$$G(x-x',y-y') = \frac{1}{2\pi}\iint_{-\infty}^{+\infty} \frac{\exp\left[-\mathrm{j}k_x(x-x')-\mathrm{j}k_y(y-y')\right]}{\sqrt{k_x^2+k_y^2-k^2}}\,dk_x dk_y. \quad (3.21)$$

By using this spectral representation in the definition (3.18) of the integrals I_x, I_y and I_z it is possible to reduce the order of integration to a double integral:

$$\begin{matrix} I_x \\ I_y \\ I_z \end{matrix} = \iint_{-\infty}^{+\infty} \begin{matrix} T_s \\ T_c \\ T_c \end{matrix}(m,a_i,x_i,k_x) \begin{matrix} T_c \\ T_s \\ T_c \end{matrix}(n,b_i,y_i,k_y) \cdot \begin{matrix} T_s \\ T_c \\ T_c \end{matrix}(m',a_j,x_j,-k_x) \begin{matrix} T_c \\ T_s \\ T_c \end{matrix}(n',b_j,y_j,-k_y)\frac{dk_x dk_y}{\sqrt{k_x^2+k_y^2-k^2}}, \quad (3.22)$$

where

$$\begin{matrix} T_s \\ T_c \end{matrix}(m,a,d,k) = \int_d^{d+a} \begin{matrix} \sin \\ \cos \end{matrix}\left[\frac{m\pi}{a}(x-d)\right] e^{-\mathrm{j}kx}\,dx, \quad (3.23)$$

admit the following analytical solutions:

$$\begin{bmatrix} T_s \\ T_c \end{bmatrix}(m,a,d,k) = \begin{cases} \frac{e^{-\mathrm{j}kd}\left[(-1)^m e^{-\mathrm{j}kd}-1\right]}{(m\pi)^2-(ka)^2} \begin{bmatrix} m\pi a \\ \mathrm{j}ka^2 \end{bmatrix}; & (m\pi)^2 \neq (ka)^2 \\ \pm\mathrm{j}e^{-\mathrm{j}\frac{m\pi d}{a}} + \frac{e^{-\mathrm{j}kd}\left[(-1)^m e^{-\mathrm{j}kd}-1\right]}{(m\pi)+(ka)} \begin{bmatrix} -\frac{a}{2} \\ \mathrm{j}\frac{a}{2} \end{bmatrix}; & m\pi = ka \\ \pm\mathrm{j}e^{-\mathrm{j}\frac{m\pi d}{a}} - \frac{e^{-\mathrm{j}kd}\left[(-1)^m e^{-\mathrm{j}kd}-1\right]}{(m\pi)-(ka)} \begin{bmatrix} \frac{a}{2} \\ \mathrm{j}\frac{a}{2} \end{bmatrix}; & m\pi = -ka \\ \begin{bmatrix} 0 \\ a \end{bmatrix}; & m\pi = -ka = 0 \end{cases}. \quad (3.24)$$

The infinite integrals in (3.22) has to be evaluated numerically. The convergence of these quadratures can be improved by employing an appropriate change of variables

$$k_x = k \sin\alpha \cos\beta, \tag{3.25}$$

$$k_y = k \sin\alpha \sin\beta, \tag{3.26}$$

with the integration domain defined by:

$$\left\{\alpha \in [0, 2\pi], \beta \in [0, \frac{\pi}{2}]\right\} \cup \left\{\alpha = \frac{\pi}{2}, \beta \in [\mathrm{j}0, \mathrm{j}\infty]\right\}. \tag{3.27}$$

Note that the substitution (3.25) and (3.26) also eliminates the singular points k_x and k_y, which satisfy $k_x^2 + k_y^2 = k^2$. The integration path in the complex η plane has to be truncated at a certain value $\Im\{\beta\} = T$ such that the contribution to the integral over the interval $[\mathrm{j}T, \mathrm{j}\infty]$ can be neglected.

Finally, it is worth mentioning that this change of variables is also recommended in solving the mutual coupling admittance derived from the Fourier representation of the radiated field (3.12).

Lewin's method

Lewin has proposed in [79, pp. 121–126] a method to reduce the order of integration for the self-admittance of the TE_{10} mode of a rectangular waveguide with an infinite metallic flange. The extension to the multi-modal analysis of the mutual coupling between different sized rectangular apertures was proposed in [16], and it will be briefly outlined in the following. Initially it is pointed out that in (3.18) it is possible to change the order of integration such that instead of integrating over the source (x', y') and the observer (x, y) domains one can integrate over the (x, x') and (y, y') domains. Furthermore, the following changes of variable are adopted:

$$\sigma = x - x', \tag{3.28}$$

$$v = x + x' - a_i, \tag{3.29}$$

$$\lambda = y - y', \tag{3.30}$$

$$u = y + y' - b_i, \tag{3.31}$$

where the (σ, v) domain is assigned to the (x, x') domain and (λ, u) to (y, y'), respectively. After some lengthy, though straightforward algebra, the integrals over the variables v and u can be integrated out in closed forms. At this point the coupling admittance reduces to a sum of double integrals over the variables σ and λ (for the exact relation see Appendix E). These integrals

can be reduced to a generic form, which is given by

$$I = \int_0^{\sigma_1}\int_0^{\lambda_1} \sin(t_1\sigma)\cos(t_2\sigma)\sin(t_3\lambda)\cos(t_4\lambda) \cdot \frac{\exp\left[-\mathrm{j}k\sqrt{(\sigma+d_1)^2+(\lambda+d_2)^2}\right]}{\sqrt{(\sigma+d_1)^2+(\lambda+d_2)^2}}\, d\sigma d\lambda, \tag{3.32}$$

where $\{t_1, t_2, t_3, t_4, d_1, d_2\} \in \mathbb{R}$. In [79] and [16] it was indicated that for mode coupling in the same aperture ($d_1 = 0$ and $d_2 = 0$) the integral (3.32) can be reduced to a sum of two line integrals. This is possible by converting the integration variable (σ, λ) to polar coordinates (t, ϕ) and integrating out the variable t. Moreover, the singularity at $(\sigma = 0, \lambda = 0)$ is eliminated with this substitution. The change of variable is illustrated graphically in Fig. 3.3.a, where D_1 and D_2 represent the integration sub-domains that allow for the complete integration of the variable t. For the more general case of coupling between the modes of different apertures, not necessarily of the same size, the following substitution of variables is proposed:

$$\sigma + d_1 = t\cos\phi, \tag{3.33}$$

$$\lambda + d_2 = t\sin\phi. \tag{3.34}$$

Subsequently, the integration domain $\{\sigma \in [0, \sigma_1], \lambda \in [0, \lambda_1]\}$ is divided into three sub-domains denoted with D_1, D_2 and D_3.

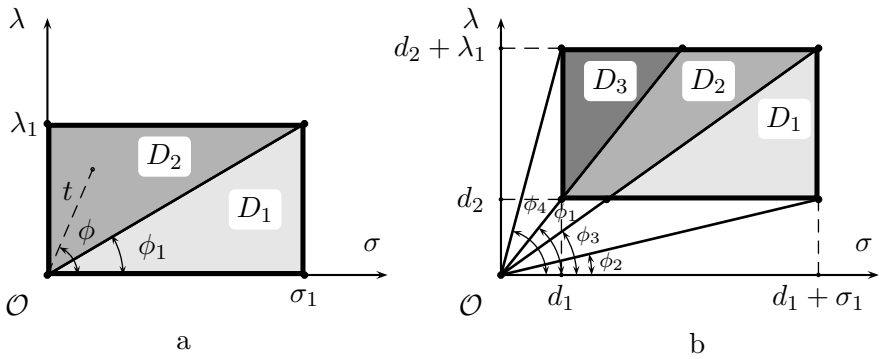

Figure 3.3: Change of variables and the computation sub-domains for reducing the order of integration. (a) - self admittance; (b) - coupling admittance between different waveguides.

The change of variables and the integration zones in the case of coupling admittances are depicted in Fig 3.3.b. From this figure it is easy to show that the limits of the integration sub-domains in the polar coordinates are

given by:

$$D_1 = \begin{cases} t \in [r_1, r_2]; & r_1 = \frac{d_2}{\sin\phi}, & r_2 = \frac{d_1+\sigma_1}{\cos\phi} \\ \phi \in [\alpha_1, \alpha_2]; & \tan\alpha_1 = \frac{d_2}{d_1+\sigma_1}, & \tan\alpha_2 = \frac{d_2+\lambda_1}{d_1+\sigma_1} \end{cases}, \quad (3.35)$$

$$D_2 = \begin{cases} t \in [r_1, r_3]; & r_1 = \frac{d_2}{\sin\phi}, & r_3 = \frac{d_2+\lambda_1}{\sin\phi} \\ \phi \in [\alpha_2, \alpha_3]; & \tan\alpha_2 = \frac{d_2+\lambda_1}{d_1+\sigma_1}, & \tan\alpha_3 = \frac{d_2}{d_1} \end{cases}, \quad (3.36)$$

$$D_3 = \begin{cases} t \in [r_4, r_3]; & r_4 = \frac{d_1}{\cos\phi}, & r_3 = \frac{d_2+\lambda_1}{\sin\phi} \\ \phi \in [\alpha_3, \alpha_4]; & \tan\alpha_3 = \frac{d_2}{d_1}, & \tan\alpha_4 = \frac{d_2+\lambda_1}{d_1} \end{cases}. \quad (3.37)$$

Note that these definitions are valid for $d_1 \geq 0$ and $d_2 \geq 0$. When $d_1 < 0$ or $d_2 < 0$ the position of the integration domain, in the variables (σ, λ), moves to other quadrants of the Cartesian frame and therefore the sub-domains D_1, D_2 and D_3 have to be re-defined.

The t variable can be now integrated out completely in a similar manner as the one adopted for the self-admittance. Finally the mutual coupling admittance is reduced to a sum of simple, line integrals over angle ϕ. One can also try to solve the integrals over ϕ analytically. From our studies this seems to be possible in a form of a series expansion. However, the functions in variable ϕ are smooth and the numerical integration of these quantities is more advantageous than using complicated analytical expressions that involve series representations.

3.3 Computer implementation and numerical validation

A key aspect concerning the radiation from waveguide apertures is the efficient and accurate modeling of the field behavior in the vicinity of the apertures. This has a direct consequence on the radiation properties of antennas and on the circuit parameters. An exhaustive investigation of the possibilities to calculate the field radiated by an array of aperture antennas is presented in Appendix F.

The theoretical formulations presented in the Section 3.2 and in the Appendix F have been implemented in a number of modeling tools developed under the MATLAB® environment. These software routines were partially combined with a user-friendly shell, resulting in a simulation platform for educational purposes, called WGEMLab. The features and the potential of the WGEMLab platform in the educational process have been presented in references [27, 73, 74].

For validating these numerical implementations a number of scenarios involving isolated radiating apertures or arrays of identical and non-identical

elements were investigated. The reference data were taken from the literature and, in some cases, were generated using the CST Microwave Studio® commercial software package.

Singular behavior at the edge of the aperture

It is known that the field components perpendicular to a 90° edge formed between the waveguide end and the flange exhibits a singularity of the order $r^{-1/3}$ whereas the parallel field quantities vanishes as $r^{2/3}$ [96] at the edges. To illustrate this behavior, by means of the waveguide mode expansion technique, one should be able to evaluate accurately the mutual coupling between a large number of modes in the radiating aperture. In Fig. 3.4 is depicted the variation of the E_y electric field component in the aperture of a WR90 waveguide ($a = 22.86\,\text{mm}$ and $b = 10.16\,\text{mm}$), along a line (parallel with the $\mathcal{O}y$ axis in Fig. 3.1) taken at the middle of the wide side ($x = 11.43\,\text{mm}$). The analysis was performed at 10 GHz for different numbers of modes. It was supposed that the aperture is excited by means of TE_{10} with the amplitude of the direct wave being 1V/m. From the detailed view presented in Fig. 3.1).b it is evident that, by increasing the number of the modes, the solution converges to the singular variation already mentioned. From this analysis we have learned that the selection of the modes plays an important role in emphasizing a certain aspect of the radiation phenomena. For example, in case of field representations, it is useful to consider only the higher order modes that have symmetries similar to these of the excited (fundamental) mode.

The computation times of the modal coefficients were: 64 seconds for the 50 modes analysis, 4.2 minutes for the 100 modes analysis and 17 minutes for the 200 modes analysis. The calculation were performed on a Intel® Pentium® 4 PC at 2.4 GHz with 256 MB of RAM and having installed the Microsoft Windows XP operating system (the further computation times will refer, except when specified, to this computer architecture). Note that all the coupling (line) integrals were evaluated numerically using a Simpson's adaptive rule with the interval bisection until the error in the approximation of the integral is less than 10^{-3}.

Field continuity

From electromagnetic perspectives another important aspect to be addressed in the study of waveguide end antennas is the preservation of the continuity of the field components at the aperture discontinuity. The modal analysis outlined in Section 3.2 is based on the continuity of the tangential components of the electric and magnetic field quantities. Therefore, the computed modal coefficients have to preserve this property of the field at one side and the other side of the discontinuity. In addition the continuity of the

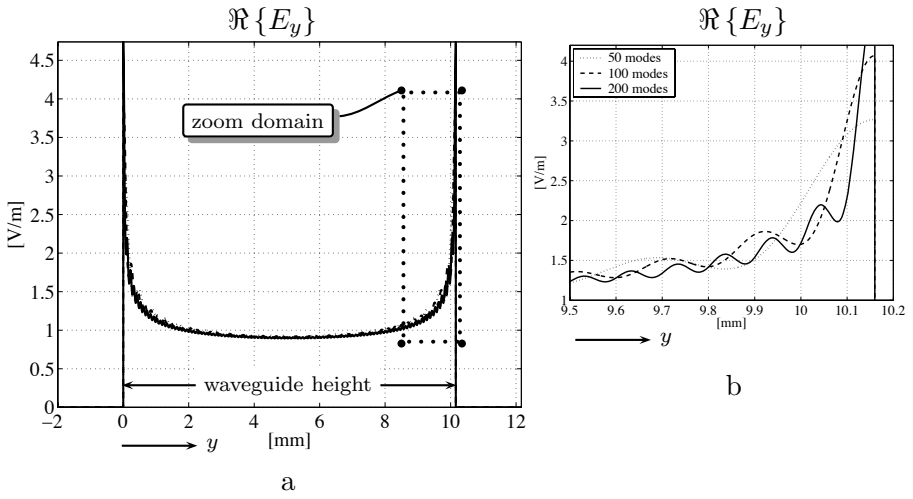

Figure 3.4: Distribution of the electric field in the aperture of an waveguide end antenna for different number of modes taken into account: dotted line - 50 modes, dashed line - 100 modes, solid line - 200 modes. a) - section on the entire aperture, b) - detailed view of the zoom domain

longitudinal components follows as an intrinsic property of the Maxwell's equations.

To illustrate these characteristics, all the electric and magnetic field components have been evaluated in the aperture and in front of the WR90 aperture (in free space) over very short distance. The results are presented in Fig. 3.5 and 3.6. The field in the aperture was excited by means of the TE_{10} mode with the amplitude of the electric field intensity of 1 V/m and oscillating at 10 GHz. In these figures, the singular behavior of the field in the proximity of the aperture's edges is clearly visible. Note that, for being able to highlight this phenomenon, a number of 200 modes were employed in the representation of the field in the waveguide. The coupling coefficients between the modes in the aperture were evaluated by solving the single integrals with a precision of 10^{-3}.

The radiated field was evaluated using the Green's function in free space and the coupling coefficients obtained from the modal analysis. The electric strength components have been evaluated at 0.1 mm in front of the aperture (located $z = 0$) at different points in the $x\mathcal{O}y$ plane. The radiated magnetic field components were calculated in a plane located at $z = 1$ mm. The reason for evaluating the magnetic quantities at a larger distance is due to the numerical instabilities resulted from the integration of quantities that incorporate the second order derivatives of the Green's function. From Fig. 3.5 and 3.6 it is clear that all field quantities have similar distributions inside

the waveguide and in the vicinity of the aperture.

To further prove this observation the E_y component was evaluated in two orthogonal planes, containing the longitudinal axis of the waveguide, inside and outside of the transmission line. The field variation is depicted in Fig. 3.7. Note that the continuity of the field is self evident even in the case when the singular behavior manifest itself at the edges of the aperture (E plane plot in Fig. 3.7).

The computed field components were also used in the study of the radiation phenomena in the near-field region of the antenna. This analysis is presented in Annex D.

Self admittance

Another class of parameters, which have been investigated within the validation study, refers to the scattering parameters of waveguide ended antennas. In Fig. 3.8 is reported the reflection coefficient on the TE_{10} mode in the aperture of a standard WR90 rectangular waveguide. In the literature there are several theoretical and experimental studies of this problem, which can be readily used for verifying the numerical implementation. In Fig. 3.8.a are depicted two calculated solutions with the spatial and spectral approaches described in the previous section. In addition, the measured data reported in [97] have been included for the consistency of the analysis. There is an excellent agreement between calculated and measured data. It is noted that at the cut-off frequency of the TE_{10} mode there are some positive values (in dB) of the reflection coefficient, which are attributed to the representation with a reduced number of modes of the numerical indeterminacy related to the study of this particular frequency (a solution to this kind of problems is discussed in [19]). In both numerical investigations a number of 15 modes were considered at the aperture. The analysis frequencies were taken in the range from 5 GHz to 15 GHz at 256 equidistant points. The single integrals in the spatial technique and the double quadratures in the spectral approach were solved with a precision of 10^{-5}. The computation times amounted to 6.8 minutes in the case of spatial integration and about 2.1 hours when the problem was solved in the spectral domain. Since solving the problem in the spatial domain is faster, further analyses will be reported for this variant only. An often occurring question in the numerical electromagnetic investigations is related to the convergence of the analysis. In this sense we have investigated the self admittance of the WR90 waveguide antenna with an increased number of modes. The results are presented in Fig. 3.8.b.

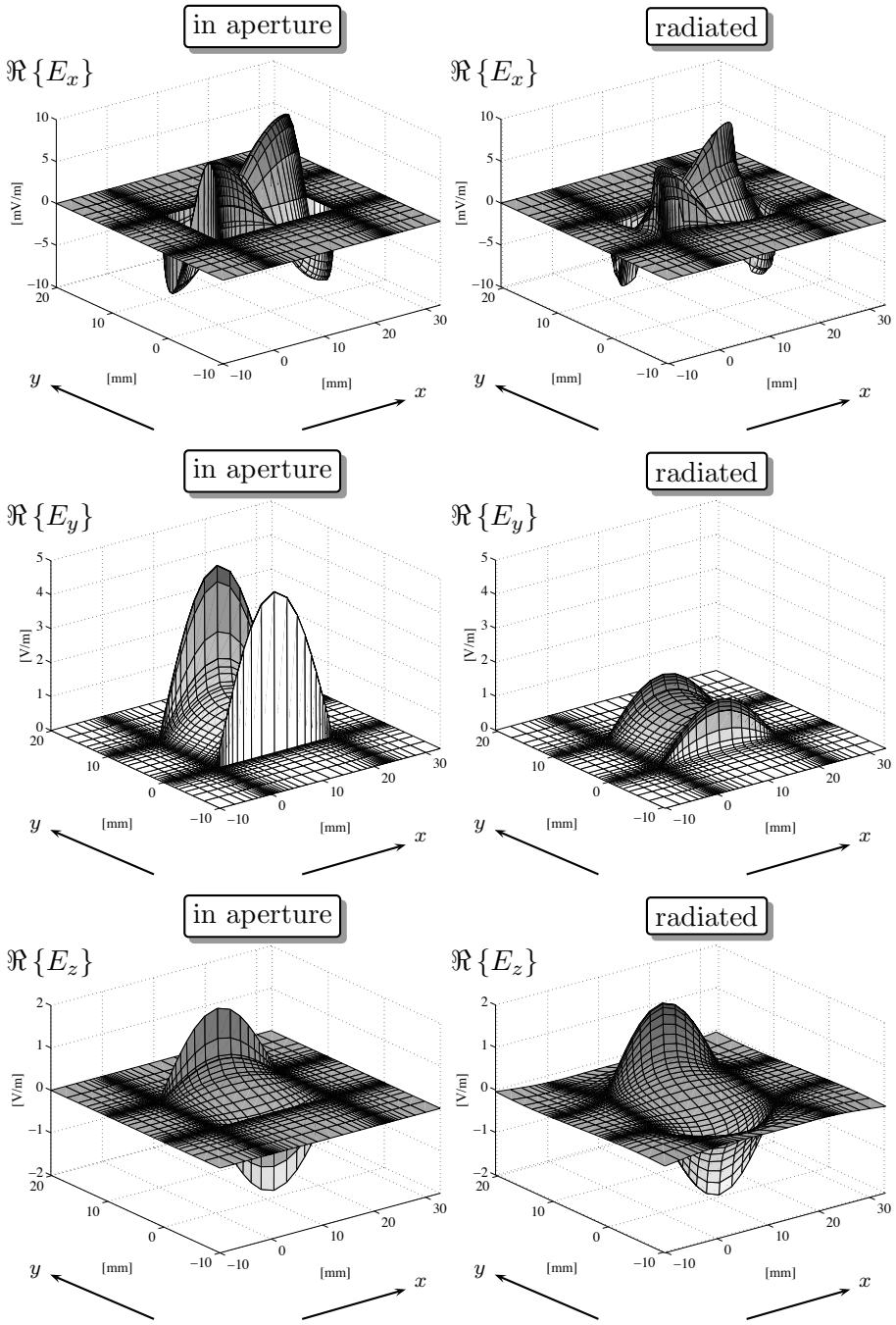

Figure 3.5: Distribution of the electric field components at the aperture of a waveguide end antenna ($z = 0$) and the radiated field in the proximity of the aperture ($z = 0.1$mm).

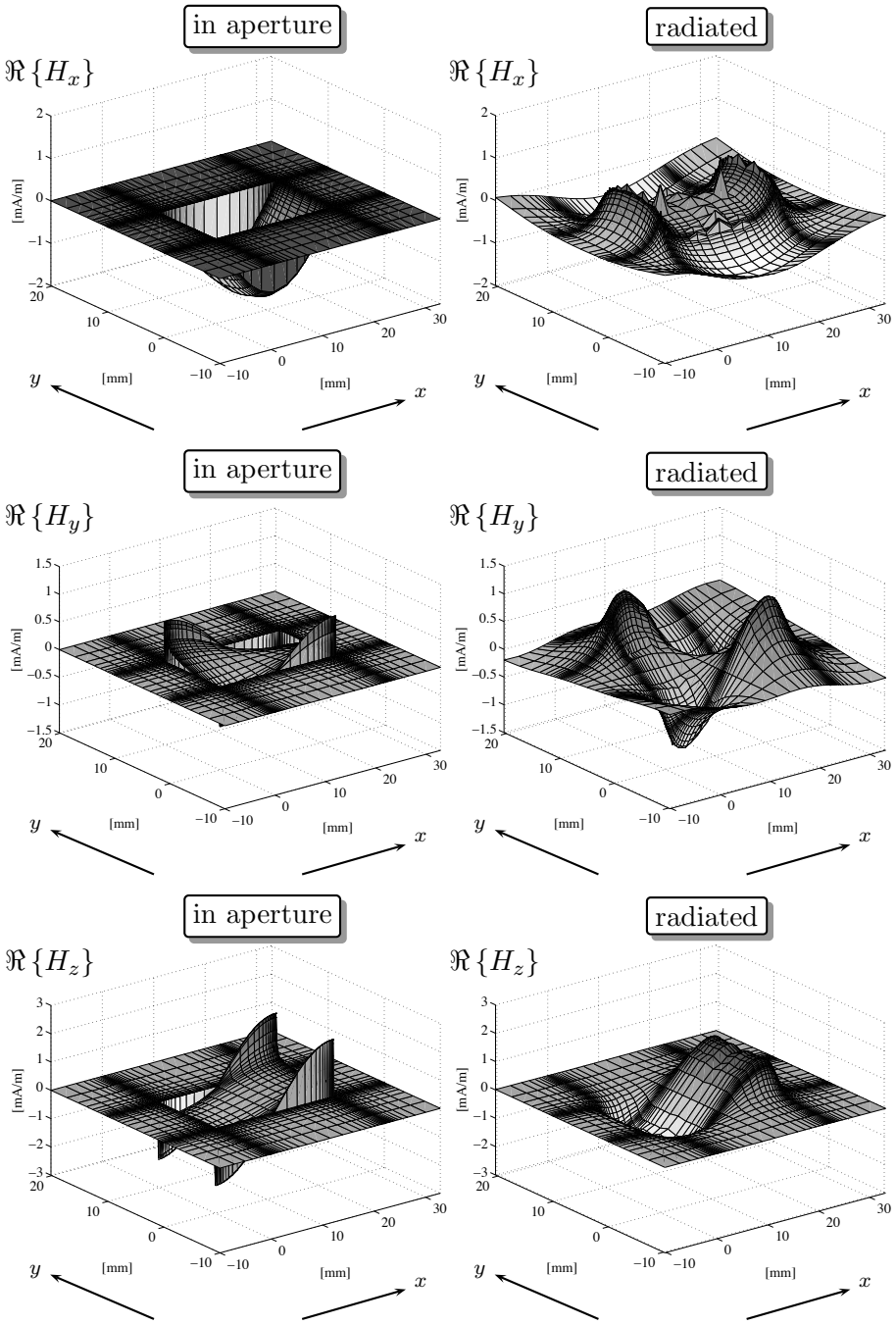

Figure 3.6: Distribution of the magnetic field components at the aperture of a waveguide end antenna ($z = 0$) and the radiated field in the proximity of the aperture ($z = 1$mm).

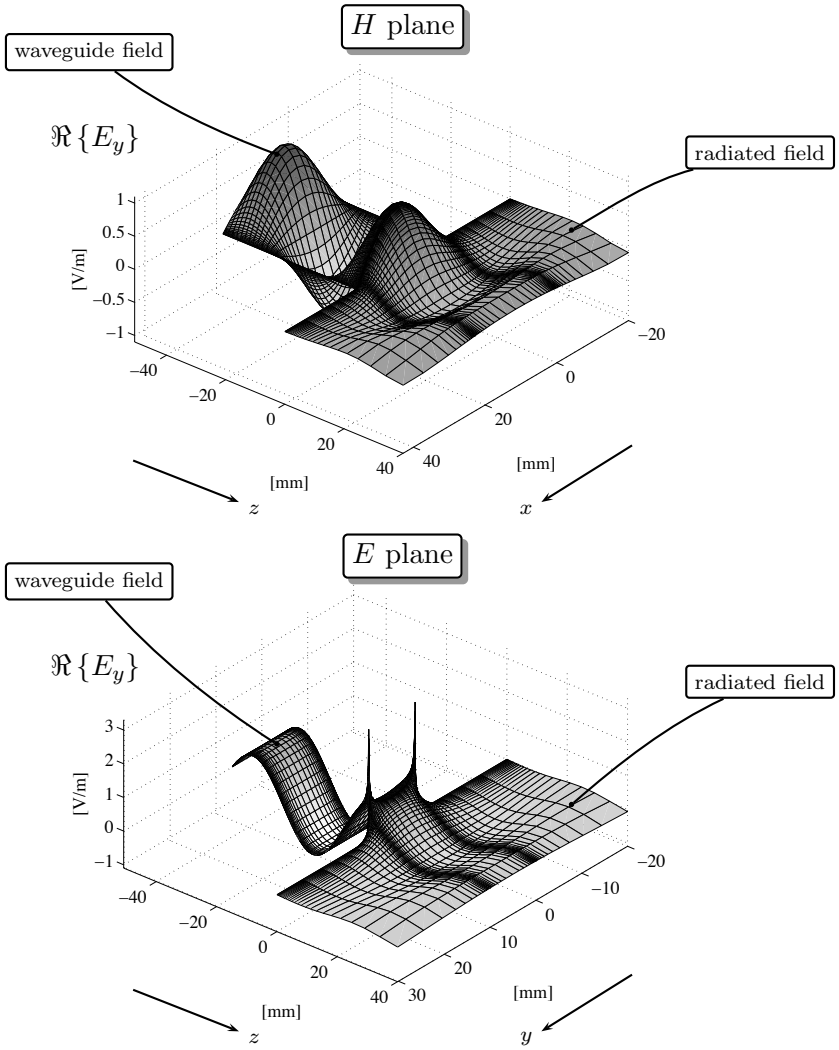

Figure 3.7: Distribution of the E_y electric field component inside a waveguide end antenna and in the vicinity of the aperture, in two orthogonal planes ($x\mathcal{O}z$ and $y\mathcal{O}z$). A number of 200 waveguide modes (TE and TM) were considered in the representation of the field.

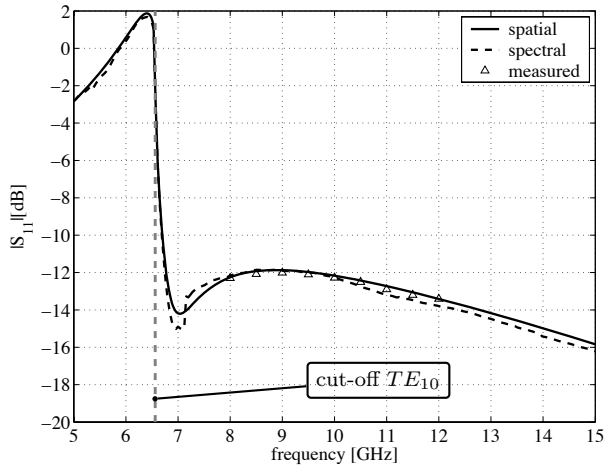

a

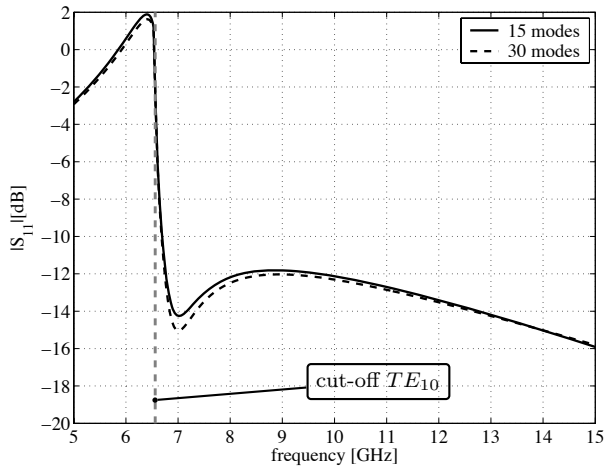

b

Figure 3.8: Reflection coefficient of the TE_{10} modes in a rectangular waveguide antenna (replicating the dimensions of a WR90 waveguide) mounted on an infinitely extended flange. (a) - validation study; (b) - convergence study.

Mutual coupling between identical apertures

To verify the numerical implementation for the evaluation of the mutual coupling between identical apertures we have chosen for the Mailloux's example consisting of two square waveguides coupled in their 45° plane [89, 16]. The size of the apertures are $a = b = 20\,\text{mm}$ and the relative distance between is $x_0 = y_0 = 40\,\text{mm}$. The coupling coefficients between the two apertures were evaluated by means of our MMM implementation and by using the CST Microwave Studio. The Mailloux's measured data and the calculated values are shown in Fig. 3.9 for the $TE_{10} \leftrightarrow TE_{10}$ and $TE_{10} \leftrightarrow TE_{01}$ coupling coefficients. In the mode matching analysis a number of 15 modes were considered in each waveguide (TE_{10}, TE_{01}, TE_{11}, TM_{11}, TE_{20}, TE_{02}, TE_{21}, TM_{21}, TE_{12}, TM_{12}, TE_{22}, TM_{22}, TE_{30}, TE_{03} and TE_{31}). The self admittances of the rectangular apertures were evaluated in less than 1 second whereas the computation of the coupling admittances between separated apertures took 1.1 hours. The large difference in the computing times is mainly due to the fact than the coupling coefficient between modes of separated apertures was done by solving double integrals in the spatial domain.

Mutual coupling between different apertures

Verification of the numerical analysis is now provided for differently sized waveguides by comparing results evaluated with different methods on a three element test array for which measurements are also available in [16]. The test configuration consists of a square waveguide (denoted as aperture 1) with the side lengths $a_1 = b_1 = 22.8\,\text{mm}$ positioned in the center of a metallic flange and two rectangular waveguides (denoted as aperture 2 and aperture 3) having the dimensions $a_2 = a_3 = 15.7\,\text{mm}$ and $b_2 = b_3 = 7.7\,\text{mm}$, respectively. The aperture 2 was located at $(0, -30)\,\text{mm}$ relative to the center of the square waveguide and the aperture 3 was deployed in the H plane at $(30, 0)\,\text{mm}$ relative to the center of the aperture 1. The reflection coefficients of the fundamental modes (TE_{10}) on each aperture and the coupling between these modes are depicted in Fig. 3.10. An excellent agreement is noted between the results obtained with our MMM implementation and those calculated with the CST Microwave Studio. It is worth mentioning that the reflection and the coupling coefficients are very close to the measurements presented in [16].

In the plots contained in Fig. 3.10 the cut-off frequency of the TE_{10} mode on the rectangular waveguides (9.55 GHz) was indicated with a vertical dashed line. Some differences are observed below this frequency because the MMM method evaluated the values of the scattering parameters exactly in the aperture whereas in CST it was necessary to move the measurement point at 5 mm inside the waveguide (this causing a visible attenuation when the modes becomes evanescent).

For the computation ten modes were used on each aperture. The con-

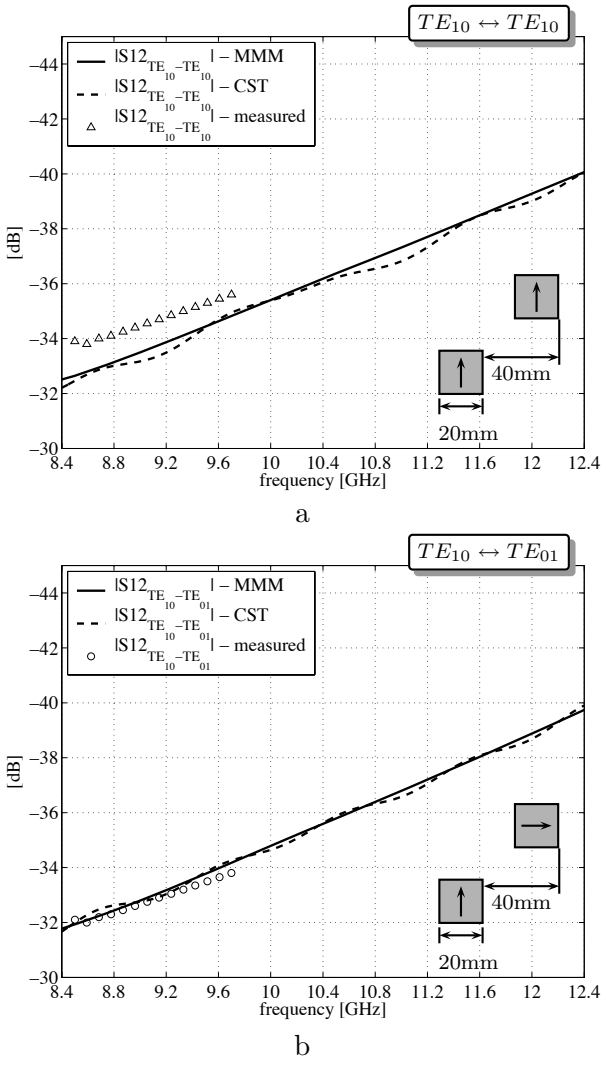

Figure 3.9: Coupling coefficients between modes of two identical square waveguides arranged at 45° on an metallic flange. (a) - $TE_{10} \leftrightarrow TE_{10}$; (b) - $TE_{10} \leftrightarrow TE_{01}$.

sidered modes were: TE_{10}, TE_{01}, TE_{11}, TM_{11}, TE_{20}, TE_{02}, TE_{21}, TM_{21}, TE_{12} and TM_{12} in the aperture 1 and TE_{10}, TE_{20}, TE_{01}, TE_{11}, TM_{11}, TE_{21}, TM_{21}, TE_{30}, TE_{31} and TM_{31} in apertures 2 and 3.

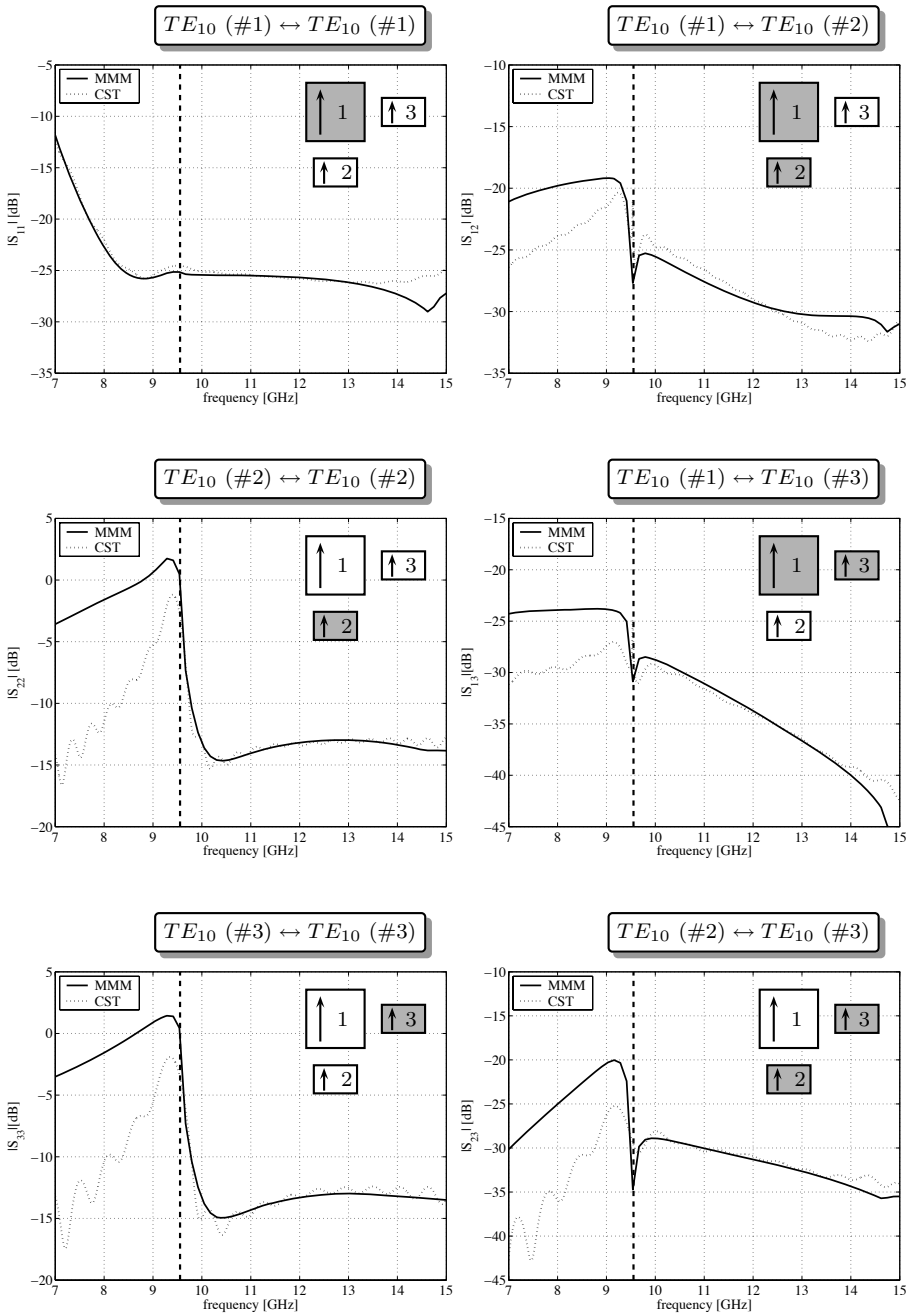

Figure 3.10: Reflection coefficients and coupling coefficients between fundamental modes (TE_{10}) in a three-element array problem. With a vertical dashed line is indicated the cut-off frequency of the TE_{10} mode in the small rectangular waveguides (9.55 GHz).

Radiation from coupled apertures

Calculation of the radiated field is straightforward once the modal equivalent voltages are known. As an example, Fig. 3.11 shows some field radiation patterns in the case of the three element array. The modal distribution of the field in each of the apertures was obtained by using the scattering parameters calculated in the previous example (concerning the mutual coupling) and setting the amplitude of the incident wave (electric field) of the TE_{10} mode on the square waveguide to 1V/m. The other two rectangular waveguides were supposed to be terminated with matched loads. The principal radiation patterns represent the absolute values of the antenna directivity as function of elevation angle θ. These patterns were also evaluated by using an array model with a finite metallic flange (dimensions 200 mm $\times$ 200 mm) in the CST commercial software package. From Fig. 3.11 the similarity between the two patterns (MMM and CST) in the H plane is evident. Moreover, the antenna gain was estimated by the two methods very close at about 10dB. The differences above 60° noticed in the E plane patterns are attributed to the finiteness of the metallic flange in the CST model. The co-polar and cross-polar field radiation patterns were evaluated in the 45° plane of the three element array. These pattern are similar to the one presented in reference [16]. The reason for evaluating the co-polar and cross-polar (x-polar) field components in the 45° plane is clearly indicated by the three dimensional representations in Fig. 3.11 (in the E and H planes the cross-polar component has its minimum values).

3.4 Fast evaluation of the mutual coupling effect

For being able to realistically model physical antennas deployed in array configurations, it is necessary to take into consideration the mutual coupling effect in an accurate manner. The electromagnetic interaction between closely spaced, radiating apertures has a significant influence on the antenna radiation properties (as polarization or side lobes) and on the circuit parameters of the antenna (as input impedance or isolation).

Note that for analyzing sparse array antennas or arrays accommodating different elements the popular approach involving periodic boundary conditions (Floquet's theory) is not applicable. Therefore, the numerical investigation of coupling admittances between rectangular apertures on a ground plane should be done as described previously in Section 3.2.3. This approach involves the numerical evaluation of double or single integrals, which significantly increases the computation time for the full-wave investigation of an array consisting of many elements. To circumvent this time consuming procedures, the following solutions are readily available in the literature:

- the *asymptotic* approximation of the mutual coupling (including higher order modes) between sufficiently far apart radiators [17, 99] (aperture

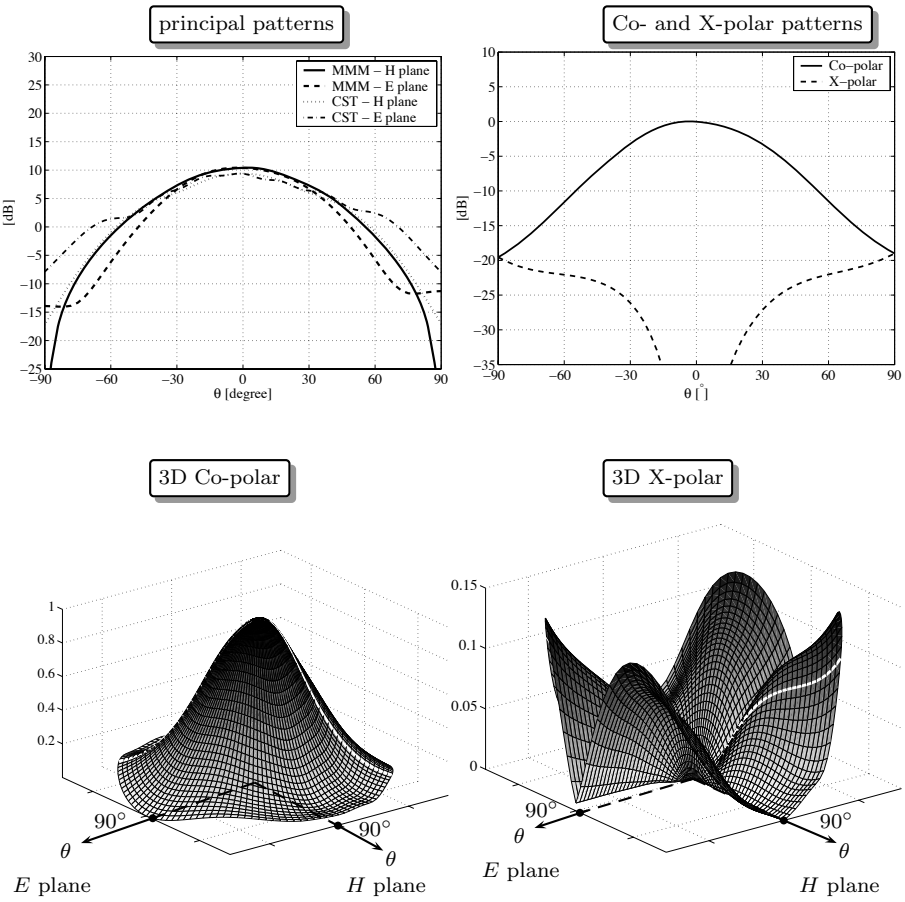

Figure 3.11: Field radiation patterns of the three element array at 12.5 GHz. The square aperture is fed with the TE_{10} mode and the other two rectangular waveguides are terminated on matched loads. The three-dimensional field patterns depict the relative magnitude of the pertinent field quantity normalized to the maximum value of the Co-polar component.

coupling, in the terminology of [17], to the "far-field" assumption);

- the *polynomial* approximation of the mutual coupling between the dominant modes in aperture antennas (the radiators could been closely packed) [9].

These approaches have been developed on the basis of some assumptions that are not valid in our investigation. On one hand, the "far field" assumption is seldom applicable in a phased array (requiring, even in sparse configurations, the radiators to be closely packed). On the other hand, the single-mode analysis obscures some highly relevant features of the antenna, for example

the matching properties in case of a very compact radiator when the feeding point is close to the aperture. To sidestep these obstacles one has to think at a solution that, in a broad sense, exhibits the following characteristics: *allows for a fast evaluation, as a function of distance, of a quantity that describes the mutual coupling effect (including the higher order modes) and which is amendable to the application of the superposition principle.* The requirement regarding the superposition is extremely important in designs that search for an optimum architecture of the array configuration (this is often the case in conceiving sparse arrays).

By observing that the modal coupling admittances between aperture antennas on ground planes depend only on the relative position of these apertures and their size (3.14), it is appropriate to search for an approximation of these quantities as a function of distance.

3.4.1 Polynomial interpolation

Initially, we made use of a neural networks method to approximate the mutual coupling between modes in aperture antennas. However, due to the storage requirements a polynomial interpolation/ extrapolation solution was preferred, as was initially described in [9]. Hence, we reformulated the polynomial interpolation such that it allows for the evaluation of the mutual coupling between the higher order modes, as well.

It is worth mentioning that sparse array antennas with arbitrary deployed elements are mainly of interest in linear configurations. Planar architectures are preferred to be realized by means of thinning techniques, where the elements are located at arbitrary positions on a uniform grid. Therefore the interpolation of the mutual coupling effect as a function of distance is not really beneficial in planar sparse array antennas.

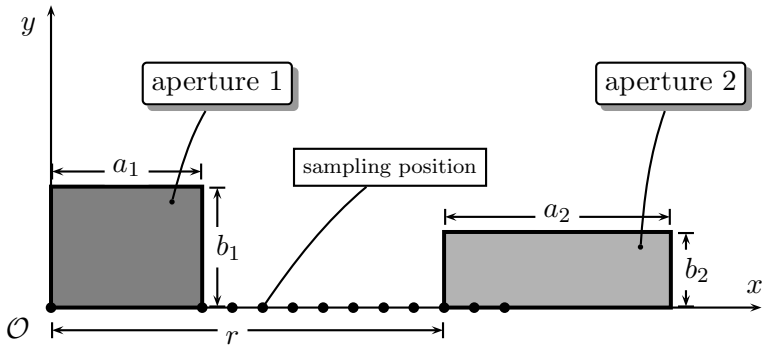

Figure 3.12: Linear arrangement of two apertures for polynomial approximation of the mutual coupling admittances.

In the followings the formulation for linear array antennas will be presented, the extension to planar configurations being straightforward. Let us consider two rectangular apertures on an infinite metallic flange as depicted in Fig. 3.12. The mutual coupling admittance between the mode p of aperture 1 and the mode q of aperture 2 can be expressed in a general form, as function of distance:

$$Y_{p,q}^{1,2}(r) = A(r)e^{-\mathrm{j}\varphi(r)}e^{-\mathrm{j}kr}, \tag{3.38}$$

where r is the distance between the two apertures, $A(r)$ represents the modulus of the mutual coupling admittance, $\varphi(r)$ denotes the variation of the phase with distance, and k is the wavenumber in free space. Some theoretical and experimental characteristics of the mutual coupling between aperture antennas can be used in selecting an analytic expression for A and φ. Some of them are hereafter catalogued:

- the coupling between widely separated apertures varies inversely with the separation distance in the E-plane and inversely with the square of the separation distance in the H-plane.

- the field near a radiation source varies inversely with the cube of the distance from the source.

- the phase also changes with the distance in the near field of a radiator.

To illustrate these phenomena, we have investigated numerically the coupling between two identical square apertures (with the dimensions $a_1 = 15\,\mathrm{mm}, b_1 = 15\,\mathrm{mm}$) and the coupling between two differently sized apertures (with the dimensions $a_1 = 15\,\mathrm{mm}, b_1 = 15\,\mathrm{mm}$ and $a_1 = 20\,\mathrm{mm}, b_1 = 20\,\mathrm{mm}$) as a function of their relative distance. In each case the two radiators were arranged, on a metallic flange, in the H-plane and in the E-plane, respectively. The analysis frequency was taken to be 12 GHz. For illustrative purposes only five modes (TE_{10}, TE_{01}, TE_{11}, TE_{11} and TE_{20}) were considered in each aperture, this leading to a number of twenty five modal coupling admittances to be evaluated. The absolute values of the coupling admittances (normalized to the maximum values) are depicted in Fig. 3.13. Additionally, for the consistence of the analysis, the $1/r$ and $1/r^3$ laws were also indicated with dashed lines. From the plots contained in this figure it is observed that the coupling admittances between higher order modes in two rectangular apertures vary inversely with the distance at an order between one and three. Moreover, this behavior is perceived in both E and H coupling planes.

Based on the above observations we proposed the following polynomial interpolation formulas for the amplitude and the phase of the mutual

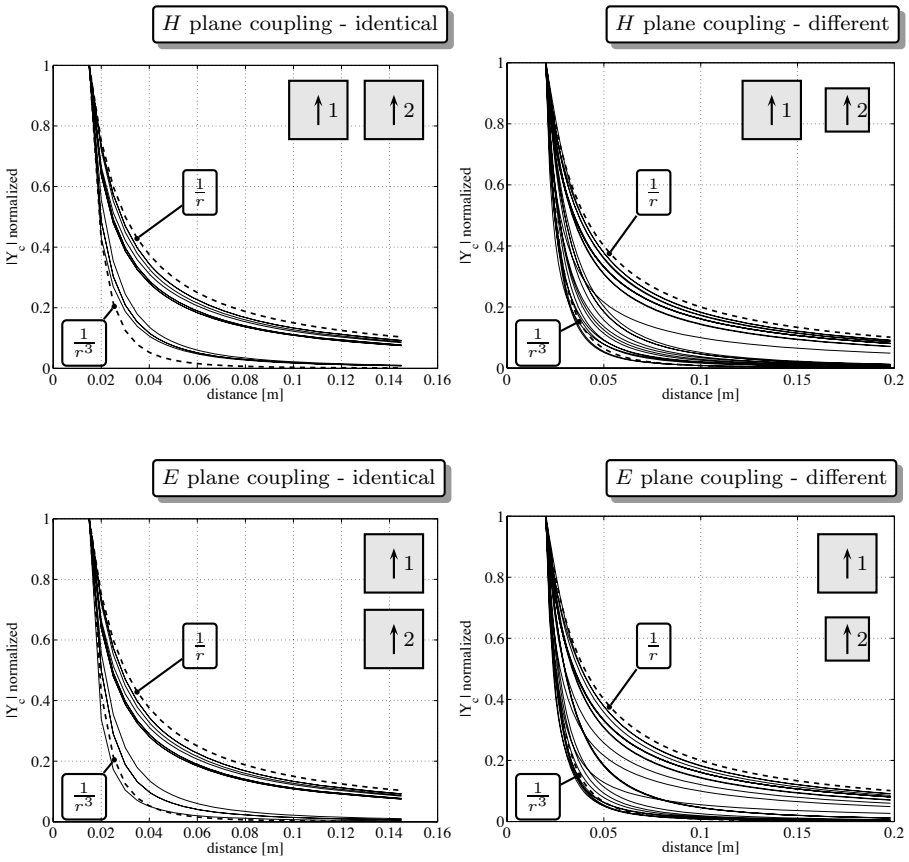

Figure 3.13: The absolute value of the coupling admittances between the modes of two identical apertures and the modes of two different sized apertures as function of distance. Analysis performed at 12GHz for apertures arranged in the E plane and in the H plane. Each of the continuous lines represents the coupling admittance between two particular modes.

coupling admittance:

$$A(r) = A_1 \left(\frac{1}{kr}\right) + A_2 \left(\frac{1}{kr}\right)^2 + A_3 \left(\frac{1}{kr}\right)^3, \tag{3.39}$$

$$\varphi(r) = B_1 \left(\frac{1}{kr}\right) + B_2 \left(\frac{1}{kr}\right)^2 + B_3 \left(\frac{1}{kr}\right)^3, \tag{3.40}$$

where A_i and B_i with $i = 1 \cdots 3$ are real coefficients to be found. A minimum number of six sampling points in distance, at which the coupling admittance has to be known, are sufficient for determining the unknown coefficients of

the polynomial interpolations (3.39) and (3.40). These points should be taken in the near field and in the far field as well. To increase the accuracy of the approximation it was found that taking a larger number of sampling points is a valuable strategy. In case of coupling between different sized apertures one can also experiment with good results polynomial interpolations with orders higher than three.

In conclusion, it is stated that the mutual coupling between the modes (including the higher order ones) of aperture antennas on a ground plane can be evaluated very fast (precise computing times will be provided in the following Section) by making use of the polynomial interpolations (3.39) and (3.40) in (3.38). Another positive aspect of this polynomial approach refers to the storage requirements which, in this case, reduces to six real coefficients for any considered coupling admittance.

3.4.2 Numerical study

The approximation methodology proposed in Section 3.4.1, for the evaluation of the mutual coupling effect in array antennas, was implemented in a computer program. Several array configurations and polynomial approximations of different order were analyzed within a validation study aimed to prove the robustness of the method. Two relevant test problems will be hereafter discussed.

In a first scenario, the mutual coupling between two identical apertures (denoted as 1 and 2) was evaluated as a function of distance over the range $0, \cdots, 0.145\,\mathrm{m}$ at 14 equidistant points in the H plane. The size of the apertures was $a = 15\,\mathrm{mm}$ and $b = 15\,\mathrm{mm}$ and the analysis frequency fixed at $12\,\mathrm{GHz}$. Five modes, namely TE_{10}, TE_{01}, TE_{11}, TM_{11} and TE_{20} were considered on each of the apertures 1 and 2. Consequently, 25 modal couplings need to be accounted for.

The results of this analysis are exemplified in Fig. 3.14 for the case of couplings between the modes $TE_{10} \leftrightarrow TE_{10}$, $TE_{10} \leftrightarrow TE_{20}$, $TE_{01} \leftrightarrow TE_{11}$ and $TE_{01} \leftrightarrow TM_{11}$. From these plots it is evident that the polynomial representation of the mutual coupling admittances is accurate and can be utilized for extrapolating the data, as well. As regarding the computation times it is pointed out that, for example, the evaluation of a generalized admittance matrix containing 300×300 modal coupling admittances was performed for a single frequency in less than one second.

Subsequently, the validation study was extended to the case of coupling between non-identical apertures. The dimensions of the two radiating apertures were $a_1 = 20\,\mathrm{mm}$ and $b1 = 20\,\mathrm{mm}$ and $a_2 = 15\,\mathrm{mm}$ and $b_2 = 15\,\mathrm{mm}$, respectively. The mutual coupling analysis was performed at $12\,\mathrm{GHz}$ as a function of distance over the interval $0, \cdots, 0.198\,\mathrm{m}$ at 23 equidistant points in the E plane. Again five modes, namely TE_{10}, TE_{01}, TE_{11}, TM_{11} and TE_{20}, were considered in both apertures. In Fig. 3.15 the

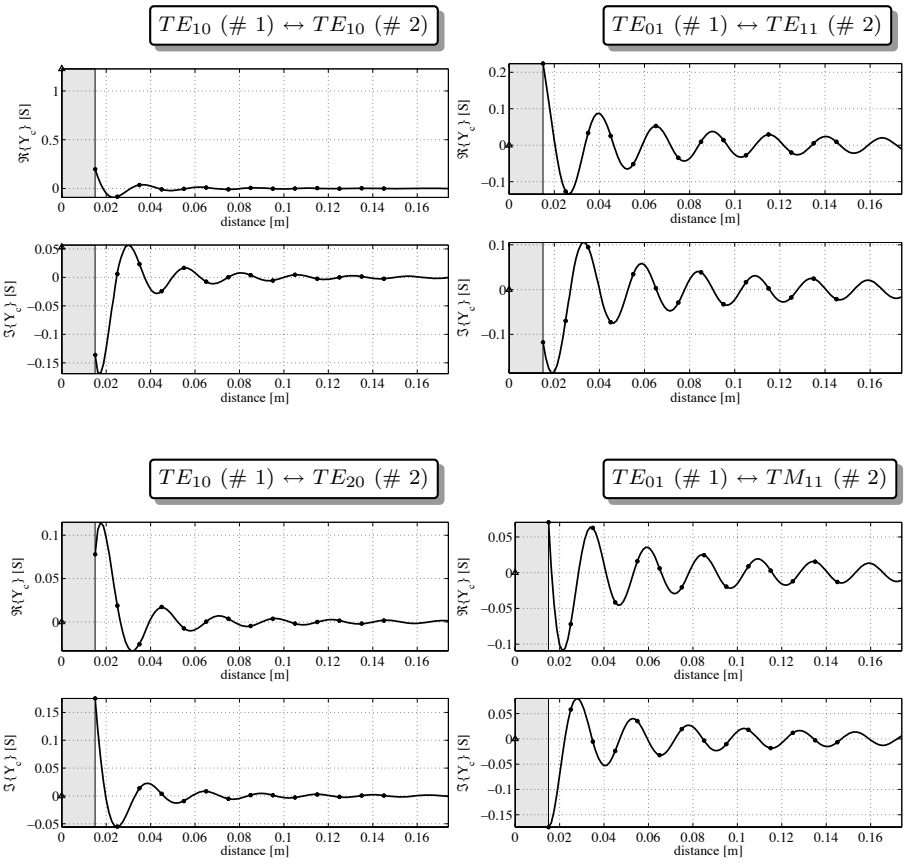

Figure 3.14: The coupling admittance (real and imaginary parts) between two apertures (denoted as 1 and 2) as a function of the relative distance along the $\mathcal{O}x$ axis (coupling in the H plane); the analysis frequency is 12 GHz; dots: coupling between apertures 1 and 2 - *computed values*; solid line: coupling between apertures 1 and 2 - *interpolated values*

results of the polynomial approximation solution for coupling between the modes $TE_{10} \leftrightarrow TE_{10}$, $TE_{20} \leftrightarrow TE_{10}$, $TE_{11} \leftrightarrow TE_{10}$ and $TM_{11} \leftrightarrow TE_{10}$ are presented. From these experiments it was learnt that the polynomial approximation of the phase of the modal coupling admittances has a beneficial effect when the apertures are closely deployed to each other. Note that the gray area in Fig. 3.14 and Fig. 3.15 indicates the aperture 1.

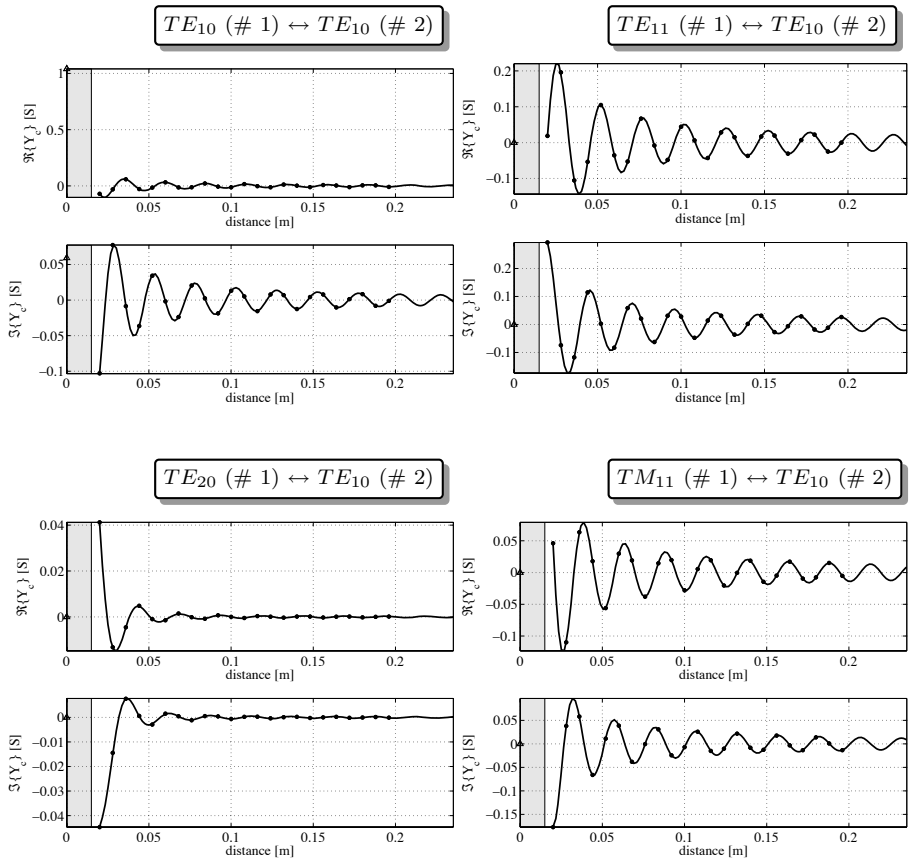

Figure 3.15: The coupling admittance (real and imaginary parts) between two different sized apertures (denoted as 1 and 2) as a function of the relative distance along the $\mathcal{O}x$ axis (coupling in the H plane); the analysis frequency is 12 GHz; dots: coupling between apertures 1 and 2 - *computed values*; solid line: coupling between apertures 1 and 2 - *interpolated values*

3.5 Conclusions

This chapter discussed the Mode Matching method used in the analysis of the radiation from aperture antennas arranged in arbitrary array configurations. Two techniques, namely, the Fourier approach and the solution based on the Green's function were presented in detail. These methods were implemented in software tools which will be later used in the design of shared aperture array antennas. The validation of these numerical routines was done by studying different test configurations and observing specific aspects related to the electromagnetic field and to the scattering parameters of the aperture

antennas. By analyzing the field distribution on a rectangular aperture, the singular behavior of some field components in the vicinity of the aperture's edges was clearly demonstrated. Moreover, the accuracy of the electromagnetic solution was tested by studying the continuity of all field components at the aperture level (inside and outside of the transmission line). Furthermore, the validity and the capabilities of the software implementations were demonstrated by calculating the self admittance of a waveguide antenna and by evaluating the mutual coupling between differently sized apertures. These results were confirmed against results published in the literature and results obtained with commercial software packages.

In array antennas consisting of a large number of elements the evaluation of the mutual coupling effect and, consequently, the behavior of individual radiators requires very long (often prohibitive) computation times. In this chapter a solution for the fast evaluation of the mutual coupling effect was proposed. This fast technique is based on a polynomial interpolation of the coupling admittances between the modes used to represent the field on the aperture antennas.

Elements of novelty

The calculation of the mutual coupling between different apertures is commonly done by solving fourfold integrals, this requiring large computation times. A solution to reduce the order of integration (to two) was proposed in this chapter. By adopting a convenient change of variables, it was demonstrated that two of the integrals in the coupling admittance can be solved analytically.

The solution proposed for the fast evaluation of the mutual coupling effect in array antennas is applicable to closely spaced apertures and can be used to approximate the coupling admittances between fundamental modes and higher order modes, as well. The fast calculation of the mutual coupling effect has a relevant impact in the process of designing arbitrary arrays where the subject to optimization are the positions of the elementary radiators.

Chapter 4

Elementary antennas

In this chapter some elementary antennas that can be used in array configurations are discussed. The basic requirements which a primary radiator should satisfy for being employed in arrays are introduced in the first section. A concise literature survey reveals a large number of antenna topologies that have been used in array systems. In particular, two types of radiators for moderate and wide band applications, that aim at robust, low profile antenna configurations have been proposed and investigated in detail. These models are the dielectric filled waveguide end antennas and the cavity backed patch antennas. The numerical electromagnetic analysis of these radiators is done in an efficient manner by making use of the theory and the software implementations presented in Chapter 2 and 3. Subsequently, some design strategies are discussed in relation with the influence of the relevant dimensions on the antenna's characteristics (matching properties). Experimental results are presented at the end of the chapter.

4.1 Elementary radiators for array antennas

The performances of an array antenna are closely related to the features of the primary radiating elements. The choice for an element type or another is in many cases motivated by the antenna specifications in terms of bandwidth, beamwidth, polarization, maximum scanning angle in array configuration, weight, occupied volume, technological complexity and cost.

Among the requirements imposed to individual radiators, the *size limitations* are the most restrictive one. It is well known that, for avoiding the formation of the grating lobes in a hemispherical field of view, the size of the primary radiator (in the array's plane) should be smaller than the wavelength at the maximum operational frequency. Moreover, when it is necessary to scan the main beam electronically, the elements in the array

should be deployed at a distance between each other not exceeding half of the wavelength corresponding to the highest spectral component in the array bandwidth [11, pp. 249–338]. Hence, the elementary antennas in array architectures should be electrically small. However, it is well documented that there are some fundamental limitations of small antennas concerning the bandwidth, efficiency, quality factor, etc. [144, 145, 146, 54]. Therefore, it is evident that there is a reduced number of antenna topologies that can be used in array configurations.

The quest for enlarging the antenna bandwidth is a reality of the nowadays research in the antenna field. Antennas having large bandwidths, as for example broadband dipoles (bow-tie, biconical geometry), broadband antennas (loops, helical structures) or frequency independent antennas (spirals, log-periodic) are in general characterized by large dimensions. The dimensional constraints make them less appropriated for being employed in array architectures. In the past years, for wide band array applications, a particular attention has been given to the notch antenna (also known as Vivaldi antenna) [149, 83]. This category of radiators can be easily arranged in array architectures due to the relative small dimensions in the relevant plane associated to the end-fire radiation mechanism. Exhibiting large bandwidths and quite satisfactory radiation properties, these arrays still occupy a large volume and they are not suitable for equipping mobile platforms.

Moderate bandwidth radiators, as for example dipoles, apertures (waveguide ends) and microstrip (patch) antennas are the most commonly used elements in practical array realizations [45]. These elements show a good compromise between dimensions and bandwidth. They are also characterized by large radiation patterns which are extremely beneficial in phased arrays with scanning capabilities.

The waveguide end antennas are among the most utilized radiating elements in systems that must handle large powers [45]. Often, the waveguide transmission line is filled with a dielectric material, having a high dielectric permittivity, in order to miniaturize the antenna [76, 130].

Currently, there is a manifest trend towards developing low-profile and low-cost antenna systems. Frequently, a dual polarization requirement is formulated, as well. A popular answer to this set of demands is provided by the class of (stacked) microstrip patch antennas [24, 13, 126, 49]. These are moderate to wide bandwidth radiators, covering fractional frequency ranges from 5 to 75%.

By accounting for all these features, a *dielectric filled waveguide* antenna and a *cavity-backed, stacked-patches* antenna have been selected as preferred elementary radiators in the analysis and design of sparse arrays and shared aperture antennas. In the following, the two types of elements will be discussed separately.

4.2 Dielectric filled waveguide antennas

The remarkable matching properties of the standard waveguide transmission lines with the free space has been at the origin of the use of these elements as antennas. The theoretical bandwidth of an open-ended waveguide antenna is bounded by the cut-off frequencies of the fundamental mode and of the first higher order mode. For a rectangular configuration, the ratio of these two frequencies is approximately 1.4. Another characteristic of the rectangular apertures is that at least one side length equals half of the wavelength corresponding to the fundamental mode (TE_{10}). As a consequence, the direct use of this element in array arrangements will result into a narrow band antenna system due to the limitations introduced by the formation of the grating lobes. For circumventing this problem, a simple solution is to fill the waveguide with a material having a relative dielectric permittivity higher than one. However, in most of the cases, the use of the dielectric filling is at the origin of a (strong) mismatch between the aperture and the waveguide transmission line. To cancel these reflections and to assure the transmission of the energy in the free space a matching circuit is needed to be included between the aperture and the feeding point.

Different techniques for matching the aperture to its feeding line have been reported in the literature. In general, the solution resorts to introducing a reactive discontinuity in the vicinity of the aperture, such that the reactive character of the dielectric filled aperture will be compensated. In [76] an experimental study was presented, in which the impedance of a circular radiating aperture was matched by introducing a circumferential air grove in the dielectric plug. A more efficient technique was introduced in [80, p. 101], where a simple air gap was used as matching circuit for rectangular dielectric-filled apertures. This solution will be also adopted in this work for the study of dielectric filled waveguide antennas. For two decades the IRCTR has been involved in analyzing, designing and measuring dielectric filled antennas using air-gaps [80, 128, 100, 53, 129, 132, 131]. The analysis methods were in general based on the power conservation condition and the modal representation of the field at the aperture. As regards the design of the matching circuit, it is pointed out that this was commonly performed as a trial-and-error procedure. In the following, the accurate modal analysis described in Chapter 2 and 3 is employed for the full-wave investigation of the dielectric filled antenna. Subsequently a design strategy, that makes use of the lumped-element representation of the antenna and some mathematical programming techniques, is proposed.

4.2.1 Analysis procedure

The configuration used in the analysis of dielectric filled waveguide antenna is depicted in Fig. 3.1. The rectangular aperture is taken to be mounted on an infinite, conducting flange. The filling material is taken to be homoge-

neous, isotropic and lossless, with a relative dielectric permittivity ε_r. For compensating the reflection from the aperture a dielectric discontinuity (air gap) is considered at a certain position inside the rectangular waveguide. All the transitions along the transmission line from one dielectric material to another are considered as a jump in the entire section of the waveguide. In the calculations, it is assumed that the antenna is fed by means of waveguide modes (commonly the TE_{10} mode). The exclusion from the calculation of a more practical feeding circuit, like, for example, a coaxial cable or a microstrip line, is motivated by the fact that the waveguide antennas are in general realized such that the influence of the feeding on the aperture is minimized. Besides, the excitation of the fundamental mode on a waveguide transmission line is an already solved problem and there is a large diversity of commercially available transitions from coaxial and microstrip lines to waveguides.

At the aperture, the field distribution is represented by means of a sum of waveguide modes. The Generalized Admittance Matrix (GAM) of the radiating part (the aperture) is estimated by imposing the field continuity conditions at the plane of the flange. Outside the waveguide, the electromagnetic quantities are evaluated using the Green's function of the free space.

The size of the rectangular waveguide is selected such that only the TE_{10} mode is propagating at the operational frequency. Consequently, the higher order modes that are excited at the aperture are of evanescent nature and, thus, vanish rapidly on the feeding transmission line. For compensating the reflections on the fundamental mode, an air gap is placed at a certain distance from the aperture, inside this transmission line. The ensemble consisting of the air gap (a hollow waveguide) and the dielectric filled waveguide up to the aperture (see Fig. 4.1.a) form, together, a matching circuit.

Inside of the transmission line the combination of different waveguide segments can be accurately modeled by means of the MM method and the GAM representation. It is worth observing that, for configurations where there are only jumps in the permittivity along the propagation direction, the modal coupling matrices at the interfaces are identity matrices. Once the internal junctions between different waveguide segments are solved, the calculation of the GAM pertaining to the complete matching and feeding structure will follow after some basic, algebraic manipulations.

The last step in the analysis procedure is to combine the two GAM's, of the internal and of the external problem, and to evaluate the input admittance matrix of the antenna. One should note that the internal problem is approximated by a multi-modal, two-port circuit (connected to the aperture and to the feeding waveguide) whereas the aperture is seen as a multi-modal, single-port network (connected to the transmission line). As a consequence the GAM of the antenna (including the feeding waveguide segment, the matching circuit and the aperture) is associated with a multi-modal, single-port circuit. The scattering parameters of the antenna (the most important

being the reflection coefficient of the excited mode) are furthermore derived from the admittance matrix. For evaluating the matching properties of the antenna over a frequency range, the analysis procedure must be repeated for every spectral component of interest.

Previous studies [80] have shown that, by increasing the relative permittivity of the dielectric filling, the reflections from the aperture are increasing, as well. Another factor that significantly affects the reflection from a dielectric filled aperture is the ratio between the side lengths of the rectangular, transverse section. For example, it was observed that a square aperture generates lower reflections towards the feeding line than a similar, rectangular antenna where one of the side length was reduced at half of the other one.

To compensate the undesired reflections from the apertures, at a certain frequency or over a frequency range, the air gap should have a specific length and must be located at a particular distance from the aperture. The search for these dimensions represents in fact a design procedure and will be detailed in the next section.

4.2.2 Design methodology

The design of antennas having complex topologies is commonly performed as a trial-and-error procedure, in which some structural parameters of the radiator are changed and the performances evaluated by means of a numerical electromagnetic analysis tool. When the design aims at assuring a good matching of the antenna to the feeding line, the scattering parameters are, more often than not, made subject to an optimization problem.

In the case of the dielectric filled waveguide antenna a different design procedure has been proposed in [29]. The approach is based on the lumped-element representation of the matching structure. The equivalent circuit of the antenna is then tuned in the desired bandwidth by imposing some matching conditions from the circuit theory in conjunction with a mathematical programming algorithm. In the following, this design technique will be outlined, for dielectric filled waveguide antennas that use air gaps to suppress the reflections from the aperture.

It is assumed that the ensemble consisting of the air gap (a hollow waveguide) and the dielectric filled waveguide up to the aperture (see Fig. 4.1.a) form, together, the matching circuit. The GAM of this matching section can be calculated by combining the coupling matrices of the air-to-dielectric transitions with the GAM's of the uniform waveguide segments.

Let N_1 and N_2 be the total number of modes (TE and TM) that are accounted for at the input (1) and output (2) ports (feed line and aperture, respectively) of the *complete structure*. Let $\boldsymbol{V}_1 = \{V_{1;p} \,|\, p = 1, \cdots, N_1\}$, $\boldsymbol{V}_2 = \{V_{2;p} \,|\, p = 1, \cdots, N_2\}$, $\boldsymbol{I}_1 = \{I_{1;p} \,|\, p = 1, \cdots, N_1\}$ and $\boldsymbol{I}_2 = \{I_{1;p} \,|\, p = 1, \cdots, N_2\}$ the (column) equivalent modal voltage and current vectors at the input and output ports. (Here, for simplicity, a single-index denoting of

the waveguide modes, in the order of their increasing cutoff frequencies, was considered.) The aggregate network GAM is then defined as

$$\begin{bmatrix} \boldsymbol{I}_1 \\ \boldsymbol{I}_2 \end{bmatrix} = \mathrm{GAM} \begin{bmatrix} \boldsymbol{V}_1 \\ \boldsymbol{V}_2 \end{bmatrix} = \begin{bmatrix} \mathrm{GAM}_{11} & \mathrm{GAM}_{12} \\ \mathrm{GAM}_{21} & \mathrm{GAM}_{22} \end{bmatrix} \begin{bmatrix} \boldsymbol{V}_1 \\ \boldsymbol{V}_2 \end{bmatrix}, \tag{4.1}$$

where the entries $Y_{ij;p_i,p_j}$ in the GAM_{ij} blocks, with $i, j = 1, 2$, $p_i = 1, \cdots, N_i$ and $p_j = 1, \cdots, N_j$, represent the coupling admittances corresponding to the $\{ p_i , p_j \}$ pair of modes. Note that, in view of the examined matching circuit being symmetric, the condition $\mathrm{GAM}_{12} = {\mathrm{GAM}_{21}}^T$ (with T denoting the transposition operator) holds. Now, by taking into account the fact that all higher order modes are evanescent, a sub-array $\mathrm{GAM}_{TE_{10}}$, pertaining to the fundamental TE_{10} mode, is extracted from the GAM defined in (4.1). This reduction of the order of the model is also motivated by the observation that at the air gap discontinuity there is no transfer of energy between different modes. Due to the TE_{10} mode having the lowest cutoff frequency, this sub-array has the entries

$$\mathrm{GAM}_{TE_{10}} = \begin{bmatrix} Y_{11;11} & Y_{12;11} \\ Y_{21;11} & Y_{22;11} \end{bmatrix} = \begin{bmatrix} Y_{11} & Y_{12} \\ Y_{21} & Y_{22} \end{bmatrix}, \tag{4.2}$$

with $Y_{12} = Y_{21}$. This GAM corresponds to a *single-mode*, two-port structure that is amenable to an equivalent Π (or T) lumped elements network representation, as indicated in Fig. 4.1,b. From (4.2), the values of the elements

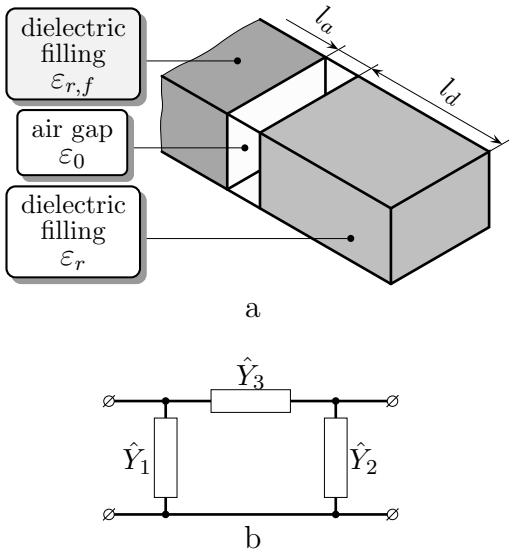

Figure 4.1: The matching circuit. (a) the air gap matching structure; (b) its equivalent Π lumped elements circuit.

of the Π equivalent circuit read

$$Y_1 = Y_{11} + Y_{12}, \tag{4.3}$$

$$Y_2 = Y_{22} + Y_{12}, \tag{4.4}$$

$$Y_3 = -Y_{12}. \tag{4.5}$$

On the other hand, the circuit theory [139] provides directly the values of an ideal network that matches the aperture admittance Y_a to the characteristic admittance $Y_{TE_{10}}$ of the TE_{10} mode. Let Y_1^t, Y_2^t and Y_3^t be the theoretical values of the lumped elements in the Π ideal network, the indices of the elements corresponding to those in Fig. 4.1,b. It then follows that, by fitting $\{ Y_1 , Y_2 , Y_3 \}$ on $\{ Y_1^t , Y_2^t , Y_3^t \}$, the aperture of the dielectric filled, open-ended waveguide antenna is matched to its feeding transmission line optimally. To this end, a *cost function* that measures the Euclidean distance between the two sets of lumped elements values is defined. Note, however, that the design parameters are, in fact, the length of the air gap l_a and that of the dielectric-filled waveguide section l_d. The evaluation of the cost function will then require a mapping $\{ l_a , l_d \} \leftrightarrow \{ Y_1 , Y_2 , Y_3 \}$ that can only be constructed by (repeatedly) solving the electromagnetic field problem concerning the matching circuit. Nevertheless, the chosen numerical analysis method renders this task elementary, since the GAM's of the air-to-dielectric transitions are constant and, thus, must only be evaluated once, and the GAM's pertaining to the uniform (dielectric filled) waveguide segments are analytical, their corresponding GAM_{ij} blocks, with $i, j = 1, 2$, being, moreover, diagonal.

With these prerequisites, the determination of the optimum dimensions $\{ l_a , l_d \}$ amounts to minimizing the cost function. In the case when, based on practical considerations (such as the fact that a compact structure is aimed at), the solution space is restricted to a domain were the cost function exhibits a single minimum, the minimization can be carried out highly efficiently by using direct search methods for multidimensional, unconstrained minimization [72]. In the case when such a restriction of the solution space cannot be achieved or when other design parameters (for example, the dielectric permittivity of the filling ε_r) are accounted for, the above mentioned methods may stop in local minima. In such cases, other optimization algorithms (like the Genetic Algorithm or the Simulated Annealing) may have to be called upon for finding the solution of the problem.

4.2.3 Numerical and experimental results

The proposed algorithm was implemented in a computer code for designing dielectric filled, waveguide-end radiators. Different antenna models were analyzed in order to validate and to evaluate the robustness of the design strategy. Hereafter, an example will be discussed concerning the design of an L-band waveguide antenna with dimensions of the aperture $a = 83\,\mathrm{mm}$

and $b = 10\,\text{mm}$. The relative dielectric permittivity of the filling material was taken to be 2.53.

Initially, the admittance and the scattering parameters of the aperture have been evaluated by means of the mode matching method. By examining the reflections from the aperture (see Fig. 4.3.a) it is obvious that they have an unacceptably high level ($S_{11} \approx -1\,\text{dB}$), which calls for the use of a matching circuit (air gap).

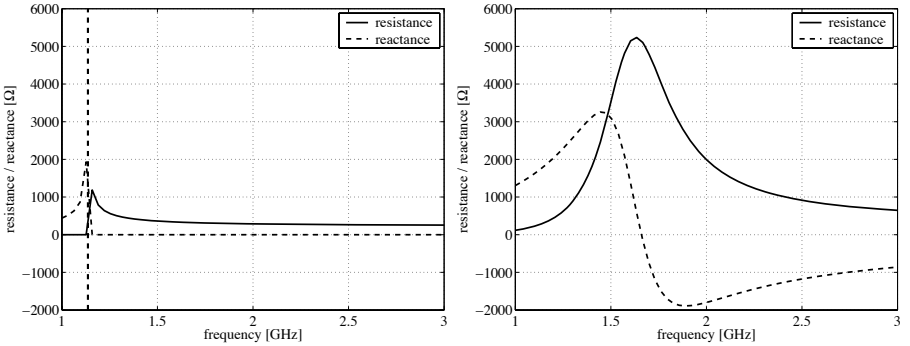

Figure 4.2: Frequency behavior of the input and output impedances of the matching circuit. (a) - line impedance (input); (b) - aperture impedance (output)

Commonly the analysis of the radiating part of an antenna involves complex numerical calculations. To sidestep these time consuming procedures, in the further design steps the radiating part of antenna is replaced by its admittance (of the fundamental mode), which is seen as a load by the matching circuit. In Fig. 4.2.b are depicted the real and the imaginary parts of the aperture impedance in the bandwidth of analysis. The frequency behavior impedance of the feeding line, attached to the input port of the matching structure, is given in Fig. 4.2.a.

By imposing an operational frequency of 1.6 GHz, a cost function, plotted in Fig. 4.4, was constructed for determining the optimum values of the air gap's length and position. This function being *convex* in the examined domain, a few iterations of the *Nelder-Mead simplex direct search* algorithm [72] were sufficient for finding its minimum. More specifically, in the case of the problem at hand, a number of 46 iterations (requiring 91 evaluation of the cost function) were carried out in order to determine the optimum combination $\{l_a\,,\,l_d\} = \{65\,,\,13\}\,[\text{mm}]$.

The performance of the matched aperture is illustrated in Fig. 4.3. In it, an excellent matching of the aperture to the feeding line is observed at 1.6 GHz. It should, however, be noted that the resulting radiator is rather

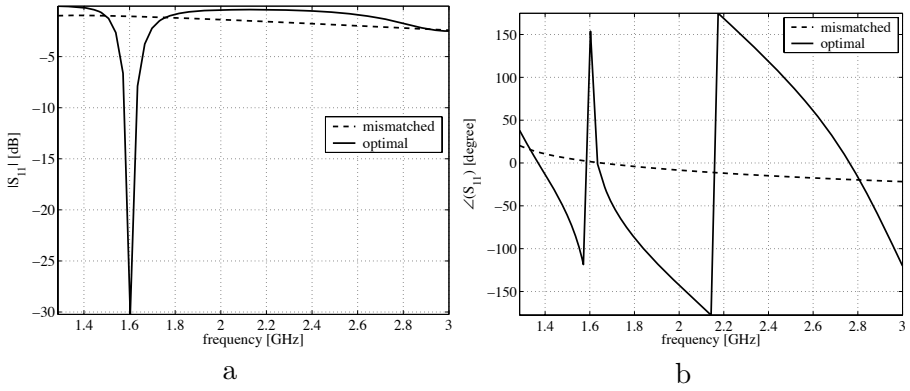

Figure 4.3: The reflection coefficient in the case when the matching circuit is omitted and included. (a) - absolute value; (b) - phase.

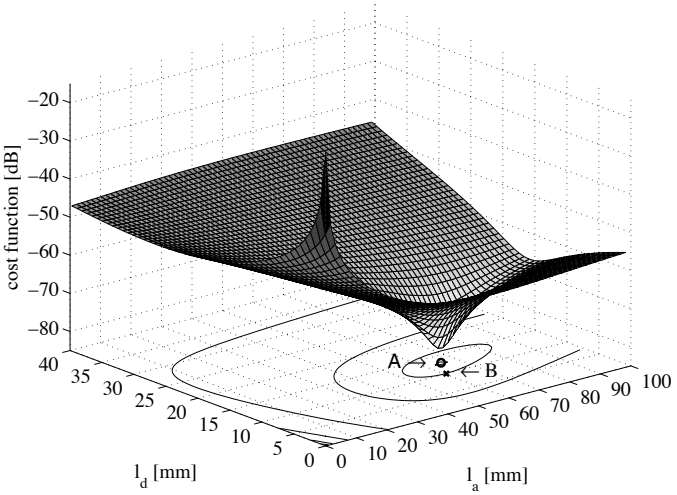

Figure 4.4: The cost function employed for determining the air gap's length l_a and position l_d for the operational frequency 1.6 GHz; A – the combination $\{l_a\,,\,l_d\}$ corresponding to the minimum of the cost function; B – the combination $\{l_a\,,\,l_d\}$ corresponding to the physical model.

narrow-band (with a relative bandwidth of $\approx 7\,\%$ for $S_{11} = -10\,\mathrm{dB}$).

The efficiency of the proposed algorithm is further demonstrated by computing the air gap's positions and lengths for 64 operational frequencies in the range $1.3, \ldots, 2.2\,\mathrm{GHz}$, the results being indicated in Fig. 4.5. The computation time for completing this task amounted to 2.61, seconds, only.

The numerical results were validated by means of measurements performed on the experimental set-up discussed in [130]. The investigated physical model concerned a dielectric filled, open-ended waveguide antenna, having an aperture of dimensions $a = 83\,\text{mm}$ and $b = 10\,\text{mm}$ (the same as those considered in the beginning of this Section). However, unlike in the case of the theoretical model, the waveguide antenna was mounted on a flange of *finite extent*. The employed dielectric filling had a relative permittivity $\varepsilon_r = 2.53$ and it was available *in blocks having lengths of multiples of 10 mm, only*. The experiments reported in [130] aimed at matching the aperture to the feeding waveguide at a frequency of 1.6 GHz. By physically tuning the air gap's length and position, a deep resonance was measured at the targeted frequency for a combination of dimensions $\{l_a\,,\,l_d\} = \{60\,,\,10\}\,[\text{mm}]$ (see Fig. 4.6). The measured results are in a reasonable agreement with the numerical experiments that predicted an optimal combination of dimensions $\{l_a\,,\,l_d\} = \{65\,,\,13\}\,[\text{mm}]$.

Based on the variation of the cost function depicted in Fig. 4.4, it may be argued that the combination of dimensions provided by the physical experiments (obtained under the restriction of l_d being adjustable in discrete steps of 10 mm, only) is slightly sub-optimal. This can be further substantiated by computing the values of the reflection coefficients for $\{l_a\,,\,l_d\} = \{60\,,\,10\}\,[\text{mm}]$ with the MMM method and by using the CST Microwave Studio commercial package (the results are depicted in Fig. 4.6). From this plot, it can be derived that the calculated resonance is shifted above the targeted frequency (at $\approx 1.67\,\text{GHz}$). This discrepancy is attributed

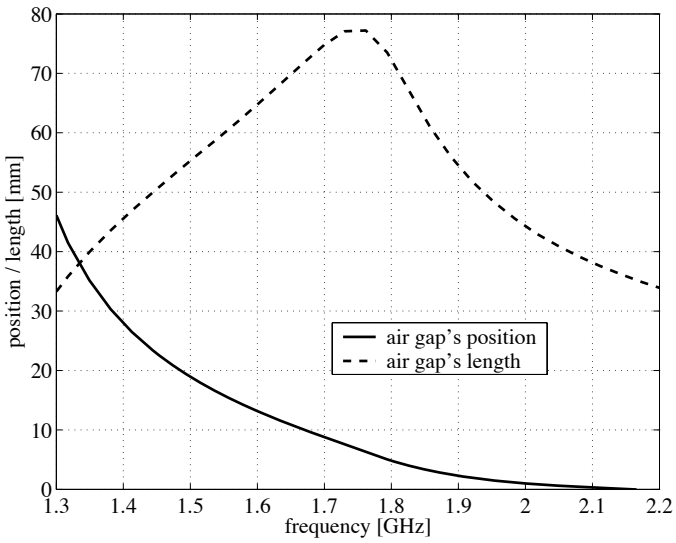

Figure 4.5: The values of the air gap's position l_a and length l_d for matching frequencies in the range $1.3, \ldots, 2.2\,\text{GHz}$.

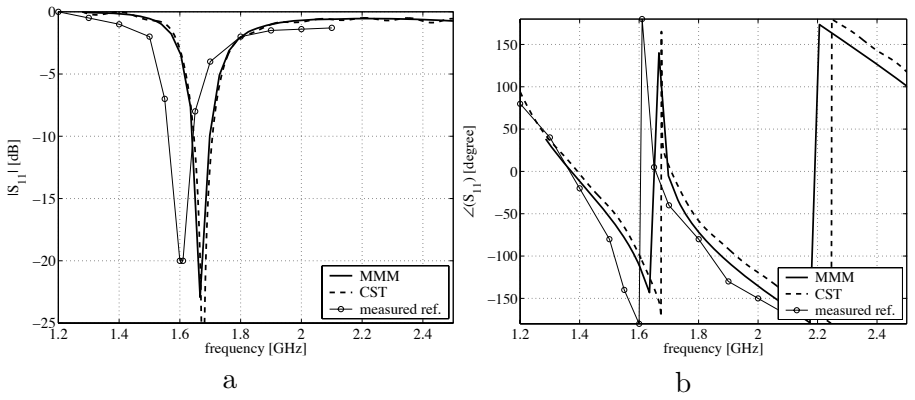

Figure 4.6: The computed and the measured reflection coefficients in the case of the physical model. (a) - absolute value; (b) - phase.

to the fact that the theoretical and the physical models differ, most notably, that the dielectric relative permittivity in the physical model could not be accurately measured. Another source of the noticed inconsistencies can be the occurrence of small dimensional deviations during the manufacturing process.

Extensions of the concept

The idea of translating the design of the matching circuit into an optimization problem that is at the core of the computational approach described in section 4.2.2 has a number of extremely favorable features. This immediately prompts to some possible extensions of the applicability of the advocated design methodology.

It is firstly noted that, by conveniently limiting the solution space of the variational problem (and, possibly, by ensuring the convexity of the cost function) efficient multidimensional minimization algorithms may be employed for determining the optimum dimensional and/ or physical parameters of the matching circuit. In this manner, the number of evaluations of the cost function (notoriously computationally-intensive tasks) are drastically reduced. It then follows that any numerical technique may be employed for analyzing the matching structure, without impeding excessively on the time-effectiveness of the design process. The only requirement is that the relevant technique should provide a GAM (or, alternatively, $S-$parameter) description of the complete matching network. One attractive option is to include a (commercially available) electromagnetic analysis tool in the global optimization loop (by using a "black box" program architecture). This will create the conditions for being able to account for more complex filtering structures, that may not be amenable to the MMM – GAM representation.

Secondly, the hereby discussed computational approach may also be adapted for designing broad-band matching networks that implement complex transfer functions. To this end, the poles of the transfer functions will be associated with elementary structures consisting, for instance, of air gap – dielectric filled waveguide segments. Each such cell is straightforwardly obtained by applying the cost function minimization. Finally, for achieving the desired transfer, these elementary structures need being cascaded.

4.2.4 Conclusions and discussion

A general methodology for the design of the dielectric filled open-ended antennas was proposed. The Mode Matching Method was used for finding the aperture admittance and the Generalized Scattering Matrix of the waveguide discontinuities. The matching structure, accounted for by its Generalized Admittance Matrix, was translated into an equivalent, lumped circuit. The physical dimensions of the structure were found by using a Nelder-Mead simplex direct search method that performed the inverse transformation of a lumped circuit into a waveguide architecture.

Due to the chosen segmentation of the problem and to the imposition of the matching conditions for each waveguide segment, the optimization process assumed by the proposed design methodology acts on a reduced number of parameters. This deviates from the traditional approaches, employing the scattering parameters directly in the optimization procedure and thus, requiring the characterization of the entire structure *as a whole*, with the accompanying large(r) number of design parameters. From a computational point of view, the choices made in the present design strategy largely improve the speed and the robustness of the iterative process. Furthermore, the employed formulation also presents benefits from a conceptual point of view, since it provides an adequate handle to understanding the matching of the discontinuities in the case of radiating apertures or filtering structures.

From this study it was learned that dielectric filled waveguide antennas can be easily miniaturized for accommodating the size requirements in the array architectures. The reflection from the radiating aperture can be compensated over a moderate frequency range by simply using an air gap. The radiation properties of a rectangular aperture were also found very attractive for array applications. There are, however, some practical aspects that limit the use of the dielectric filled waveguide antenna in array systems. One of these problems is related to the manufacturing process that is quite expensive and takes considerable time. The length of the antenna, including the matching circuit and the feeding structure (commonly a coaxial to waveguide end-launcher), is in order of a few wavelengths at the operational frequency, which is not acceptable in low profile applications. Moreover, assembling an array of waveguides is a delicate process that can introduce some alignment errors or deformations.

4.3 Cavity-backed patch antennas

Cavity-backed, microstrip patch antennas have a topology similar to the dielectric filled waveguide antenna but they are low profile, low cost and lightweight structures. Enclosing a microstrip antenna into a metallic cavity has been often indicated as a solution for increasing the bandwidth or for reducing the level of the back radiation. When patch antennas are employed in array environments, the surface waves that are generated (the more so in the case of stacked-patches antennas) have a detrimental effect on the antenna's efficiency, especially at large scanning angles [67]. The most adequate solution to the suppression of the surface waves is to place the radiating patch(es) in a metallic cavity [66, 40, 42]. Note that this solution also contributes to the reduction of the mutual coupling between elements. For feeding such radiators, either protruding probes [24, 40, 42] or an aperture coupling [126] have been proposed. While the latter option is generally considered to ensure a wider operational bandwidth, the former provides a better isolation between the channels and a more direct access to individual elements, that is essential for measurement purposes (a highly relevant aspect during the system development phase).

Within the WiSE project, attention has been given to antenna topologies consisting of rectangular cavities and circular patches. Initially a single patch configuration was investigated. By imposing some technological restrictions (type of the dielectric material, height of the microstrip substrate, etc.) it was found that this configuration exhibits a relatively narrow bandwidth ($\leq 5\%$). To enlarge the bandwidth, two other topologies were analyzed: a capacitively coupled structure (as indicated in [42]) and a stacked patch architecture.

Similar steps were adopted in the analysis and the design of all these radiators. Therefore, in the followings these procedures will be exemplified for the stacked patch antenna, only.

4.3.1 Analysis procedure

The geometry of the analyzed configuration is depicted in Fig. 4.7. It consists of a metallic rectangular cavity filled with a dielectric and having inside a circular patch that is connected to the coaxial cable. On top of this patch there is another circular patch, which is capacitively coupled with the excited patch. In the approach adopted in this work, the combination of the two patches and the segment of rectangular coaxial waveguide is seen as a matching circuit that should adapt the aperture impedance to the impedance of the coaxial cable (50Ω). The metallic flange at the aperture is infinitely extended, this ensuring a facile extrapolation of the analysis method to the case when the elementary antenna is incorporated in a finite or sparse array configuration.

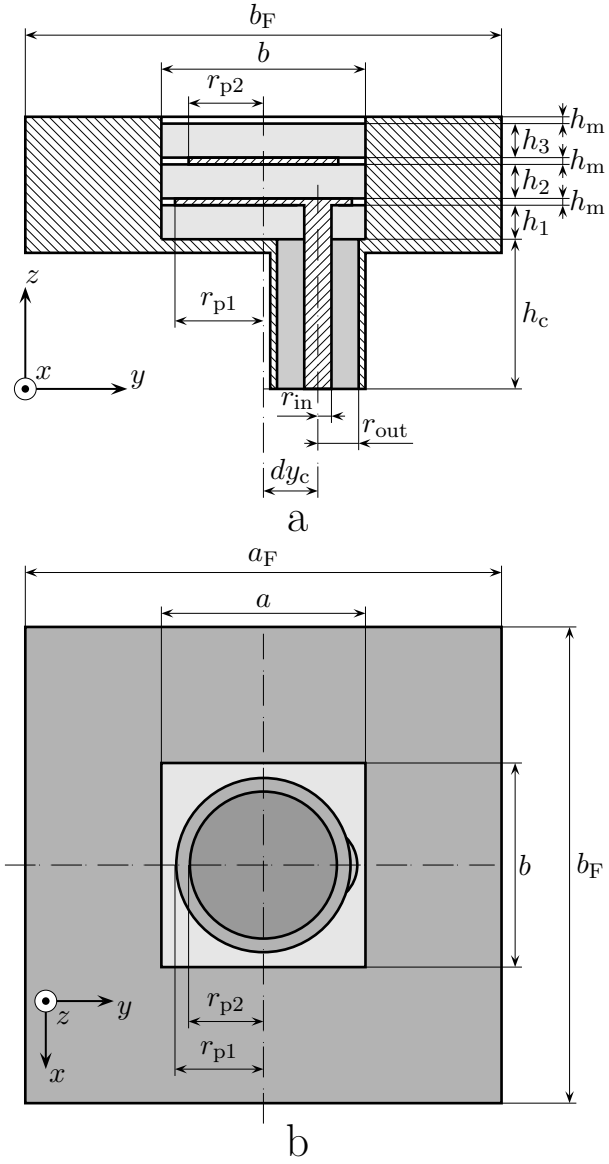

Figure 4.7: The configuration concerning the double patch antenna. (a) – Axial cross-section; (b) – top view.

The solution of the electromagnetic problems concerning the analysis of the cavity-backed patch antennas can be obtained by either resorting to a three-dimensional grid (as in the case of the finite-differences and finite-element methods [66, 140]) or by applying an integral-equations approach (as in the case of the mode-matching method). For efficiency considerations, the design strategy discussed in this work employs a mode-matching technique.

The application of this method requires the knowledge of the modal distributions in all cross-sections along the transmission channel having as input port the coaxial cable and as output port the aperture. From Fig. 4.7, it is evident that the configuration under investigation contains a combination of rectangular and coaxial waveguide sections. As for the latter variant, it is noted that the following cases occur:

- circular waveguides with concentric circular inner conductors and
- rectangular waveguides with both concentric and eccentric circular inner conductors.

The modal representation on the coaxial segments was calculated by means of the BI-RME method while that on the rectangular waveguide segments is known analytically. The transmission channel is completed by including a load that mimics the radiation into the free-space. The theoretical background for the analysis of the radiation from rectangular apertures relies on the methods presented in Chapter 3.

4.3.2 Design methodology

From the beginning it is worth noting that for simplifying the manufacturing process and for reducing the cost of the antenna, a stratified technology was assumed in the manufacturing process. With this technological standpoint, the cavity-backed, stacked-patch antenna (presented in Fig. 4.7) can be assembled by using three layers of microstrip laminates. The patches can be easily etched on the metallic sides of the microstrip substrates. Furthermore, it is assumed that the lower substrate, referred to as $S1$, has the relative dielectric permittivity ε_{r1} and the height h_1. The relative dielectric permittivities and the heights of the middle layer (denoted as $S2$) and of the upper substrate (denoted as $S3$) are taken to be ε_{r2}, h_2 and ε_{r3}, h_3, respectively.

The design of the antenna depicted in Fig. 4.7 can be seen as a search for the optimum constructive parameters that provide a good matching between the feeding line and the free space, over a specific frequency range. Among these parameters, the most relevant are: the dimension of the cavity, the dielectric permittivity of the substrates, the heights of the substrates, the radii and the positions of the two patches, and the offset of the feeding point. The parameters of the feeding coaxial cable were fixed for all the antenna models at specific values that replicate the dimensions of a SMA (SubMiniature version A) connector ($r_{\text{in}} = 0.64\,\text{mm}$, $r_{\text{out}} = 2.05\,\text{mm}$ and the relative permittivity of the dielectric material $\varepsilon_c = 1.951$). Furthermore, it was assumed that the radius of the protruding pin, in the rectangular cavity, equals the radius of the inner conductor of the coaxial cable ($r_{\text{in}} = 0.64\,\text{mm}$).

Size of the cavity

By tacking into account the fact that the antenna is intended for use in array configurations, the dimensions of the cavity can be derived from the relation between the operational bandwidth and the grating lobes condition. The shape of the aperture was chosen as being square for the following considerations. Firstly, it is observed that a square aperture can support two orthogonal polarizations. From a theoretical study of dielectric filled aperture antennas it was concluded that the level of reflections in the case of a square topology is lower than in the situations when the aperture is of rectangular shape. Additionally, it is pointed out that this work focussed on array configurations that can scan the beam in two orthogonal planes and, therefore, a square cell will address in an adequate manner the grating lobes restrictions associated to this requirement.

Dielectric permittivities of the layers

It is known that the operational bandwidth of an antenna can be translated to a lower domain by filling the cavity with a dielectric material, which has a relative dielectric permittivity higher than one. Commonly, antennas designed to operate in the X band are using dielectric materials with relative permittivities between 1 and 10. The microstrip laminates having high permittivities allow for a significant miniaturization of antennas. However, these materials (characterized by high permittivities) are associated with high costs and some technological difficulties. Another aspect related to the dielectric materials for antenna applications is that the commercial substrates are available in a limited range of discrete values of relative dielectric permittivities.

Heights of the substrates

In the topology of the cavity-backed, stacked-patch antenna depicted in Fig. 4.7 the heights of the dielectric substrates control the position of the metallic patches along the longitudinal axis. These positions have a significant influence on the input reflection coefficient of the antenna and they are often made subject to an optimization problem during the design process. It is worth observing that the commercial microstrip substrates are available in a finite number of thicknesses and, therefore, the dimensions h_1, h_2 and h_3 can only take some fixed values. In the selection of the layer heights one should consider the dielectric permittivities of the layers and some phenomenological aspects as for example: the bottom layer controls the inductance introduced by the protruding pin, the middle layer influences the capacitance formed between the stacked patches and the top layer determines the distance from the aperture where is placed the matching circuit. Moreover, the choice for the microstrip substrates is also influenced by the environmental

requirements imposed on the antenna and by the technology adopted in the manufacturing process.

At this point it can be concluded that in the design of the cavity-backed, stacked-patch antennas (using commercial microstrip laminates) the size of the cavity and the dielectric permittivities and the heights of the substrates must satisfy some requirements, which make them less suitable to be used as tuning parameters. The remaining three antenna parameters, namely the size of the top patch (r_{p2}), the size of the bottom patch (r_{p1}) and the offset of the feeding point (dy_{c}), have been adopted in this work as the ones to be changed within the design process. This choice has been motivated by the following observations:

- they have a significant influence on the matching properties of the antenna;
- they can take any value within some bounds imposed by the topology of antenna (the patches must fit inside the cavity and the feeding point should remain inside the domain defined by the surface of the bottom patch);
- the variation of the dimensions r_{p2}, r_{p1} and dy_{c} can be realized technologically in a facile manner and with a high accuracy.

In view of an automatic design procedure, the search for the optimum antenna parameters can be performed efficiently by means of mathematical programming algorithms. Two methodologies, which aim at the optimization of the matching properties of the antenna, have been implemented in conjunction with a conjugate gradient method. In a first approach, the design procedure based on the admittance parameters, presented in Section 4.3.1, was applied to the cavity-backed, stacked-patch antenna. Additionally the classical approach based on the minimization of the input reflection coefficient of the antenna was applied to similar problems. The results obtained by means of the two methods were comparable and the calculation times were in the same range.

Nevertheless, the experiments with these automated design approaches revealed two inconveniences. Firstly, the objective functions in both optimization procedures have multiple minima, which often prevent the algorithm from reaching the optimum solution. A second problem was that the mathematical solution was provided with a very high accuracy, which is frequently beyond the precision of the technological process. To circumvent these drawbacks, a grid search algorithm was also included in the design process in order to find the values of the design parameters r_{p2}, r_{p1} and dy_{c} that can be used as the coordinates of the initial point in the mathematical programming procedure.

The design strategy presented above has been implemented in some computer routines which were used in dimensioning cavity-backed, stacked-patch antennas operating in the X band. Table 4.1 catalogues the results

obtained by considering differently sized cavities and various microstrip laminates. In order to find the optimum antenna configuration, the design parameters (r_{p2}, r_{p1} and dy_{c}) have been given values within the intervals specified with square brackets in the table. The significance of the antenna dimensions indicated in Table 4.1 is provided in Fig. 4.7. The meaning of the additionally quantities included in this table is as follows:

- $B = 2\frac{(f_{max}-f_{min})}{(f_{max}+f_{min})}$ is the fractional bandwidth of the antenna;
- f_{min} is the lowest frequency limit of the bandwidth measured at the point where the return loss equals 10 dB;
- f_{max} is the highest frequency limit of the bandwidth measured at the point where the return loss equals 10 dB;
- dy_{c}^{opt}, r_{p1}^{opt} and r_{p2}^{opt} represent the dimensions of the optimum model (for which the bandwidth is provided).

From this parametric study it was observed that cavity-backed, stacked-patch and probe-fed antennas, exhibit moderate bandwidths with relative values between 5% and 15%. These results are comparable with those presented in the literature for similar configurations [41, 50]. Moreover, the exhaustive, mathematical investigation of the influence of the design parameters on the antenna characteristics allowed for achieving optimum models with improved matching performances. Another remark is that the combination of the microstrip laminates bounds the maximum value of the antenna impedance bandwidth that can be attained by changing the offset of the feeding point and the radii of the stacked patches.

For the fine tuning of the antenna, even in the case of an automated design procedure. It is important to recognize the individual effects of the variation of the design parameters on the antenna characteristics. In this respect the antenna model D10 (see Table 4.1) was analyzed in more details. In this study, all the antenna dimensions were kept fixed, except for one of the design parameters (r_{p2}, r_{p1} or dy_{c}), which was varied around the optimum value (also provided in Table 4.1).

Variation of the radius of the upper patch

The input reflect coefficient of the antenna evaluated for different dimensions of the upper patch is presented in Fig. 4.8.a. The radius r_{p2} was given values in the range from 2.5 mm to 5.5 mm at 33 equidistant points. From this picture it is observed that at small values of r_{p2} the reflections at the feeding point are high and there is no transfer of energy to the free space. By increasing the size of the patch, the matching characteristics are improved and at one point, when the two patches become comparable, the antenna

Table 4.1: Parameter study of cavity-backed, stacked-patch antennas consisting of different dielectric substrates. The analysis parameters were the offset of the feeding point (dy_c) and the radius of the circular patches (r_{p1} and r_{p2}). The dimensions are expressed in mm and the frequencies in GHz.

Model	a	b	h_1	h_2	h_3	ε_1	ε_2	ε_3	dy_c	r_{p1}	r_{p2}	B_{max}	f_{min}	f_{max}	dy_c^{opt}	r_{p1}^{opt}	r_{p2}^{opt}
D1	11	11	0.524	1.5	0.12	3.5	3.5	3.5	$[1,3]$	$[3,4.5]$	$[3,4.5]$	9.5%	10.8	11.9	3	3.5	3
D2	11	11	0.508	1.5	0.508	3.5	3.5	3.5	$[1,3]$	$[3,4.5]$	$[3,4.5]$	4.5%	8.8	9.3	2	4	3.5
D3	11	11	0.13	1.5	0.508	3.5	3.5	3.5	$[1,3]$	$[3,4.5]$	$[3,4.5]$	4.8%	9.4	10	2.5	4	3.5
D4	12	12	1.6	1.6	1.6	2.2	2.2	2.2	$[2,4.5]$	$[3.5,5]$	$[3.5,5]$	9.4%	9.5	10.4	4	4	3.5
D5	12	12	0.787	0.787	0.787	2.2	2.2	2.2	$[2,4.5]$	$[3.5,5]$	$[3.5,5]$	11.1%	10.7	12	4.5	4.5	4
D6	12	12	0.508	0.508	0.508	2.2	2.2	2.2	$[1,4]$	$[3.5,5]$	$[3.5,5]$	5%	10.8	11.3	3.5	3.5	4.5
D7	12	12	3.2	0.508	0.508	2.2	2.2	2.2	$[1,3]$	$[3.5,4.5]$	$[3.5,4.5]$	11.2%	10.2	11.5	3	3.5	3.5
D8	12	12	0.8	0.8	0.8	2.5	2.5	2.5	$[1,4]$	$[3.5,4.5]$	$[3.5,4.5]$	10%	10.2	11.3	3.5	4.5	4
D9	12	12	0.338	1.5	0.338	3.48	3.48	3.48	$[3,4.5]$	$[3.5,5]$	$[3.5,5]$	8.8%	9.6	10.4	4	4.5	3.5
D10	12	12	0.508	1.5	0.305	3.38	3.38	3.38	$[3,4.8]$	$[4,5.5]$	$[3.5,4.4]$	10.6%	8.9	9.9	3.3	4.6	3.8
D11	14	14	0.338	1.5	0.338	3.48	3.48	3.48	$[3.5,5.5]$	$[4,6]$	$[4,6]$	7.3%	7.9	8.5	3.5	5	4.5
D12	14	14	0.508	1.5	0.305	3.38	3.38	3.38	$[4,4.4]$	$[4.5,5.9]$	$[4,5]$	8.2%	8.2	8.9	4	5.1	4.4

starts radiating over a significant bandwidth (of almost 1 GHz). By further enlarging the radius r_{p2} the bandwidth of antenna is narrowed and shifted to a lower frequency domain. This behavior can be interpreted as a resonance of the upper patch, which diminishes the influence of the other two design parameters. By increasing the size of the upper patch the capacitance formed by the two stacked patches is also increased. This effect is clearly indicated on the Smith chart presented in Fig. 4.8.b, by the rotation of the loci of the input impedance from the inductive domain to the capacitive domain. Note that in Fig. 4.8.a the horizontal dashed lines indicate the r_{p2} values corresponding to the antenna models referred in Fig. 4.8.b. The circles of VSWR = 2 and VSWR = 1.5 are depicted in Fig. 4.8.b with dashed lines, as well.

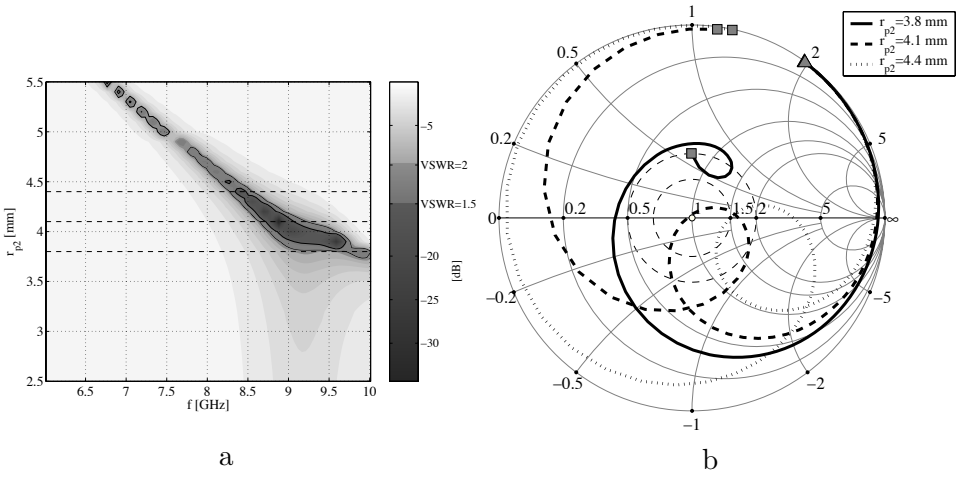

Figure 4.8: Influence of the size of the top patch on the antenna matching characteristics. (a) The absolute value of the input reflection coefficient; (b) the input admittance on the coaxial cable for three values of the radius of the top-patch (triangles correspond to the minimum frequency - 6 GHz and squares correspond to the maximum analysis frequency - 10 GHz)

Variation of the radius of the bottom patch

The influence of the size of the bottom patch was investigated by varying the radius r_{p1} in the range from 2.5 mm to 5.5 mm at 33 equidistant points. The input reflection coefficients of these antenna models are plotted as a function of frequency in Fig. 4.9.a. From this picture it is evident that this patch does not affect the position of the resonant frequency. Hence, it can be inferred that the bottom patch contributes more in the feeding mechanism of the top patch than in the resonant behavior of the antenna. This observation was

also confirmed by other studies in which the bottom patch was completely removed without a significant effect on the performances of the antennas. Analogously to the variation of the upper patch, by increasing the radius r_{p1} the capacitance formed between the two patches increases, as well. This effect is graphically indicated on the Smith chart presented in Fig. 4.9.b.

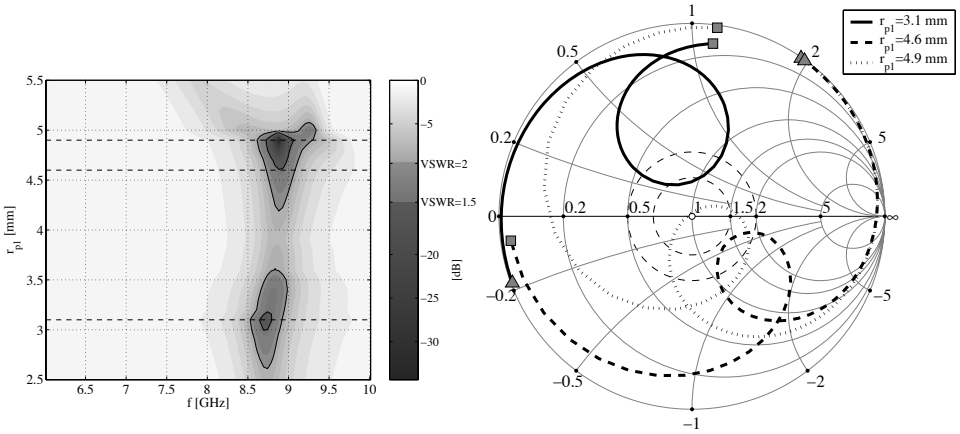

Figure 4.9: Influence of the size of the bottom patch on the antenna matching characteristics. (a) The absolute value of the input reflection coefficient; (b) the input admittance on the coaxial cable for three values of the radius of the top-patch (triangles correspond to the minimum frequency - 6 GHz and squares correspond to the maximum analysis frequency - 10 GHz)

Change of the position of the feeding point

Due to the coupling mechanism between the fundamental modes of the coaxial (feeding) cable and of the (radiating) aperture, the position of the feeding point has to be moved out of the longitudinal axis of the cavity. Aiming at antennas with linear polarization, the position of the feeding probe has been shifted in the positive direction of the $\mathcal{O}x$ axis, only. The influence of the offset dy_{c} on the input reflection coefficient of the antenna is depicted in Fig. 4.10.a. From this figure it is noted that at low values of dy_c a narrow resonance is present. By increasing the value of the offset, the resonance shifts towards higher frequencies. At a certain point ($dy_{\mathrm{c}} \approx 3\,\mathrm{mm}$) one can notice the presence of a second resonance. By further enlarging the value of the offset, the two resonance are approaching each other until they become only one resonance with a larger bandwidth. The input admittances for three antenna models having their feeding point located at different positions are depicted in Fig. 4.10.b. The consequence of increasing the value of the offset

dy_c can be interpreted as a reduction of the inductive character associated to the protruding pin.

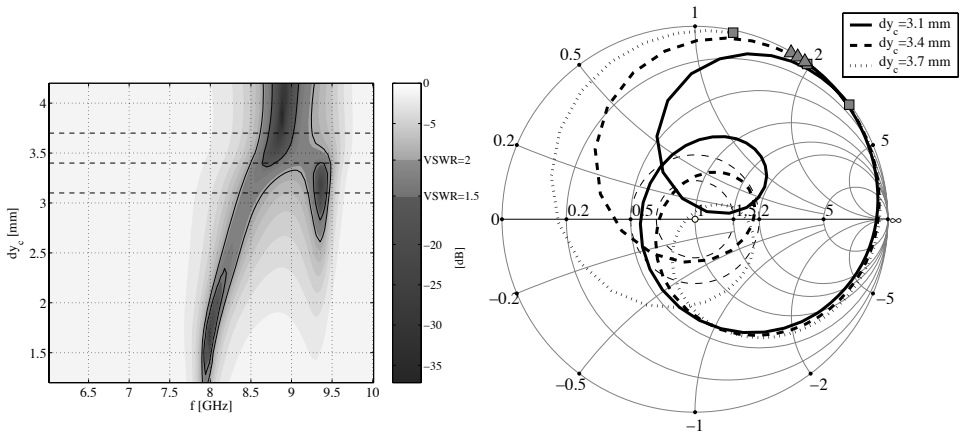

a b

Figure 4.10: Influence of the offset of the feeding point on the antenna matching characteristics. (a) The absolute value of the input reflection coefficient; (b) the input admittance on the coaxial cable for three values of the radius of the top-patch (triangles correspond to the minimum frequency - 6 GHz and squares correspond to the maximum analysis frequency - 10 GHz)

The influence of each of the design parameters (r_{p2}, r_{p1} and dy_c) on the impedance matching properties of the antenna have been analyzed by keeping fixed all the other dimensions. It is worth noting that the antenna characteristics are controlled by a collective effect of the design parameters. Hence, the observations made during this study should be used within the design process in a broad sense. A valuable approach in searching for the optimum antenna dimensions is to investigate the configurations specified in a multidimensional domain defined by the intervals of variation associated to each of the design quantities.

The accuracy and the efficacy of the design strategy presented in this section have been further investigated by comparisons with numerical simulations performed with commercial software tools and with measurements on physical models.

4.4 Technological aspects and experimental results

Replicating the antenna model used in the numerical analysis into a physical structure is often a difficult task, which is very much dependent on the

available technology. In the case of the cavity-backed, stacked-patch antenna one of the most intricate aspect is the realization of the metallic cavity. For isolated elements there are some technological solutions that allow a facile and accurate fabrication of the model used in the theoretical study. However, when these radiators have to be integrated into an array configuration, the construction of the metallic cavities becomes more difficult and requires complex engineering and high costs.

A simple solution to circumvent the onerous aspect related to the manufacturing of the metallic cavities is to simulate them by means of vertical, metallic pins. In the microstrip technology, adopted in this work, this can be easily done by performing metalized vias around the edges of the aperture. The technological process associated to the microstrip laminates is well established and the manufacturing accuracy is very high (tens of microns). When looking in detail at the antenna topology under investigation, there are a few aspects to be considered carefully. These problems are hereafter summarized.

- It is evident from Fig. 4.7 that the antenna can be realized by overlapping three microstrip layers. The vias, replicating the cavity, must connect the metallic upper part of the top layer to the lower metalized side of the bottom layer.
- In order to attach the protruding pin to the bottom patch it is advisable to have a hidden via. By using such a technique, the pin can be connected to the patch by soldering inside the vias and, therefore, the upper part of the patch can be kept flat.
- In the manufacturing process all the vias should have a small metallic pad at the ends. Hence, at the aperture and at the two metallic sides of the middle layer the cross section of the cavity will be diminished. Additionally, the protruding pin will have a small ring at the entry in the cavity.
- From a technological perspective it is quite complicated to realize multi-layer structures with thick substrates and with hidden vias. In the case of the cavity-backed antenna topology under investigation, it is proposed to process each of the layers separately and to stack them together after the inner pin was attached to the bottom layer.

To simplify and to reduce the cost of the manufacturing process the architecture of the antenna was slightly changed with respect to the model used in the numerical analysis. Despite of these transformations imposed by the manufacturing process, it was assumed that the behavior of the antenna remains by and large unchanged over a certain frequency range.

The design approach summarized in Section 4.3.2 was employed in conceiving a number of antenna models, which were also manufactured in the microstrip technology. The characteristics of the theoretical models are

Table 4.2: Parameters of the manufactured antennas. The dimensions are expressed in mm and GHz.

Model	a	b	dy_c	r_{p1}	r_{p2}	B	f_{min}	f_{max}
A2	14	14	4	5.1	4.4	7.2%	8.0	8.7
A3	14	14	4	5.3	4.6	8.1%	7.7	8.4
A6	14	14	3.8	5.3	4.6	7.6%	7.7	8.3
B1	12	12	3.8	4.6	3.8	7.5%	9.0	9.7
B5	12	12	3.8	4.8	4.1	5%	8.6	9.0
B6	12	12	3.8	4.9	4.1	7.4%	8.5	9.2

given in the Table 4.2. The layers were chosen to be Rogers' material type RO4003 with the relative dielectric permittivity of 3.38 and having different thicknesses ($h_1 = 0.508\,\mathrm{mm}$, $h_2 = 1.524\,\mathrm{mm}$ and $h_3 = 0.305\,\mathrm{mm}$). The vias used to replicate the cavity had a diameter of 0.7 mm and were deployed at approximately 2 mm from each other. Each of the manufactured models had a metallic flange of dimensions $50\,\mathrm{mm} \times 50\,\mathrm{mm}$ (the radiating aperture is placed at the center of the flange).

The top and bottom views of the constitutive parts of an antenna are presented in Fig. 4.11. Some constructive details can also be identified from these pictures. In order to facilitate the realization of the vias, the substrates were selected to be metalized on both sides. Further, it is noted that each of the patches was printed on the two adjacent layers (the lower patch was printed on the top of $S1$ and on the bottom of $S2$; similarly the upper patch was printed on $S2$ and $S3$). This solution offers a twofold advantage: firstly, the soldering point associated to the protruding pin is hidden between two metallic layers (thus increasing the accuracy) and, secondly, the formation of an air gap between the metallic patches and the dielectric materials is prevented. Images of a completely assembled antenna are presented in Fig. 4.12. The three constitutive layers were fastened together by using metallic screws and the SMA connector was attached to the antenna by means of soldering.

Experimental results

The measurements presented in this thesis were performed in the anechoic chamber of IRCTR (also known as DUCAT - Delft University Chamber for Antenna Tests). DUCAT is a moderate size ($3 \times 3 \times 6\,\mathrm{m}$) anechoic chamber that allows the measurement of most of the antennas parameters (scattering parameters, radiation patterns, gain, etc.) in the frequency domain and in the time domain, as well. The shielding of the chamber is for frequencies above 2 GHz up to 18 GHz and it is at least 120 dB all around. All walls are covered with pyramidally shaped absorbers. It is found that the walls have a

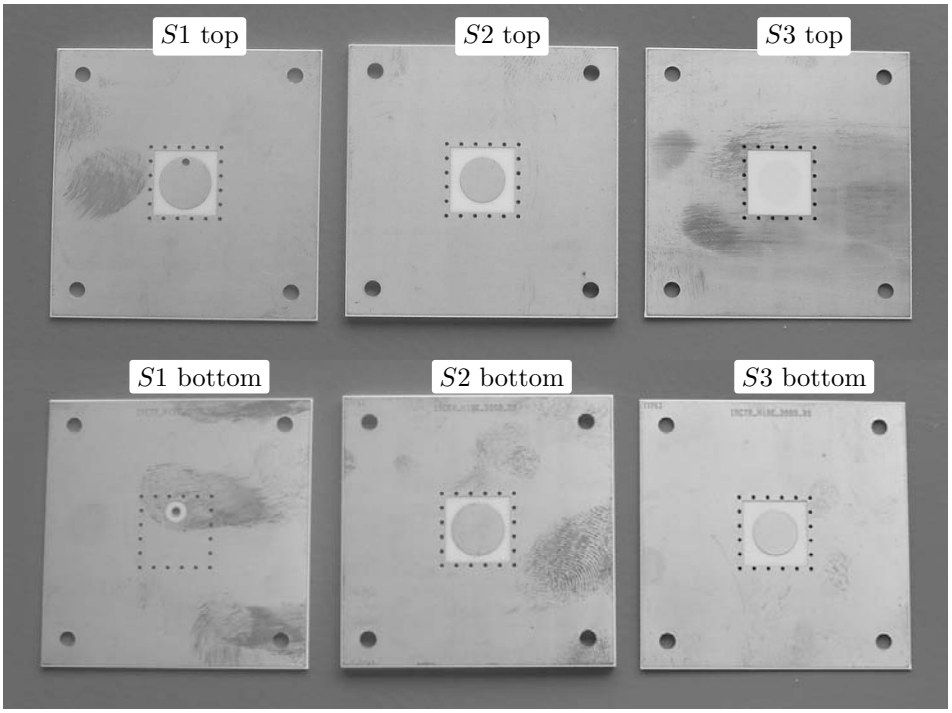

Figure 4.11: Constitutive parts of a cavity-backed, stacked patch antenna. $S1$ - RO4003 microstrip laminate with thickness of 0.508 mm; $S2$ - RO4003 with the thickness of 1.524 mm; $S3$ - RO4003 with the thickness of 0.305 mm.

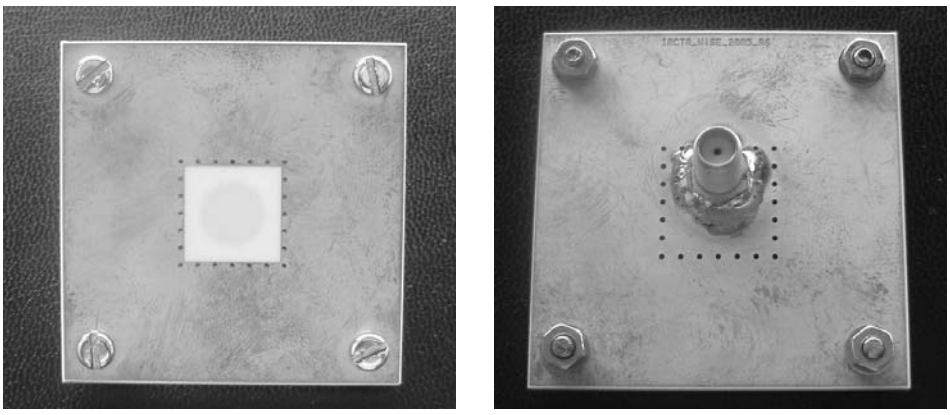

a b

Figure 4.12: Assembled cavity-backed, stacked-patch antenna. (a) - top view; (b) - bottom view.

reflection coefficient of less than $-36\,\mathrm{dB}$. The distance between the antenna under test and the standard gain antenna is around $3.5\,\mathrm{m}$. A picture of the DUCAT anechoic chamber, focussing on the antenna under test, is presented in Fig. 4.13.a.

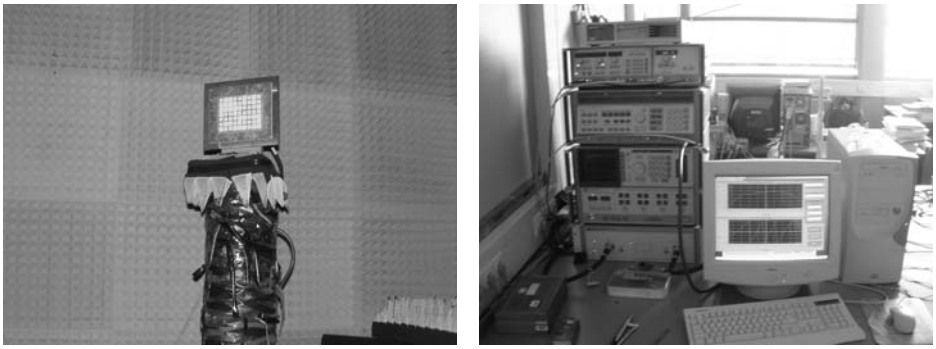

a b

Figure 4.13: Antenna measurement facilities at IRCTR. (a) - the anechoic chamber (DUCAT - Delft University Chamber for Antenna Tests); (b) - vector network analyzer integrated with a data acquisition system.

The measurements in the frequency domain (the ones presented in this thesis) are performed using the following equipment: a HP 8510B network analyzer, a HP 8341 B synthesized sweeper, a HP 8350 B/HP 83592 B sweep oscillator and a HP 8515A S-parameter test set. Moreover, a PC (Personal Computer) is used to control the equipment and to execute automated measurements controlling the antenna positioners. A photo of the measurement equipment and the control system is depicted in Fig. 4.13.b.

The experimental investigation of the matching properties of the manufactured antennas was done outside the anechoic chamber by using the network analyzer. The results of these measurements are presented in Fig. 4.14 (with dashed lines). The outcomes of the numerical simulations are also provided in this figure. The results achieved by applying the mode matching method as indicated in Section 4.3.1 are indicated with continuous lines. In the modal analysis the cavities of the antennas were assumed to be continuous. It is worth noting that the manufactured radiators have the cavity replaced by a number of metallic vias. For the completeness of the study, the physical models were also simulated by using the CST Microwave Studio commercial package, the results being indicated in Fig. 4.14 with dotted lines. By comparing the simulation results it is evident that at low frequencies (the useful ones) the vias replicate the metallic cavity with a good accuracy. At higher frequencies (above $12\,\mathrm{GHz}$) the distance between the vias appears to be too large for a fair mimicking of the cavity.

Of course, this can be corrected by using more vias closely packed but the higher frequency range is of no interest in this work. At low frequencies there is also a fair similarity between the simulation results are the measured ones. The small differences between measurements and simulations are mainly attributed to the manufacturing process, in particular to the soldering of the coaxial connector and the assembling of the three constitutive layers.

During the measurement campaign it was possible to investigate a simplified solution for connecting the coaxial connector to the antenna. The new model has been realized by eliminating the soldering of the inner pin to the bottom patch and introducing a small air gap between the pin and the patch. By this approach the transfer of the energy is done by means of a capacitive coupling. These models are hereafter referred to as the *capacitive* ones whereas the radiators having the protruding pin soldered to the patch are denoted as the *inductive* solutions. The measurements performed on some of the antennas realized in both capacitive and inductive technologies are presented in Fig. 4.15. From these pictures it is noted that the capacitive models have a larger bandwidth. More specifically, the bandwidth of the antenna model A2 has been increased from 7.2% (inductive model in Table 4.2) to 12%, that of the model A3 from 8.1% to 11.8% and in the case of the antenna A6 the bandwidth has been enlarged from 7.6% to 11.8%. The attractive matching properties of the capacitive modes are diluted by the accuracy required in controlling the size of the gap between the pin and the patch. In the models presented here the gap was in the order of 0.1 mm. The exact size of the gap was difficult to evaluate in the normal laboratory conditions due to some less accurate manufacturing steps, such as: the shorting of the pin, the soldering procedure and the fastening method.

The radiation properties of the manufactured antennas were also investigated by means of measurements in the anechoic chamber available at IRCTR. The measured radiation patterns of the antenna model B6 are depicted in Fig. 4.16 . The field patterns were measured in the principal planes (E and H) and the diagonal plane of the antenna (45° plane). The results obtained from the modal analysis of this antenna model B6 are included in Fig. 4.16, as well. The measurements are in tolerably good agreement with the simulations in spite of the significant difference between the theoretical model (having an infinitely extended flange) and the physical model. The effect of the finite flange is more visible at large angles in the E plane and in the cross-polar pattern measured in the diagonal plane. The field patterns in the principal planes (E and H) were also investigated at different frequencies in the bandwidth of the radiator. From these measurements (also provided in Fig. 4.16) it can be concluded that over a bandwidth of almost 1 GHz the shape of the antenna's radiation pattern remains unchanged.

To further understand the cause of the dissimilarities at large angles the electric field component oriented along the $\mathcal{O}y$ axis has been calculated at the aperture of the theoretical model. The distribution of the E_y field quantity in the aperture is presented in Fig. 4.17.b for the antenna model B6. From this figure one can speculate that the singular behavior in the

proximity of the aperture's edges, which are orthogonal to the $\mathcal{O}y$ axis, is replicated in the far field more evident by a finite flange. For the same model (B6) in Fig 4.17.a are provided the relative amplitudes (normalized to the amplitude of the TE_{10} mode) of the modes considered in the representation of the aperture field. Note that the modal quantities in Fig. 4.17.a were evaluated for an unitary excitation of the TEM mode pertaining to the coaxial cable connected to the antenna. From Fig. 4.17 one can observe that the field in the aperture is dominated by the TE_{10} mode of the square cavity. However, despite of the relatively low amplitudes, the higher order modes are affecting in a visible manner the field in the aperture, the influence being traceable in the far field, as well.

A final set of measurements, refers to the gain of the elementary radiator. In Fig. 4.18 are depicted the calculated and the measured values of the absolute gain of the antenna model B6, as a function of frequency. In Fig. 4.18.a is depicted the antenna gain that also includes the losses arising from impedance mismatches. The antenna has a measured gain higher than 4 dBi over the range from 8.6 GHz to 9.6 GHz (11%). The antenna gain according to the standard definition given by The Institute of Electrical and Electronics Engineers (IEEE) [63, p. 15] is provided in Fig. 4.18.b. With the observation that the theoretical and the physical models have slightly different architectures, one can conclude that there is a fair agreement between the measurements and the simulated results. Moreover, it is pointed out that of interest in this work are sparse array configurations and, therefore, the inclusion of the finiteness of the metallic flange in the modal analysis is not of a significant relevance.

4.5 Conclusions

The properties of two type of antennas, namely the dielectric filled waveguide antenna and the cavity-backed, stacked-patch antenna (physically realized in the microstrip technology), have been investigated. The mode matching methods presented in the Chapters 2 and 3 have been successfully used for the full-wave analysis of these primary radiators. The design stage employed some mathematical programming procedures in conjunction with the computational engine based on the modal analysis.

A particular attention was given to the optimization and to the manufacturing of cavity-backed, stacked-patch antennas. The systematical design procedure adopted in this work has provided antenna models with bandwidths of around 10%. These results are superior to the ones reported by other authors in the literature for similar antenna models [41, 50]. The numerical simulations were validated by comparisons with measurements performed on physical models. The technological aspects have been meticulously investigated and some practical solutions were proposed in the context of simplifying the manufacturing process and reducing the fabrication cost.

Two of the manufactured antenna models, namely the model A6 and the model B6, have been selected for being further used in the analysis and design of the sparse array configurations.

Elements of novelty

A number of design procedures were proposed for the contriving of dielectric filed waveguide antennas and of cavity-backed, stacked-patch antennas. In particular, the design of dielectric filled waveguide antennas having an air gap matching structure was formulated as mathematical optimization problem in which use was made of the impedance matching principle from the circuit theory.

When dielectric filled waveguide antenna are used in array configurations, a key aspect refers to the transition from the feeding line to the waveguide. In this chapter a very compact transition from a coaxial cable to a rectangular waveguide was proposed (in order of $2 - 3\,\text{mm}$). An exhaustive investigation of this compact transition is presented in the references [120, 119].

Detailed technological aspect were discussed and the solution used for manufacturing the antennas is characterized by a low fabrication costs. It is pointed out that the cost were significantly reduced by using the microstrip technology and by choosing to replace the metallic cavity by means of segmented vias (pertaining to separated layer).

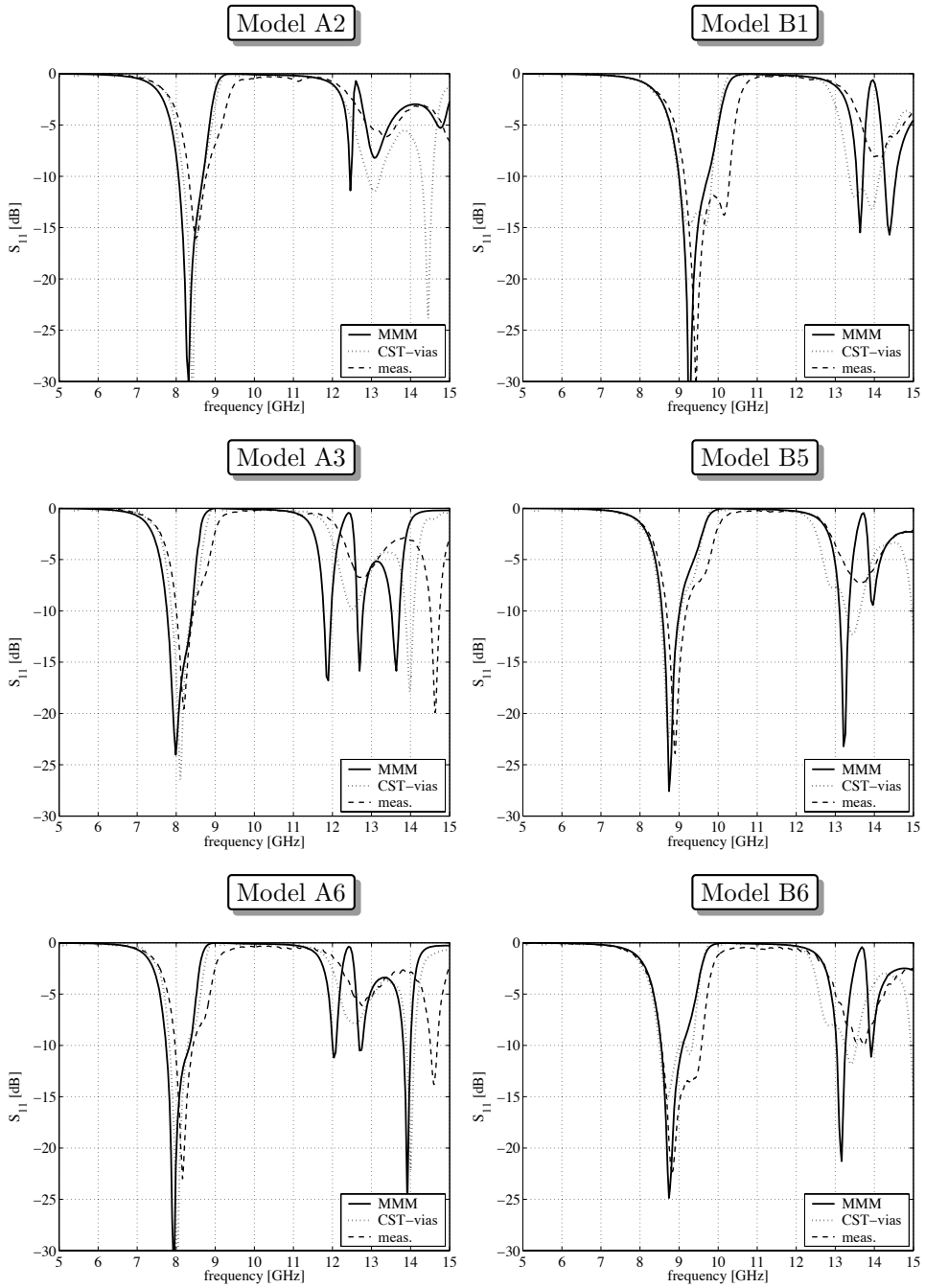

Figure 4.14: Computed and measured input reflection coefficient of the antenna models catalogued in Table 4.2.

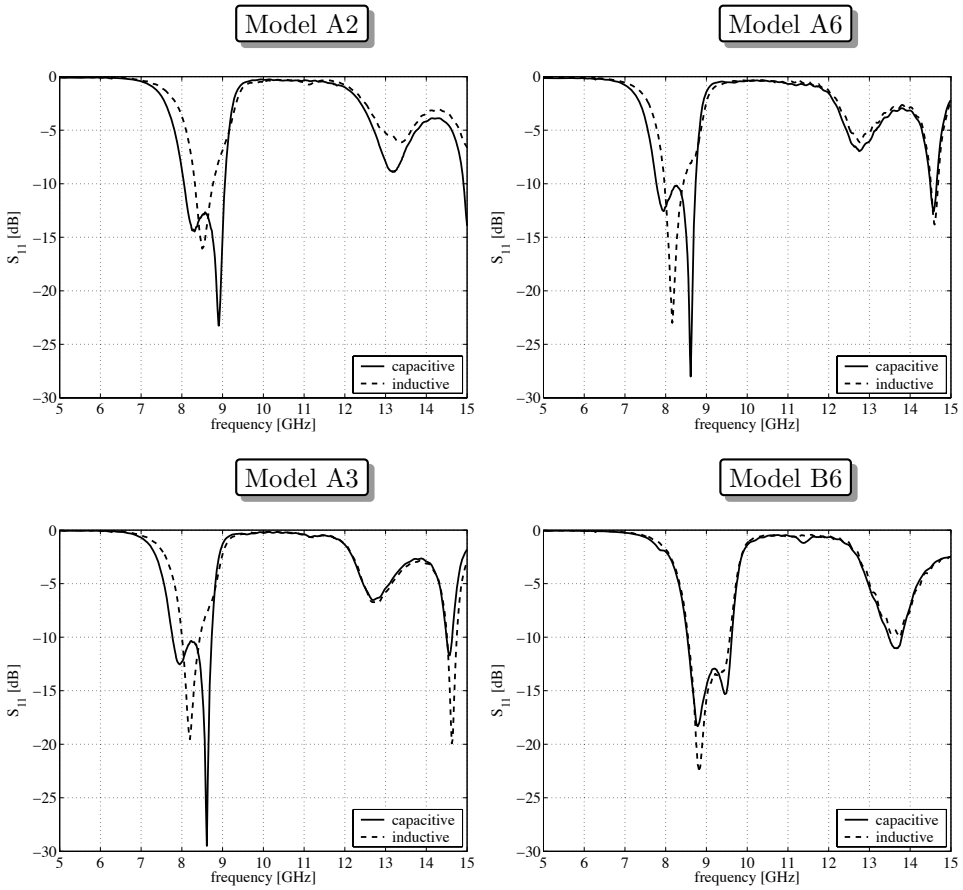

Figure 4.15: Measured input reflection coefficient of some of the antenna models catalogued in Table 4.2. The *inductive* configurations have the protruding pin soldered to the bottom patch while in the *capacitive* models the pin does not touch the patch (the gap is around 0.1 mm).

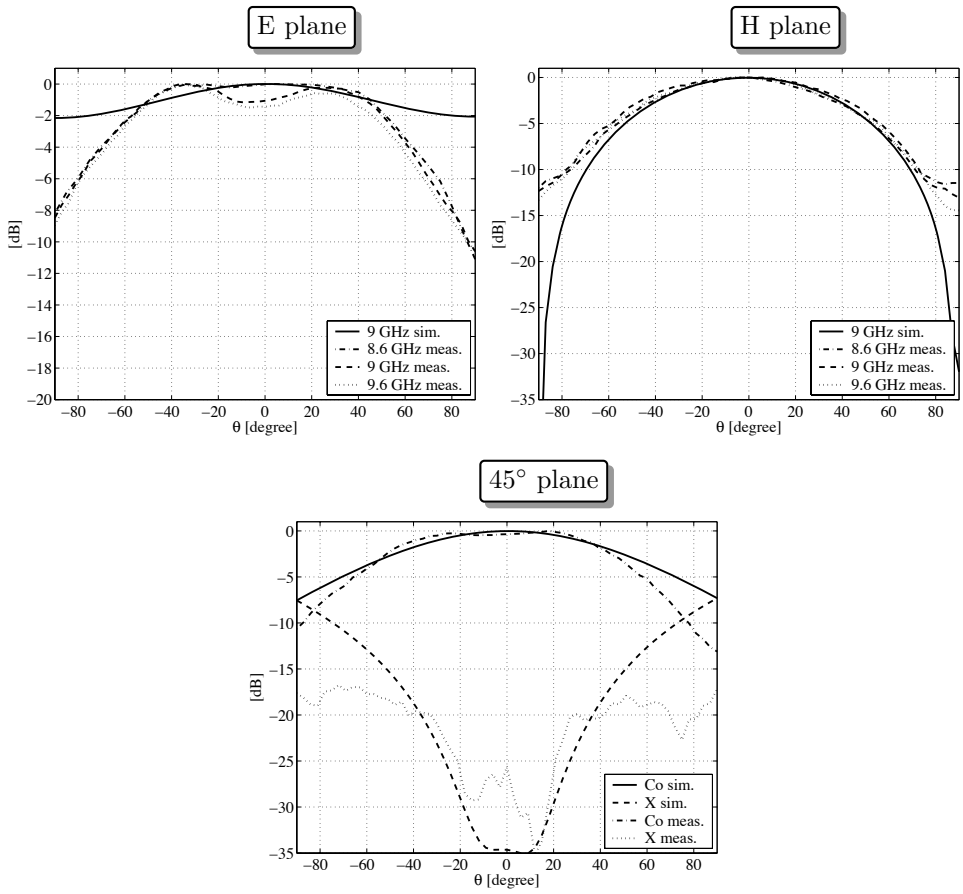

Figure 4.16: Calculated and measured radiation patterns of the antenna model B6 (dimensions are given in Table 4.2). In the 45° plane the patterns are evaluated at the frequency of 9 GHz.

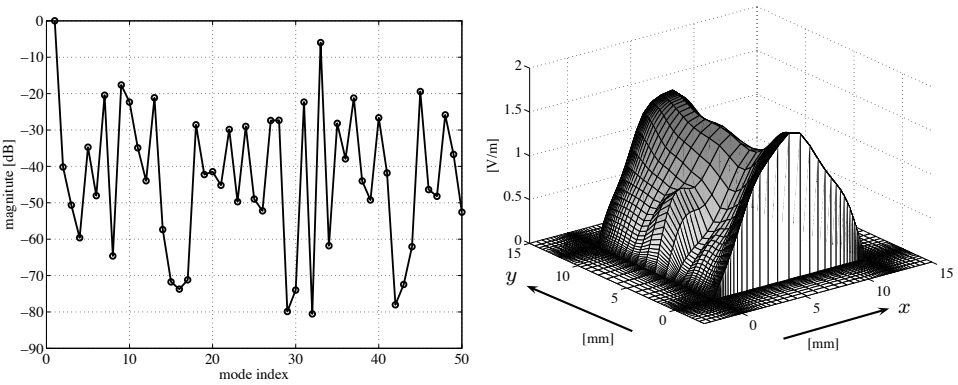

a b

Figure 4.17: Aperture field for the antenna model B6 at 9 GHz. (a) - relative amplitude of the modal equivalent voltages; (b) - absolute value of the electric field component oriented along the $\mathcal{O}y$ axis (E_y).

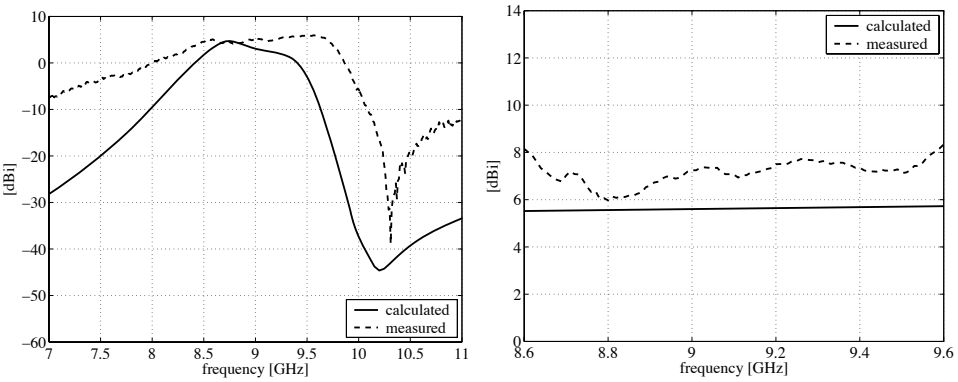

a b

Figure 4.18: Computed and measured gain of the antenna model B6 at. (a) - antenna gain including the losses arising from impedance mismatches; (b) - absolute gain according to the IEEE definition.

Chapter 5

Sparse array antennas

In this chapter the relevant aspects related to the field of sparse array antennas are discussed. Firstly, the synthesis of array antennas with non-uniformly spaced elements is formulated as a problem of mathematical optimization. While such a mathematical approach covers most of the design algorithms presented in the literature, it may not always provide a realistic solution. Consequently, some specific aspects concerning sparse array antennas are highlighted. Furthermore, the most effective design algorithms are catalogued and some of them are succinctly described. Numerical examples and measurement results are provided in the last part of the chapter.

5.1 Introduction

The idea of developing electronically controlled antenna radiation patterns (RP) goes back to 1940. It stemmed from the requirement to replace the mechanical steering of the antenna main beam by a more reliable, electronic method. Later, the fact that the elementary antennas used in array configurations act as sampling devices in the spatial domain was also employed for enhancing antenna capabilities. The most important benefits from using array antennas are:

- reduced (completely eliminated) mechanical movement;
- well-controlled beam width and side-lobe region;
- fast scanning in the field of view;
- ability to control the positions of the nulls in the radiation pattern;
- electronically re-configurable antenna radiation pattern.

While phased array antennas have such attractive features, their realization represents a challenging task. In this respect, it is known that for applications where a high resolution (narrow beam width) is required the antenna should have a wide spatial dimension. At the same time, in order to prevent the apparition of grating lobes (i.e. alias effects due to spatial under-sampling) the inter-element spacing (in uniform configurations) should be less than half of the wavelength ($\lambda_{\min}/2$) at the maximum operational frequency (for a maximum scanning of 90°). The combination of the fine resolution requirement with the $\lambda_{\min}/2$ condition will often result in a large number of elements. As each primary radiator is associated with a transmitting/ receiving module, the cost of a fully populated, large aperture array antenna becomes quickly prohibitive. The manufacturing of array antennas is subject to technical limitations, as well. Commonly, the characteristic size of radiators is approximately equal to half of the wavelength at the minimum operational frequency, that is obviously conflicting with the $\lambda_{\min}/2$ condition. Consequently, the individual elements to be employed in fully sampled arrays must be miniaturized, an often technologically difficult solution. Furthermore, the individual radiators are positioned very close to each other, the mutual coupling being, thus, very high. This phenomenon affects detrimentally the antenna performance, most notably as concerns the side-lobe level and the maximum scanning angle.

The problems mentioned above (cost, conflicting dimensional requirements, mutual coupling) can be more effectively solved by reducing the number of elements in the array configuration (with its accompanying increase of the inter-element spacing). The resulting antenna will be a *sparse array*. When the sparse configuration follows from eliminating radiators from a fully populated array, the antenna is referred to as a *thinned array* [58]. (Note that sparse arrays are also referred to as *space tapered*, *random*, *nonuniform*, *aperiodic* or *arbitrary arrays* [147, 124, 113, 20, 138, 136].) The benefits of employing sparse array antennas are not restricted to cost and mutual coupling. Such aspects as: bandwidth, weight, power consumption, heat dissipation and (multi) functionality are also expected to improve when the distance between radiators is larger than $\lambda_{\min}/2$. The main drawback of these antenna configurations is their high level of the side-lobes in the radiation pattern, which is considered unacceptable in many applications. However, by controlling the number of elements, their positions and their relevant weights (both in amplitude and in phase) it becomes possible to ensure adequate RP properties for most practical applications.

Many techniques have been proposed in the literature for the realization of sparse array antennas. To assure a unified treatment of these methods a rigorous formulation of the array design problem is proposed in the following.

5.2 Problem formulation

Consider an array antenna comprised of N elementary radiators distributed at known locations in the $x\mathcal{O}y$ plane as indicated in Fig. 5.1). The observation point is denoted in Fig. 5.1 as P. It is noted that the radiation properties of the array are determined from the evaluation of the collective contribution of the primary radiators at different observation points, typically located on a (hemi)sphere around the antenna [11, pp. 249–338].

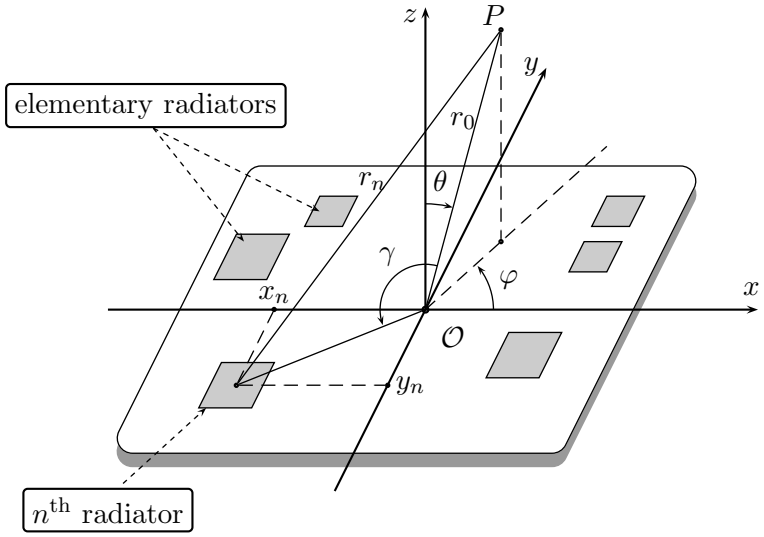

Figure 5.1: Geometry of a generic, sparse array antenna.

For ensuring a maximum flexibility, each element is allowed to have a different, known, spatial response (radiation pattern). Moreover, the array is assumed to transmit a narrow band signal, justifying the single frequency analysis to be carried out. (The wide band aspects concerning the sparse array antennas are briefly discussed in the Section 5.3.) The field radiation pattern of the array can then be expressed as

$$f(\theta, \varphi) = \boldsymbol{w}^T \boldsymbol{v}(\theta, \varphi), \tag{5.1}$$

where $\boldsymbol{w}$ is a vector of complex weights w_n $(n = 1, \ldots, N)$ applied to each element and $\boldsymbol{v}(\theta, \varphi)$ is a vector representative for the array's architecture, for the elements' radiation patterns and for the direction of observation, the superscript T indicating the transposition operator. By denoting as g_n $(n = 1, \ldots, N)$ the radiation patterns of the elements and as $\{x_n, y_n\}$ $(n = 1, \ldots, N)$ their locations in the xOy plane, the entries in the vector

$\boldsymbol{v}(\theta,\varphi)$ read

$$\boldsymbol{v}(\theta,\varphi)=\begin{bmatrix} g_1(\theta,\varphi)e^{j\frac{x_1+y_1}{\sqrt{x_1^2+y_1^2}}(k_x x_1+k_y y_1)} \\ g_2(\theta,\varphi)e^{j\frac{x_2+y_2}{\sqrt{x_2^2+y_2^2}}(k_x x_2+k_y y_2)} \\ \vdots \\ g_N(\theta,\varphi)e^{j\frac{x_N+y_N}{\sqrt{x_N^2+y_N^2}}(k_x x_N+k_y y_N)} \end{bmatrix}, \tag{5.2}$$

where $k_x = k\sin(\theta)\cos(\varphi)$ and $k_y = k\sin(\theta)\sin(\varphi)$, with $k = 2\pi/\lambda$ denoting the propagation constant (often referred to as the wavenumber). It is worth observing that in most cases [11, 55] the quantities $(x_n + y_n)/\sqrt{x_n^2 + y_n^2}$ with $n = 1, 2, \cdots, N$ are approximately one. Note that (5.2) covers also the case of linear array configurations, by taking, for example, $y_n = 0$ for $n = 1, \ldots, N$.

The design goal is then to adjust $f(\theta,\varphi)$ such that it mimics a specified radiation pattern $f_{\mathrm{d}}(\theta,\varphi)$ over the field of view $\mathcal{D} = \{\{\theta,\varphi\}|\ 0 \leqslant \theta \leqslant 90,\ 0 \leqslant \varphi < 360\}$ (with θ and φ in degrees)

$$\begin{array}{ll} \texttt{minimize:} & F(\boldsymbol{w},\boldsymbol{v},\theta,\varphi), \\ \texttt{subject to:} & H(\boldsymbol{w},\boldsymbol{v},\theta,\varphi) \leqslant 0, \\ & \{\theta,\varphi\} \in \mathcal{D},\ \boldsymbol{w} \in \mathcal{C}_1 \text{ and } \boldsymbol{v} \in \mathcal{C}_2, \end{array} \tag{5.3}$$

where, F is the objective function that measures the deviation between f and f_{d}, H represents the constraints imposed to the array, and $\mathcal{C}_1$ and $\mathcal{C}_2$ are two sets of complex numbers (N dimensional) that define the possible values of the elements' positions and weights.

The solution to this problem consists of the number of elements, their positions and the relevant weights that, together, provide the best approximation $f(\theta,\varphi) \approx f_{\mathrm{d}}(\theta,\varphi),\ \forall\{\theta,\varphi\} \in \mathcal{D}$. In most practical cases, an exact solution ($f(\theta,\varphi) = f_{\mathrm{d}}(\theta,\varphi)$) to the hereby formulated problem does not exist. Consequently, attaining the design goal will call upon the solution of a *constrained optimization problem*.

For an array with a given number of elements, some representative formulations of the problem are as follows:

- Determine the locations of the elements such that the side-lobe level of a narrow beam width radiation pattern is minimized. (Note that this is the classical formulation referring to the design of sparse array antennas.)

- Determine the elements' weights for different objective functions such as: maximum signal to noise ratio (SNR) or minimum approximation error with respect to the desired pattern.

- Determine the locations of the elements and their weights in order to satisfy a twofold objective: the minimization of the number of elements and the minimization of the approximation error with respect to the desired pattern.

The problem of finding the optimum positions of the radiators for a given aperture is often reduced to a thinning procedure. This allows for the reformulation of the optimization problem as: Find the minimum number of elements from a fully populated array (with given dimensions) that, together, constitute an array meeting the radiation pattern specifications. This simplified problem has quite well known mathematical solutions, which estimate (truly, but with limited accuracy) the behavior of the array in practical applications. A more accurate approximation of the performances can be obtained by adding supplementary constraints to the optimization problem.

5.3 Specific aspects

Let $f_{\mathrm{d}}(\theta, \varphi)$ be the desired pattern for a sparse array antenna. The approximation level in (5.3) can be measured in several manners. Typically, the peak errors over the domain $\mathcal{D}$, the mean-square error over $\mathcal{D}$, or the ratio between the powers received over different ranges of arrival angles are employed. For example, when the peak approximation error is considered, the optimization problem reads

$$\begin{array}{ll} \texttt{minimize:} & \epsilon, \\ \texttt{subject to:} & |f(\theta,\varphi) - f_{\mathrm{d}}(\theta,\varphi)|^2 \leq \epsilon \ \forall\{\theta,\varphi\} \in \mathcal{D}. \end{array} \tag{5.4}$$

The feasible set [138] for this problem is defined by the elements' locations $\{x_n, y_n\}$ and/ or the weighting coefficients w_n assigned to them. Theoretically, the coordinates of the array elements can be any real numbers $x_n, y_n \in \mathbb{R}$ and the weights can have any complex value $w_n \in \mathbb{C}$. However, supplementary restrictions apply to these quantities in practical applications. The following discussion elaborates on these particular aspects in the realm of the array antennas.

Amplitude limitation

The amplitudes of the signals feeding the elementary radiators have always limited values and the phases can vary in the interval $[0, 2\pi]$. This limitation can be incorporated in (5.4) using an additional constraint in linear form

$$|w_n| \leq \gamma \quad n = 1, \ldots, N \tag{5.5}$$

or in quadratic form

$$\sum_{n=1}^{N} |w_n|^2 = \boldsymbol{w}^H \boldsymbol{w} \leq \gamma, \tag{5.6}$$

(with H denoting the Hermitian operator), where $\gamma > 0$ is related to the maximum value of the signal that is applied to an elementary antenna.

Power limitation

Frequently, a requirement on the maximum power transmitted or received by the array within a range of angles is included among the antenna design specifications

$$\sum_{(\theta,\varphi)\in\mathcal{D}_{\text{pow}}} |f(\theta,\varphi)|^2 \leq \xi, \tag{5.7}$$

where $\xi > 0$ denotes the maximum power to be transmitted or received over the discrete range of directions $\mathcal{D}_{\text{pow}} = \{(\theta,\varphi)_1, \ldots, (\theta,\varphi)_{\text{pow}}\} \in \mathcal{D}$. Equation (5.7) can be written in matrix form [138] resulting into an other quadratic constraint to be added to the optimization problem (5.4).

Discrete amplitude and phase

In modern phased array antennas, the electronic control of the radiation pattern is often done in a discrete manner. Digital phase shifters or vector modulators are employed to control the complex weights applied to the elements. However, vector modulators can provide discrete values of weights, only. Assuming that M bits are employed for controlling the amplitude and P bits for the phase, the signal applied to an elementary radiator reads

$$w_n = m\,\Delta A e^{j\,p\,\Delta\Theta}, \quad n = 1, \ldots, N, \tag{5.8}$$

with $m \in \{0, 1, 2, \ldots, 2^M - 1\}$, $p \in \{0, 1, 2, \ldots, 2^P - 1\}$ and ΔA and $\Delta\Theta$ denoting the step increments in amplitude and phase, respectively. With (5.8) added to (5.4) the optimization problem becomes very hard and, moreover, defined over a non-convex set. Note that this constraint is critical when M and P are low, as is the case in online beamforming operations carried out using discrete components. In the case of the receiving mode, when the processing is performed numerically after the array manifold was recorded, the very high representation accuracy makes it virtually irrelevant.

Uncertainties

Addressed here is the problem of designing robust array antennas. The radiation pattern of an array system is always subject to uncertainties in the

amplitude and phase of the elements' excitations (responses). Therefore, the complex coefficients associated to each of the radiators can be expressed as

$$\boldsymbol{w} = \begin{bmatrix} (|w_1| + \delta_1)e^{j\arg(w_1)+j\psi_1} \\ (|w_2| + \delta_2)e^{j\arg(w_2)+j\psi_2} \\ \vdots \\ (|w_N| + \delta_N)e^{j\arg(w_N)+j\psi_N} \end{bmatrix} \tag{5.9}$$

where $\delta_i, \psi_i \in \mathbb{R}$ for $i = 1, \ldots, N$ are the gain and phase uncertainties that satisfy $|\delta_i| \leq \rho$ and $|\psi_i| \leq \alpha$, respectively, with ρ and α being known bounds. During the design procedure, (5.9) can be appended to (5.4) such that the obtained solution provides an acceptable confidence in the performance of the array radiation properties in the presence of uncertainties.

Application of high resolution algorithms

It is of common use in receiving mode to process the array's response by means of high resolution algorithms. A well known category of such processing techniques is that represented by the subspace estimation methods [133]. In sparse array applications, the subspace based estimators suffer from manifold ambiguity, which arises from the linear dependence of the columns of the array manifold matrix. Due to this ambiguity, the high resolution algorithms fail to properly identify sources that illuminate a sparse array.

A number of proposals to solve the sparse array ambiguities are available in the literature [1, 148]. It was demonstrated that, under certain restrictions, the subspace based methods can be adjusted in such a manner that the radiation sources can be identified from ambiguous array response. With these conditions attached to the problem (5.4), the array radiation pattern and the array manifold ambiguity can be addressed simultaneously.

Wide band applications

The narrow band assumption employed in Section 5.2 does not apply to high resolution applications, in which signals with large bandwidths have to be handled by the antenna system. Equations (5.1) and (5.2) define the antenna radiation pattern at a single frequency and are not applicable to wide band radiators. Different formulations were proposed for the antenna pattern in the case when a short pulse (a wide band signal) is used [102, 44]. By substituting in (5.4) the function $f(\theta, \varphi)$ by a wide band equivalent of the array pattern $f_{\text{wb}}(\theta, \varphi)$, the thinned array antennas for applications involving signals with large bandwidths can be optimized [135].

Mutual coupling

It is well known that the radiators deployed in an array configuration are subject to the mutual coupling effect. When designing array structures, the distortions induced by the coupling between primary radiators is usually neglected. However, in practical realizations of array systems this effect strongly influences the side-lobe level, particularly at wide scanning angles. A large amount of work has been dedicated to the evaluation of the electromagnetic coupling between antennas located close to each other. Once this effect is known, it can be incorporated in the antenna radiation pattern in (5.1), that reads (in a matrix form)

$$f(\theta, \varphi) = (C\boldsymbol{w})^T \boldsymbol{v}(\theta, \varphi) \tag{5.10}$$

where C is a square matrix having the size $N \times N$, with the element $c_{i,j}$ denoting the mutual coupling between the elements i and j in the thinned array. By using the definition (5.10) in the optimization problem (5.4), a thinned array antenna can be designed in a more realistic manner.

5.4 Design techniques

For a uniformly spaced array, with distance between elements equaling half of the wavelength, a classical solution that optimizes the relation between beam width and side-lobe level was given by Dolph [43]. He uses the Chebyshev polynomials to find the weights of the elements that produce a radiation pattern that has the minimum beamwidth for an imposed maximum level in the side-lobes region. Unfortunately, the Dolph method can not be applied for the design of sparse array antennas. One option to (slightly) increase the inter-element spacing was to deploy the elements in a triangular lattice configuration [117]. However, this procedure avoids the formation of grating lobes for limited scanning angles of the main beam, only.

Among the earliest solutions of designing sparse array antennas, one can mention the method of *spatial tapering*. This technique is in essence similar to the method of amplitude tapering in uniform array antennas, the main objective of the two approaches being the tapering of the current distribution on the aperture. More rigorous methods were employed when the design of sparse array antennas was formulated as an optimization problem. From a mathematical point of view this problem has the following characteristics:

- non-convex optimization with multiple local minima;
- linear or nonlinear objective function;
- single objective function or multiple objective function.

For solving such optimization problems *mathematical programming* algorithms, *stochastic methods* and *combinatorial theory* have been used with notable results in many theoretical and practical antenna applications. Recently, the *fractal* theory has been introduced in the field of antennas, one of the most straightforward application being in the realm of conceiving sparse array architectures. For arrays operating in the receiving mode, a number of *signal processing* algorithms have been proposed in conjunction with sparse configurations, as well.

A list of the most relevant techniques proposed in the literature for the design or sparse array antennas is presented in Fig. 5.2. In this figure the pertinent references are also indicated for the convenience of the reader. Hereafter some of these methods will be shortly outlined,

5.4.1 Spatial tapering

It is well known [147] that array antennas consisting of equally powered and equally spaced elements exhibit a constant level of the first sidelobe which is independent of the number of elements and the size of the array and only depends on the lattice used for deploying the radiators. For example, in square or rectangular arrays the first sidelobe level will be $-13.2\,\mathrm{dB}$ and for circular arrays this amounts to $-17.6\,\mathrm{dB}$. To reduce the sidelobe level, a simple solution is to taper the current distribution on the antenna's aperture in accordance with a specific function. For arrays with closely spaced elements (typically 0.5 wavelength) the current tapering is commonly approximated by changing the relative amplitude of the radiators. A similar effect (of tapering the current distribution) can be achieved by varying (increasing) the distance between the elementary radiators characterized by the same amplitude. A number of specific techniques have been proposed in the past for conceiving spatially tapered sparse array antennas [82, 106, 121, 137, 147]. These methods can be adopted for linear arrays and for planar configurations, as well. The radiation pattern of such a thinned configuration exhibits a slightly larger beamwidth when compared with that of the fully populated array but the energy in the sidelobe region is more uniformly distributed. In general, these methods are used for large array consisting of thousands of elements (this is necessary for assuring a good approximation of the current distribution on the aperture).

5.4.2 Mathematical programming

For optimally designing the weights or element locations for thinned arrays, several algorithms have been developed by formulating the synthesis problems as mathematical programming ones. Either linear or nonlinear methods have been proposed for solving the problem of thinning a full array with constraints on the side-lobe level [23, 113, 121]. Similar techniques have been

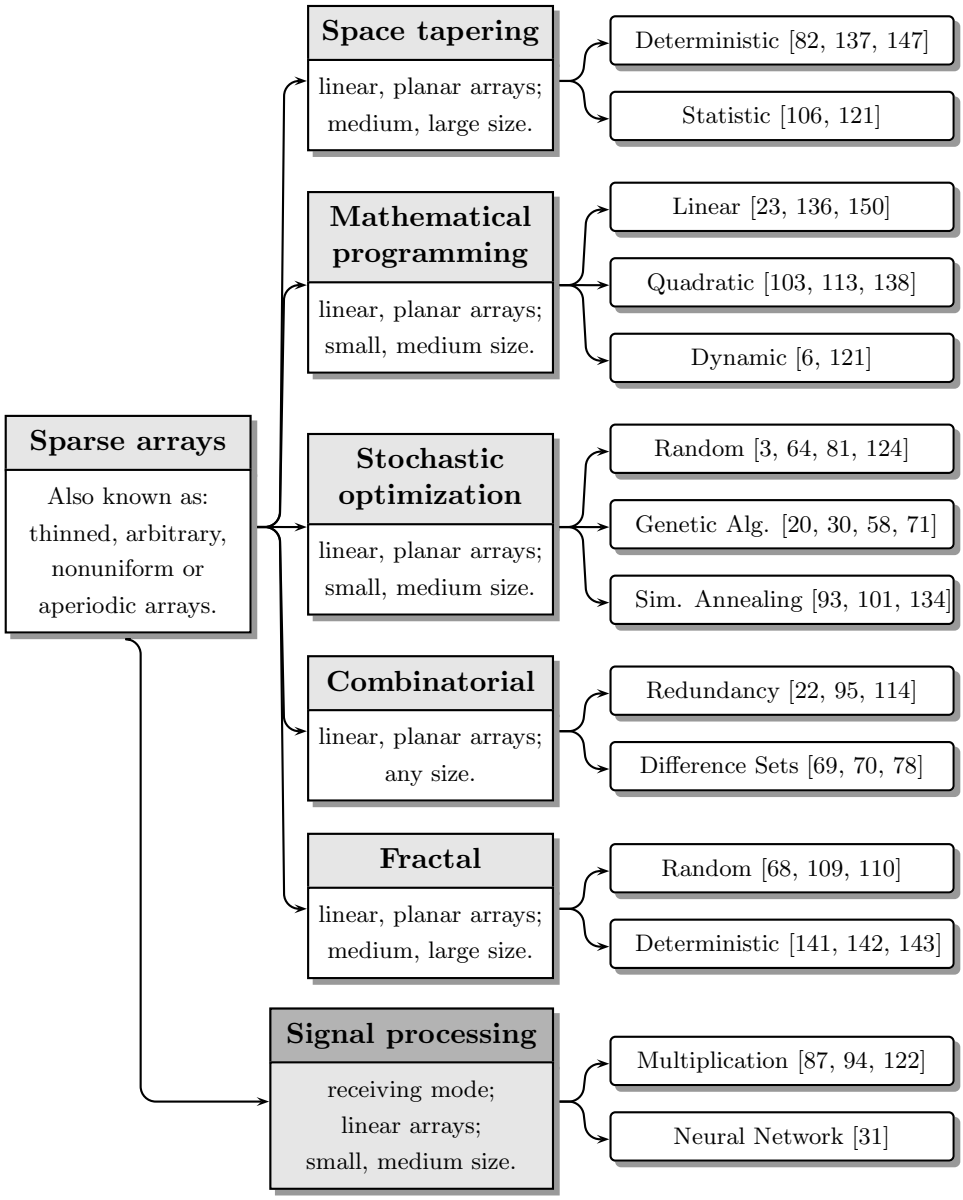

Figure 5.2: Relevant techniques used in designing sparse array antennas. The following equivalencies have been assumed: small sized arrays - tens of elements; medium sized arrays - hundreds of elements; large sized arrays - thousands of elements.

used to improve the quality of the array systems by optimally searching array weights [136, 138]. These methods yield the optimal solution in a very

short time but they exhibit two major drawbacks: excessive memory requirements when the number of elements is large (typically, more than 100) and, since they can only handle real valued antenna patterns, their abilities to synthesize sparse configurations are limited.

5.4.3 Stochastic algorithms

The optimization problem 5.4, which is at the core of designing sparse array antennas, becomes very hard when additional constraints, as described in Section 5.3, are imposed. For such difficult problems, stochastic methods seem to represent the most adequate approach. One of the simplest method to design thinned array antennas is to randomly choose the location of the elements on a uniform grid. The *a priory* description of such arrays is given statistically in terms of a probability that the peak side-lobe level will not exceed the predicted one [123]. For large arrays, the simple statistical method falls far too short of the optimum configurations and more elaborated procedures involving genetic algorithms [58] or simulated annealing [101] need to be called upon. The most attractive feature of these methods is that they can handle multi-criteria objective functions. It should, however, be stressed that stochastic methods require a large computational time and the convergence is not always ensured.

In [135], a simulated annealing procedure has been employed for minimizing the approximation error with respect to a desired pattern, in conjunction with the minimization of the number of elements in the array. These procedure acted simultaneously on the positions and on the relevant weights of the individual radiators.

5.4.4 Combinatorial approaches

Massively thinned arrays can be obtained by exploiting the properties of combinatorial sets. Leeper [77, 78] firstly pointed out that, by using difference sets in establishing the location of the elements in a thinned configuration, the beam width of the full array is preserved whereas the peak side lobe-level is kept at an *a priory* known value. When compared with thinned arrays with randomly placed elements, the arrays based on the difference sets have a peak side-lobe level of at least 3dB lower. Specific problems related to the use of difference sets in planar arrays were discussed in [70].

Perfect binary arrays [69], minimum redundancy arrays and non-redundancy arrays are special cases of using difference sets in thinned antennas. The performances of these methods can be summarized as:

- straightforward implementation;
- they exhibit the beam width of the full array;

- uniform level of the side-lobe region;
- they provide the elements' positions without optimizing the values of the weights;
- they do not provide the optimal solution for a given thinning rate.

In this work, the difference sets have been often used for designing sparse configurations. For reasons of completeness, a short description of this technique is hereafter included.

By definition, a (V, K, Λ) difference set is a set of K unique integers $D = \{d_0, d_1, \cdots, d_{K-1}\}$, with $0 \leq d_i \leq (V-1)$, such that for any integer $1 \leq \alpha \leq (V-1)$

$$(d_i - d_j)(\text{mod } V) = \alpha, \quad \text{for } i \neq j, \tag{5.11}$$

has exactly Λ solution pairs $\{d_i, d_j\}$ from the set D, with "mod" standing for the "modulo" operation. Note that the set $D^* = [0, V-1] \setminus D$ (referred to as the *complementary* of D) is also a difference set with parameters $(V, V-K, V-2K+\Lambda)$.

From a difference set D having the parameters (V, K, Λ), one can construct a sequence of ones and zeros

$$A_D(i) = \begin{cases} 1 & \text{if } i \in D \\ 0 & \text{if } i \notin D \end{cases}, \tag{5.12}$$

with $i = 0, 1, \cdots, V-1$.

The A_D sequence exhibits some remarkable properties. In [78] it was indicated that the autocorrelation function of an infinite vector obtained by periodically repeating A_D is a *two-valued* function. A similar observation can be made with respect to the Discrete Fourier Transform (DFT) of the sequence A_D derived from a CDS (V, K, Λ). In this case, by taking V points in the DFT, the spectrum exhibits one maximum, only, that has a level equaling K, whereas all the other spectral components have an identical, low value (related to Λ). Note that, due to the fact that the radiation pattern of an (array) antenna is associated to the (discrete) Fourier transform of the aperture's current distribution, this property is of higher relevance in the field of (array) antenna studies than that of the autocorrelation.

The DFT test on CDS is illustrated in Figs. 5.3 and 5.4 for the case of the CDS $(63, 31, 15)$. The sampling positions in the space domain given by the elements retained in a linear sparse configuration generated by means of the relevant CDS are plotted in Fig. 5.3. The DFT of this sparse sequence of ones and zeros is depicted in Fig. 5.4. As long as the DFT is evaluated at the same number of sampling points in both the space- and the frequency-domain, the spectrum is a *two-valued* function: it has a maximum that equals 31 (imposed by the K parameter in the CDS's definition) and all the other values are at the same level (referred to as L_0). Upon increasing

the sampling resolution in the frequency-domain, the spectrum in the side-lobes region starts oscillating around L_0. However, the maximum value still remains at the previously obtained level (namely, 31).

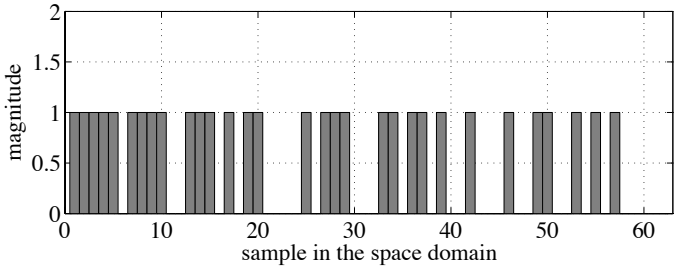

Figure 5.3: Distribution of the sampling points (solid bars) in the spatial domain corresponding to a CDS $(63, 31, 15)$.

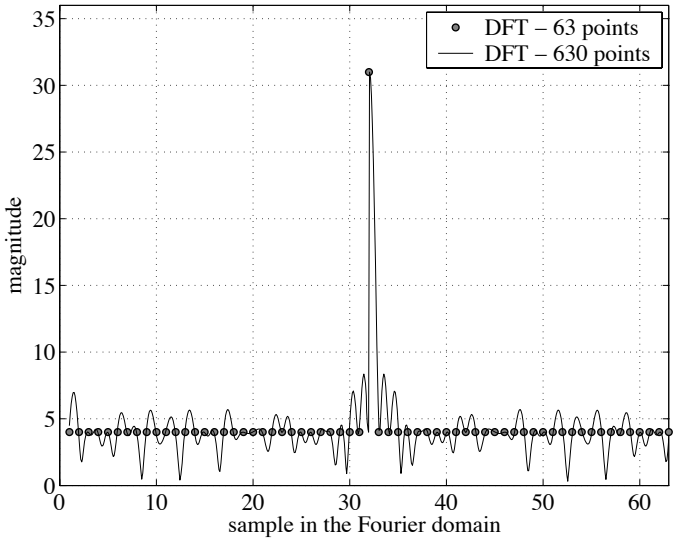

Figure 5.4: The DFT of the sparse sampling sequence in Fig. 5.3. Bullets – the spectrum is evaluated at the same number of sampling points in both the space- and the frequency-domain; continuous line – the spectrum is evaluated at ten times more sampling points in the frequency-domain with respect to those in the spatial-domain.

By placing the elements in a linear, thinned array at the positions of the ones in A_D, the antenna radiation pattern preserves the beamwidth of the full array (consisting of V uniformly distributed radiators) whereas the side-lobes level is approximately constant, oscillating around $1/(2K)$ of the main beam's level [78].

A planar, thinned array of dimensions V_x and V_y can be obtained from the difference set D with parameters (V, K, Λ) by defining the matrix of ones and zeros:

$$M_D\left[i(\text{mod } Vx), i(\text{mod } Vy)\right] = \begin{cases} 1 & \text{if } i \in D \\ 0 & \text{if } i \notin D \end{cases}, \tag{5.13}$$

with $i = 0, 1, \cdots, V-1$ and $V_x V_y = V$. Using one set from the elements of matrix M_D (ones or zeros) to deploy the radiators in the sparse configuration, the power pattern of the thinned array has a beamwidth similar to the one of the full planar array, whereas the side lobe level is approximately constant and low.

It is noted that the combinatorial approach can be easily extended to the design of three dimensional array architectures by, for example, adding a third index to the matrix defined in (5.13). A limitation of these techniques is that they can not be used in shaping the antenna pattern.

5.4.5 Fractal theory

The self-similarity nature of the fractal geometry has been shown to have beneficial effects in the design of multi-band (wide band) radiators and sparse array architectures [68, 109, 110, 143, 141, 142]. For array applications, the fractal structure is expressed as a set of ones and zeros, those numbers being indicative for the deployment of the elements in the thinning procedure. Commonly, a uniform array antenna is transformed into a fractal one by turning on and off the elementary radiators in accordance to the ones and the zeros of the fractal geometry. The fractal array antennas exhibit radiation patterns characterized by a narrow beamwidth (given by the size of the filled array) and by the fact that the energy in the sidelobe region is randomly distributed, this avoiding the formation of the grating lobes. The most attractive feature of these arrays is that they can be obtained in a very short time with minimum requirements as regards the computational resources.

5.4.6 Signal processing

As concerns the signal processing, the techniques enumerated above do not require any particular algorithm. Consequently, arrays designed in these manners are amenable to most of the antenna basic functions such as: scanning a narrow beam in transmission mode, shaping the antenna radiation pattern, synthetic aperture radar imaging (SAR) or direction of arrival estimation (DOA). In the case when the antennas are expected to work in receiving mode, only, non-linear signal processing algorithms can be considered, as well. For example, in [94, 122, 87] a thinned array is used for SAR processing. The antennas proposed in these papers consist of two subarrays: a small size, filled array and a large size, sparse array. By positioning

the nulls of the filled array in the grating lobes of the sparse array and by multiplying the patterns, a narrow beam pattern with low side lobes results. The design strategies discussed thus far make no reference to any physical constraints in deploying the elementary radiators. However, experience demonstrates that in many practical situations (e.g. in aeronautic or automotive industries) hard constraints do occur. In such cases, the positioning of the elements in the sparse array is restricted to certain regions. It is then the task of the signal processing algorithm to ensure the desired antenna parameters.

During the research involved by this thesis a new signal processing algorithm was proposed to be employed in conjunction with massively thinned arrays [31]. The algorithm applies a neural network (NN) approach to the estimation of the angle of arrival (AOA). Furthermore, it also prevents the occurrence of false targets (that are the correspondents of the grating lobes in the case of the receiving mode operation).

5.5 Numerical and experimental results

Some of the algorithms presented in the previous section have been implemented in computer routines, which were subsequently used for the design of different sparse array antennas. Particular attention has been given to practical aspects as, for example, the inclusion of the mutual coupling effect in the design technique and the validation of the numerical results by means of experimental measurements. In the following, three of the most significant study cases will be presented in detail.

Firstly, a design technique for sparse array configurations consisting of dielectric-filled, open-ended waveguide antennas is discussed. The positions of the elements in the thinned array are determined by applying a genetic algorithm strategy that searches for configurations with the lowest side-lobe level. By employing as design parameter the relative inter-element spacing, the formulated optimization problem allows for an arbitrary deployment of the elements on the aperture. The design strategy accounts for the mutual coupling between elements, as well. To this end, an efficient technique for estimating the Generalized Scattering Matrix of a-periodic arrays was proposed.

Secondly, the performance of large, highly thinned array antenna configurations are investigated in view of surface imaging radar applications. The suitability of a spatial tapering method, of a fractal structure and of a combinatorial algorithm for processing (focussing) radar data was evaluated. To this end, fully vectorial information, obtained from bistatic, synthetic aperture measurements performed with a stepped frequency radar, was employed. The images generated with sparse configurations show attractive features even for large thinning rates of up to 75%.

The last example is considered relevant for key aspects related to the numerical analysis, the manufacturing and the measurement of planar, sparse array antennas consisting of cavity-backed, stacked patch antennas. The thinned array antenna is designed by using a combinatorial approach. The full wave analysis of the sparse array antenna is performed my means of a modal analysis. The simulation results are furthermore compared with measurements performed on the manufactured sparse array model.

5.5.1 Linear sparse arrays

Classically, the way to obtain a linear sparse architecture has been to consider a uniform array configuration with the distances between elements equaling half of the wavelength and to remove elements, while observing the radiation properties of the remaining antenna. All the algorithms presented in Section 5.4 have been applied to the design of linear sparse array configurations. The problems that were solved by means of such methods were formulated in terms of thinning a fully populated array with the elements confined to a uniform grid. Note that, more often than not, such approaches did not take into account the coupling between the elements in the array configurations. Recently, [20] presented an optimization methodology that accounted for the mutual coupling (in a simplified manner), while also allowing for variations in the positions of the elements around the nodes of the (initially) uniform grid. However, that formulation was not applicable to the design of sparse arrays having elements placed at arbitrary locations on the antenna aperture.

In this section, a new formulation for the problem of designing linear sparse array antennas is advocated. The quantities subject to optimization are the *relative* distances between antenna elements. This approach presents immediately a twofold advantage: on one hand, the radiators can be deployed at *arbitrary locations* on the aperture and, on the other hand, it automatically prevents their overlapping. A second aspect had in view by the design strategy is the inclusion of the effects of the mutual coupling, traditionally, a computationally intensive task. For being able to maintain the computational feasibility of the optimization process, the method presented in Section 3.4 for the estimation of the mutual coupling has been used.

Optimization strategy

The analyzed configuration, concerning a *linear* array of dielectric-filled, open-ended waveguide antennas deployed on an infinite flange is depicted in Fig. 5.5. The locations of the radiators in the array antenna are determined by applying a genetic algorithm (GA) [58]. A justification of this choice for the use of the GA is hereafter provided.

Experience demonstrates that the convergence of the GA depends heavily on the choice for coding the investigated problem. In the present ap-

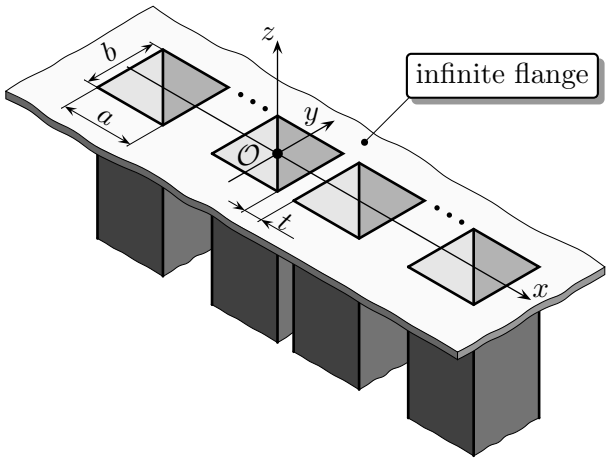

Figure 5.5: Geometry of the linear array antenna under investigation.

proach, the quantities subject to optimization are the *relative distances between the antenna elements*. This choice, inspired by the techniques employed for the design of large sparse arrays, most notably by the space tapering method [147], represents a beneficial development with respect to traditional implementations of the GA [58, 20], using *point sources* that are located at positions related to a *uniform* grid. Furthermore, the design strategy allows for the physical dimensions of the radiators to be made a part of the formulation, while leaving complete freedom for deploying them on the aperture. Note that, by imposing a zero lower bound for the relative inter-element distances, overlapping of the elementary apertures is automatically ruled out.

The employed cost function aims, primarily, to minimizing the side-lobe level. However, for being able to realistically model physical antennas, it is desirable to incorporate in this cost function the effect of the mutual coupling between elementary antennas, as well. This aspect is commonly omitted from the formulation of the optimization problems associated to the design of sparse arrays due to the complexity of the electromagnetic problem involved by the evaluation of the relevant cost function, that translates into unacceptably large computation times. Even by restricting the electromagnetic problem to the analysis of the interaction of nearby located elements (an often irrelevant concept in a sparse array) the computation time required by each GA iteration still remains prohibitive. It then follows that the use of an *analytical approximation* of the mutual coupling is instrumental for maintaining the feasibility of the optimization process.

To avoid this obstacle, the polynomial interpolation technique presented in Section 3.4 is used to estimate the coupling between elements located at arbitrary distances. Initially, the *coupling admittances* between elements located at a number of relevant positions in the array are evaluated by means of the modal analysis method introduced in Section 3.2. These

values are then input to a curve-fitting procedure, that, in turn, provides an estimation of the coupling effect. Note that these operations are performed prior to the starting of the optimization loop and require negligible computation time during the iterative process itself.

Numerical results

The optimization strategy described in the section above was implemented in a Matlab code. In the present version, the sparse array is taken to contain *identical* elements (waveguides). All numerical experiments were carried out for the case of square waveguides of dimensions $a = b = 0.015\,\mathrm{m}$ (see Fig. 5.5) and having dielectric filling with relative permittivity of 2.53. The array was taken to operate at 10 GHz. The distance between the first and the last radiator in the array, denoted as the *array length*, is determinant for the width of the main beam. The number of radiators in the array is heuristically estimated from the side-lobe level (SLL) requirement. The array's scanning capabilities are taken into account by solving the optimization problem for the main beam being steered at the maximum desired angle (in this case, at 60°).

After choosing the array length and the number of radiators, the configuration is subject to a GA optimization. To this end, each individual sparse array configuration is associated to one chromosome taken to be the real valued vector of the relative inter-element distances. The generations in the GA are limited to 80 chromosomes. The fitness function is given by the maximum side-lobe level, normalized to the level of the main beam. The realistic modeling of the configuration at hand requires the accounting for the effect of the mutual coupling in the cost function. The two optimization goals (the lowering of the SLL and the lowering of the mutual coupling level) are simultaneously incorporated in the cost function in a *weighted manner*. Note that the evaluation of the SLL was done for the case of ideal radiators, positioned at the center of the considered waveguides, while the physical dimensions of the waveguides were employed in the case of the mutual coupling computations.

One of the key ingredients to ensuring the computational feasibility of our GA variant is the use of an analytical approximation of the mutual coupling between radiating elements. The theoretical aspects concerning this approximation were discussed in Section 3.4. The mutual admittance between two apertures (denoted as 1 and 2) was evaluated as a function of distance over the range $0, \ldots, 0.15\,\mathrm{m}$, sampled at 23 equidistant points. Ten modes, namely TE_{10}, TE_{01}, TE_{11}, TM_{11}, TE_{20}, TE_{02}, TE_{21}, TM_{21}, TE_{12} and TM_{12}, were considered on each of the apertures 1 and 2. Consequently, 100 modal couplings needed being accounted for. The accuracy of this interpolation procedure is demonstrated in Fig. 5.6 where the relative error in the case of employing the interpolated values (with respect to the full wave numerical analysis) is depicted for all examined couplings.

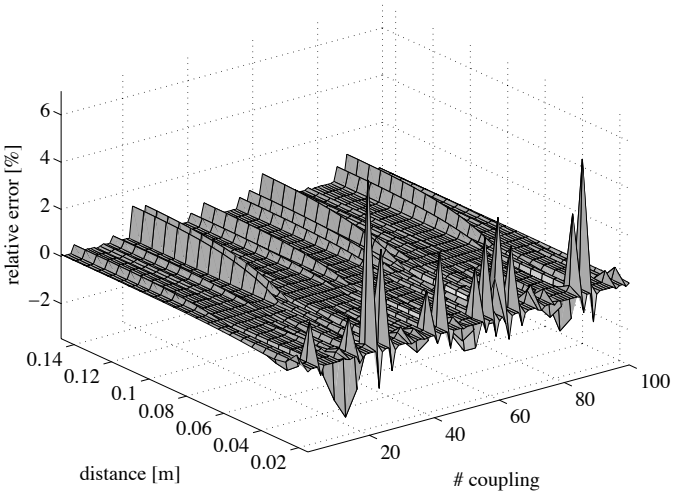

Figure 5.6: The relative error in the case of employing the interpolated values, for all examined couplings; dependence on the relative distance between the considered apertures.

The robustness of this computational approach was evaluated by carrying out a study of the convergence of the GA. These tests were also meant for assessing the GA coding of the optimization problem. Several ratios of the weights attributed to the two optimization goals were tested. The observed convergence is illustrated in Fig. 5.7 for the case when equal weights (unitary) are given to the reduction of the maximum SLL and to the minimization of the coupling $TE_{01} \leftrightarrow TE_{11}$. There, the solid line represents the SLL corresponding to the best chromosome in each generation, while the dots indicate the average fitness in each generation. The iterative process was run over 500 generations. The radiation pattern pertaining to the best chromosome at the completion of the GA, the main beam being steered at the maximum scanning angle (60°), corresponds to the solid line in Fig. 5.8. For comparison, this figure also contains a plot of the radiation pattern pertaining to a *uniform* array containing the same number of elements and having the same array length. In this case, due to the inter-element spacing exceeding half a wavelength, two grating lobes appear in the antenna's visible domain. This is a further proof of the validity of the solution provided by the GA.

The optimized array configuration is depicted in Fig. 5.9. Note that another positive effect obtained in the optimized configuration was the reduction of the average mutual coupling $TE_{01} \leftrightarrow TE_{11}$ (known to be at the origin of increased cross-polar levels) with values between 1 and 8 dB as compared with that of a uniform array with elements spaced at $\lambda/2$.

In this example a design technique for sparse array configuration consisting of dielectric-filled, open-ended waveguide antennas was presented. The design strategy was constructed around an optimization problem solved by means of the genetic algorithm. An original coding of the problem, in terms of the relative inter-element spacing, was proposed. A computationally effective manner for incorporating the mutual coupling between radiators was introduced.

The application of the proposed design method can be extended to the case of the fully populated array antennas, in view of counteracting such adverse effects as the blind-angles during scanning.

5.5.2 Sparse SAR

For meeting the cross range resolution requirements in high-resolution radar applications, it is essential to have antennas with a very narrow beamwidth. It is known that, for reducing the width of the main beam of an antenna, it is necessary to increase correspondingly its spatial dimension. When array antennas are aimed at, the distance between the farthest positioned elements is used to control the size of the main beam (in the relevant planes). Conventionally, filled array antennas have the inter-element spacing in the range $0.5\lambda \ldots \lambda$ (where λ is the free space wavelength at the operational frequency) for avoiding the apparition of grating lobes. Therefore, fully populated, large size array antennas will require a huge number of elements, a fact that will

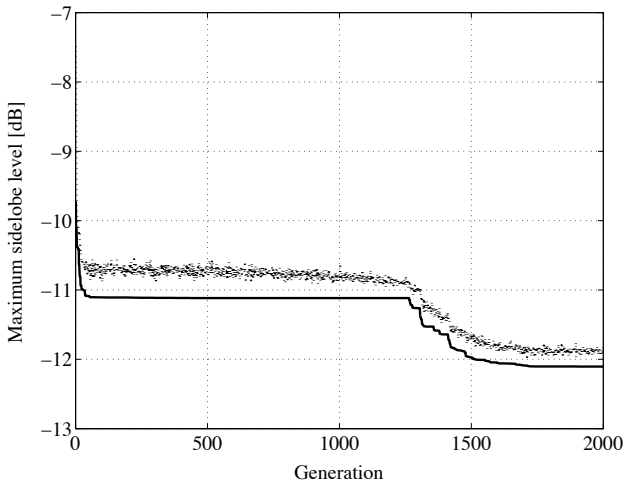

Figure 5.7: Fitness level during the optimization procedure; solid line: the best chromosome in each generation; dots: the average value at each generation.

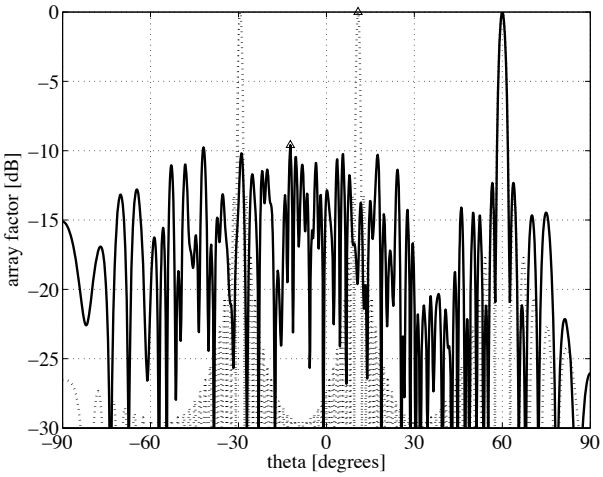

Figure 5.8: Radiation pattern of the (sparse) array antenna; solid line: sparse GA optimized antenna; dotted line: uniform array antenna.

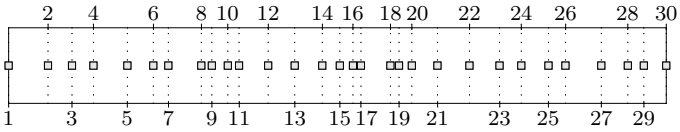

Figure 5.9: The optimized distribution of elementary radiators.

increase the cost and the complexity (particularly the beamforming network) beyond economically feasible limits. Antennas for radar applications should also have a low side-lobe level (SLL) for ensuring the target detection in a noisy environment. Uniform array configurations with $\lambda/2$ inter-element spacing, having elements of equal amplitudes, exhibit a maximum side-lobe level that only depends on the array architecture and that cannot be reduced by increasing the number of elements (SLL $\approx -13.2\,\mathrm{dB}$ for rectangular arrays and SLL $\approx -17.6\,\mathrm{dB}$ for circular configurations [147]). A method for controlling the maximum SLL in array antennas is to taper the amplitudes of the constitutive radiators [43]. However, in active arrays with a large number of radiators, this solution is less attractive due to the fact that each transmitter-receiver module attached to a radiating element must have a variable amplification.

In Section 5.4 it has been indicated that the radiation properties of an array antenna can be controlled by changing the position of the elementary radiators. A notable advantage of the a-periodic arrays with the inter-element spacing exceeding $\lambda/2$ is that, by using only a small fraction of the elements in the fully populated architecture, it is possible to obtain a narrow beamwidth. Another favorable aspect concerns the fact that the side-lobe

level can be controlled by modifying the elements' position, only, without resorting to transmitter-receiver modules with variable amplification. Nevertheless, these positive features are counterbalanced by the thinned structures having a high mean SLL. Note, however, that this phenomenon would also manifest itself when the same number of elements were deployed on a $(\lambda/2)$ uniformly spaced grid, in the case when the amplitude tapering of the radiators is chosen such that the same beamwidth as that of the thinned array is to be obtained. It can then be inferred that the mean SLL is, in fact, given by the number of elements in the array.

This study focuses on the evaluation of the performances of large, two-dimensional, thinned array architectures. To this end, synthetic aperture radar (SAR) measurements obtained in an indoor set-up that uses a two-dimensional scanner are employed. Three thinned architectures are used to generate (sparse) SAR images. The suitability of these architectures for processing radar data is assessed by comparing the relevant images with the SAR image obtained with the complete set of measurements.

Thinning methods

Firstly, a spatial tapering method [147] is used for thinning a two-dimensional array antenna with the elements arranged on a uniform grid. By controlling the density of the elements over the aperture a *Taylor illumination* for a SLL set to -40dB is aimed at. The thinned array is subsequently confined to a circular architecture (exhibiting a lower SLL when compared with that of a rectangular one). The array architecture obtained by this method (referred to as array **A1**) is depicted in Fig. 5.10.a. In this example, the inter-element spacing in the full array is 2 cm and the operational frequency is taken to be 4.5 GHz. From the fully populated, rectangular array having 6561 elements, only 1504 elements are retained in the thinned configuration (yielding a thinning factor of 77%).

The radiation properties of **A1** are plotted in Fig. 5.10.b. For a comprehensive understanding, radiation patterns in the elevation plane were evaluated for different azimuth angles and then overlapped on the same graph. Note that the azimuth angle is defined in this work in the array plane while the elevation angle is measured from the direction normal to the aperture. The possibility of formation of grating lobes has been tested by steering the main beam at 60° in elevation and 0° in azimuth. In this case the maximum SLL is 25 dB (mean SLL $\approx$ 30 dB) and the 3dB beamwidth is 7°.

A second thinned configuration is designed based on a fractal geometry [142]. By using a two-dimensional version of the Cantor set $\{1, 0, 1\}$, the thinned array configuration depicted in Fig. 5.11.a (hereafter referred to as array **A2**) is obtained after four growing stages. In this case, from 6561 elements of the fully populated array, 2465 radiators are kept in the a-periodic configuration (yielding a thinning factor of 62.4%).

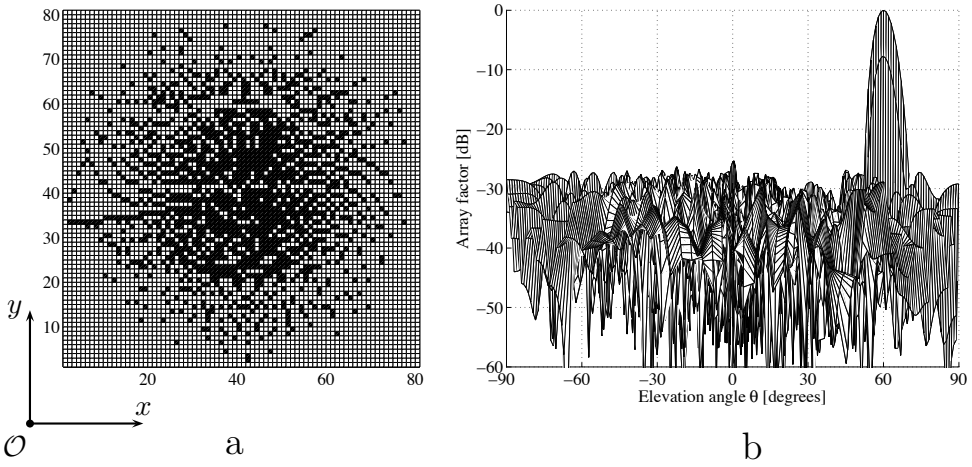

Figure 5.10: Thinned array obtained by space tapering (-40dB Taylor illumination). (a) - array architecture (the numbers on the axes correspond to the indices of the elements); (b) - array factor at 4.5 GHz.

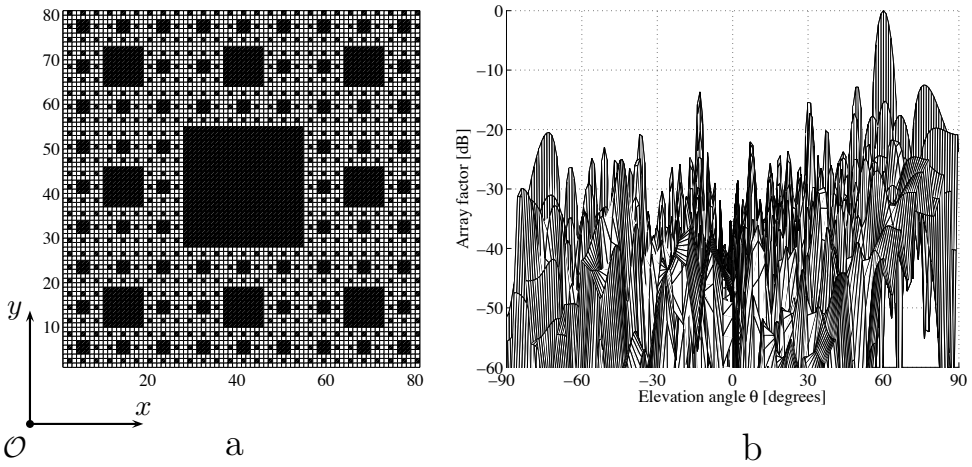

Figure 5.11: Fractal thinned array. (a) - array architecture (the numbers on the axes correspond to the indices of the elements); (b) - array factor at 4.5 GHz.

The array factor of the configuration **A2** is shown in Fig. 5.11.b for an inter-element spacing of 2 cm and an operational frequency of 4.5 GHz. The maximum SLL in this case is 13 dB (mean SLL $\approx$ 25 dB) and the beamwidth amounts to 4°.

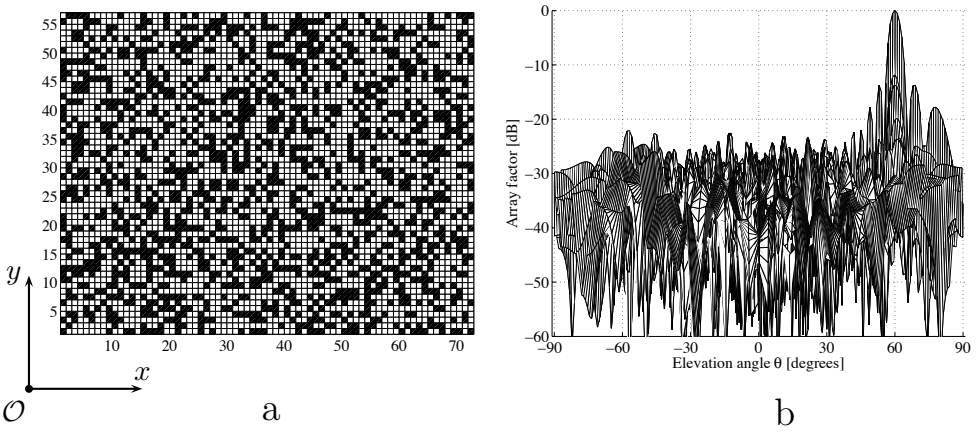

Figure 5.12: Combinatorial thinned configuration. (a) - array architecture (the numbers on the axes correspond to the indices of the elements); (b) - array factor at 4.5 GHz.

The third thinned array is obtained by making use of the combinatorial method presented in [78]. Massively thinned arrays can be obtained by exploiting the properties of combinatorial sets. It was firstly pointed out in [77] that, by using difference sets in determining the location of the elements in a thinned configuration, the beamwidth of the full array is preserved while the peak SLL is kept at an *a priory* known value. The thinned configuration considered here has 1530 elements deployed on a 73 by 57 uniform grid (representing a thinning factor of 63.2%). The positioning of the elements in the sparse structure (referred to as **A3**) is presented in Fig. 5.12.a.

The array factor of the configuration **A3** is depicted in Fig. 5.12.b, for an inter-element spacing equaling 2 cm and for the operational frequency of 4.5 GHz. In the side-lobe region, the energy is uniformly distributed (with a mean level of 25 dB) except for a small region in the vicinity of the main beam where the maximum SLL is 14 dB. The 3dB beamwidth is 4°.

Note that all presented radiation patterns are evaluated by taking the elementary antennas to be ideal, isotropic radiators of unit amplitudes and with no mutual coupling between them.

Experimental results

As mentioned before, due to the size of the problem at hand, the testing of very large, thinned arrays is technically difficult and economically impractical. A habitual manner to circumvent this is to synthesize a "virtual" thinned array by collecting the samples measured by means of a *single* sensor

that scans the complete aperture.

To this end, the needed measurements were performed using the indoor ground penetrating radar set-up of the International Research Centre for Telecommunication-transmission and Radar (IRCTR). This experimental set-up consists of a two-dimensional scanner, driven in the horizontal plane by stepping motors, which allows the accurate positioning of the antenna system. Two separate spiral (Archimedean) antennas were used for transmitting and receiving the signal. More details about this antenna system are presented in [105]. A vector network analyzer was utilized as radar transmitter and receiver. The measurements have been performed with the antenna elevated at 60 cm above the ground (for indoor experiments a box filled with dry sand was used to simulate the ground). Four metallic objects, namely a large disc, two rectangular plates and a tinfoil wrapped tennis ball, were deployed on the surface of the sand in the middle of the scene (see Fig. 5.13.a for a description of the investigated configuration). Complex radar data were recorded over a scanning area of 1.5×1.5m with a step of 2 cm. The measurements were done at 4.5 GHz.

Due to the wide radiation patterns of the transmitting and receiving antennas, it was impossible to detect (from clutter) the presence of the metallic objects in the raw data generated by the network analyzer. A focussing algorithm had then to be called upon for improving the signal to clutter ratio. Following a procedure described in [125], the reflections from the targets were coherently added, a fact that significantly improved the quality of the radar image. Fig. 5.13.a presents the SAR image generated when all the measurements where used in the focussing process. In this picture, the targets are visible and their location and size are correctly indicated.

For testing the performances of the thinned architectures introduced in this section, three (sparse) SAR images were then generated for comparison purposes. All these picture were obtained by using, in the data processing, the measurements performed at the locations corresponding to the elementary radiators of the sparse configurations, exclusively. Due to the fact that the apertures described in Figs. 5.10.a, 5.11.a and 5.12.a are larger than the area for which measured data were available, a zero input was assigned to the regions of the apertures falling outside the examined scene. In all cases, the centers of the sparse apertures were aligned with the center of the examined configuration. The capabilities of the three approaches to (sparse) SAR data processing are hereafter catalogued.

*Method **A1** (space tapering).* The results of the application of the method **A1** are shown in Fig. 5.13.b. Despite the fact that the thinned array **A1** exhibits the lowest maximum SLL, the reflection from the tennis ball (object D in Fig. 5.13.a) was not improved enough to become visible from clutter. This may be a consequence of the fact that **A1** has a large beamwidth and, therefore, the resolution is insufficient. The other three objects are visible, albeit at a lower contrast when compared to the reference image generated with the whole set of data.

*Method **A2** (fractal structure).* The SAR image obtained with the sparse configuration **A2** is depicted in Fig. 5.13.c. Here, all the four objects are visible, but the background shows some localized high values (strips around the objects).

*Method **A3** (combinatorial method).* The image obtained with the thinned configuration **A3** is presented in Fig. 5.13.d. All four objects are visible. The clutter has a relatively high value but it is uniformly distributed, a feature that may be advantageous in the detection process. The radiation characteristics of the configuration **A3**, namely a uniform SLL (although high side-lobes may exist in the proximity of the main beam) and a narrow beamwidth, seem to qualify this solution as the most viable sparse candidate for SAR applications.

Note that the presented SAR images are obtained after the application of the focussing algorithm, only, without any additional post-processing (e.g. target detection or clutter subtraction). The focal distance was chosen to be 60 cm and the radar pictures were normalized at the maximum reflection attained after the SAR processing.

This section documents an experimental study on thinning techniques appropriate for designing large array antennas. Synthetic aperture radar measurements have been performed and radar images generated using three different thinned configurations. For thinning rates between 65% and 75% it was possible to generate images comparable with that obtained by processing the whole measurement set. However, the relaxation in the SAR sampling (by performing measurements only at the position in the thinned configuration) limits the attainable improvement of the signal to clutter ratio after the processing. Employing a thinning procedure in SAR measurements is advantageous when a fast evaluation of the measurement scenario is required or when the reflections from the targets are strong enough such that after the sparse SAR processing they are visible from the clutter.

5.5.3 Planar sparse arrays

In the past, sparse array antennas have been given a substantial attention as regarding the theoretical aspects related to the radiation properties, in particular the formation of grating lobes when the inter-element spacing is larger than the wavelength at the maximum operational frequency. In Section 5.4 it was indicated that there are many techniques that can be employed for conceiving sparse configurations with no grating lobes. It is worth observing that most of these techniques have been validated by simulations using ideal, elementary antennas (isotropic radiators) and by neglecting the mutual coupling effect. However, it is well recognized that in practical arrays the properties of elementary antennas and the electromagnetic coupling between array's elements have a significant influence on the array characteristics. These fine aspects can be accounted for during the design stage by making use of the numerical electromagnetic techniques.

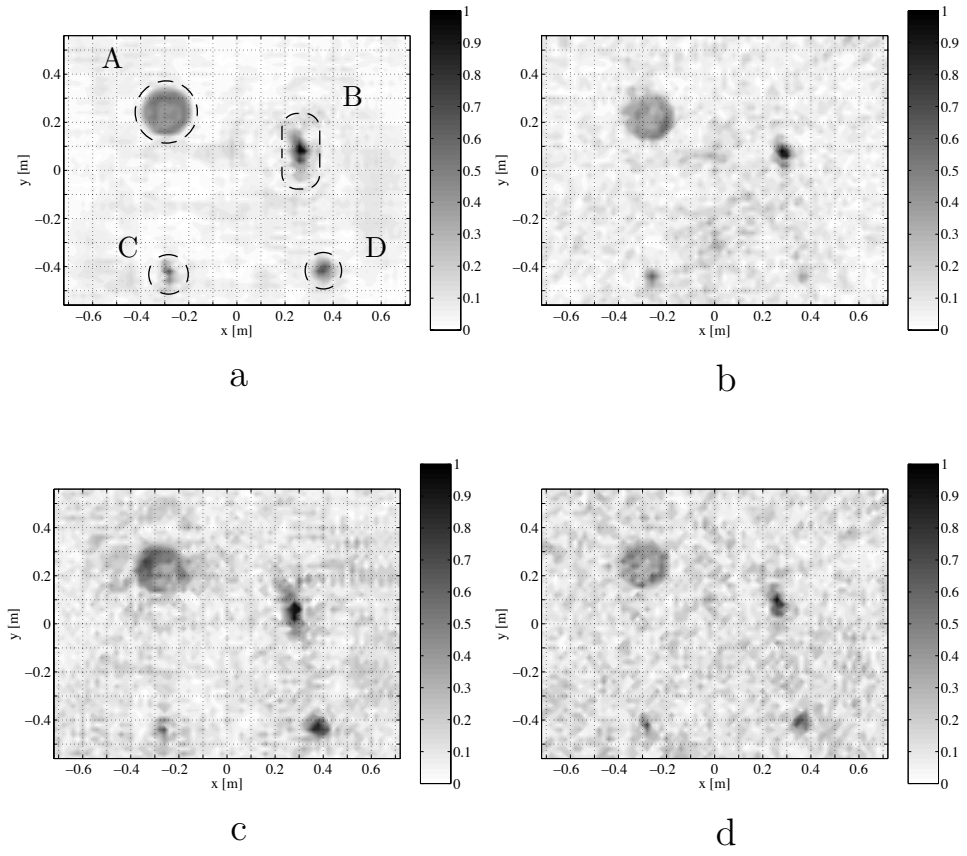

Figure 5.13: SAR images obtained with the complete set of measurements and with thinned configurations. (a) - full array; (b) - space tapering thinned array; (c) - fractal thinned array; (d) - combinatorial thinned array. The deployed objects: A – metallic disk of 0.2 m diameter, B – metallic strip of dimensions 0.23×0.045 [m], C – metallic objects of dimensions 0.02×0.03 [m] and D – tinfoil wrapped tennis ball.

In this section the properties of a planar sparse array are investigated by means of numerical simulations and experimental measurements.

Design and analysis procedures

The first step in the design algorithm is represented by the determination of the array's architecture. The analyses presented in Chapter 4 have shown that it is possible, by using a dielectric substrate with high permittivity, to obtain elementary radiators with the aperture size $a = b = 12$ mm which have good matching properties in the frequency range from 8 GHz to 10 GHz

(see the measurements presented in Fig. 4.15). By also considering the fact that in an array configuration the minimum separation between two primary radiators is bounded by the thickness of metallic walls (vias) associated to the cavity of the elementary radiator, the elementary cell in the array architecture was taken to have the size 15 mm × 15 mm. Note that a rectangular, uniform array having this cell size (15 mm × 15 mm) exhibits no grating lobes for frequencies below 10 GHz. Having selected the cell size, the sparse configuration resulted after applying a combinatorial thinning technique (see Section 5.4.4 for details) to a uniform architecture. In this respect, the difference set CDS $(63, 31, 15)$ was used for deploying the elements in the sparse configuration (a 9×7 uniform grid was used in this procedure). The geometry of the resulted array antenna is depicted in Fig. 5.14. In this figure the white squares indicate the cells in the sparse configuration and the gray background represents the metallic flange. Each of the elementary cells has assigned a number that will be further used in designating the array's element that coincides with the respective cell.

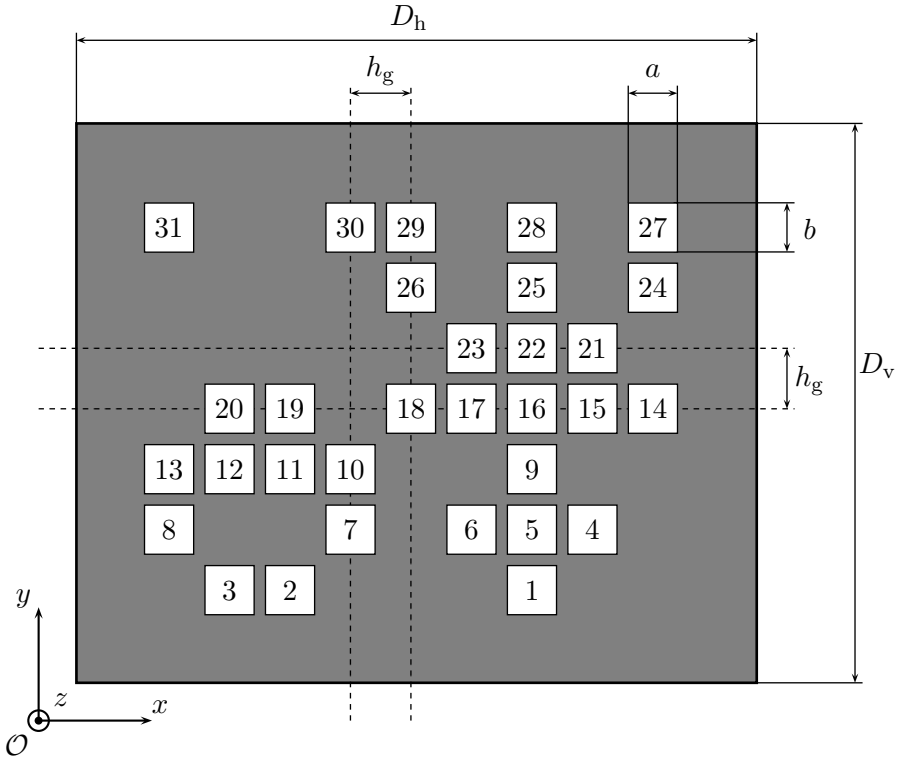

Figure 5.14: Distribution of the elementary antennas (white squares) in the sparse array architecture (front view). Principal dimensions: $D_\mathrm{h} = 165\,\mathrm{mm}$, $D_\mathrm{v} = 135\,\mathrm{mm}$, $a = b = 12\,\mathrm{mm}$ and $h_\mathrm{g} = 15\,\mathrm{mm}$.

The next step in the design procedure is to select the primary radiators

to be arranged in the sparse array architecture. Aiming at a low-profile and low-cost antenna system, a cavity-backed, stacked-patches antenna, fed by means of a coaxial probe has been selected as preferred elementary radiator. This kind of radiator was exhaustively investigated in Section 4.3 and, therefore, its characteristics will be hereafter summarized in the context of with the array functionality, only.

The numerical approach adopted for the full wave analysis of this sparse array antenna relies on the decomposition of the electromagnetic problem at hand into an *external* and an *internal* problem, the former addressing the radiation phenomena and the latter the matching between the elementary feeding structures (down to the coaxial cables) and the free-space. The two problems are solved separately and they are expressed in terms of Generalized Admittance Matrix (GAM).

The geometry of the generic radiator is depicted in Fig. 4.7. Following the discussion in Section 4.3, it is pointed out that this structure can be accurately investigated by means of the mode matching method (MMM). The application of this method requires the knowledge of the modal distributions in all cross-sections along the transmission channel having as input port the coaxial cable and as output port the aperture. From Fig. 4.7, it is evident that the configuration under investigation contains a combination of rectangular and coaxial waveguide sections. The modal representation on the coaxial segments was calculated by means of the BI-RME method whereas that on the rectangular waveguide segments is known analytically. The transmission channel is completed by including a load that mimics the radiation into the free-space and that accounts for the mutual coupling between the elements in the sparse array configuration.

The theoretical background for the analysis of the radiation from rectangular apertures and for evaluating the mutual coupling between arbitrary apertures relies on the methodology presented in Chapter 3. However, the straightforward application of that methodology in the case of large, finite, sparse arrays (containing hundreds, possibly thousands of elements) is prohibitive from the point of view of the computing resources. For still ensuring the feasibility of the numerical calculations, the following observations turn out to be of key relevance:

- The GAM of an array antenna consisting of rectangular apertures includes partial GAM-s evaluated for doublets of apertures, only (the self-admittance being a particular case, in which an aperture is coupled with itself).
- For widely spaced apertures, the mutual coupling is small enough for being neglected in practical applications.

By observing that the elements in the shared aperture antenna are deployed on a fixed grid and by taking into account the fact that the couplings are evaluated for an area of reduced dimensions, it can be concluded that the

partial GAM-s need to be computed for a limited number of positions, only. These results can be precooked for a given combination of aperture dimensions and grid steps and be subsequently employed in a "table look-up" manner for evaluating the properties of *any* array architecture that complies to the chosen design parameters (aperture dimensions and grid steps).

The sparse array presented in Fig. 5.14 was manufactured in a stratified technology by using high frequency, laminated materials (RO4003, having $\varepsilon_r = 3.38$ [37]) with different thicknesses. The primary radiator used in the sparse configuration is identical with the element B6 discussed in Section 4.4. The principal dimensions of this elementary antenna are (see Fig. 4.7): $a = b = 12\,\text{mm}$, $dy_c = 3.8\,\text{mm}$, $r_{p1} = 4.9\,\text{mm}$, $r_{p2} = 4.1\,\text{mm}$,$h_1 = 0.508\,\text{mm}$, $h_2 = 1.524\,\text{mm}$ and $h_3 = 0.305\,\text{mm}$). The vias, used for replicating the cavity, have the diameter of 0.7 mm and were deployed at approximative 2 mm from each other.

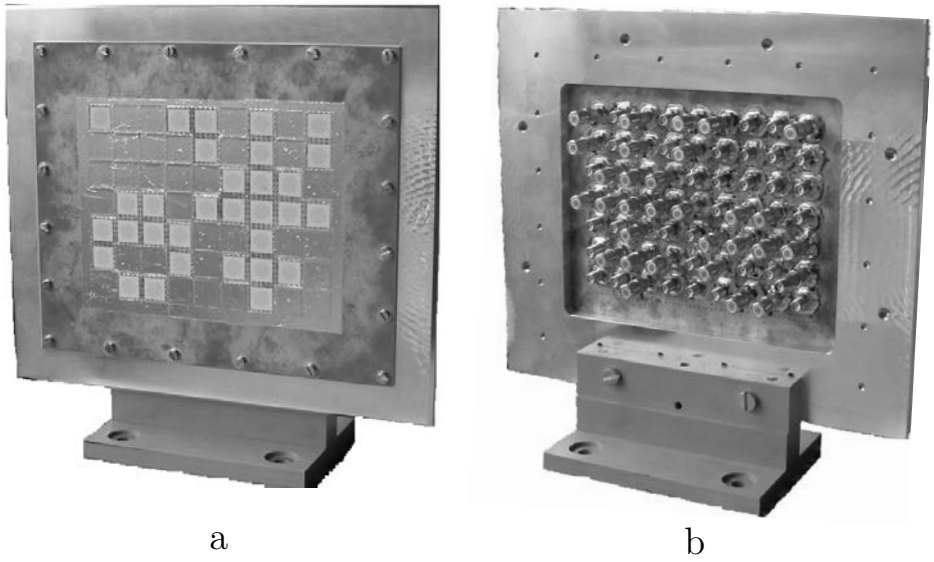

Figure 5.15: Manufactured sparse array antenna. (a) - front view; (b) - rear view.

The manufactured planar sparse array antenna is presented in Fig. 5.15. In fact the manufactured model represents a shared aperture consisting of two interwoven sparse arrays (which will be presented in Section 6.2). One of these sub-arrays is similar to the one discussed in this section and, for the measurements campaign, it was isolated from the shared aperture by covering with tinfoil the elements of the other sub-array.

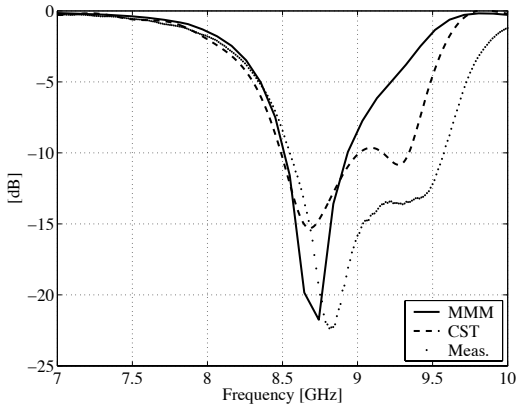

Figure 5.16: Measured and simulated input reflection coefficient of the isolated, elementary radiator. Continuous line - calculated by MMM; dashed line - calculated with CST Microwave Studio; dotted line - measured.

Measured and simulated results

The experimental and numerical investigations focus on two aspects which have been considered as being of key importance: the matching properties of the individual radiators functioning in non-periodic, finite array environments, and the evaluation of the radiation properties of the sparse array antenna, while also accounting for the effect of the mutual coupling.

The characterization of the elementary antenna, operating as an isolated element, has been performed in Section 4.4. At that point it was concluded that there is a good agreement between the measurements and the numerical simulations. The input reflection coefficient of the elementary antenna B6 is provided once again in Fig. 5.16 with a finer resolution in the frequency domain. The simulations were performed with the mode matching method (MMM), as indicated in Section 4.3, and with the CST Microwave Studio package. From this figure it is noticed a fair similarity between the measurements and the simulations. The differences in the upper part of the spectrum (from 9 GHz to 9.5 GHz) are attributed to dissimilarities between the theoretical and manufactured models. The most notable deviations are:

- the MMM model has an infinitely extended metallic flange whereas the CST model and the physical antenna have a finite flange (of dimensions 50 mm × 50 mm)

- in the MMM analysis the cavity is considered continuous whereas the CST model and the physical model have the cavity simulated by metallic vias;

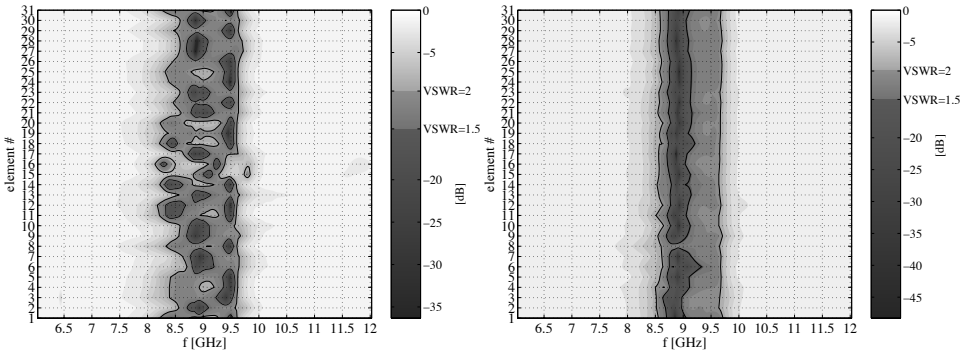

Figure 5.17: Preliminary measurements of the input reflection coefficient of the elements in the sparse array. (a) - capacitive feeding; (b) - inductive feeding.

- the practical realizations of the metallic vias have required that a small pad exists on both sides of the microstrip laminate. Therefore, the protruding pin exhibits a small ring at the entrance in the cavity (not considered in the numerical simulations) and the vias replicating the cavity have been deployed on a square larger than the aperture of the primary antenna (accounted for in the CST analysis, only).

It is also noted that the simulations performed with the MMM were done by considering a number of ten waveguide modes in the aperture (a parametric study showed no significant differences between calculations with 10 and 50 modes in the apertures).

Turning to the sparse array antenna, Figure 5.17 illustrates some preliminary measurements performed on the manufactured model. Initially, the inner pin for each element was not soldered to the bottom patch of the elementary antennas. In Section 4.4 it was observed that such a capacitive model (having an air gap between the protruding pin and the bottom patch) exhibits a larger bandwidth compared with the inductive model (where the pin touches the patch). The measurements performed on the sparse array consisting of capacitive models are presented in Fig. 5.17.a. From this figure it is noticed that there are significant differences between the matching characteristics of the primary radiators operating in the array environment. This behavior impedes the performance of the array antenna as regards the matching properties. Improved results were obtained after the protruding pins were soldered to the corresponding patch. The input reflection coefficients of the inductive models operating in sparse array arrangement are presented in Fig. 5.17.b. Still, from this figure it is noted that the element number 8 (see Fig. 5.14) has a different behavior compared with the other elements in the array. After a meticulous investigation it was observed

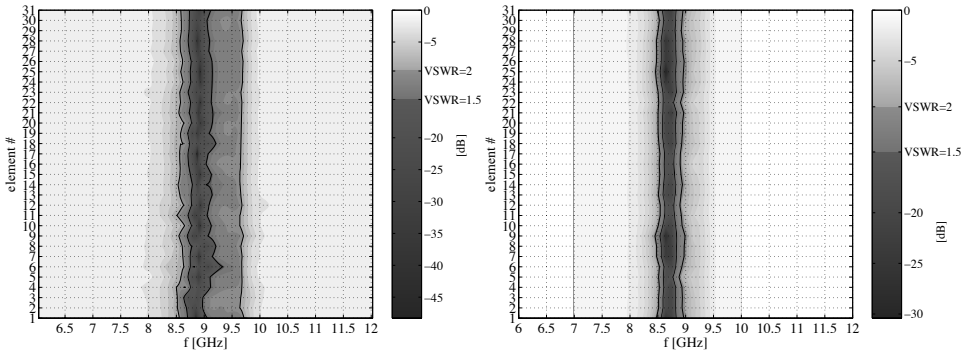

Figure 5.18: Frequency behavior of the input reflection coefficient of the elementary antennas in the sparse configuration. (a) - measured; (b) - calculated by means of the MMM.

that in the region of this element the microstrip layers were not appropriately fastened together. A new set of measurements was performed after the layers were attached firmly. The results presented in Fig. 5.18.a clearly evidence that arranging cavity-backed, stacked-patches radiators in sparse array configurations does not affect detrimentally the matching properties of the elements when compared with similar isolated radiators. A similar conclusion can be draw from the MMM numerical simulations presented in Fig. 5.18.b.

The radiation characteristics of the sparse array antenna were evaluated by measuring the individual patterns of the elementary radiators. The measurements were performed in the anechoic chamber available at IRCTR. The elementary patterns were measured in the H-plane at the frequency of 9 GHz. The measurement results are presented in Fig. 5.19.a with thin, dashed lines. From this figure it is observed that the individual patterns exhibit variations with respect to each other in the order of 5 dB. Despite of these dissimilarities, the radiation pattern of the sparse array antenna (thick line in Fig. 5.19.a), calculated from the measured data, has a narrow beamwidth (of about 15°) and the side lobes are below −10 dB. The results obtained by the full wave, modal analysis of the sparse array antenna are presented in Fig. 5.19.b. It is evident from Figs. 5.19.a and 5.19.b that the measurements are in good agreement with the simulations.

To substantiate the validity of the MMM numerical analysis, the measured and the simulated radiation patterns of the sparse array were plotted in Fig. 5.20 for different scanning angle. Note that the measured data were post-processed in order to direct the main beam at a specific angle.

During the scanning procedure the maximum level of the main beam

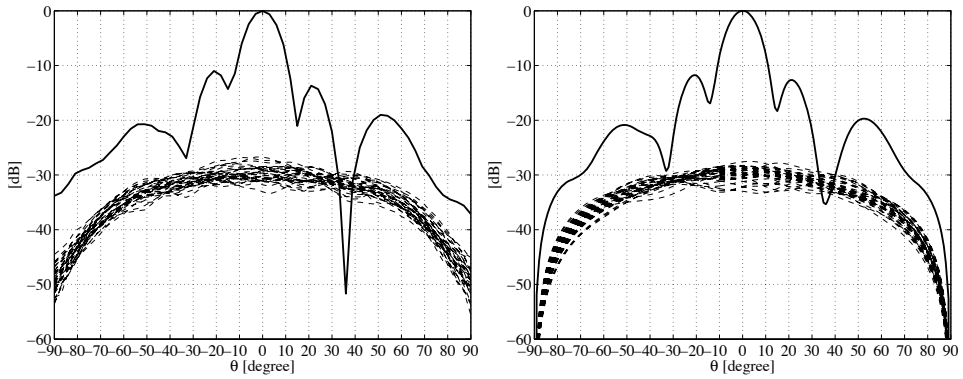

Figure 5.19: Radiation patterns of the elementary antennas in the sparse array architecture (dashed lines) and the radiation pattern of the sparse array. (a) - measurements; (b) - simulations (MMM).

decrease in accordance with a cosine law, which is similar to the pattern of the primary radiator. This effect is illustrated in Fig. 5.21 by using measured data.

Note that the measurements presented in this section were performed on each element in the sparse configuration by having all the other radiators terminated on matched loads ($50\,\Omega$).

A final numerical investigation on the sparse array antenna refers to the evaluation of the active reflection coefficient associated to each primary radiator. For comparisons purposes the filled array antenna, from which the sparse array has been derived, was analyzed as well. The uniform array consists of 9×7 elementary antennas, which are identical with the one used in the sparse architecture. The active reflection coefficients were calculated by means of the mode matching method at a fixed frequency of 8.7 GHz. The results presented in Fig. 5.22 demonstrate that in sparse configurations there is a significant dissimilarity between the active reflection coefficients of the primary radiators. The mean value of the active reflection coefficients in the sparse array has a smaller fluctuation (with the angle) compared with the mean value in the case of the uniform array. This property suggests that in sparse array antennas there are always a few elements that radiate properly at each scanning angle in the field of view. On the contrary, in uniform arrays, due to the coherent phase addition, most of the energy is reflected to the generator for scanning angles larger than a certain value.

The analysis of the active reflections coefficient is enlightening for the potential of the use of sparse architectures for ensuring a wide angle impedance matching (WAIM).

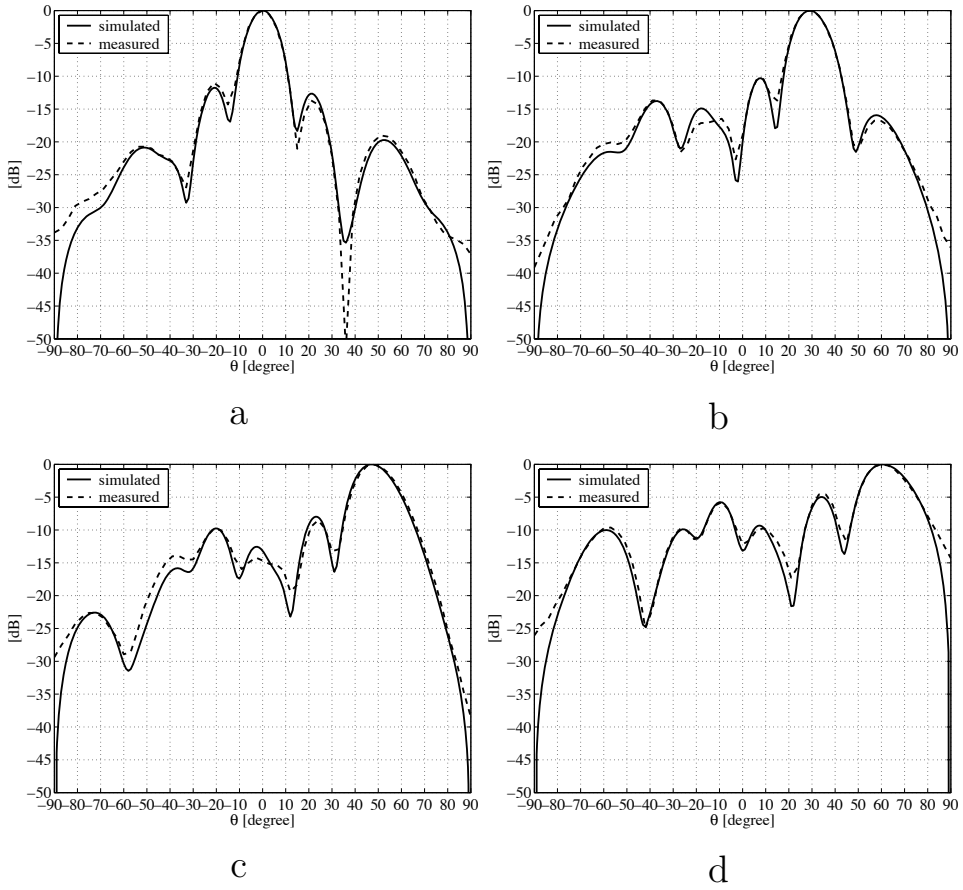

Figure 5.20: Radiation patterns of the sparse array antenna for different scanning angles. (a) - scanning angle of 0°; (b) - scanning angle of 30°; (c) - scanning angle of 50°; (d) - scanning angle of 70°.

5.6 Conclusions

A general formulation, in terms of a constrained optimization problem, was proposed for addressing the design of sparse array antennas. This formulation provides an adequate handle for understanding the large variety of specific methods devoted to this topic that are readily available in the literature. Specific aspects stemming from practical limitations that are intrinsically associated to the design of sparse antenna systems, most notably in the case of digital beamforming, were highlighted. In view of the complex set of constraints that need being accounted for, stochastic methods seem to be the best candidates for designing effective sparse antenna arrays. A catalog of the design techniques used in conceiving sparse array antenna was

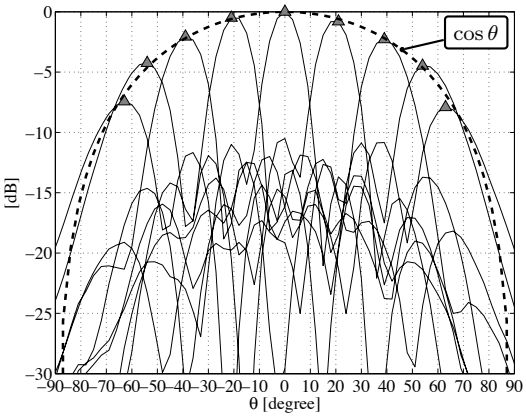

Figure 5.21: Variation of the amplitude of the sparse array's main beam while scanning in different directions. With a thick, dashed line a cosine variation law ($\cos\theta$) is indicated and with triangles the maxima of the sparse array's main beam are marked for the considered scan angles ($0°, \pm 20°, \pm 40°, \pm 60°, \pm 80°$).

presented and some of these techniques were discussed in detail.

A number of numerical and experimental examples were also presented. The experimental and numerical investigations focused on two relevant aspects, namely: the estimation of the matching properties of the individual radiators functioning in non-periodic, finite array environments, and the evaluation of the radiation properties of the sparse array antenna, while also accounting for the effect of the mutual coupling.

Elements of novelty

In this chapter it was demonstrated that the discrete Fourier transform of a cyclic different set is a set characterized by the fact that the constitutive elements have only two absolute values.

The design of sparse array antennas by using genetic algorithms was reformulated in order to eliminate the restriction of positioning the elements relative on an uniform grid. Moreover, the mutual coupling between elements in the array configuration was accurately evaluated during the design procedure and its effect was incorporated in the expression of the cost function to be minimized.

A synthetic aperture radar (SAR) procedure, using sparse measurements, was proposed. Different sparse array configurations consisting of large number of elements were experimentally investigated by processing the measurements acquired with a ground penetrating radar.

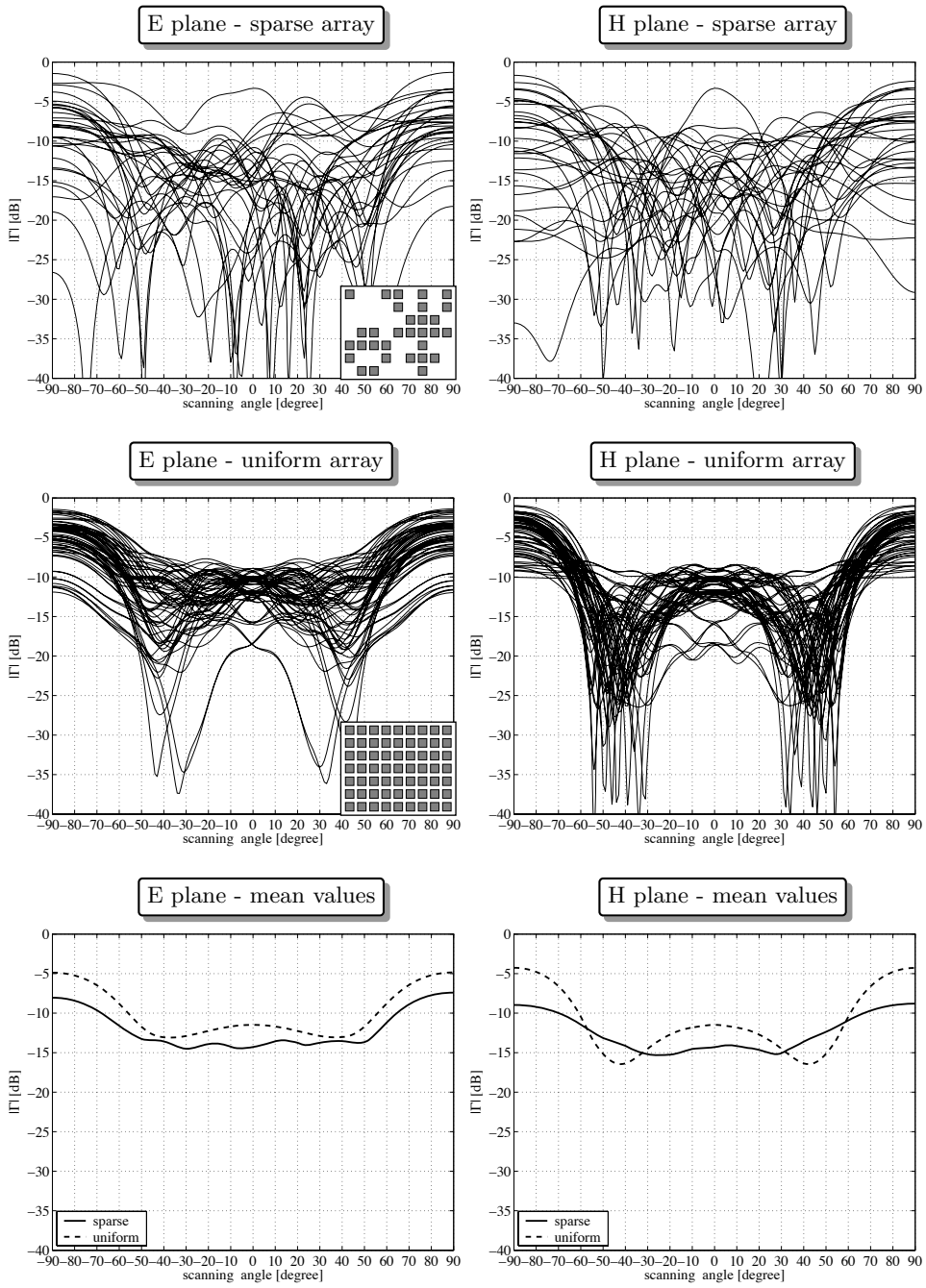

Figure 5.22: Active reflection coefficient at the terminals of primary antennas arranged in sparse and uniform architectures.

Experimental investigations of a planar sparse array antenna were presented. The measurement were compared with simulation results obtained by using the theory and the software modules presented in Chapters 2 and 3. By numerical simulations it was demonstrated that in sparse array antennas the coupling effect has a reduced influence (compared to uniform arrays) on the performance of individual radiators while electronically scanning the antenna beam. This observation can be used in designing array antennas characterized by wide angle impedance matching (WAIM) properties.

Chapter 6

Shared aperture array antennas

In this chapter some relevant aspects of the shared aperture array antennas are discussed. In particular, attention is given to the problem of designing finite array antennas consisting of elementary radiators operating at different frequency bands. This approach is seen here as a solution for increasing the total bandwidth of the antenna system in particular for applications requiring a highly multi-functionality. The necessary real estate for accommodating different sub-arrays is created by using sparse configurations which possibly have large distances between the elements and, besides, exhibit no grating lobes. Some techniques that can be adopted for preventing the overlapping of the elements pertaining to distinct sparse configurations are also discussed. The effect of the mutual coupling between identical and differently sized elements is accurately evaluated and it is accounted for in predicting the performance of each individual radiator. The last part of the chapter is dedicated to numerical and experimental results.

6.1 Interleaving sparse configurations

Upon focussing on the aperture sharing concept, it is noted that it can be implemented by placing on the relevant aperture either identical or different radiators. The former choice [7, 59] allows a facile (possibly dynamic) reconfiguration of the aperture. However, the various tasks to be accomplished are often associated with spectra that are spread over a wide frequency range and, consequently, the antenna elements need to be of the wide-range variety. Apart from the fact that these type of antennas have, intrinsically, a large electric size (that becomes a critical issue when beam-scanning is aimed at) this approach also yields a considerable interference between the implemented functions as a result of the out-of-band mutual coupling. When

using different radiators, they can be tuned for each individual application, thus improving the isolation between the different systems. A straightforward modality for achieving an aperture sharing is by deploying next to each other a number of compact sub-arrays [45](pp. 206). However, each sub-array is confined to a small area, thus providing but limited angular resolution. To sidestep this drawback, the radiators pertaining to the various sub-arrays may be distributed over the entire available area, in an interleaved manner, for example by deploying the elementary antennas on interlaced, uniform array topologies [118, 112, 83]. While this option is conceptually simple, it results in severe limitations as far as scanning range, polarization and the ratio between the frequency bands pertaining to the sub-arrays are concerned.

Most of the deleterious aspects mentioned above can be circumvented by calling upon the use of interwoven, sparse arrays. To substantiate this, it is noted that:

- by applying an adequate thinning technique, in conjunction with an interweaving procedure that avoids the overlapping of the elements, the grating lobes (that would occur in the case of widely-spaced uniform architectures) are suppressed,
- the side-lobes level can be controlled without resorting to amplitude tapering (that would be needed in uniform arrays) and
- the large inter-element distances result into a reduced in-band mutual coupling.

For implementing the concept of shared aperture based on sparse array antennas one has to deal with two design stages: one of these is dedicated to the design of different sparse sub-arrays operating in isolated mode and the other one focuses on the interleaving procedure that will allow for deploying the sparse architectures on a common aperture.

With regard to the first design step it is noted that the theory of sparse array antennas is well established, a comprehensive presentation of this topic being provided in Chapter 5. In that chapter the large variety of design techniques that can be used in conceiving sparse configurations was also catalogued. Contrary to the thinning techniques, the topic of interleaving sparse sub- arrays is seldom encountered in the literature. The main goal of this design step is to preserve the sparsity properties of the sub-arrays (especially in the sense of avoiding the generation of grating lobes), while preventing the overlapping of elementary radiators.

From the beginning it is pointed out that, in conceiving shared aperture array antennas consisting of differently sized elements, two solutions may be adopted:

- a *uniform cell* strategy where the maximum physical size in the aperture's plane of the elementary radiators must accommodate the real

estate associated to the array's cell;

- a more general, *non-uniform cell* approach when the dimensions of the elementary radiators pertaining to each sub-array are not limited to those of a common cell.

By using identical cells it is possible to associate a uniform grid to the array antenna, an aspect that improves significantly the mathematical formulation of the problem. However, the utilization of this method is limited by two conflicting requirements: on one hand, the cell size should be small enough in order to the conception of a sparse configuration, exhibiting no grating lobes, to be feasible and, on the other hand, the cell must be large enough to accommodate the primary radiators operating at the lower bandwidth (and having, inherently, the largest dimensions). The restriction regarding the ratio between the dimensions of the elementary antennas to be interlaced on a common aperture can be eliminated by adopting a non-uniform cell approach. In this case, some difficulties are encountered in the mathematical formulation of the problem due to the fact that it is not possible to associate a grid to the array's topology.

Some relevant techniques that can be adopted for interleaving sparse configurations will be hereafter presented.

6.1.1 Random placement

In Section 5.4.3 it was indicated that the radiation patterns of sparse array antennas can be controlled by selecting stochastically the locations of the elementary radiators in the array configuration. Similarly, a shared aperture antenna can be obtained by deploying randomly the elements of different sub-arrays on a common grid. In this case the overlapping of the elementary radiators is automatically ruled out by the fact that the sparse sub-arrays have no predefined architectures. After deploying the primary radiators on the shared aperture, the design methodology proceeds with the evaluation of the radiation properties of each sub-array. If these radiation characteristics do not satisfy the requirements, a new configuration is randomly defined and then characterized. This iterative process is repeated until each sub-array has met the antenna specifications.

A study of shared aperture antennas consisting of randomized interlaced sub-arrays is presented in [21, p. 10-1]. Different types of radiators have been deployed on a square grid, all the radiators being confined (as concerns the physical size in the aperture's plane) to a uniform square cell. The main goal off this experiment was to demonstrate that such a shared aperture configuration allows for a significant reduction of the maximum phase shift when compared to a uniform arrangement of the elements in the sub-arrays (approximative 50% reduction in the maximum phase shift for a conical scanning sector of 10°).

It is worth noting that, by adopting a uniform cell approach, the application of the random method in conceiving shared aperture antennas is straightforward. However, a limitation is introduced in this procedure by the fact that all the radiators in the shared aperture have to be smaller than the cell size. By taking into account that the size of the elementary antennas is related to the operational bandwidth and that the miniaturization of these primary radiators is but limited, the shared aperture would have a relatively narrow bandwidth. This drawback can be circumvented by associating to each sub-arrays a differently sized cell. In this non-uniform cell approach the simple random placements of the elementary radiators is not longer appropriate and more advanced techniques (as for example genetic algorithms, simulated annealing or evolutionary programming) need to be called upon. Such elaborate methods would probably offer the most non-restrictive treatment of the problem with the possibility to easily incorporate multiple design goals in the optimization process.

The random placement methods avoids the overlapping of the elements by simultaneously designing and interleaving the sparse sub-arrays. The design of the sparse configurations is slightly complicated by including different types of elements while the process of interleaving the sub-arrays is significantly simplified.

The less attractive aspects of the stochastic methods are related to the following aspects:

- the convergence to an optimum solution is not guaranteed;
- the large computation times will restrict the dimension of the problems that can be solved to small and medium sized arrays (tens or hundreds of elements);
- the use of differently sized cells makes these methods to suffer from a poor coding of the problem which will affect the convergence, the computation time and the quality of the solution.

Some of these drawbacks can be suppressed by using deterministic methods for designing the sparse sub-arrays and than interleaving them.

6.1.2 Complementary solution

Among the design methods used in the field of sparse array antennas the combinatorial procedures and the fractal geometries are the most attractive as concerns the computational times and the sizes of the arrays that can be contrived (from small arrays having a few tens of elements up to large arrays of thousands of elements). A well known property of these thinning procedures is that they always split a fully populated array antenna in two complementary sub-arrays, which have a main lob with the beamwidth comparable with that of the full array and exhibit no grating lobes (note that

the energy of the grating lobes is distributed in the side-lobe region). Therefore, by using the complementary sub-arrays to accommodate two types of the radiators on a common aperture one can easily obtain a shared aperture, sparse array antenna. Moreover, the aperture is used in a very efficient manner, the empty space on the shared aperture being minimized. It is worth observing that a uniform cell strategy must be considered in conjunction with this method. Hence, the drawbacks associated to the uniform cell approach are the main limitations of this design methodology.

Another limitation of the complementarity method is that it allows only two types of elementary radiators to be deployed on the common aperture. An extension of the complementary concept, which aims at splitting a full array into more than two sparse sub-arrays, is provided in [32]. There, the difference set method has been used to interweave eight sparse sub- arrays on a common grid.

6.1.3 Multi grid approach

In Chapter 5 it was suggested that most of the methods used in conceiving sparse array antennas are, in fact, thinning procedures associated to a uniform grid. In particular, planar arrays containing a large number of elements (hundreds or thousands) are obtained exclusively by using a uniform grid on which the elements of the sparse array are deployed according to a specific rule. Therefore the sparse configurations obtained with different elementary radiators will be associated to uniform grids having differently sized cells. For interleaving these sub-arrays on a common aperture it is necessary to align the relevant grids such that there is no overlapping of the primary radiators. In the case when the sparse sub-arrays have overlapping elements an iterative process based on the trial-and-error philosophy can be contrived for re-arranging the elements in the sparse configurations such that the collocation of the primary radiators is avoided.

In [28] a wide band, shared aperture, sparse array antenna was designed by means of interleaving two sub-arrays operating at adjacent bandwidths. The sub-arrays were conceived using the difference set method starting from two grids having the cell dimensions in a ratio of two. For avoiding the overlapping of the elements, the sub-arrays were interactively re- arranged by making use of the cyclic shift property of the difference set.

Note that the multi grid solution is suitable for solving non-uniform cell problems and can be used in conjunction with most of the sparse algorithms presented in Chapter 5. The less attractive aspects of this method are related to the fact that it is difficult to design sparse sub-arrays having no overlapping elements. In general, the configurations with a high thinning rate are preferred for avoiding the collocation of the primary radiators. Therefore, the resulted shared aperture, sparse array antenna has a poor efficiency as concerns the use of the aperture's real estate.

6.2 Design of shared aperture antennas

In this section a consistent strategy for the design of finite array antennas consisting of differently sized radiating elements is discussed. In view of increasing the total bandwidth of the antenna system, while maintaining a low mutual coupling between the elementary radiators, sparse subarrays, operating at adjacent frequency ranges, are interleaved on a common (shared) aperture. The sparse architectures are designed using a combinatorial method that ensures an acceptable behavior in the side lobe region in conjunction with a narrow beamwidth. The effect of the mutual coupling between identical and differently sized elements is accurately evaluated and it is accounted for in predicting the performance of each individual radiator. The concept is illustrated by designing and measuring a shared aperture antenna consisting of two interwoven sub-array that jointly cover a fractional bandwidth of 14% in the X-band. Cavity-backed, stacked-patches antennas with coaxial feeding are used as elementary radiators.

6.2.1 Rationale and design philosophy

Multifunctionality of the antenna systems is a key issue in the case of mobile platforms performing simultaneously multiple tasks, such as communication, remote sensing, electronic warfare, etc. Traditionally, there is a twofold approach to ensuring the multifunctionality of these systems [45](section 2.7):

- time sharing (time multiplexing) – the antenna resources are employed sequentially by different systems at distinct time slots;
- aperture sharing (aperture segmentation) – separate radiators are employed for concurrently serving each required functionality; since, more often than not, the space for deploying antennas is limited, the relevant radiators have to be closely packed.

While the former approach is, in principle, compatible with any type of antenna, the latter implies, necessarily, the use of a collection of elementary radiators that are integrated in an antenna array. In it, each functionality is associated with a specific sub-array.

The present work advocates a multifunctional antenna architecture based on the shared aperture, sparse array antenna approach [33]. For implementing this concept, two aspects are of paramount importance: the design of the individual radiators functioning in non-periodic, finite array environments, and the evaluation of the radiation properties of the densely populated shared apertures, while also accounting for the effect of the mutual coupling. To this end, a novel, consistent design strategy, having as main purpose to ensure that all radiators in the array configuration do radiate

adequately, is proposed. The numerical approach underlying this strategy relies on the decomposition of the electromagnetic problem at hand into an *external* and an *internal* problem, the former addressing the radiation phenomena and the latter the matching between the elementary feeding structures (down to the coaxial cables) and the free-space.

The account now proceeds with a detailed description of the adopted design philosophy. As a first step towards obtaining the antenna system that is aimed at, a deterministic thinning method, corroborated with a suitably chosen interweaving strategy, is applied for the placement of the individual radiators. Subsequently, the solution of the external problem is discussed by evaluating the inter-element mutual coupling, as well. The result of this step is a Generalized Admittance Matrix (GAM) that models the radiation from the complete structure, that provides, in turn, the boundary conditions for the internal problem concerning each elementary antenna. The proposed algorithm is illustrated by means of designing a shared aperture antenna consisting of two interwoven sub-arrays that use as elementary radiators cavity-backed, stacked-patches antennas with coaxial feedings.

6.2.2 Design strategy

The antenna architecture promoted by the present work is schematically illustrated in Fig. 6.1. This concept relies on the fact that, by eliminating a (sizeable) number of array elements as a result of applying a thinning technique, a lot of space becomes available on the aperture. This space can then be occupied by radiators belonging to another sub-array, providing the overlapping of elements is prevented. Note that by using this strategy for sub-arrays with distinctive, but contiguous operational bandwidths, an (ultra-) wide-band antenna system can be synthesized.

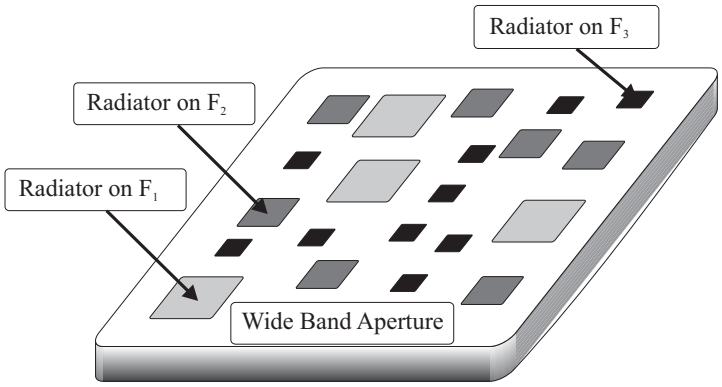

Figure 6.1: Illustrative for the shared aperture antenna concept.

The realization of this concept assumes addressing a number of impor-

tant aspects:

- the choice for a type of primary radiator;
- the choice for a suitable thinning technique;
- the design of an interleaving procedure that is consistent with the previously chosen thinning technique;
- the rigorous analysis of the internal and the external problems, as defined in the concluding part of Section 6.2.1.

These aspects are hereafter examined individually.

A detailed analysis of some elementary radiators that can be integrated in array configurations was presented in Chapter 4. From that analysis it was concluded that the cavity-backed, stacked-patches antenna is a suitable candidate for designing low profile and moderate band array antennas. Some other attractive properties of this type of antenna are: moderate bandwidth, good isolation in array environments, easy manufacturing in stratified technology, lightweight and low cost. By accounting for all these features, the cavity-backed, stacked-patches antenna, fed by means of a coaxial probe is selected as the preferred elementary radiator.

After a preliminary analysis of the antenna requirements, a complementary solution (as presented in Section 6.1.2) making use of the difference set technique was adopted for conceiving the shared aperture, sparse array antenna. Among the most relevant aspects which have motivated these choices are: the difference set method allows for obtaining a sparse configuration having low side lobes in a very short time; the distribution of the energy in the sidelobe region is more uniform than in the case of random or fractal architectures; it can be used for designing a medium sized array which is preferred by a low cost concept demonstrator; since the size of the manufactured antenna should be small it is preferable to have an efficient use of the aperture.

For efficiency considerations, the solution of the electromagnetic problems concerning the analysis of the cavity-backed, stacked-patches antennas in a shared aperture, sparse array configuration employs the mode-matching techniques presented in Chapter 2 and Chapter 3.

The evaluation of the radiation parameters is traditionally carried out by either isolating the elementary radiators and analyzing them outside the array environment or by accounting for an infinitely extended (periodic) array. The former approach has as main drawback the fact that the radiation properties of the individual elements are significantly affected when placing them in the array environment. An example in this sense is provided in [62, 52] where including the excellent type of radiator described in [126] in a 5×5 array results in a massive deterioration of the matching properties in the case of the elements located at the center of the array. The infinitely extended

array correctly addresses the radiation properties in array antennas, on the provision that true periodicity of the structure is enforced. The use of this model is, nevertheless, not applicable to the case of the sparse sub-arrays under investigation since no periodic properties can be asserted to them. The present work proposes a full-wave analysis of the complete radiating structure, such that the behavior of the elements in the array environment to be consistently taken into account.

6.2.3 Implementation of the design strategy

The design strategy described in the Section 6.2.2 is demonstrated for the case of a shared aperture antenna consisting of two sub-arrays operating at adjacent frequency ranges, that must jointly cover a fractional frequency band of at least 10% within the X-band. The sub-arrays are hereafter referred to as SA_H and SA_L, where the indices "H" and "L" designate the higher and the lower frequency bandwidths, respectively.

The objective is to obtain a medium-sized array antenna offering scan capabilities in the hemispherical field of view. The antenna must be amenable to manufacturing in a printed, stratified technology, by using commercially available, high-frequency, plated laminates.

The design of the sparse array's architecture

The first step in the design algorithm is represented by the determination of the array's architecture. Preliminary analyses (see Chapter 4) have shown that it is possible, by using a dielectric substrate with high permittivity (for example RO4003 with the relative dielectric permittivity of 3.38 [37]), to reduce the maximum size of the elements in the SA_L sub-array below the value $\lambda_{X,min}/2$, with $\lambda_{X,min}$ denoting the wavelength at the upper limit of the X-band (10 GHz). (The correlation between frequency and size implies that the elements in the SA_H sub-array are smaller.) Consequently, a common grid, having square cells with edge lengths of $\lambda_{X,min}/2 = 15\,\text{mm}$, can be employed for deploying all elements. After having selected the grid, the design proceeds by applying the difference sets method. In this respect, the difference set $DS = (63, 51, 15)$ is used for deploying the elements of the SA_H sub-array, while its complement provides the positions of the radiators of the other one. This automatically resolves the interleaving problem, since no overlapping is possible anymore. Note that the possibility to use a common grid in conjunction with the difference set method results in a substantial simplification of the placement algorithm when compared to the multi grid solution discussed in [28].

The result of the application of the above placement procedure is depicted in Fig. 6.2. In it, the white boxes designate the area allocated to the radiators in the SA_H sub-array and the black ones the area allocated to

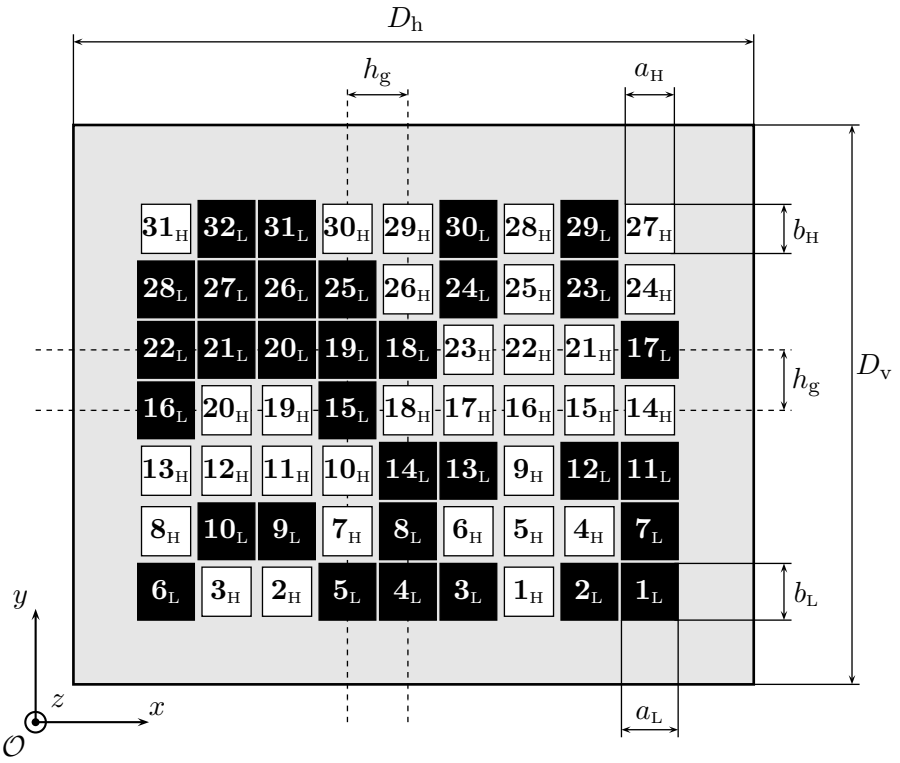

Figure 6.2: Distribution of the elementary antennas in the shared aperture architecture (front view). The white squares represent the elements of the $\mathrm{SA_H}$ sub-array and the black squares denote the elements of the $\mathrm{SA_L}$ sub-array. With gray is indicated the metallic flange. Principal dimensions: $D_\mathrm{h} = 165\,\mathrm{mm}$, $D_\mathrm{v} = 135\,\mathrm{mm}$, $a_\mathrm{H} = b_\mathrm{H} = 12\,\mathrm{mm}$, $a_\mathrm{L} = b_\mathrm{L} = 14\,\mathrm{mm}$ and $h_\mathrm{g} = 15\,\mathrm{mm}$.

the $\mathrm{SA_L}$ sub-array. Furthermore, for being able to describe the directions of radiation in the free-space, a Cartesian reference frame, having the origin $\mathcal{O}$ located at the aperture's plane and the orientation specified in the figure, is accounted for. The elevation angle is taken with respect to the $\mathcal{O}z$ axis and is denoted as ϑ while the azimuth angle, measured in the $x\mathcal{O}y$ plane with respect to the $\mathcal{O}x$ axis, is denoted as φ.

By examining Fig. 6.2, it is obvious that the deployment strategy uses the available real estate in a highly efficient manner, since the non-radiating part of the aperture is insignificant. The radiation properties of the designed shared aperture antenna are illustrated by plotting the array factor for the case when the main beam was scanned to $\vartheta = 50^\circ$ and $\varphi = 0^\circ$ (see Fig. 6.3). Note that this is just a preliminary test, carried out for ideal (isotropic) radiators and by neglecting the mutual coupling. The $-3\,\mathrm{dB}$ beamwidth is

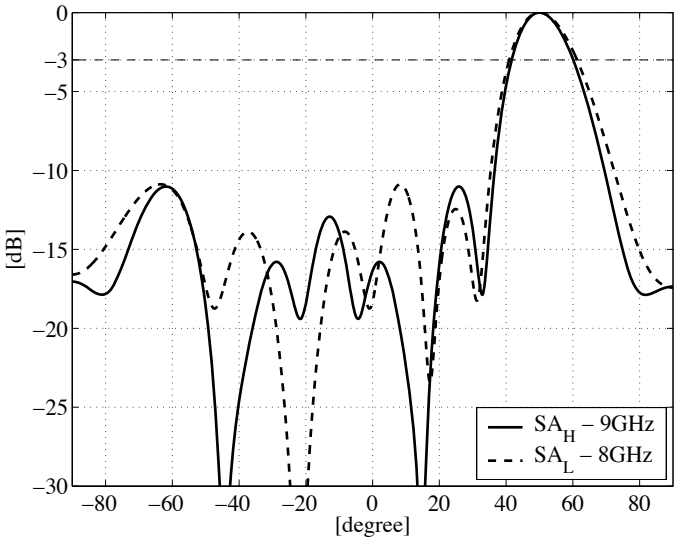

Figure 6.3: The array factor in the case of a beam-scanning at $\vartheta = 50°$ and $\varphi = 0°$. The solid line corresponds to the SA_H sub-array (at a frequency of 9 GHz) and the dashed one to the SA_L sub-array (at a frequency of 8 GHz).

narrower than 20° in the $x\mathcal{O}z$ plane. At the same time, it can be observed that the side-lobes level is below −10 dB.

Characterization of the primary radiators

After defining the array topology, the next step is the design of the elementary radiators. The radiators in each sub-array are taken to be identical. Let R_H and R_L be the elements of the sub-arrays operating at the high and the low frequencies, respectively. The topology of the generic radiator (that is representative for both R_H and R_L) is depicted in Fig. 4.7. It consists of two stacked circular patches, the lower one being fed by means of a protruding pin. The two patches are etched on a commercially available microstrip laminate (RO4003, having $\varepsilon_r = 3.38$) and are stacked together inside a metallic cavity. Both patches are centered with respect to the cavity. The thicknesses of the high-frequency laminates are identical in the case of both types of radiators, namely $h_1 = 0.508$ mm, $h_2 = 1.524$ mm and $h_3 = 0.305$ mm. The thickness of all metallic layers amounts to $h_m = 0.07$mm. Note that all dimensions were chosen in compliance with the data specifications of the employed microwave material. Furthermore, by choosing laminates of identical thicknesses for both R_H and R_L, the conditions are prepared for manufacturing the aperture antenna in a printed, stratified technology. The dimensions of the coaxial cable replicate those of a sub-miniature, type A (SMA) connector ($r_{in} = 0.64$ mm and $r_{out} = 2.05$ mm), the relative dielectric

permittivity inside it being $\varepsilon_{\mathrm{r,c}} = 1.951$. The free design parameters are the dimensions of the cavity (a and b), the radii of the two patches (r_{p1} and r_{p2}) and the offset dy_{c} of the protruding pin in the y-direction.

This structure was analyzed by means of the mode-matching technique as described in Chapter 4. The application of this method requires the knowledge of the modal distributions in all cross-sections along the transmission channel having as input port the coaxial cable and as output port the aperture. The modal representation on the coaxial segments was calculated by means of the BI-RME method while that on the rectangular waveguide segments is known analytically. The transmission channel is completed by including a load that mimics the radiation into the free-space and (possibly) that accounts for the mutual coupling between the elements in the array configuration. The full-wave technique that is employed for calculating the load's GAM will be introduced later in the coming section.

Let now N_{c} and N_{a} be the number of modes that are accounted for at the input (the coaxial cable) and output (aperture) ports of each of the 63 radiators pertaining to the shared aperture depicted in Fig. 6.2. The application of the mode-matching method finally yields a GAM for each radiator in the array, that interrelates the currents and the voltages at the above indicated ports by means of the relation

$$\begin{bmatrix} \boldsymbol{I}_{\mathrm{c}_i} \\ \boldsymbol{I}_{\mathrm{a}_i} \end{bmatrix} = \begin{bmatrix} \boldsymbol{Y}_{11_i} & \boldsymbol{Y}_{12_i} \\ \boldsymbol{Y}_{21_i} & \boldsymbol{Y}_{22_i} \end{bmatrix} \cdot \begin{bmatrix} \boldsymbol{V}_{\mathrm{c}_i} \\ \boldsymbol{V}_{\mathrm{a}_i} \end{bmatrix}, \; i = 1, \ldots, 63, \tag{6.1}$$

where:

the index i collectively identifies all the $\mathrm{R_H}$ and $\mathrm{R_L}$ radiators pertaining to the shared aperture;

$\boldsymbol{I}_{\mathrm{c}_i}$ denote the column vector of equivalent modal currents at the coaxial port i (its length being N_{c});

$\boldsymbol{I}_{\mathrm{a}_i}$ denote the column vector of equivalent modal currents at the aperture port i (its length being N_{a});

$\boldsymbol{V}_{\mathrm{c}_i}$ denote the column vector of equivalent modal voltages at the coaxial port i (its length being N_{c});

$\boldsymbol{V}_{\mathrm{a}_i}$ denote the column vector of equivalent modal voltages at the aperture port i (its length being N_{a});

$\boldsymbol{Y}_{11_i}$, $\boldsymbol{Y}_{12_i}$, $\boldsymbol{Y}_{21_i}$ and $\boldsymbol{Y}_{22_i}$ are matrices of dimensions $N_{\mathrm{c}} \times N_{\mathrm{c}}$, $N_{\mathrm{c}} \times N_{\mathrm{a}}$, $N_{\mathrm{a}} \times N_{\mathrm{c}}$ and $N_{\mathrm{a}} \times N_{\mathrm{a}}$, respectively, containing the admittances coupling the relevant equivalent modal currents and voltages.

Note that, since the elements in the $\mathrm{SA_H}$ and $\mathrm{SA_L}$ sub-arrays were taken to be respectively identical, two sets of admittance matrices of the type

indicated in (6.1) are sufficient for a complete description of the problem at hand.

In a first approximation, the transmission channel's load was taken to account for the radiation into the free-space of isolated elements, located on an infinitely extended flange. A parameter study, using as computational engine the numerical approach described above, has provided the following optimal sets of dimensions:

- for the R_H radiators: $a = b = 12\,\text{mm}$, $r_{p1} = 4.9\,\text{mm}$, $r_{p2} = 4.1\,\text{mm}$ and $dy_c = 3.8\,\text{mm}$;
- for the R_L radiators: $a = b = 14\,\text{mm}$, $r_{p1} = 5.3\,\text{mm}$, $r_{p2} = 4.6\,\text{mm}$ and $dy_c = 3.8\,\text{mm}$.

Note that the R_H radiators are identical with the B6 antenna presented in Chapter 4 and the R_L radiators are identical with the A6 model, respectively. During the design procedure, it was observed that accounting for the following sets of modes at the input and output ports suffices for ensuring the accuracy of the computed results:

- $N_c = 7$ circular coaxial waveguide modes associated with the *coaxial cable*, i.e. the fundamental TEM mode and 6 TE modes having the cut-off frequency below 100 GHz and
- $N_a = 10$ waveguide modes associated with the rectangular waveguide section that corresponds to the aperture (see Fig.4.7 (b)), i.e. TE_{10}, TE_{01}, TE_{11}, TM_{11}, TE_{20}, TE_{02}, TE_{21}, TM_{21}, TE_{12}, TM_{12}.

With these choices, the frequency behavior of the reflection coefficient was examined for both types of radiators, the results being given in Fig. 6.4.a. From that behavior, it can be derived that two bands $8 \ldots 8.4\,[\text{GHz}]$ and $8.5 \ldots 9.6\,[\text{GHz}]$ (separated by a narrow gap of 0.1 GHz) are obtained for a voltage standing wave ratio VSWR = 2. The two bands collectively yield a fractional bandwidth of approximative 17%.

The mode-matching results were also validated by means of a commercial software package (CST – Microwave Studio^{TM}), the results being in good agreement. The small differences observed are a result of the fact that, while in the mode-matching model the metallic flange at the aperture was of infinite extent, the CST model employs a finite flange of dimensions $a = b = 50\,\text{mm}$. Furthermore it is worth noting that the metallic cavity in the CST model was replaced with a series of metallic pines (vias) similar to the antenna models discussed in Section 4.4. As regards the computation times required for solving the internal problem, it is mentioned that the mode-matching analysis requires approximately 3 minutes on a Pentium 4 CPU/ 2.4 GHz equipped personal computer having 256 MB of internal memory, while the CST code needed for the same task about 2 minutes on an identical machine.

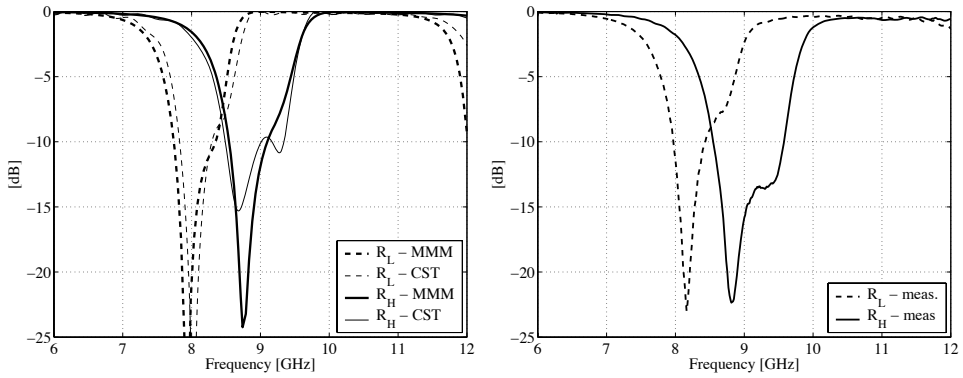

Figure 6.4: The frequency dependence of the reflection coefficient in the case of isolated elements. (a) - numerical results; (b) - measured data. Solid lines – the "type H" radiator; dashed lines – "type L" radiators. Thick lines - mode-matching analysis; thin lines – FDTD analysis.

The measured performed on the isolated models of the R_L and R_H radiators are depicted in Fig. 6.4.b. Note that the experimental isolated elements are identical with the antenna models A6 and B6 discussed in Section 4.4. It is evident from pictures included in Fig. 6.4 that the numerical results are similar to the measurements ones.

At the previous section, the radiation properties were examined for the case of ideal, uncoupled radiators. However, in an interwoven, sparse array configurations, these assumptions fail to account appropriately for the electromagnetic phenomena associated with such complex structures. The performances of the individual radiators and of the array are strongly influenced by the concrete radiation environment (neighboring elements), an assessment that was substantiated in [20].

The theoretical formalism for the analysis of the radiation from rectangular apertures and for evaluating the mutual coupling between arbitrary apertures relies on the methodology presented in Chapter 3. However, the straightforward application of that methodology in the case of large finite, sparse arrays (containing hundreds, possibly thousands of elements) is prohibitive from the point of view of the computing resources. For still ensuring the feasibility of the numerical calculations, the following observations turn out to be of key relevance:

- The GAM of an array antenna consisting of rectangular apertures includes partial GAM-s evaluated for doublets of apertures, only (the self-admittance being a particular case, in which an aperture is coupled with itself).

- For widely spaced apertures, the mutual coupling is small enough for being neglected in practical applications.

These observations allowed conceiving an effective computational strategy. It is hereafter exemplified for the case of an interwoven shared aperture antenna consisting of two differently sized apertures (the kind of which are investigated in this section).

1. Since two differently sized apertures are included in the array, three types of partial GAM-s need to be computed, only. They refer to the cases of couplings between identical elements (2 GAM-s) and of couplings between different elements (the third GAM). It is stressed that these partial GAM-s refer exclusively to doublets of apertures.

2. Due to the fact that above a certain inter-element distance the mutual coupling can be neglected, it is sufficient to compute the partial GAM-s for doublets falling within a beforehand specified area of relatively small dimensions.

3. Assuming that the elements in the shared aperture antenna are deployed on a fixed grid and by taking into account the fact that the couplings are evaluated for an area of reduced dimensions, it can be concluded that the three types of partial GAM-s need to be computed for a limited number of positions, only. These results can be precooked for a given combination of aperture dimensions and grid steps and be subsequently employed in a "table look-up" manner for evaluating the properties of any array architecture that complies to the chosen design parameters (aperture dimensions and grid steps).

This computational strategy was implemented in a Matlab® code, that has been run on a Pentium 4 CPU/ 2.4 GHz equipped personal computer having 256 MB of internal memory. In the case of the shared aperture depicted in Fig. 6.2, 663 partial GAM-s were computed for generating the necessary information required in the analysis of any 9×7 array containing any combination of elements R_H and R_L. The GAM-s were evaluated for 32 frequency points, in a range of $7, \ldots, 10$ GHz. With these settings, the computational times for filling in the GAM-s were of 98 hours in the case of the differently sized apertures and of 53 hours in the case of the couplings between identical apertures. Although these computation times may seem too large for the examined case, it is stressed that, by using the thus precalculated results, it is possible to perform the analysis of arrays of arbitrary size and architecture, as long as they use the same grid steps and aperture dimensions.

With respect to the details of the computer code implementation, it is noted that several mathematical artifices were employed for increasing the efficiency of the computations. For example, by partially solving the integrals occurring in the case of the evaluation of the self-admittances in an

analytical manner, the relevant computation time amounted to only 47 seconds. However, the bulk of the computation time was spent for estimating the couplings between different apertures. One option that could significantly increase the efficiency of these calculations is to employ the far-field approximation, as described in [99]. However, this approach fails in the case of closely packed apertures, that includes the vast majority of the situations encountered in practical antenna arrays. Another option is adopting the reduced order polynomial approximation that was originally introduced in [9] and demonstrated for the case of multi-modal analyses in [30].

Upon applying this computational strategy, the set of all equivalent modal currents and voltages at the 63 apertures in Fig. 6.2 can now be related as

$$-\begin{bmatrix} \boldsymbol{I}_{\mathrm{a}_1} \\ \boldsymbol{I}_{\mathrm{a}_2} \\ \vdots \\ \boldsymbol{I}_{\mathrm{a}_{63}} \end{bmatrix} = \mathrm{GAM}^{\mathrm{ext}} \cdot \begin{bmatrix} \boldsymbol{V}_{\mathrm{a}_1} \\ \boldsymbol{V}_{\mathrm{a}_2} \\ \vdots \\ \boldsymbol{V}_{\mathrm{a}_{63}} \end{bmatrix}, \tag{6.2}$$

in which $\mathrm{GAM}^{\mathrm{ext}}$ represents the 630×630 matrix of coupling admittances. The minus sign in (6.2) accounts for the fact that the modal currents at the aperture are taken to be directed towards the generator. Note that the fact that the partial GAM-s were evaluated for 7×7 generic cells implies that some of the entries in $\mathrm{GAM}^{\mathrm{ext}}$ are intrinsically 0 (for example, the coupling between the modal quantities pertaining to the elements 1_{L} and 6_{L}).

The aggregate problem

The final step in the numerical analysis is to integrate the internal and the external problems. Initially, the equations pertaining to the internal problem (6.1), that were written for each element, separately, are now assembled in a single matrix equation that is valid for the complete array. Furthermore, by combining this system of equations with the equations given in (6.2), one can easily find an input impedance matrix that relates the modal equivalent currents and voltages at the input port of each elementary radiator in the array configuration.

In the demonstrated example, the input impedance matrix is associated with the coaxial cables (the true input ports of the examined configuration) and incorporates the effect of the radiation into the free-space and of the mutual couplings, as well. This matrix can be, in turn, employed for computing the generalized scattering matrix of the complete structure and, hence, of the reflection coefficients pertaining to the modes at the input port.

The frequency behavior of the reflection coefficients referring to the fundamental TEM mode on the coaxial cables are depicted in Fig. 6.6 for the two sub-arrays, separately. These plots clearly illustrate the fact that the matching properties of the elementary radiators are affected when they are

placed in an array environment. The variation in the matching properties may result in the deterioration of the antenna efficiency (in the case when parts of the operational spectrum are not radiated by the elements) and, at the same time, introduces an amplitude modulation that has consequences in the radiation pattern of the shared aperture antenna. In the concrete case of the currently examined antenna, the elements 20_{L}, 27_{L}, 25_{H}, and 29_{H} (see Fig. 6.2 for their location) have a visibly narrower bandwidth while 18_{L}, 29_{L}, 8_{H} and 27_{H} have a slightly enlarged bandwidth. However, no correlation between the location in the array and the manner in which the bandwidth is affected can be derived from comparing Figs. 6.2 and 6.6.

At this point of the design strategy, the behavior of the embedded elements can be judged. In the case when the matching properties of the elementary antennas are considered satisfactory, the elements in each sub-array are kept identical. However, when the shared aperture contains elements that do not meet the bandwidth requirements, supplementary measures need to be taken. To this end, the design tool discussed in this paper includes an automatic procedure for tuning the elementary antennas individually. The method is based on a mathematical programming algorithm (conjugate-gradient) that searches for the optimum antenna dimensions (coaxial cable offset and radius of the stacked patches) that minimize the input reflection coefficient over a certain frequency range. For evaluating the input admittance at each feeding point, the radiation from the aperture is replaced by an equivalent impedance, which takes into account the coupling effect and has different values for each antenna in the shared aperture. Hence, the external problem need not being solved again. Moreover, due to the modularity of the Mode Matching method, there are but a few blocks of the internal problem that need to be re-calculated. Apart from its intrinsic computational benefits, the tuning methodology based on the changing of the offset of the feeding point and of the radius of the two patches allows for the shifting of the bandwidth of the elementary radiator over a large frequency range.

In the particular configuration under investigation, it is indicated that the results depicted in Fig. 6.6 refer to the case of sub-arrays consisting of identical elements. Since the matching properties of the resulting system were appreciated as being satisfactory, no additional individual tuning phase was carried out.

Measured results

The shared aperture antenna depicted in Fig. 6.2 was manufactured in a stratified technology similar to the one presented in Section 5.5.3. The layout of the completely assembled, shared aperture antenna is presented in Fig. 6.5. The aggregate thickness of the ensemble amounts to 2.5 mm (the SMA connectors excluded), that is consistent with the originally assumed design requirement for obtaining a low-profile architecture.

The experimental investigations were performed in the anechoic cham-

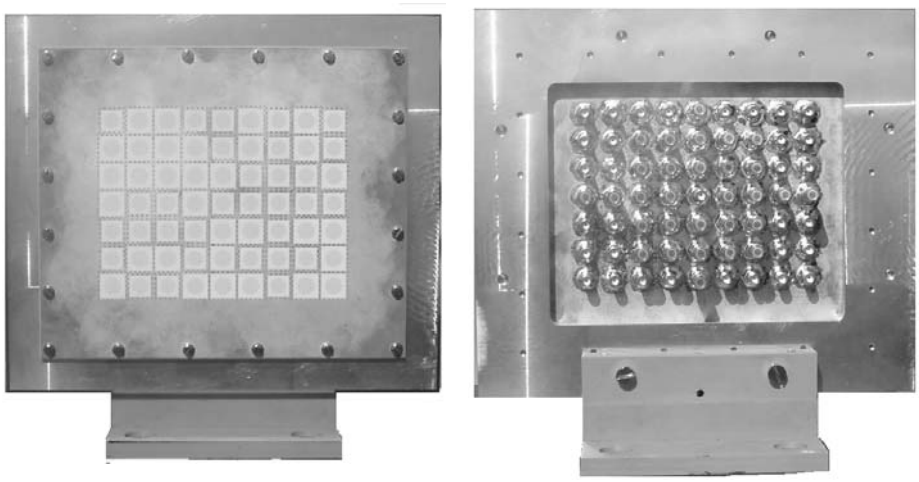

Figure 6.5: Manufactured shared aperture, sparse array antenna. (a) - front view; (b) - rear view.

ber of the IRCTR by using a vector network analyzer type HP 8510B. A first set of measurements was performed on the reflection coefficient of each elementary radiator operating in the shared aperture configuration. The results are presented in Fig. 6.6 distinctly for each of the sub-arrays, SA_H and SA_L. By tacking into account the differences between the physical and the theoretical antenna models it is worth observing that the measurements are in a fair agreement with the simulations presented in the same figure. The measured bandwidth of the SA_H sub-array (approximative 10% at VSWR=2) is twice as large as that of the simulated model, this behavior been consistent with that of the isolated elements presented in Fig. 6.4. A good agreement between the measurements and the simulations was noted in case of the SA_L sub-array, which exhibits a bandwidth of 7% at VSWR=2. From the measurements it was found that the manufactured shared aperture antenna exhibits a total bandwidth of 17% at VSWR=2, which demonstrated that wide band antennas can be obtained by using moderate band radiators arranged in interleaved, sparse configurations.

The radiation characteristics of the sparse array antenna were evaluated by measuring the individual patterns of the elementary radiators. The elementary patterns of the antennas in the SA_H sub-array were measured in the $x\mathcal{O}z$ plane at the frequency of 9 GHz while those of the antennas in the SA_L sub-array were measured in the same $x\mathcal{O}z$ plane at the frequency of 8.2 GHz. The measurement and the full wave, MMM simulations, of the elementary patterns are presented in Fig. 6.7 with thin, dashed lines. From this figure it is observed that the individual patterns exhibit variations with

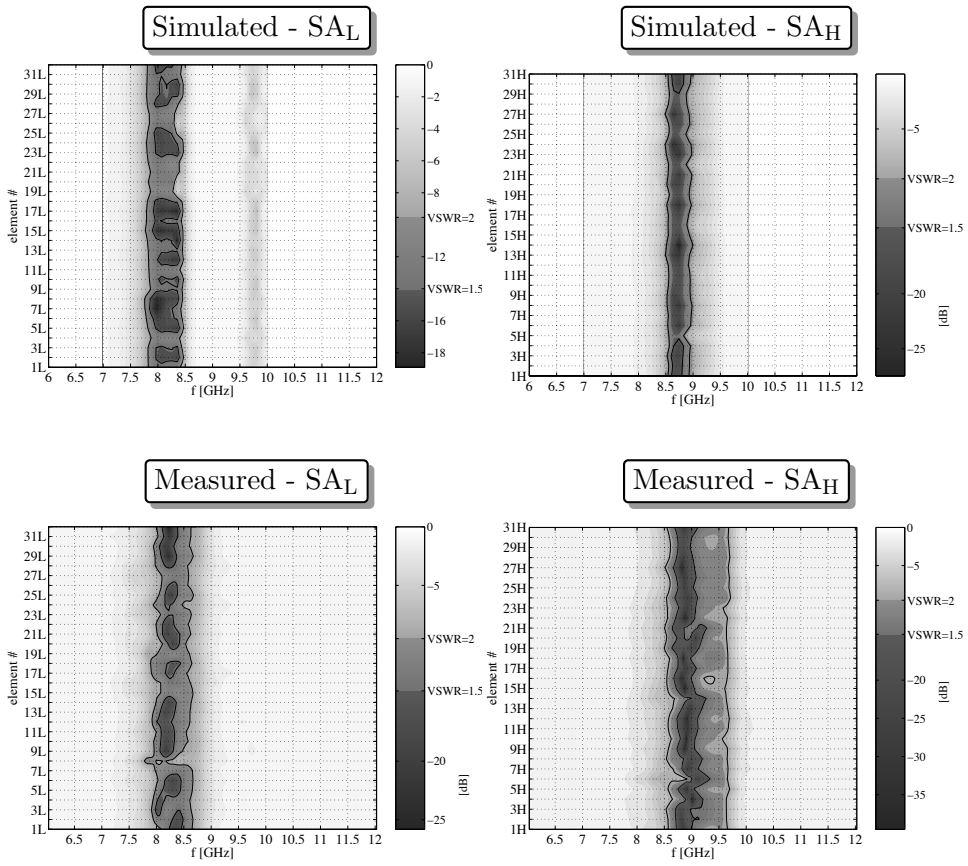

Figure 6.6: Simulated and measured frequency behavior of the input reflection coefficient of the elementary antennas in the shared aperture configuration. The solid contours indicate the levels corresponding to VSWR=2 and VSWR=1.5, respectively.

respect to each other over approximately 5 dB. Despite of these dissimilarities, the radiation patterns of the sparse sub-array antennas calculated from the measured data (thick line in Fig. 6.7) have a narrow beamwidth and low side lobes. More specifically, the sub-array SA_L exhibits a beamwidth of about 14° (measured at −3 dB from the maximum) and the side lobes are below −12 dB, whereas the SA_H sub-arrays has a beamwidth of 13° and the maximum side lobe level is below −11 dB. From the comparison of the measurement and simulated results (see Fig. 6.7) it is evident that they are in good agreement.

To further substantiate the validity of the numerical analysis, the measured and the simulated radiation patterns of the sparse sub-arrays were plotted in Fig. 6.8 for different scanning angles. Note that the measured

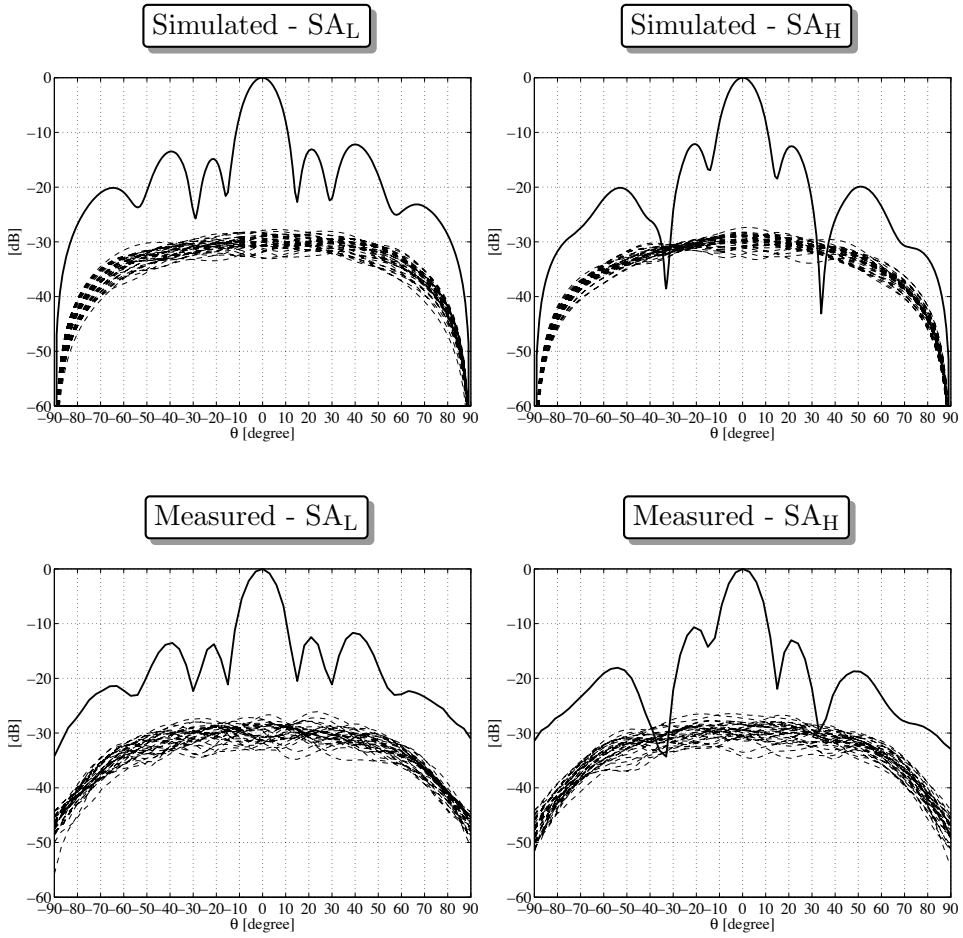

Figure 6.7: Radiation patterns of the elementary antennas in the shared aperture array antenna (dashed lines) and the radiation patterns of the sparse sub-array. The patterns of the elements in the SA_L are evaluated at 8.2 GHz and these of the elements in SA_H are evaluated at 9 GHz.

data were post-processed in order to steer the main beam at a specific angle.

6.3 Conclusions and discussions

Some strategies for the design of finite array antennas consisting of differently sized radiating elements arranged in sparse configurations were presented. In particular, by resorting to a shared aperture array architecture, an increased bandwidth, which is instrumental for implementing multifunctional-

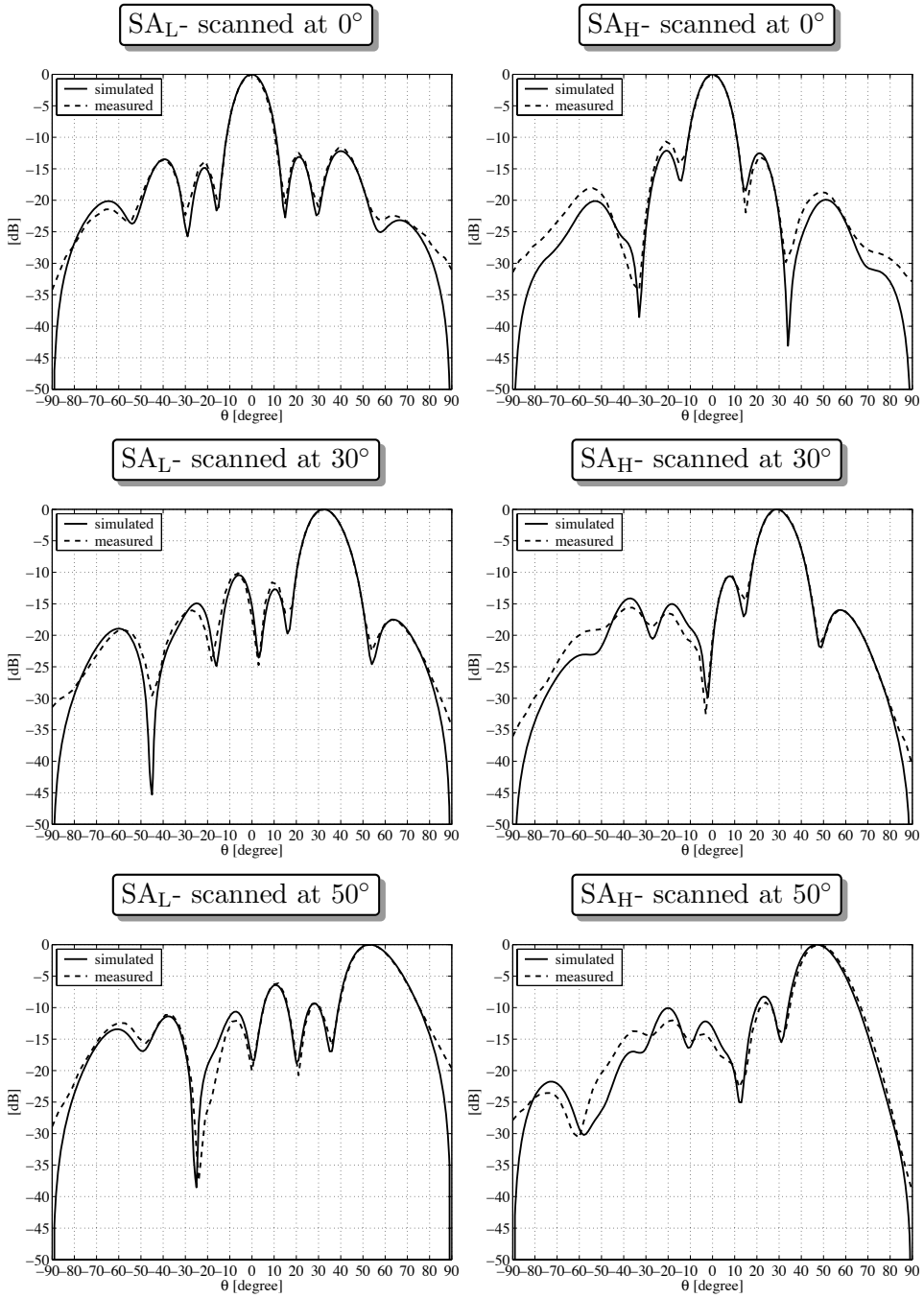

Figure 6.8: Measured and simulated radiation patterns of the sparse subarrays in the shared aperture antenna. The patterns of the SA_L are evaluated at 8.2 GHz and these of the SA_H are evaluated at 9 GHz

ity in antenna systems, was obtained. An effective computational formalism, incorporating a full-wave analysis of the individual radiators in conjunction with a full-wave investigation of the phenomena related to the radiation from finite, non-periodic arrays, was described. The formalism allows for an accurate analysis of the complete transmission channel, starting from the feeding coaxial cable, that is commonly the true input port of antennas. At the same time, the advocated numerical strategy enables a full-wave analysis of large, non-periodic array antennas containing differently sized elements, while maintaining computational feasibility. Measurements were performed on an experimental shared aperture, sparse array antenna. The experimental results and the numerical ones obtained by different full wave analysis are in a good agreement.

The design strategy that incorporates the numerical electromagnetic analysis of the radiation phenomena lends itself to several extensions. Firstly, it is observed that, once the external problem was addressed and the $\mathrm{GAM}^{\mathrm{ext}}$ matrix was stored, the individual radiators can be designed without requiring the (highly time consuming) evaluation of the radiation part. Furthermore, the complete analysis of elementary antennas is computationally very efficient. Corroborating these two features, it becomes realistic to devise an automatic tuning procedure, using the geometrical parameters of the internal problem as variables subject to optimization. Secondly, the "table look-up" procedure that was employed for solving the external problem opens the possibilities to examine array antennas having a large number of elements in configurations combining elements of various sizes. In a multifunctional array, this provides the possibility to a priori estimate the interaction between the systems sharing the antenna resources.

Elements of novelty

A new solution for conceiving shared aperture array antennas was proposed. The method is based on the concept of interleaving sparse sub-arrays consisting of elementary radiators operating at different frequency ranges.

Two interleaving procedures, namely, the complementary solution and the multi grid approach were proposed.

The concept was demonstrated by experimental measurements on a shared aperture array antenna designed by means of combinatorial theory.

Chapter 7

General conclusions and discussion

In this dissertation it was demonstrated that it is possible to increase the total bandwidth of an array antenna by interleaving sparse configurations. It was also found that the resulted shared aperture antenna is characterized by an intrinsic multi-functionality. Other positive aspects of this new concept are hereafter indicated: the beamwidth of the radiation patterns associated to each sub-array are related to the size of the entire aperture; the distribution of the energy in the side lobe region is controlled by changing the positions of the elementary radiators (without resorting to the amplitude tapering); by interleaving sparse configurations, the scanning properties are not affected; the mutual coupling effect does not influence in a similar manner all the primary radiators, this improving the wide angle impedance matching properties of the antenna.

The theoretical and experimental investigation of shared aperture antennas consisting of interleaved sparse sub-arrays revealed some limitations as well. It is firstly noted that such a shared aperture configuration exhibits a reduced flexibility in controlling the beamwidth and the side lobe region of antenna due to the fact that sparse configurations can only approximate slow variations of the current on the aperture. Secondly, it was found that the deployment of the elementary antennas, especially when differently sized elements have to be interwoven, requires a hard optimization problem to be solved. Consequently, the design of optimum shared apertures, consisting of interleaved sparse sub-arrays will be restricted to small and medium size configurations (tens, hundreds of elements). Finally it is pointed out that in sparse array antenna it is not possible to characterize the elementary radiators by using a generic element and the numerical electromagnetic investigation has to be performed on the full configuration.

For demonstrating the advantages and the limitations of this new con-

cept a systematic approach was adopted. From the beginning, two main research directions were identified. Attentions was given to the design of elementary antennas operating in an arbitrary array environment and to the conceiving of array topologies when differently sized radiators are sharing a common aperture. Subsequentially, in the analysis of the elementary radiators three distinctive aspects where accounted for. These were the radiating part, the matching structure and the feeding circuit related to the elementary radiator. The study of array architectures focussed on the evaluation of the mutual coupling between elementary antennas, the design of sparse array topologies and the investigation of shared aperture arrays.

For being able to investigate all these features of the shared aperture, sparse array antennas a full wave analysis methodology, based on the Mode Matching Method (MMM), was formulated and implemented in numerical routines. It is noted that the numerical analysis and the design of the manufactured antenna and arrays presented in this thesis were mainly done by making use of these MMM software routines.

The theoretical and numerical implementation of the electromagnetic analysis of the antenna's segments comprised between the feeding line and the radiating aperture were presented in the Chapter 2. In that chapter a special attention was given to the problem of computing the modes of uniform waveguide segments with arbitrary cross-section by means of the Boundary Integral - Resonant Mode Expansion (BI-RME). Numerous mathematical aspect related to the calculation of the BI-RME modes were presented. The problem of selecting the modes in the BI-RME method was extended and an analytical solution was proposed for the optimum rotation angle that should be used in the case of processing quasi-degenerate modes. It was also demonstrated that the BI-RME modes are quasi-orthogonal and the orthogonality of these modes can be improved by increasing the numbers of canonical modes used in the series representation of the Green's function. The software implementations of the MMM / BI-RME analysis was accurately investigated by solving a large number of test problems. From these numerical tests it is concluded that the modal techniques are the most appropriated full wave methods for the analysis of waveguide structures. These methods offer a high and controllable accuracy without requiring expensive computational resources. The modal techniques are also characterized by fast computation times, the performances of the software implementations presented in that section being comparable with those of commercial packages.

The analysis of the radiation of the electromagnetic waves from apertures arranged in arbitrary array configurations was done by means of a Mode Matching Method, as well. Two variants of this technique, namely, the Fourier approach and the solution based on the Green's function were presented in Chapter 3. These methods were implemented in software tools which were subsequentially validated by studying different test configurations and observing specific aspects related to the electromagnetic field and to the scattering parameters of the aperture antennas. By evaluating the

field distribution on a rectangular aperture, the singular behavior of some field components in the vicinity of the aperture's edges was clearly demonstrated. The accuracy of the electromagnetic solution was tested by studying the continuity of all the field components at the aperture level. Furthermore, the capabilities of the software implementations were demonstrated by calculating the self admittance of a waveguide antenna and by evaluating the mutual coupling between differently sized apertures. These results were validated against results published in the literature and results obtained with commercial software packages. In array antennas consisting of a large number of elements, the evaluation of the mutual coupling effect and, consequently, the behavior of individual radiators requires very long (often prohibitive) computation times. To sidestep this hard limitation in the design of sparse array antennas when the coupling effect is also accounted for, a solution for fast evaluation of the mutual coupling effect was proposed. This fast technique is based on a polynomial interpolation of the coupling admittances between the modes used to represent the field on the aperture antennas.

Commonly, the design of elementary antennas is done either under the assumption that they operate as isolated elements or by investigating the properties of a generic model operating in periodic, infinitely extended conditions. It is noticed that none of these hypothesis are applicable in the study of elementary antennas functioning in finite, sparse array architectures. Consequently, the study of elementary radiators in sparse configurations should be performed element by element. In this sense, the design of primary radiators has to be done in an efficient manner since in many practical applications it is necessary to use a large number of elements. Chapter 4 was dedicated to the numerical analysis and the design of elementary antennas to be used in sparse and shared aperture array configurations. A number of time efficient design procedures have been presented in connection with two antenna topologies: the dielectric filled waveguide antennas with an air gap matching circuit and the cavity-backed, stacked-patch and probe fed antennas. In relation to the cavity-backed, stacked-patch antennas, it is noted that the systematical design methodology adopted in this work has provided antenna models with bandwidths of around 10%. These results are superior to the ones reported by other authors in the literature for similar antenna models. The numerical simulations were validated by comparisons with measurements performed on physical models. Technological aspects have been meticulously investigated and some practical solutions were proposed in the context of simplifying the manufacturing process and reducing the fabrication cost.

In Chapter 5 a general formulation, in terms of a constrained optimization problem, was proposed for addressing the design of sparse array antennas. This formulation provides an adequate handle for understanding the large variety of specific methods devoted to this topic that are readily available in the literature. A number of numerical and experimental examples were also presented in this section. The experimental and numerical investi-

gations concentrated on two relevant aspects, namely, the estimation of the matching properties of the individual radiators functioning in non-periodic, finite array environments, and the evaluation of the radiation properties of the sparse array antenna, while also accounting for the effect of the mutual coupling. It was demonstrated that synthetic aperture radar imagines can be obtained by using sparse measurements, this reducing significantly the acquisition and the computing times. Another important finding was that the mutual coupling is not correlated in sparse array configurations and, therefore, the coupling effect has a reduced influence (when compared to uniform arrays) on the performances of individual radiators, while electronically scanning the antenna beam. This observation can be used in designing array antennas characterized by wide angle impedance matching (WAIM) properties. Despite the fact that, often, thinned array antennas exhibit beamwidths which are similar to those of the full configurations having a larger number of elements, it is indicated to compare the performances (gain, sidelobe level, etc.) of the sparse configurations with those of the uniform configurations having the same number of elements and, possibly, different amplitudes.

Chapter 6 was dedicated to the problem of interleaving sparse configurations and to the full wave and experimental investigations of shared aperture antennas. Three techniques have been proposed for solving the problem of interleaving sparse configurations. When compared to uniform and amplitude tapered array antennas, the sparse configurations offer the advantage of using elementary radiators having identical amplitudes at the cost of increasing the physical size of the array. The empty space remaining in sparse configurations can be interpreted as a non-efficient use of the aperture, this aspect being at the origin of the limited utilization of the sparse array concept in applications where the size limitations are highly relevant. By using the empty space in a sparse configuration to accommodate elements pertaining to a different sparse array antenna, the efficiency of the use of the aperture is increased and the resulted shared aperture can be deployed on platforms where the size requirement and the multi functionality are essential. The concept was experimentally demonstrated by manufacturing and measuring a shared aperture antenna consisting of two interleaved sub-arrays. One of these sub-arrays operates in the frequency range from 8 GHz to 8.5 GHz (relative bandwidth of 7%) and the other one is properly matched to the feeding line in the band from 8.5 GHz to 9.5 GHz (relative bandwidth of 10%), the total bandwidth of the shared aperture being around 17%. The measured radiation patterns of the shared aperture antenna were in a good agreement with these calculated by making use of the full wave MMM software routines presented in this thesis.

New directions to be explored

The relevant features of multifunction, wide band, shared aperture antennas consisting of interleaved sparse configurations were presented in this thesis.

During the research stage a number of new problems, which require further investigations, have been identified. These are related to the full wave analysis of elementary radiators operating in finite, non-uniform arrays and to the study of the capabilities and the limitations of sparse array antennas. A list of new directions to be investigated is hereafter included:

- increasing the accuracy of the numerical simulations while also maintaining fast computation times, by combining different numerical electromagnetic techniques;
- extension of the fast approximation technique proposed in Chapter 3 Section 3.4 to the case of planar array configurations;
- investigation of the fundamental limitations of the sparse array antennas with respect to the minimum sidelobe level that can be achieved with a given number of elements, a given aperture size and a fixed beamwidth;
- examination of the sparse array capabilities in relation to specific application requirements (for example spatial diversity or monopulse processing);
- experimental investigation of the wide angle impedance matching features in sparse array antennas;
- analysis of the possibilities to design sparse array antennas which exhibit a particular radiation pattern (sparse techniques for beam shaping problems);
- study of conformal, sparse array antennas;
- study of the possibilities to transmit a wide band signal with a shared aperture antenna composed of moderate band radiators. In particular attention should be given to the beam forming network that must divide the signal spectrum in sub-bands to be transmitted by different sub-arrays. Moreover, the effect of the position of the sub-arrays phase centers on the transmitted, wide band signal should be examined in detail.

In the end it is pointed out that since this Ph.D. work was not related to a specific application there are a number of system aspects of this new shared aperture concept that should also be taken into account.

Appendices

Appendix A

Quasi-static 2-D Green's function for rectangular domains

The Green's functions g and G_{st} introduced in the Section 2.2.1 can be expressed using eigenfunction expansions or rapidly converging series. The geometry of the rectangular domain is depicted in Fig. A.1. Note that the

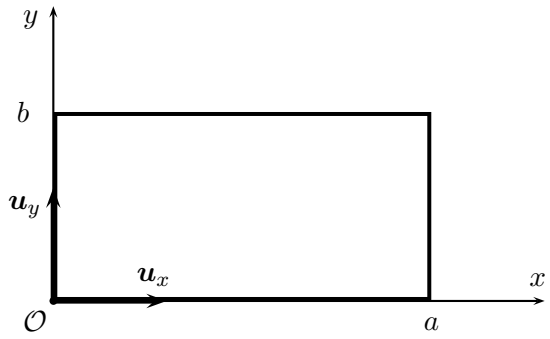

Figure A.1: Geometry of the rectangular domain considered in the definition of the Green's functions.

origin of the coordinate frame coincides with the bottom-left corner of the rectangular waveguide and that the width a is greater than the height b.

A.1 Eigenfunction expansions

The eigenfunctions and the eigenvectors of a rectangular domain can be used [36, p. 325] to express the scalar and the dyadic Green's functions introduced in Section 2.2.1

$$g(\boldsymbol{s},\boldsymbol{s}') = \sum_{i=1}^{\infty} \frac{\psi_i^{TM}(\boldsymbol{s})\psi_i^{TM}(\boldsymbol{s}')}{{k_i'}^2}, \tag{A.1}$$

$$\overline{\boldsymbol{G}}_{st}(\boldsymbol{s},\boldsymbol{s}') = \sum_{i=1}^{\infty} \frac{\boldsymbol{e}_i^{TE}(\boldsymbol{s})\boldsymbol{e}_i^{TE}(\boldsymbol{s}')}{k_i^2}. \tag{A.2}$$

Another Green's function that is useful in the representation of the field quantities (Section 2.2.5) is given by

$$F_0(\boldsymbol{s},\boldsymbol{s}') = \sum_{i=1}^{\infty} \frac{\phi_i^{TE}(\boldsymbol{s})\phi_i^{TE}(\boldsymbol{s}')}{{k_i}^2}. \tag{A.3}$$

The eigenfunctions of the TM modes ψ_i^{TM} and the eigenfunctions ϕ_i^{TE} and eigenvectors $\boldsymbol{e}_i^{TE}$ of the TE modes introduced in (A.1), (A.1) and (A.3) have the expressions

$$\psi_{mn}^{TM}(x,y) = \frac{2}{\sqrt{ab}} \sin\frac{m\pi x}{a} \sin\frac{n\pi y}{b}, \tag{A.4}$$

$$\text{with} \quad m = 1,2,\cdots;\ n = 1,2,\cdots;$$

$$\phi_{mn}^{TE}(x,y) = A_{mn} \cos\frac{m\pi x}{a} \cos\frac{n\pi y}{b}, \tag{A.5}$$

$$\begin{aligned} \boldsymbol{e}_{mn}^{TE}(x,y) &= -A_{mn}\frac{n\pi}{b} \cos\frac{m\pi x}{a} \sin\frac{n\pi y}{b}\boldsymbol{u}_x \\ &\quad + A_{mn}\frac{m\pi}{a} \sin\frac{m\pi x}{a} \cos\frac{n\pi y}{b}\boldsymbol{u}_y, \end{aligned} \tag{A.6}$$

$$\begin{aligned} &\text{with} \quad m = 0,1,2,\cdots;\ n = 0,1,2,\cdots;\ m = n \neq 0, \\ &\qquad A_{mn} = \sqrt{\frac{\epsilon_m\epsilon_n}{ab}}\frac{1}{k_{mn}}; \quad \epsilon_j = \begin{cases} 1 & j = 0 \\ 2 & j \neq 0 \end{cases}, \\ &\text{and} \quad k_{mn} = k'_{mn} = \sqrt{\left(\frac{m\pi}{a}\right)^2 + \left(\frac{n\pi}{b}\right)^2}. \end{aligned}$$

In writing the expressions (A.4), (A.5) and (A.6) the position vector $\boldsymbol{s}$ was replaced with its Cartesian coordinates (x,y) and the index i substituted with the pair m,n.

A.2 Rapidly converging series

The key aspect of the BiRME method resides on the use of some fast converging series to represent the Green's functions g and $\overline{\boldsymbol{G}}_{st}$. These series are given by one-index infinite summations [35]

$$g(x,y,x',y') = \frac{1}{4\pi}\sum_{m=-\infty}^{\infty}(-1)^m \ln\frac{T_m - D}{T_m - B}, \tag{A.7}$$

$$\begin{aligned}
\overline{\boldsymbol{G}}_{st}(x,y,x',y') \;=\; & \frac{\boldsymbol{u}_x\boldsymbol{u}_x}{4\pi}\sum_{m=-\infty}^{\infty}\left[\frac{1}{2}\ln\frac{T_m - D}{T_m - B} + \frac{IMX_mS_m}{(T_m - B)(T_m - D)}\right] \\
& -\frac{\boldsymbol{u}_x\boldsymbol{u}_y}{4\pi}\sum_{m=-\infty}^{\infty}\frac{GY_m(V_mF - H)}{(V_m - A)(V_m - C)} \\
& -\frac{\boldsymbol{u}_y\boldsymbol{u}_x}{4\pi}\sum_{m=-\infty}^{\infty}\frac{MX_m(T_mL - N)}{(T_m - B)(T_m - D)} \\
& +\frac{\boldsymbol{u}_y\boldsymbol{u}_y}{4\pi}\sum_{m=-\infty}^{\infty}\left[\frac{1}{2}\ln\frac{V_m - C}{V_m - A} + \frac{EGY_mU_m}{(V_m - A)(V_m - C)}\right],
\end{aligned} \tag{A.8}$$

with

$$\begin{aligned}
A &= \cos\left[\pi(x - x')/a\right], \\
B &= \cos\left[\pi(y - y')/b\right], \\
C &= \cos\left[\pi(x + x')/a\right], \\
D &= \cos\left[\pi(y + y')/b\right], \\
E &= \sin(\pi x/a), \\
F &= \cos(\pi x/a), \\
G &= \sin(\pi x'/a), \\
H &= \cos(\pi x'/a), \\
I &= \sin(\pi y/b), \\
L &= \cos(\pi y/b), \\
M &= \sin(\pi y'/b), \\
N &= \cos(\pi y'/b),
\end{aligned}$$

$$
\begin{aligned}
x_m &= (m+1/2)a + (-1)^m(x' - a/2),\\
y_m &= (m+1/2)b + (-1)^m(y' - b/2),\\
X_m &= \pi(x - x_m)/b,\\
Y_m &= \pi(y - y_m)/a,\\
S_m &= \sinh(X_m),\\
T_m &= \cosh(X_m),\\
U_m &= \sinh(Y_m),\\
V_m &= \cosh(Y_m).
\end{aligned}
$$

The F_0 Green's function can also be represented as an infinite series

$$
\begin{aligned}
F_0(x,y,x',y') &= \frac{a}{12b} + \frac{x^2+y^2}{2ab} - \frac{|x-x'|}{2b}\\
&\quad -\frac{1}{4\pi}\sum_{m=-\infty}^{\infty}(-1)^m \ln\frac{4(T_m - D)(T_m - B)}{e^{2|X_m|}}. \quad \text{(A.9)}
\end{aligned}
$$

An equivalent formula for g was given in [25]

$$
g(\boldsymbol{s},\boldsymbol{s}') = \frac{1}{4\pi}\sum_{m=-\infty}^{\infty}\ln\frac{T_m^{10}T_m^{01}}{T_m^{00}T_m^{11}}, \quad \text{(A.10)}
$$

where

$$
T_m^{p,q} = 1 - 2e^{\tau_{mp}}\cos\frac{\pi}{b}(y - (-1)^q y') + e^{2\tau_{mp}}, \quad \text{(A.11)}
$$

$$
\tau_{mp} = -|x - (-1)^p x' + 2am|\frac{\pi}{b}. \quad \text{(A.12)}
$$

The singularities in (A.7) (A.8) and (A.10) are exhibited by the terms corresponding to $m = 0$. These terms have a behavior of $\lim_{\xi\downarrow 0}\ln(\xi)$ when the observation point approaches the source point.

A.3 Order of the singularity in the scalar Green's function

The T_0^{00} term in the definition of the scalar Green's function (A.10) introduces a singularity when the field point (x, y) coincides with the source point (x', y'). In order to solve this problem it is useful to determine the order of the singularity. This can be done by analyzing the Taylor series of the T_0^{00}

when $x \to x'$ and $y \to y'$. The expression of the T_0^{00} term for a fix source point (x', y') reads

$$T_0^{00}(x,y) = 1 - 2e^{-\frac{\pi}{b}|x-x'|}\cos\frac{\pi}{b}(y-y') + e^{-\frac{2\pi}{b}|x-x'|}. \tag{A.13}$$

The Taylor representation of (A.13) in the vicinity of the point (x', y') is of the following form

$$\begin{aligned} T_0^{00}(x,y) &= T_0^{00}(x',y') + \frac{1}{1!}\frac{\partial}{\partial x}T_0^{00}\Big|_{\substack{x=x'\\y=y'}}(x-x') + \frac{1}{1!}\frac{\partial}{\partial y}T_0^{00}\Big|_{\substack{x=x'\\y=y'}}(y-y') \\ &+\frac{1}{2!}\frac{\partial^2}{\partial x^2}T_0^{00}\Big|_{\substack{x=x'\\y=y'}}(x-x')^2 + \frac{1}{2!}\frac{\partial^2}{\partial y^2}T_0^{00}\Big|_{\substack{x=x'\\y=y'}}(y-y')^2 \\ &+\frac{1}{2!}\frac{\partial^2}{\partial x\partial y}T_0^{00}\Big|_{\substack{x=x'\\y=y'}}(x-x')(y-y') + \cdots . \end{aligned} \tag{A.14}$$

Further, the values of the T_0^{00} and its derivatives have to be evaluated for $x = x'$ and $y = y'$

$$T_0^{00}(x',y') = 0, \tag{A.15}$$

$$\frac{\partial}{\partial x}T_0^{00}\Big|_{\substack{x=x'\\y=y'}} = \frac{2\pi}{b}e^{-\frac{\pi}{b}|x-x'|}\left[\cos\frac{\pi}{b}(y-y') - e^{-\frac{\pi}{b}(x-x')}\right]\Big|_{\substack{x=x'\\y=y'}} = 0, \tag{A.16}$$

$$\frac{\partial}{\partial y}T_0^{00}\Big|_{\substack{x=x'\\y=y'}} = \frac{2\pi}{b}e^{-\frac{\pi}{b}|x-x'|}\sin\frac{\pi}{b}(y-y')\Big|_{\substack{x=x'\\y=y'}} = 0, \tag{A.17}$$

$$\begin{aligned} \frac{\partial^2}{\partial x^2}T_0^{00}\Big|_{\substack{x=x'\\y=y'}} &= \frac{2\pi^2}{b^2}e^{-\frac{\pi}{b}|x-x'|}\left[-\cos\frac{\pi}{b}(y-y') + 2e^{-\frac{\pi}{b}(x-x')}\right]\Big|_{\substack{x=x'\\y=y'}} \\ &= \frac{2\pi^2}{b^2}, \end{aligned} \tag{A.18}$$

$$\frac{\partial^2}{\partial y^2}T_0^{00}\Big|_{\substack{x=x'\\y=y'}} = \frac{2\pi^2}{b^2}e^{-\frac{\pi}{b}|x-x'|}\cos\frac{\pi}{b}(y-y')\Big|_{\substack{x=x'\\y=y'}} = \frac{2\pi^2}{b^2}, \tag{A.19}$$

$$\frac{\partial^2}{\partial x\partial y}T_0^{00}\Big|_{\substack{x=x'\\y=y'}} = -\frac{2\pi^2}{b^2}e^{-\frac{\pi}{b}|x-x'|}\sin\frac{\pi}{b}(y-y')\Big|_{\substack{x=x'\\y=y'}} = 0. \tag{A.20}$$

$$\tag{A.21}$$

By considering in (A.14) the terms up to the third order the approximation of the T_0^{00} about the point (x', y') yields

$$T_0^{00}(x,y,x'y') \approx \frac{\pi^2}{b^2}\left[(x-x')^2 + (y-y')^2\right]. \tag{A.22}$$

Observing that the distance between two points in the Cartesian frame is given by $R = \sqrt{(x-x')^2 + (y-y')^2}$, it can be concluded from (A.10) and (A.22) that the singularity of the scalar Green's function is of $\ln R$ type.

Appendix B

Base functions and matrix calculation in BI-RME

In Chapter 2 it was indicated that for the calculation of the waveguide modes, by means of the BI-RME method, it is necessary to solve some improper integrals. A straightforward solution to this problem is to split the integrals into two parts: a regular component that can be easily integrated numerically and a singular part that can be solved analytically.

In this appendix some indications on the procedure adopted for solving the singular integrals are given. The notations adopted here are similar to those introduced in Section 2.2.

B.1 Base functions

Commonly, uniform B-spline blending functions are used for the representation of the current density on σ. The order of these curves and the specific sequence should be selected in accordance to the type of the mode (TE, TM, or TEM) and the topology of σ. A detailed discussion on this subject is presented in [36, p. 136].

In this work, piecewise parabolic base functions are used in the evaluation of TE, TM and TEM modes. The choice was motivated by the facile computer implementation and the particular geometry to be analyzed. A small inconvenience of employing this type of functions can appear in the evaluation of the TE modes when the eigenproblem (2.68) admits some zero eigenvalues. However, by recalling the fact that the number of the spurious solutions equals the number of the internal closed curves, one can easily circumvent this problem.

Making use of these functions within the BI-RME method requires their

parametric representation in accordance to the definition of the contour σ. It seems, from a paper published in 2003 [25], that most of the implementations of this method have used an approximation of the σ with straight segments. In the case when σ has parts described by analytical expressions, it is sensible to define the base function using this mathematical representation of the contour.

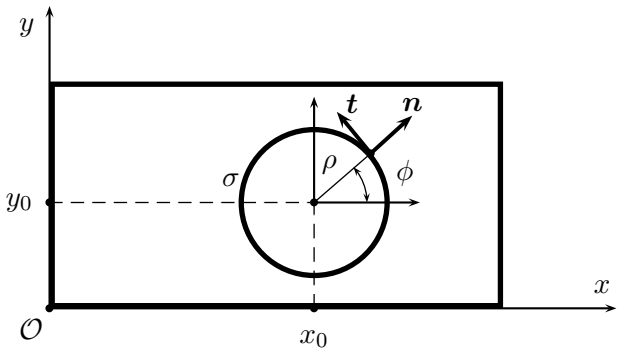

Figure B.1: Geometry of the rectangular waveguide perturbed by a cylindric conductor.

Referring to the case of rectangular waveguides perturbed by circular curves (Fig. B.1) it is appropriate to define the base functions in polar coordinates [36, p. 322]

$$w_i(\phi) = \begin{cases} \frac{2}{3\Delta^2}(\phi - \phi_i)^2 & \phi_i \le \phi \le \phi_i + \Delta \\ -\frac{4}{3\Delta^2}(\phi - \phi_i - \frac{3\Delta}{2})^2 + 1 & \phi_i + \Delta \le \phi \le \phi_i + 2\Delta \\ \frac{2}{3\Delta^2}(\phi - \phi_i - 3\Delta)^2 & \phi_i + 2\Delta \le \phi \le \phi_i + 3\Delta \end{cases} , \qquad \text{(B.1)}$$

where Δ denotes the angle corresponding to a segment of σ and ϕ_i is the lower limit of the i^{th} angular interval. In (B.1) the angular information was used only. Note that the angle ϕ corresponds to a certain point on the curve σ and that this point has the coordinates in the Cartesian frame attached to the waveguide given by

$$\begin{cases} x &= x_0 + \rho\cos\phi \\ y &= y_0 + \rho\sin\phi \end{cases} , \qquad \text{(B.2)}$$

where (x_0, y_0) are the coordinates of the center of the circular domain and ρ is the radius of the circle.

B.2 Matrix calculation

The practical implementation of the BI-RME method requires the numerical evaluation of the entries in the eigenproblems (2.68) and (2.74). This should be done with attention since it requires the numerical integration of some singular integrals. The remaining part of this section is dedicated to the presentation of the solutions that have been adopted for solving these quadratures.

Elements of the C matrix

The elements of the $\boldsymbol{C}$ matrix are obtained by integrating an expression that involves the scalar Green's function g and the first derivative of the base function w_i.

$$C_{ij} = \int_\sigma \int_\sigma g(\boldsymbol{s}, \boldsymbol{s}') \frac{\partial w_i(l)}{\partial l} \frac{\partial w_j(l')}{\partial l'} \, dl dl'. \tag{B.3}$$

The two dimensional Green's function for the rectangular domain O can be expressed using the rapidly converging series [25]

$$g(\boldsymbol{s}, \boldsymbol{s}') = \frac{1}{4\pi} \sum_{m=-\infty}^{\infty} \ln \frac{T_m^{10} T_m^{01}}{T_m^{00} T_m^{11}}, \tag{B.4}$$

where:

$$T_m^{p,q} = 1 - 2e^{\tau_{mp}} \cos \frac{\pi}{b}(y - (-1)^q y') + e^{2\tau_{mp}}, \tag{B.5}$$

$$\tau_{mp} = -|x - (-1)^p x' + 2am| \frac{\pi}{b}. \tag{B.6}$$

The generic points $\boldsymbol{s}$ and $\boldsymbol{s}'$ are substituted in (B.5) and (B.6) with their Cartesian coordinates (x, y) and (x', y'), respectively. The singularity of g is introduced by the $\ln\left(T_0^{00}\right)$ when the observation point (x, y) approaches the source point (x', y'). Dealing with singular integrals is a well known problem in the implementation of electromagnetic analysis methods based on the integral equations. For solving such quadratures there are some specific techniques [116], which appear to be more appropriated in the case of expressions involving Green's functions.

In this work, the method of subtracting the singularity [25] has been adopted in solving the integrals similar to (B.3). A first step of this technique is to determine the order of the singularity. In this respect, the T_0^{00} term is expanded as a Taylor series (see Appendix A.3) and is observed that it goes to zero like R^2 (with $R^2 = (x - x')^2 + (y - y')^2$). Further, the Green's function is arranged such that the order of the singularity is clearly indicated

$$g(\boldsymbol{s}, \boldsymbol{s}') = g1(\boldsymbol{s}, \boldsymbol{s}') - \frac{1}{4\pi} \ln R^2, \tag{B.7}$$

where:

$$g1(\boldsymbol{s},\boldsymbol{s}') = \frac{1}{4\pi}\sum_{\substack{m=-\infty\\ m\neq 0}}^{\infty} \ln\frac{T_m^{10}T_m^{01}}{T_m^{00}T_m^{11}} + \frac{1}{4\pi}\ln\frac{T_0^{10}T_0^{01}}{T_0^{11}} - \frac{1}{4\pi}\ln\frac{T_0^{00}}{R^2}. \tag{B.8}$$

is a regular term that can be easily integrated using, for example, a Gauss quadrature formula. By recalling the Taylor expansion of the T_0^{00} presented in Appendix A.3, the term $\ln\left(\frac{T_0^{00}}{R^2}\right)$ when $x \to x'$ and $y \to y'$ gives

$$\lim_{\substack{x\to x'\\ y\to y'}} \ln\frac{T_0^{00}}{R^2} = \ln\left(\frac{\pi}{b}\right)^2. \tag{B.9}$$

In (B.3) the derivative of the base functions are taken with respect to the distance l along the curve σ. The link between this distance and the angular quantity ϕ, used in the definition (B.1) is given by

$$l = \rho\phi, \tag{B.10}$$

The derivative of w_i can now be written as

$$\frac{\partial w_i(l)}{\partial l} = \frac{\partial w_i(\phi)}{\partial \phi}\frac{\partial \phi}{\partial l} = \frac{1}{\rho}\frac{\partial w_i(\phi)}{\partial \phi}. \tag{B.11}$$

Moreover, the integration on σ can be done using a parameter t, which has the general expression

$$\phi(t) = \phi_i + \frac{\Delta}{2}(t+1); \quad t \in [-1,1], \tag{B.12}$$

$$\Delta = \phi_{i+1} - \phi_i; \quad i = 1, 2, \cdots, N. \tag{B.13}$$

By substituting (B.1) in (B.11) and by adopting the parametric representation (B.13), the derivative of the base functions yields

$$\frac{\partial w_i(l)}{\partial l} = \frac{1}{\rho\Delta}\begin{cases} \frac{2}{3}(t+1) & t \in [-1,1]; \quad \phi_i \le \phi \le \phi_i + \Delta \\ -\frac{4}{3}t & t \in [-1,1]; \quad \phi_i + \Delta \le \phi \le \phi_i + 2\Delta \\ \frac{2}{3}(t-1) & t \in [-1,1]; \quad \phi_i + 2\Delta \le \phi \le \phi_i + 3\Delta \end{cases}. \tag{B.14}$$

Consequently, the integration element dl is expressed as

$$dl = \rho d\phi = \rho\frac{\Delta}{2}dt. \tag{B.15}$$

The parametric representation of σ (B.13) can be also adopted in the definition of the scalar Green's function g. With this substitution of variable, the singular term in (B.7) can be re-arranged as

$$\ln R^2 = \ln\frac{R^2}{(t-t')^2} + \ln(t-t')^2. \tag{B.16}$$

By employing the expression of R^2 as function of t

$$R^2 = 2\rho^2(1 - \cos\frac{\Delta}{2}(t - t')), \tag{B.17}$$

one can observe that the first term in (B.16) is regular and its limit when the observation point approaches the source point is given by

$$\lim_{t\to t'} \frac{R^2}{(t-t')^2} = \lim_{t\to t'} \frac{2\rho^2(1 - \cos\frac{\Delta}{2}(t - t'))}{(t-t')^2} = \frac{\rho^2\Delta^2}{4}. \tag{B.18}$$

Finally, the integral (B.3) can be partitioned in a regular part and singular part for the cases when the singularity have to be circumvented

$$C_{ij} = C^r_{ij} + C^s_{ij}, \tag{B.19}$$

with

$$C^r_{ij} = \frac{1}{4}\int_\sigma\int_\sigma \left(g1(\boldsymbol{s},\boldsymbol{s}') - \frac{1}{4\pi}\ln\frac{R^2}{(t-t')^2}\right)\frac{\partial w_i(t)}{\partial t}\frac{\partial w_j(t)}{\partial t}\,dtdt', \tag{B.20}$$

$$C^s_{ij} = -\frac{1}{4}\int_\sigma\int_\sigma \frac{1}{4\pi}\ln(t-t')^2\frac{\partial w_i(t)}{\partial t}\frac{\partial w_j(t)}{\partial t}\,dtdt', \tag{B.21}$$

It is worth noting that, since the base functions are defined on three segments and some of them are partially overlapped, the singular integrals appear in a reduced number of elements C_{ij} of the matrix $\boldsymbol{C}$. These elements are located on the main, second and third diagonals of the matrix $\boldsymbol{C}$. The regular entries in $\boldsymbol{C}$ as well as the terms C^r_{ij} are evaluated in this thesis by using the three points Gauss quadrature rule. The improper integrals C^s_{ij} are solved analytically, and the results are added to the relevant terms. A detailed description of the procedure adopted in the calculation of the singular entries in the $\boldsymbol{C}$ matrix are hereafter presented.

In (B.21) the basis functions w_i and w_j are defined by three branches each and, therefore, the double integral should be divided into nine parts

$$C^s_{ij} = \sum_{m=1}^{3}\sum_{n=1}^{3} C^{mn}_{ij}, \tag{B.22}$$

where m and n represent the index of the segment pertaining to the basis functions w_i and w_j, respectively. By observing that the expression under the integrals in (B.21) remains the same if the variables t and t' are interchanged,

the following terms have to be evaluated, only:

$$C_{ij}^{11} = C_{ij}^{33} = -\frac{1}{16\pi}\int_{-1}^{1}\int_{-1}^{1}\frac{2}{3}(t+1)\frac{2}{3}(t'+1)\ln(t-t')^2\ dtdt', \quad \text{(B.23)}$$

$$C_{ij}^{12} = C_{ij}^{21} = -\frac{1}{16\pi}\int_{-1}^{1}\int_{-1}^{1}\frac{2}{3}(t+1)\left(-\frac{4}{3}\right)t'\ln(t-t')^2\ dtdt', \quad \text{(B.24)}$$

$$C_{ij}^{13} = C_{ij}^{31} = -\frac{1}{16\pi}\int_{-1}^{1}\int_{-1}^{1}\frac{2}{3}(t+1)\frac{2}{3}(t'-1)\ln(t-t')^2\ dtdt', \quad \text{(B.25)}$$

$$C_{ij}^{22} = -\frac{1}{16\pi}\int_{-1}^{1}\int_{-1}^{1}\frac{4}{3}t\,\frac{4}{3}t'\ln(t-t')^2\ dtdt', \quad \text{(B.26)}$$

$$C_{ij}^{23} = C_{ij}^{32} = -\frac{1}{16\pi}\int_{-1}^{1}\int_{-1}^{1}\left(-\frac{4}{3}\right)t\frac{2}{3}(t'-1)\ln(t-t')^2\ dtdt'. \quad \text{(B.27)}$$

The relations (B.23) to (B.27) can be reduced to a number of simple integrals having analytical solutions. The generic form of these basic integrals is represented by

$$\int_0^1 x^m\ln x\ dx = \frac{-1}{(m+1)^2}, \quad \text{for} \quad m > -1. \quad \text{(B.28)}$$

After some lengthy, though straightforward, manipulations involving a few changes of variables, the components of the singular term C_{ij}^{s} become

$$C_{ij}^{11} = C_{ij}^{33} = -\frac{1}{18\pi}\left(4\ln 2 - 7\right), \quad \text{(B.29)}$$

$$C_{ij}^{12} = C_{ij}^{21} = -\frac{1}{9\pi}, \quad \text{(B.30)}$$

$$C_{ij}^{13} = C_{ij}^{31} = -\frac{1}{18\pi}\left(5 - 4\ln 2\right), \quad \text{(B.31)}$$

$$C_{ij}^{22} = \frac{2}{9\pi}, \quad \text{(B.32)}$$

$$C_{ij}^{23} = C_{ij}^{32} = -\frac{1}{9\pi}. \quad \text{(B.33)}$$

Note, that the singular terms in the elements of the $\boldsymbol{C}$ matrix exist when the two piecewise functions w_i and w_j have one, two or three overlapping segments, only.

Elements of the $\boldsymbol{L}$ matrix

For the evaluation of the entries in the $\boldsymbol{L}$ matrix the following integral has to be computed

$$L_{ij} = \int_\sigma \int_\sigma w_i(l) w_j(l') \boldsymbol{t}(l) \cdot \overline{\boldsymbol{G}}_{st}(\boldsymbol{s}, \boldsymbol{s}') \cdot \boldsymbol{t}(l') \, dl dl', \tag{B.34}$$

Here, it is pointed out that the elements L_{ij} involving base functions defined on coinciding segments have a singular behavior. By analyzing the expressions of the scalar and dyadic Green's functions given in Appendix A one can infer that the singularity in $\overline{\boldsymbol{G}}_{st}$ is of $\ln R^2$ type. With this observation, the procedure adopted for solving the improper integrals aims at isolating the singularity in the parametric form $\ln(t-t')^2$ and to treat it analytically. Similarly to the case of the $\boldsymbol{C}$ matrix, the parameter t introduced by (B.13) will be used in the representation of the quantities under the integrals in (B.34). The definition of w_i as function of t reads

$$w_i(t) = \begin{cases} \frac{1}{6}(t+1)^2 & t \in [-1,1]; \quad \phi_i \le \phi \le \phi_i + \Delta \\ 1 - \frac{1}{3}t^2 & t \in [-1,1]; \quad \phi_i + \Delta \le \phi \le \phi_i + 2\Delta \\ \frac{1}{6}(t-1)^2 & t \in [-1,1]; \quad \phi_i + 2\Delta \le \phi \le \phi_i + 3\Delta \end{cases}, \tag{B.35}$$

Concurrently, the tangential unit vector $\boldsymbol{t}$ (see Fig. B.1) is expressed in the Cartesian frame attached to the rectangular waveguide

$$\boldsymbol{t}(\phi) = -\sin\phi \boldsymbol{u}_x + \cos\phi \boldsymbol{u}_y, \tag{B.36}$$

Note that in (B.36) the angle ϕ should be understood as a function of t, as well. Further attention is given to the scalar product between the dyadic and the vector quantities in (B.34). In this respect, the dyadic $\overline{\boldsymbol{G}}_{st}$ is written in a simplified form

$$\overline{\boldsymbol{G}}_{st} = \boldsymbol{u}_x \boldsymbol{u}_x G_{xx} + \boldsymbol{u}_x \boldsymbol{u}_y G_{xy} + \boldsymbol{u}_y \boldsymbol{u}_x G_{yx} + \boldsymbol{u}_y \boldsymbol{u}_y G_{yy}, \tag{B.37}$$

where, the scalar components G_{xx}, G_{xy}, G_{yx} and G_{yy} can be easily identified from the general expression of $\overline{\boldsymbol{G}}_{st}$ introduced in the Appendix A. With this notation, the scalar product in (B.34) yields

$$\begin{aligned} \boldsymbol{t} \cdot \overline{\boldsymbol{G}}_{st}(\boldsymbol{s}, \boldsymbol{s}') \cdot \boldsymbol{t} &= (-\sin\phi \boldsymbol{u}_x + \cos\phi \boldsymbol{u}_y) \cdot \overline{\boldsymbol{G}}_{st}(\boldsymbol{s}, \boldsymbol{s}') \cdot (-\sin\phi \boldsymbol{u}_x + \cos\phi \boldsymbol{u}_y) \\ &= \sin\phi \sin\phi G_{xx}(\boldsymbol{s}, \boldsymbol{s}') - \sin\phi \cos\phi G_{xy}(\boldsymbol{s}, \boldsymbol{s}') \\ &\quad - \cos\phi \sin\phi G_{yx}(\boldsymbol{s}, \boldsymbol{s}') + \cos\phi \cos\phi G_{yy}(\boldsymbol{s}, \boldsymbol{s}'), \end{aligned} \tag{B.38}$$

The singularity of the dyadic function is given by the static terms ($m = 0$) of the G_{xx} and G_{yy} components. As we already mentioned, to circumvent

this problem it is appropriated to subtract $\ln(t-t')^2$ from these terms. With this partition strategy, the relation (B.38) yields

$$\boldsymbol{t} \cdot \overline{\boldsymbol{G}}_{st}(\boldsymbol{s}, \boldsymbol{s}') \cdot \boldsymbol{t} = G^r_{st}(\boldsymbol{s}, \boldsymbol{s}') - \frac{1}{8\pi} \ln(t - t')^2, \tag{B.39}$$

with

$$\begin{aligned} G^r_{st}(\boldsymbol{s}, \boldsymbol{s}') &= \sin\phi \sin\phi \left[G_{xx} + \frac{1}{8\pi} \ln(t - t')^2 \right] - \sin\phi \cos\phi G_{xy} \\ &\quad - \cos\phi \sin\phi G_{yx} + \cos\phi \cos\phi \left[G_{yy} + \frac{1}{8\pi} \ln(t - t')^2 \right] \\ &\quad - \frac{1}{8\pi} \left[\cos\frac{\Delta}{2}(t - t') - 1 \right] \ln(t - t')^2, \end{aligned} \tag{B.40}$$

Note that in (B.39) and (B.40) the expressions were arranged such that the $\ln(t - t')^2$ term is distinctly indicated. After isolating the singularity it is necessary to calculate the value of the regular terms in (B.39) when $t = t'$ (as a limit).

The elements of the $\boldsymbol{L}$ matrix, which require integration on overlapping sections of the σ curve, can be expressed as a sum of two terms

$$L_{ij} = L^r_{ij} + L^s_{ij}, \tag{B.41}$$

with

$$L^r_{ij} = \frac{\rho^2 \Delta^2}{4} \int_\sigma \int_\sigma G^r_{st}(\boldsymbol{s}, \boldsymbol{s}') w_i(t) w_j(t) \, dt dt', \tag{B.42}$$

$$L^s_{ij} = -\frac{\rho^2 \Delta^2}{4} \int_\sigma \int_\sigma \frac{1}{8\pi} \ln(t - t')^2 w_i(t) w_j(t) \, dt dt'. \tag{B.43}$$

The regular term L^r_{ij} can be integrated numerically whereas the singular one L^s_{ij} lends itself to an analytical formulation. It is worth noting that the function G^r_{st} in (B.42) contains some components that are not defined at $t = t'$. Therefore, before performing the numerical integration, these components have to be evaluated as a limit when $t \to t'$. The expression of the G^r_{st} then reads

$$\begin{aligned} G^r_{st}(\boldsymbol{s}, \boldsymbol{s}') &= \sin\phi \sin\phi \left[G_{xx} + \frac{1}{8\pi} \ln(t - t')^2 \right] - \sin\phi \cos\phi G_{xy} \\ &\quad - \cos\phi \sin\phi G_{yx} + \cos\phi \cos\phi \left[G_{yy} + \frac{1}{8\pi} \ln(t - t')^2 \right] \\ &\quad - \frac{1}{8\pi} \left[\cos\frac{\Delta}{2}(t - t') - 1 \right] \ln(t - t')^2. \end{aligned} \tag{B.44}$$

The following limit, occurring in (B.44), has to be accounted for

$$\lim_{t\to t'} -\frac{1}{8\pi}\left[\cos\frac{\Delta}{2}(t-t')-1\right]\ln(t-t')^2 = 0. \tag{B.45}$$

By considering the definition of the $\overline{\boldsymbol{G}}_{st}$ Green's function given in the Appendix A.2 it can be shown that the G_{xx} component in (B.44) yields

$$\begin{aligned} G_{xx} &= G_{xx}^{m\neq 0} + \frac{1}{8\pi}\ln(T_0-D) - \frac{1}{8\pi}\ln\frac{T_0-B}{(t-t')^2} - \frac{1}{8\pi}\ln(t-t')^2, \\ &\quad + \frac{1}{4\pi}\frac{IMX_0S_0}{(T_0-B)(T_0-D)}. \end{aligned} \tag{B.46}$$

In (B.46) the limits that should be taken into account are

$$\lim_{t\to t'} -\frac{1}{8\pi}\ln\frac{T_0-B}{(t-t')^2} = -\frac{1}{16\pi}\left(\frac{\pi}{b}\frac{\rho\Delta}{2}\right)^2, \tag{B.47}$$

and

$$\lim_{t\to t'} \frac{1}{4\pi}\frac{IMX_0S_0}{(T_0-D)(T_0-B)} = \frac{1}{2\pi}\frac{IM}{(T_0-D)}\sin^2\phi(t'). \tag{B.48}$$

The G_{xy} term in (B.44) can be written as

$$G_{xy} = G_{xy}^{m\neq 0} - \frac{1}{4\pi}\frac{GY_0(V_0F-H)}{(V_0-A)(V_0-C)}, \tag{B.49}$$

where the component that has to be evaluated as a limit is given by

$$\lim_{t\to t'} -\frac{1}{4\pi}\frac{GY_0(V_0F-H)}{(V_0-A)(V_0-C)} = -\frac{1}{4\pi}\frac{G}{(V_0-C)}\sin\frac{\pi}{a}x'\sin 2\phi(t'). \tag{B.50}$$

Similarly, in the G_{yx} function having the expression

$$G_{yx} = G_{yx}^{m\neq 0} - \frac{1}{4\pi}\frac{MX_0(T_0L-N)}{(T_0-B)(T_0-D)}, \tag{B.51}$$

the following limit has to be considered

$$\lim_{t\to t'} -\frac{1}{4\pi}\frac{MX_0(T_0L-N)}{(T_0-B)(T_0-D)} = -\frac{1}{4\pi}\frac{M}{(T_0-B)}\sin\frac{\pi}{b}y'\sin 2\phi(t'). \tag{B.52}$$

The last component in (B.44) that exhibits an indeterminacy when $t\to t'$ is the G_{yy} term, which reads

$$\begin{aligned} G_{yy} &= G_{yy}^{m\neq 0} + \frac{1}{8\pi}\ln(V_0-C) - \frac{1}{8\pi}\ln\frac{V_0-A}{(t-t')^2} - \frac{1}{8\pi}\ln(t-t')^2 \\ &\quad + \frac{1}{4\pi}\frac{EGY_0U_0}{(V_0-A)(V_0-C)}. \end{aligned} \tag{B.53}$$

The limits that must be taken into consideration in (B.53) are

$$\lim_{t\to t'} \frac{1}{8\pi}\frac{V_0 - A}{(t-t')^2} = \frac{1}{16\pi}\left(\frac{\pi}{a}\frac{\rho\Delta}{2}\right)^2 \tag{B.54}$$

$$\lim_{t\to t'} \frac{1}{4\pi}\frac{EGY_0U_0}{(V_0 - A)(V_0 - C)} = \frac{1}{2\pi}\frac{EG}{(V_0 - C)}\cos^2\phi(t'). \tag{B.55}$$

A second aspect that must be accounted for in the evaluation of the elements of the $\boldsymbol{L}$ matrix is related to the calculation of the singular term L^s_{ij}. Since the basis functions w_i and w_j are defined on three segments each, the integral in (B.43) can be divided into nine parts

$$L^s_{ij} = \sum_{m=1}^{3}\sum_{n=1}^{3} L^{mn}_{ij}, \tag{B.56}$$

By substituting the expression of the basis functions (B.35, p. 207) in (B.43) the integrals L^{mn}_{ij} yield

$$L^{11}_{ij} = L^{33}_{ij} = -\frac{1}{8\pi}\frac{\rho^2\Delta^2}{4}\int_{-1}^{1}\int_{-1}^{1}\frac{1}{6}(t+1)^2\frac{1}{6}(t'+1)^2\ln(t-t')^2\,dtdt', \tag{B.57}$$

$$L^{12}_{ij} = L^{21}_{ij} = -\frac{1}{8\pi}\frac{\rho^2\Delta^2}{4}\int_{-1}^{1}\int_{-1}^{1}\frac{1}{6}(t+1)^2(1-\frac{1}{3}t'^2)\ln(t-t')^2\,dtdt', \tag{B.58}$$

$$L^{13}_{ij} = L^{31}_{ij} = -\frac{1}{8\pi}\frac{\rho^2\Delta^2}{4}\int_{-1}^{1}\int_{-1}^{1}\frac{1}{6}(t+1)^2\frac{1}{6}(t'-1)^2\ln(t-t')^2\,dtdt', \tag{B.59}$$

$$L^{22}_{ij} = -\frac{1}{8\pi}\frac{\rho^2\Delta^2}{4}\int_{-1}^{1}\int_{-1}^{1}(1-\frac{1}{3}t^2)(1-\frac{1}{3}t'^2)\ln(t-t')^2\,dtdt', \tag{B.60}$$

$$L^{23}_{ij} = L^{32}_{ij} = -\frac{1}{8\pi}\frac{\rho^2\Delta^2}{4}\int_{-1}^{1}\int_{-1}^{1}(1-\frac{1}{3}t^2)\frac{1}{6}(t'-1)^2\ln(t-t')^2\,dtdt'. \tag{B.61}$$

The analytical solutions of the integrals (B.57), ..., (B.61) are given by

$$L^{11}_{ij} = L^{33}_{ij} = -\frac{1}{\pi}\frac{\rho^2\Delta^2}{81}(\ln 2 - 2), \tag{B.62}$$

$$L^{12}_{ij} = L^{21}_{ij} = -\frac{1}{8\pi}\frac{\rho^2\Delta^2}{81}(32\ln 2 - 47), \tag{B.63}$$

$$L^{13}_{ij} = L^{31}_{ij} = -\frac{1}{8\pi}\frac{\rho^2\Delta^2}{81}(8\ln 2 - 7), \tag{B.64}$$

$$L^{22}_{ij} = -\frac{1}{\pi}\frac{\rho^2\Delta^2}{9}(\frac{16}{9}\ln 2 - \frac{11}{4}), \tag{B.65}$$

$$L^{23}_{ij} = L^{32}_{ij} = -\frac{1}{2\pi}\frac{\rho^2\Delta^2}{81}(8\ln 2 - \frac{47}{4}). \tag{B.66}$$

Elements of the $\boldsymbol{R}$ matrix

The entries in the $\boldsymbol{R}$ matrix involve regular line integrals that can be easily evaluated by using the Gauss quadrature rule. However, for a robust numerical implementation, it is indicated to express all entries under integration as functions of the t parameter.

Elements of the $\boldsymbol{L}'$ matrix

In evaluating the elements of the $\boldsymbol{L}'$ matrix the procedure presented for the calculation of the entries in the $\boldsymbol{C}$ matrix can be followed. A variation is noted in the evaluation of the improper integrals, when the logarithmic term is multiplied by base functions and not by derivatives of these functions. The analytical solutions of these integrals are similar to these given in this appendix for the elements of the $\boldsymbol{L}$ matrix.

Elements of the $\boldsymbol{R}'$ matrix

There is a similarity between elements in the $\boldsymbol{R}'$ matrix and the entries in $\boldsymbol{R}$. Therefore, the remarks above for the evaluation of the $\boldsymbol{R}$ matrix are valid here, as well.

Appendix C

Coupling integrals at steps on rectangular waveguides

The integrals involved in the evaluation of the coupling coefficients between different rectangular waveguides can be solved analytically. Referring to the notations introduced in Section 2.3.3 the quantities I_{cx}, I_{sx}, I_{cy} and I_{sy} read

$$I_{cx} = \int_{x_0}^{x_0+a_1} \cos\left(\frac{u\pi x}{a_2}\right) \cos\left(\frac{i\pi(x-x_0)}{a_1}\right)\, dx, \tag{C.1}$$

$$I_{cx} = \begin{cases} \frac{1}{\pi}\frac{ua_1^2a_2}{(ia_2)^2-(ua_1)^2}\left[(-1)^{i+1}\sin\left(\frac{u\pi(x_0+a_1)}{a_2}\right)+\sin\left(\frac{u\pi x_0}{a_2}\right)\right]; & ia_2 \neq ua_1 \\ \frac{1}{2\pi}\frac{a_1a_2}{(ia_2)+(ua_1)}\left[(-1)^{i}\sin\left(\frac{u\pi(x_0+a_1)}{a_2}\right)-\sin\left(\frac{u\pi x_0}{a_2}\right)\right] & \\ +\frac{a_1}{2\pi}\cos\left(\frac{i\pi x_0}{a_1}\right); & ia_2 = ua_1 \\ a_1; & i = u = 0 \end{cases} \tag{C.2}$$

$$I_{sx} = \int_{x_0}^{x_0+a_1} \sin\left(\frac{u\pi x}{a_2}\right) \sin\left(\frac{i\pi(x-x_0)}{a_1}\right)\, dx, \tag{C.3}$$

$$I_{sx} = \begin{cases} \frac{1}{\pi}\frac{ia_1a_2^2}{(ia_2)^2-(ua_1)^2}\left[(-1)^{i+1}\sin\left(\frac{u\pi(x_0+a_1)}{a_2}\right)+\sin\left(\frac{u\pi x_0}{a_2}\right)\right]; & ia_2 \neq ua_1 \\ \frac{1}{2\pi}\frac{a_1a_2}{(ia_2)+(ua_1)}\left[(-1)^{i+1}\sin\left(\frac{u\pi(x_0+a_1)}{a_2}\right)+\sin\left(\frac{u\pi x_0}{a_2}\right)\right] & \\ +\frac{a_1}{2\pi}\cos\left(\frac{i\pi x_0}{a_1}\right); & ia_2 = ua_1 \\ 0; & i=0 \text{ or } u=0 \end{cases} \tag{C.4}$$

$$I_{cy} = \int_{y_0}^{y_0+b_1} \cos\left(\frac{v\pi y}{b_2}\right)\cos\left(\frac{j\pi(y-y_0)}{b_1}\right)\,dy, \tag{C.5}$$

$$I_{cy} = \begin{cases} \frac{1}{\pi}\frac{vb_1^2b_2}{(jb_2)^2-(vb_1)^2}\left[(-1)^{j+1}\sin\left(\frac{v\pi(y_0+b_1)}{b_2}\right)+\sin\left(\frac{v\pi y_0}{b_2}\right)\right]; & jb_2 \neq vb_1 \\ \frac{1}{2\pi}\frac{b_1b_2}{(jb_2)+(vb_1)}\left[(-1)^{j}\sin\left(\frac{v\pi(y_0+b_1)}{b_2}\right)-\sin\left(\frac{v\pi y_0}{b_2}\right)\right] & \\ +\frac{b_1}{2\pi}\cos\left(\frac{j\pi y_0}{b_1}\right); & jb_2 = vb_1 \\ b_1; & j=v=0 \end{cases} \tag{C.6}$$

$$I_{sy} = \int_{y_0}^{y_0+b_1} \sin\left(\frac{v\pi y}{b_2}\right)\sin\left(\frac{j\pi(y-y_0)}{b_1}\right)\,dy, \tag{C.7}$$

$$I_{sy} = \begin{cases} \frac{1}{\pi}\frac{jb_1b_2^2}{(jb_2)^2-(vb_1)^2}\left[(-1)^{j+1}\sin\left(\frac{v\pi(y_0+b_1)}{b_2}\right)+\sin\left(\frac{v\pi y_0}{b_2}\right)\right]; & jb_2 \neq vb_1 \\ \frac{1}{2\pi}\frac{b_1b_2}{(jb_2)+(vb_1)}\left[(-1)^{j+1}\sin\left(\frac{v\pi(y_0+b_1)}{b_2}\right)+\sin\left(\frac{v\pi y_0}{b_2}\right)\right] & \\ +\frac{b_1}{2\pi}\cos\left(\frac{j\pi y_0}{b_1}\right); & jb_2 = vb_1 \\ 0; & j=0 \text{ or } v=0 \end{cases} \tag{C.8}$$

Appendix D

Near field analysis of the waveguide-end antennas

The Mode Matching Method (MMM) presented in Chapter 3 allows for an accurate analysis of the radiation phenomena associated with the waveguide ended antennas. By taking into consideration a large number of waveguide modes it was possible in Section 3.3 to demonstrate numerically the singular behavior of some field quantities at the aperture's edges.

In this appendix some more details are provided with respect to the propagation of the electromagnetic waves and the transfer of the energy in the near field region of the antenna. The transfer of the electromagnetic energy inside the transmission line and in the vicinity of the aperture can be explained by the time average Poynting vector (in case of harmonic waves). The Poynting vector at a generic point (x, y, z) can be written as [11, p. 36]

$$\boldsymbol{W}(x, y, z) = \frac{1}{2}\boldsymbol{E}(x, y, z) \times \boldsymbol{H}^*(x, y, z), \tag{D.1}$$

where $\boldsymbol{E}$ is the electric field strength, $\boldsymbol{H}$ is magnetic field strength and * denotes the complex conjugate operation. Note that the quantities in (D.1) are spatial vectors with complex components. From the numerical analysis of the propagation and radiation phenomena it is possible to find the complex components of the electric and magnetic field strengths. The time average Poynting vector can be expressed in a Cartesian reference frame (see, for example, Fig. 3.1, p. 63) as

$$\boldsymbol{W} = \mathbf{u}_x W_x + \mathbf{u}_y W_y + \mathbf{u}_z W_z, \tag{D.2}$$

where the components W_x, W_y and W_z are complex numbers. The real part of the Poynting vector W represents the average *active* power density at a point in space [11, p. 36] and indicates the energy transferred by the electromagnetic waves. Conversely, the imaginary part of the Poynting vector

is representative for the *reactive* (stored) power density associated with the electromagnetic fields.

To illustrate the character of the power density in the vicinity of a flanged, waveguide end antenna, a modal analysis has been performed on an antenna model replicating the dimensions of a WR90 waveguide ($a = 22.86\,\text{mm}$ and $b = 10.16\,\text{mm}$). Note that this study case is identical with the one presented in Section 3.3.

The real and the imaginary parts of the Poynting vector calculated in three orthogonal planes are depicted in Fig. D.1. A number of 200 waveguide modes (TE and TM) have been considered in the MM method. The frequency of the analysis is 10 GHz ($\lambda = 30\,\text{mm}$). Note that in Fig. D.1 the $x\mathcal{O}y$ plane is localized at 0.1 mm (0.0033λ) in front of the aperture, the $x\mathcal{O}z$ section is taken in the symmetry plane of the waveguide ($y = b/2$) and the $y\mathcal{O}z$ section is taken in the symmetry plane of the waveguide ($x = a/2$).

The real and the imaginary parts of the Poynting vector depicted in Fig. D.1 were evaluated as

$$\Re\{\boldsymbol{W}\} = \sqrt{\Re\{W_x\}^2 + \Re\{W_y\}^2 + \Re\{W_z\}^2}, \tag{D.3}$$

$$\Im\{\boldsymbol{W}\} = \sqrt{\Im\{W_x\}^2 + \Im\{W_y\}^2 + \Im\{W_z\}^2}. \tag{D.4}$$

For completeness, the orientation of the Poynting vector is also indicated with small arrows on the plots in Fig. D.1.

From the study of this figure it may be concluded that the energy is radiated in the free space by the entire aperture with some concentration in the vicinity of the singular edges of the aperture. The reactive energy is localized around the corners of the apertures and quickly drops to zero in the radiation domain.

The complex character of the propagation of the electromagnetic waves in the near-field region of an antenna can be also investigated by means of the wave impedance (or admittance). In this sense a key issue is to estimate the phase shift between the electric and magnetic field quantities in terms of total fields or by referring to the spatial components. Note that the numerical analysis yields, commonly, the field components along the axes of the chosen reference frame. Therefore, for determining the total electric or magnetic fields at a point in space, it is necessary to combine the spatial components which are complex numbers.

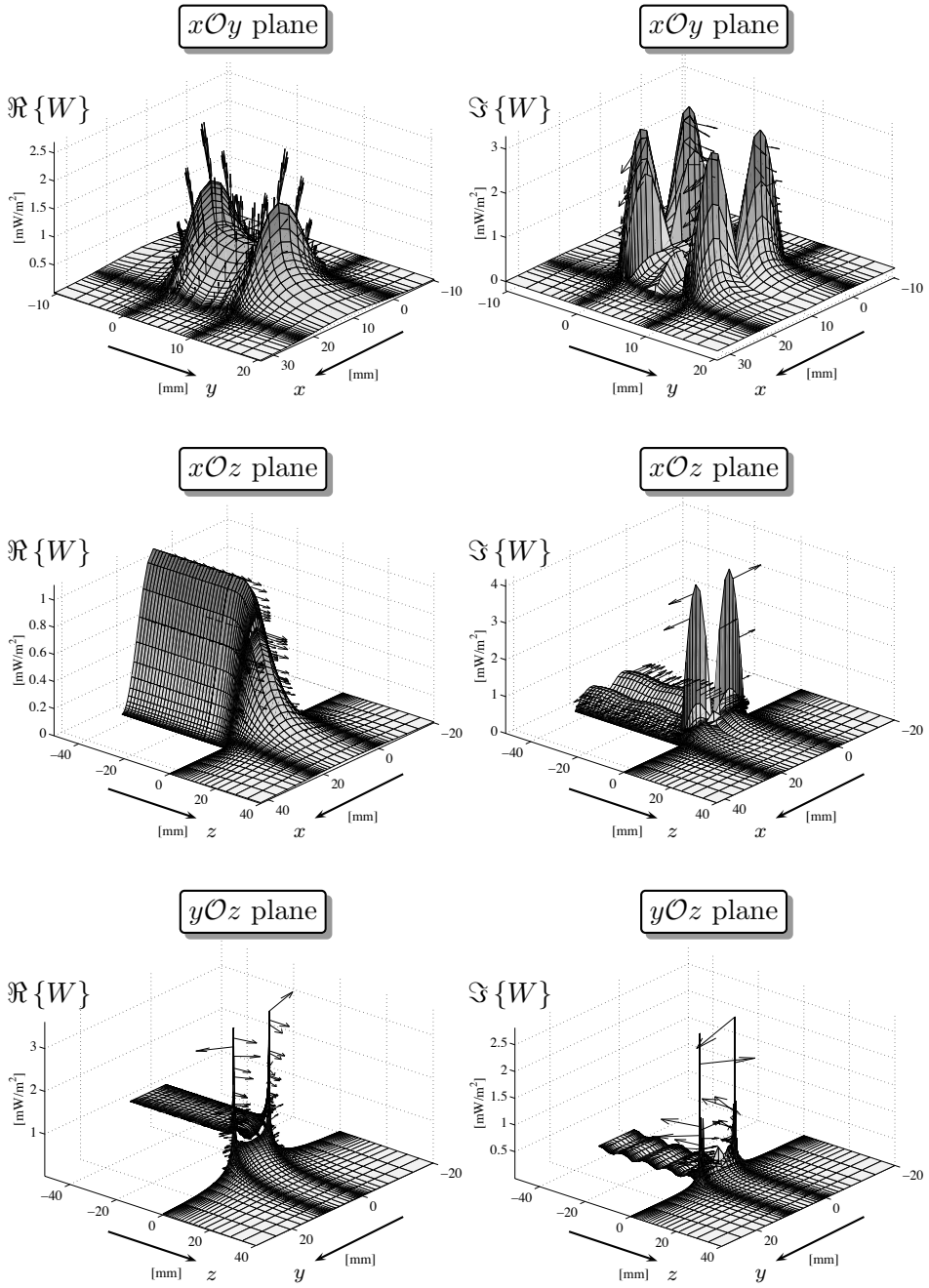

Figure D.1: Distribution of the real and imaginary parts of the time average Poynting vector (average power density) in the vicinity of the aperture of a flanged, waveguide end antenna.

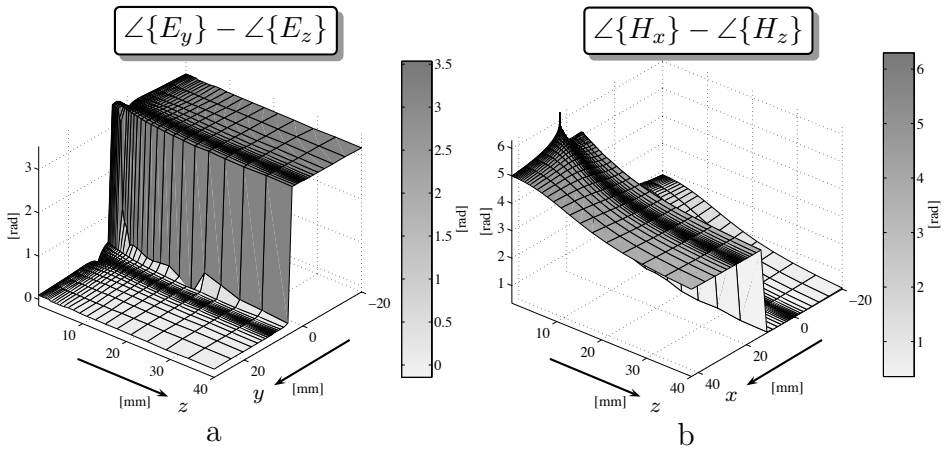

Figure D.2: Phase difference between the spatial components of the electric and of the magnetic fields radiated by a flanged, waveguide end antenna. (a) - the phase difference between the E_y and E_z components of the electric field strength in the $y\mathcal{O}z$ plane; (b) - the phase difference between the H_x and H_z components of the magnetic field strength in the $x\mathcal{O}z$ plane.

When the complex vectors to be added have the same phase it can be assumed the they correspond to a vector oriented along a certain (fixed) direction, with the modulus given by the vectorial addition of the absolute values of the components and with the phase equaling that of the spatial components.

It is well recognized that in the near field region of an antenna the spatial components of the electric and of the magnetic fields are not always in phase, and this introduces a rotation of the vector representing the total field (electric or magnetic) [11, p. 140]. To illustrate this behavior, the phase differences between the spatial components of the electric field and between these of the magnetic field in the near-field region of the waveguide end antenna discussed above are depicted in Fig. D.2. Note that these quantities were evaluated in two particular planes, where some of the field components are zero. The $y\mathcal{O}z$ plane is located at the middle of the waveguide ($x = a/2$) where, due to the symmetry (see Figs. 3.5, p. 76 and 3.6, p. 77), there is one component of the magnetic field (namely H_x) and there are two components of the electric field (E_y and E_z), only . Therefore, the total magnetic field can be identified with the H_x component and the total electric field can be estimated by combining not more than two spatial components. Similarly, in the $x\mathcal{O}z$ plane, located at $y = b/2$, the quantities E_y, H_x and H_y are nonzero only. The phase differences between the E_y and E_z components in the $y\mathcal{O}z$ plane and between the H_x and H_z components in the $x\mathcal{O}z$ plane are depicted in Fig. D.2. It is noticed from Fig. D.2.a that the E_y and E_z components are approximately in phase in the radiation domain (except for a π jump). The π step in this plot is introduced by a change in the

orientation of the E_z, which does not introduce any rotation of the total electric field obtained from the combination of the E_y and E_z. Under the assumption that

$$\angle\{E_y\} \approx \angle\{E_z\}, \tag{D.5}$$

the complex magnitude of the total electric field can be written as

$$E_t = \sqrt{|E_y|^2 + |E_x|^2}\exp\left(j\angle\{E_y\}\right), \tag{D.6}$$

where $\angle\{A\}$ denotes the phase and $|A|$ represents the absolute value of the complex number A.

Once the field components are reduced to the total electric and magnetic quantities, and with the observation that these total vectors are not of rotating nature, it is possible to define a wave impedance Z as

$$Z = \frac{E_t}{H_t}, \tag{D.7}$$

The real and the imaginary parts of the wave impedance, in the case of the $y\mathcal{O}z$ plane discussed above, are depicted in Fig. D.3. From the analysis of the plots in this figure it is noted that:

- inside of the waveguide the impedance is similar to that given by the telegrapher equations [111, p. 55]. Note that the characteristic impedance of the TE_{10} mode on the WR90 waveguide, at 10 GHz is around 499 Ω.
- the resistance of the wave in front of the aperture vary from a high value in the near-field region to the value of the free-space impedance ($\eta = 377\,\Omega$) in the far field region;
- the reactance of the wave, associated to the reactive field also evidenced by the Poynting vector, has a capacitive character in the near field region and decreases to zero in the far-field region.

When the phase difference between the spatial components of the magnetic or the electric field quantities is significant (as, for example, in the case presented in Fig. D.2.b) the total corresponding field will be given by a rotating vector of complex magnitude (analogous to the polarization problem [11, p. 140]). Under these conditions, a more general formulation must be adopted for the definition of the wave impedance. Probably, the most adequate approach is to define the wave impedance as a dyadic quantity [26, p. 175].

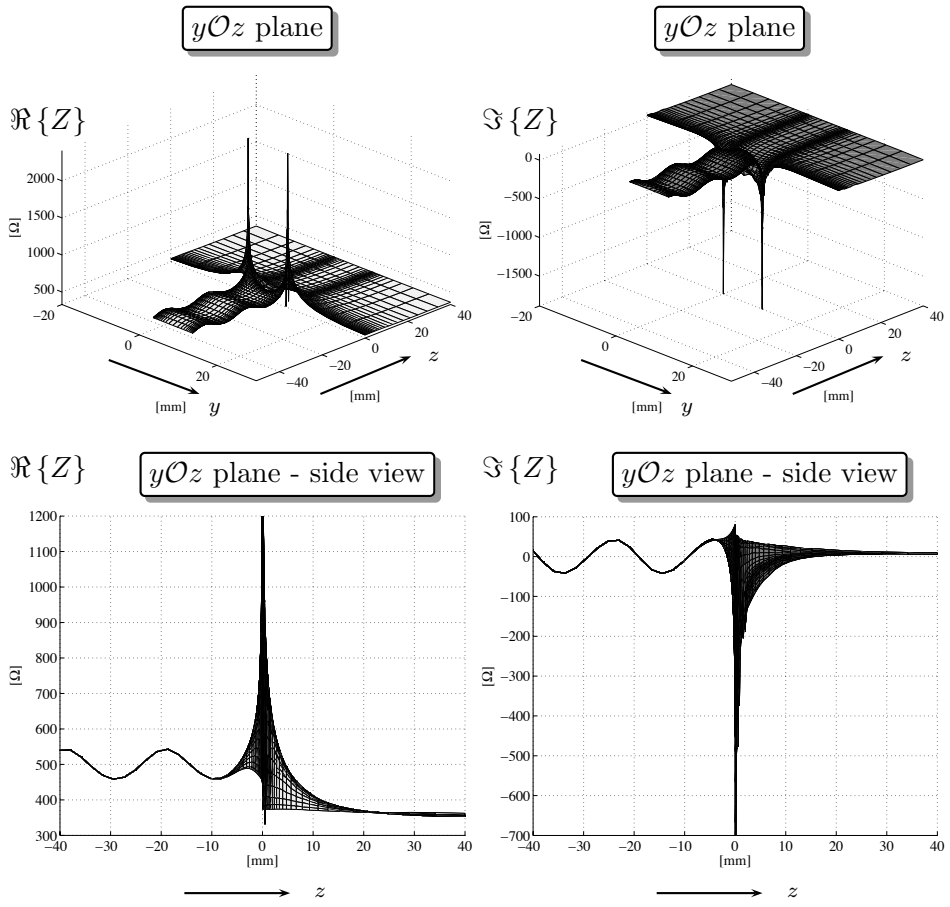

Figure D.3: Distribution of the real and the imaginary parts of the medium admittance in the $y\mathcal{O}z$ of a flanged, waveguide end antenna.

Appendix E

Coupling admittances between rectangular apertures

In Chapter 3 it was shown that the mutual coupling effect manifesting in finite array antennas consisting of rectangular apertures can be accurately evaluated by means of the Mode Matching Method. Some more details are provided in this appendix with respect to the calculation of the mutual coupling admittances between the modes of differently sized apertures, deployed on an infinitely extended ground plane. The configuration under investigation is reproduced in Fig. E.1.

The coupling admittance between the mode (m,n) at the aperture i and the mode (m',n') at the aperture j is given by [16]

$$Y^{i,j}_{(m,n),(m',n')} = \frac{\mathrm{j}kY_0}{2\pi\sqrt{Y^i_{m,n}}\sqrt{Y^j_{m',n'}}} A^i_{m,n} A^j_{m',n'} \left(c_x I_x + c_y I_y - c_z I_z\right), \quad \text{(E.1)}$$

where

$$\begin{matrix} I_x \\ I_y \\ I_z \end{matrix} = \iint\limits_{S_i} \iint\limits_{S_j} \begin{matrix} \sin \\ \cos \\ \cos \end{matrix} \left(\frac{m\pi x}{a_i}\right) \cdot \begin{matrix} \cos \\ \sin \\ \cos \end{matrix} \left(\frac{n\pi y}{b_i}\right) \cdot \begin{matrix} \sin \\ \cos \\ \cos \end{matrix} \left(\frac{m'\pi x'}{a_j}\right) \cdot \begin{matrix} \cos \\ \sin \\ \cos \end{matrix} \left(\frac{n'\pi y'}{b_j}\right) \cdot G(x-x', y-y')\, dS dS' \quad \text{(E.2)}$$

and the coefficients c_x, c_y and c_z are listed in Table E.1.

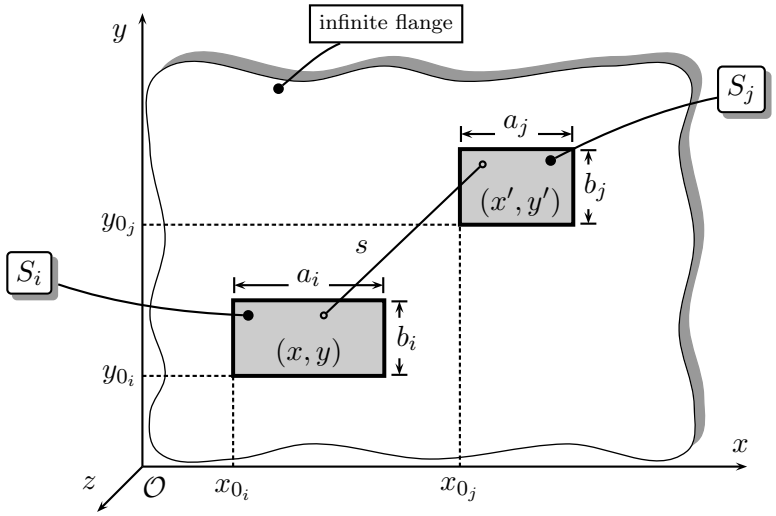

Figure E.1: Different sized rectangular apertures in a ground plane.

Table E.1: Coefficients of the Bird's coupling admittance formula.

Coupling	c_x	c_y	c_z
$TE_{mn} \leftrightarrow TE_{m'n'}$	$\pi^2 \frac{mm'}{a_i a_j}$	$\pi^2 \frac{nn'}{b_i b_j}$	$\left(\frac{k_{c,mn} k_{c,m'n'}}{k}\right)^2$
$TE_{mn} \leftrightarrow TM_{m'n'}$	$-\pi^2 \frac{mn'}{a_i b_j}$	$\pi^2 \frac{nm'}{b_i a_j}$	0
$TM_{mn} \leftrightarrow TE_{m'n'}$	$-\pi^2 \frac{nm'}{b_i a_j}$	$\pi^2 \frac{mn'}{a_i b_j}$	0
$TM_{mn} \leftrightarrow TM_{m'n'}$	$\pi^2 \frac{nn'}{b_i b_j}$	$\pi^2 \frac{mm'}{a_i a_j}$	0

By adopting the Lewin's method [79, pp. 121–126], the order of the integration in (E.2) can be reduced by two. In this respect, the way of performing the integration in (E.2) is changed such that, instead of integrating over the aperture S_i (associated to the variables x and y) and the aperture S_j (related to the variables x' and y'), the two double integrals are performed over the (x, x') and (y, y') domains. Furthermore, the following changes of

variable are adopted:

$$\sigma = x - x', \tag{E.3}$$
$$v = x + x' - a_i, \tag{E.4}$$
$$\lambda = y - y', \tag{E.5}$$
$$u = y + y' - b_i, \tag{E.6}$$

where the (σ, v) domain is assigned to the (x, x') domain and (λ, u) to (y, y'), respectively. After some lengthy, though straightforward manipulations, the integrals over the variables v and u can be integrated out in closed forms. At this point the coupling admittance reduces to a sum of double integrals over the variables σ and λ, which is given by

$$\begin{aligned} Y^{i,j}_{(m,n),(m',n')} = & -\frac{\mathrm{j}kY_0}{32\pi\sqrt{Y^i_{m,n}}\sqrt{Y^j_{m',n'}}} A^i_{m,n} A^j_{m',n'} \Bigg\{ \int_0^{a_j} d\sigma \Bigg[\int_0^{b_j} d\lambda \\ & \Big(T(-\sigma, \sigma_1, \sigma_2, -\lambda, \lambda_1, \lambda_2) + T(-\sigma, \sigma_1, \sigma_2, \lambda_3, \lambda_4, -\lambda_4) \\ & + T(\sigma_3, \sigma_4, -\sigma_4, -\lambda, \lambda_1, \lambda_2) + T(\sigma_3, \sigma_4, -\sigma_4, \lambda_3, \lambda_4, -\lambda_4) \Big) \\ & + \int_0^{b_i - b_j} d\lambda \Big(T(-\sigma, \sigma_1, \sigma_2, \lambda, \lambda_1, \lambda_5) \\ & + T(\sigma_3, \sigma_4, -\sigma_4, \lambda, \lambda_1, \lambda_5) \Big) \Bigg] \\ & + \int_0^{a_i - a_j} d\sigma \Bigg[\int_0^{b_j} d\lambda \Big(T(\sigma, \sigma_1, \sigma_5, -\lambda, \lambda_1, \lambda_2) \\ & + T(\sigma, \sigma_1, \sigma_5, \lambda_3, \lambda_4, -\lambda_4) \Big) \\ & + \int_0^{b_i - b_j} d\lambda T(\sigma, \sigma_1, \sigma_5, \lambda, \lambda_1, \lambda_5) \Bigg] \Bigg\}, \end{aligned} \tag{E.7}$$

where

$$\sigma_1 = \sigma - a_i,$$
$$\sigma_2 = 2a_j - a_i - \sigma,$$
$$\sigma_3 = \sigma + a_i - a_j,$$
$$\sigma_4 = \sigma - a_j,$$
$$\sigma_5 = 2a_j - a_i + \sigma,$$

$$\begin{aligned}
\lambda_1 &= \lambda - b_i, \\
\lambda_2 &= 2b_j - b_i - \lambda, \\
\lambda_3 &= \lambda + b_i - b_j, \\
\lambda_4 &= \lambda - b_j, \\
\lambda_5 &= 2b_j - b_i + \lambda.
\end{aligned}$$

The T functions in (E.7) have the expression

$$\begin{aligned}
T(x,\nu_1,\nu_2,y,\mu_1,\mu_2) &= G(x_{0_i} - x_{0_j} + x, y_{0_i} - y_{0_j} + y) \\
&\cdot\Big[c_x M_-(x,\nu_1,\nu_2,s_m,d_m) M_+(y,\mu_1,\mu_2,s_n,d_n) \\
&+c_y M_+(x,\nu_1,\nu_2,s_m,d_m) M_-(y,\mu_1,\mu_2,s_n,d_n) \\
&+c_z M_+(x,\nu_1,\nu_2,s_m,d_m) M_+(y,\mu_1,\mu_2,s_n,d_n)\Big], \quad \text{(E.8)}
\end{aligned}$$

where G denotes the free space Green's function, while the $M_\pm$ quantity reads

$$\begin{aligned}
M_\pm(\sigma,v_1,v_2,p,q) &= \frac{2a_i}{\pi} \\
&\cdot\left\{\frac{1}{p}\sin\left[\frac{p\pi}{2a_i}(v_2 - v_1)\right]\cos\left[\pi\Big(p + \frac{\sigma q}{a_i} + \frac{p}{2a_i}(v_1 + v2)\Big)\right]\right. \\
&\left.\pm\frac{1}{q}\sin\left[\frac{q\pi}{2a_i}(v_2 - v_1)\right]\cos\left[\pi\Big(q + \frac{\sigma p}{a_i} + \frac{q}{2a_i}(v_1 + v2)\Big)\right]\right\}, \quad \text{(E.9)}
\end{aligned}$$

and

$$\begin{aligned}
s_m &= \frac{1}{2}\left(m + m'\frac{a_i}{a_j}\right), \\
d_m &= \frac{1}{2}\left(m - m'\frac{a_i}{a_j}\right), \\
s_n &= \frac{1}{2}\left(n + n'\frac{b_i}{b_j}\right), \\
d_n &= \frac{1}{2}\left(n - n'\frac{b_i}{b_j}\right).
\end{aligned}$$

Appendix F

Evaluation of the field radiated by an array of apertures

The field radiated by an array of apertures arranged on an infinitely extended, metallic flange can be evaluated at any point in free space if the distribution of the electromagnetic field at the apertures is known. By adopting a modal analysis, the field quantities inside the waveguides, close to the aperture, can be easily calculated once the mode amplitudes are indicated. The array excitation is commonly described by a column vector $[a]$ representing the amplitudes and the phases of the direct waves reaching the apertures. In order to evaluate the mode amplitudes ($[V]$) it is necessary to combine the *imposed* excitation $[a]$ with the complex amplitudes of the reflected waves $[b]$, which are found with the help of the already known array scattering matrix $[S]$ (3.20).

$$[V] = ([U] + [S]) \cdot [a]. \tag{F.1}$$

Again, similar to the evaluation of the mutual coupling admittances (Section 3.2) there are two different approaches in the representation of the radiated field:

- the spectral technique, which makes use of the Fourier transforms;
- the spatial technique, which is based on the Green's function.

In the followings these methods will be presented briefly.

Spectral technique

The theoretical prerequisites of this method have been already discussed in the Section 3.2. By adopting the notations introduced in that section the Cartesian components of the electric field intensity at any point in the free space, identified by the position vector $\boldsymbol{r}$, are given by:

$$\begin{bmatrix} E_x \\ E_y \\ E_z \end{bmatrix}(\boldsymbol{r}) = \frac{1}{4\pi}\int_{-\infty}^{+\infty}\int_{-\infty}^{+\infty}\sum_{i=1}^{N}\sum_{p=1}^{M_i}\frac{V_p^i}{\sqrt{Y_p^i}}\begin{bmatrix} C_x \\ C_y \\ C_z \end{bmatrix}_p^i e^{-\mathrm{j}\boldsymbol{k}\cdot\boldsymbol{r}}\, dk_x dk_y. \quad \text{(F.2)}$$

Correspondingly the components of the magnetic field strength read:

$$\begin{aligned}\begin{bmatrix} H_x \\ H_y \\ H_z \end{bmatrix}(\boldsymbol{r}) &= -\frac{1}{4\pi^2 k\eta}\int_{-\infty}^{+\infty}\int_{-\infty}^{+\infty}\sum_{i=1}^{N}\sum_{p=1}^{M_i}\frac{V_p^i}{\sqrt{Y_p^i}}\begin{bmatrix} k_zC_y - k_yC_z \\ k_xC_z - k_zC_x \\ k_yC_x - k_xCy \end{bmatrix}_p^i \\ &\quad \cdot e^{-\mathrm{j}\boldsymbol{k}\cdot\boldsymbol{r}}\, dk_x dk_y. \end{aligned} \quad \text{(F.3)}$$

Note that in (F.2) and (F.3) the following entry was used

$$C_z = \frac{k_xC_x + k_yC_y}{k_z}. \quad \text{(F.4)}$$

The double integrals in (F.2) and (F.3) are quite complicated even for simple problems. Noteworthy simplifications of these integrals can be achieved if the observation is restricted to the far-field region of the antenna (see [11, p. 141] for a definition of the far-field concept). Many antenna parameters, as for example the directivity, the beamwidth and the side lobes level, are directly related to the distribution of the electromagnetic field in the far zone. For large values of $|\boldsymbol{k}\cdot\boldsymbol{r}|$ it is possible to apply the method of *stationary phase* ([11, p. 922]) and to find asymptotical solutions of (F.2) and (F.3), respectively. The far-field expressions of the electric and magnetic field intensities in polar coordinates (r,θ,ϕ) can be derived from [11, p. 629]:

$$\begin{aligned}\boldsymbol{E}(r,\theta,\phi) &\approx \mathrm{j}\frac{ke^{-\mathrm{j}kr}}{2\pi r}\sum_{i=1}^{N}\sum_{p=1}^{M_i}\frac{V_p^i}{\sqrt{Y_p^i}} \\ &\quad \cdot\left\{\mathbf{u}_\theta\left[C_{p,x}^i(k_x,k_y)\cos\phi + C_{p,y}^i(k_x,k_y)\sin\phi\right]\right. \\ &\quad \left. + \mathbf{u}_\phi\cos\theta\left[-C_{p,x}^i(k_x,k_y)\sin\phi + C_{p,y}^i(k_x,k_y)\cos\phi\right]\right\}, \end{aligned} \quad \text{(F.5)}$$

$$\boldsymbol{H}(r,\theta,\phi) \approx \sqrt{\frac{\epsilon^{(2)}}{\mu^{(2)}}}\left[\mathbf{u}_r\times\boldsymbol{E}(r,\theta,\phi)\right], \quad \text{(F.6)}$$

where the k_x and k_y wavenumbers are expressed in polar coordinates by:

$$k_x = k \sin\theta \cos\phi, \tag{F.7}$$

$$k_y = k \sin\theta \sin\phi. \tag{F.8}$$

Equations (F.5) and (F.6) indicate that the electromagnetic quantities in the far field of an array antenna can be approximated with closed form expressions. Therefore, no numerical integration is required for the estimation of the array radiation pattern.

Spatial technique

A classical approach to the problem of calculating the radiated field by electric or/ and magnetic sources is based on the concept of the *vector potential functions* ([11, p. 116]). The most common vector potential functions are $\boldsymbol{A}$ (the magnetic vector potential) and $\boldsymbol{F}$ (the electric vector potential). These auxiliary potentials can be easily expressed when the source of radiation is known in terms of a harmonic electric current $\boldsymbol{J}$ and a harmonic magnetic current $\boldsymbol{M}$ [11, p. 120]). For an array of aperture radiators deployed on an infinitely extended metallic flange, the application of the *Love's equivalence principle* [10, 85] will lead to the following relations between the field distribution in the apertures and the equivalent electric and magnetic currents:

$$\begin{aligned} \boldsymbol{M} &= \begin{cases} -2\boldsymbol{n} \times \boldsymbol{E}_t^i & \text{on } S_i, \;\; i = 1 \cdots N \\ 0 & \text{elsewhere} \end{cases}, \\ \boldsymbol{J} &= 0 \qquad\qquad\qquad\qquad \text{everywhere}, \end{aligned} \tag{F.9}$$

where $\boldsymbol{n}$ represents the unit vector normal to the aperture. By assuming that the array antenna is located in the $x\mathcal{O}y$ plane, the normal vector $\boldsymbol{n}$ coincides with the unit vector along the $\mathcal{O}z$ axis, denoted by $\boldsymbol{u}_z$. Furthermore, the vector potentials are given by ([11, p. 582]):

$$\boldsymbol{F} = \frac{\epsilon^{(2)}}{4\pi} \iint_S \boldsymbol{M} \frac{e^{-\mathrm{j}kR}}{R} \, dS', \tag{F.10}$$

$$\boldsymbol{A} = \frac{\mu^{(2)}}{4\pi} \iint_S \boldsymbol{J} \frac{e^{-\mathrm{j}kR}}{R} \, dS' = 0, \tag{F.11}$$

where $R = \sqrt{(x-x')^2 + (y-y')^2 + (z-z')^2}$ denotes the relative distance between the source point (x', y', z') and the observation point (x, y, z). Finally, the electric and magnetic field strength at a point in free space read

([11, p. 121]):

$$\boldsymbol{E} = -\frac{1}{\epsilon^{(2)}}\boldsymbol{\nabla}\times\boldsymbol{F}, \tag{F.12}$$

$$\boldsymbol{H} = -\mathrm{j}\omega\boldsymbol{F} - \mathrm{j}\frac{1}{\omega\mu^{(2)}\epsilon^{(2)}}\boldsymbol{\nabla}(\boldsymbol{\nabla}\cdot\boldsymbol{F}). \tag{F.13}$$

By making use of the relations (3.3), (F.1), (F.9), (F.10) in (F.13) the Cartesian components of the radiated electric field strength become:

$$E_x(\boldsymbol{r}) = -\frac{1}{2\pi}\sum_{i=1}^{N}\sum_{p=1}^{M_i}\frac{V_p^i}{\sqrt{Y_p^i}}\iint\limits_{S_i} e_{x,p}^i\frac{\partial}{\partial z}\left(\frac{e^{-\mathrm{j}kR}}{R}\right)\,dS', \tag{F.14}$$

$$E_y(\boldsymbol{r}) = -\frac{1}{2\pi}\sum_{i=1}^{N}\sum_{p=1}^{M_i}\frac{V_p^i}{\sqrt{Y_p^i}}\iint\limits_{S_i} e_{y,p}^i\frac{\partial}{\partial z}\left(\frac{e^{-\mathrm{j}kR}}{R}\right)\,dS', \tag{F.15}$$

$$E_z(\boldsymbol{r}) = \frac{1}{2\pi}\sum_{i=1}^{N}\sum_{p=1}^{M_i}\frac{V_p^i}{\sqrt{Y_p^i}}\iint\limits_{S_i}\left\{e_{x,p}^i\frac{\partial}{\partial x}\left(\frac{e^{-\mathrm{j}kR}}{R}\right) + e_{y,p}^i\frac{\partial}{\partial y}\left(\frac{e^{-\mathrm{j}kR}}{R}\right)\right\}\,dS'. \tag{F.16}$$

Analogously, those of the magnetic field strength read

$$H_x(\boldsymbol{r}) = -\frac{\mathrm{j}}{2\pi\omega\mu}\sum_{i=1}^{N}\sum_{p=1}^{M_i}\frac{V_p^i}{\sqrt{Y_p^i}}\iint\limits_{S_i}\left\{e_{y,p}^i\frac{\partial^2}{\partial x^2}\left(\frac{e^{-\mathrm{j}kR}}{R}\right) - e_{x,p}^i\frac{\partial^2}{\partial y\partial x}\left(\frac{e^{-\mathrm{j}kR}}{R}\right) + k^2 e_{x,p}^i\frac{e^{-\mathrm{j}kR}}{R}\right\}\,dS', \tag{F.17}$$

$$H_y(\boldsymbol{r}) = -\frac{\mathrm{j}}{2\pi\omega\mu}\sum_{i=1}^{N}\sum_{p=1}^{M_i}\frac{V_p^i}{\sqrt{Y_p^i}}\iint\limits_{S_i}\left\{e_{y,p}^i\frac{\partial^2}{\partial x\partial y}\left(\frac{e^{-\mathrm{j}kR}}{R}\right) - e_{x,p}^i\frac{\partial^2}{\partial y^2}\left(\frac{e^{-\mathrm{j}kR}}{R}\right) - k^2 e_{x,p}^i\frac{e^{-\mathrm{j}kR}}{R}\right\}\,dS', \tag{F.18}$$

$$H_z(\boldsymbol{r}) = -\frac{\mathrm{j}}{2\pi\omega\mu}\sum_{i=1}^{N}\sum_{p=1}^{M_i}\frac{V_p^i}{\sqrt{Y_p^i}}\iint\limits_{S_i}\left\{e_{y,p}^i\frac{\partial^2}{\partial x\partial z}\left(\frac{e^{-\mathrm{j}kR}}{R}\right) - e_{x,p}^i\frac{\partial^2}{\partial y\partial z}\left(\frac{e^{-\mathrm{j}kR}}{R}\right)\right\}\,dS'. \tag{F.19}$$

It is worth observing that the derivatives of the Green's function in the above relations are taken with respect to the observation coordinates (x, y, z) whereas the integrals are performed on the apertures coordinates (x', y').

Simplified expressions of the radiated field quantities can be derived under the far field assumption. For far field observations R can be approximated by:

$$\begin{array}{rcll} R & \approx & r - r'\cos\psi & \text{for phase variation,} \\ R & \approx & r & \text{for amplitude variation,} \end{array} \tag{F.20}$$

where $r = |\boldsymbol{r}|$ represents the distance to the observation point and $r'\cos\psi = (x'\sin\theta\cos\phi + y'\sin\theta\sin\phi)$, with (x', y') denoting the coordinates of the source point in the $x\mathcal{O}y$ plane.

Combining (3.3), (F.1), (F.9), (F.10), (F.13) and (F.20) the far-field expressions of the electric and magnetic field strengths in polar coordinates (r, θ, ϕ) yield:

$$\boldsymbol{E}(r,\theta,\phi) \approx \mathrm{j}\frac{ke^{-\mathrm{j}kr}}{4\pi r}\sum_{i=1}^{N}\left[-\mathbf{u}_\theta L_\phi^i + \mathbf{u}_\phi L_\theta^i\right], \tag{F.21}$$

$$\boldsymbol{H}(r,\theta,\phi) \approx \mathrm{j}\frac{ke^{-\mathrm{j}kr}}{4\pi r\eta}\sum_{i=1}^{N}\left[-\mathbf{u}_\theta L_\theta^i - \mathbf{u}_\phi L_\phi^i\right], \tag{F.22}$$

where

$$L_\theta^i = 2\sum_{p=1}^{M_i}\frac{V_p^i}{\sqrt{Y_p^i}}\iint\limits_{S_i}\left[e_{y,p}^i\cos\phi - e_{x,p}^i\sin\phi\right]\cos\theta e^{\mathrm{j}kr'\cos\psi}, \tag{F.23}$$

$$L_\phi^i = 2\sum_{p=1}^{M_i}\frac{V_p^i}{\sqrt{Y_p^i}}\iint\limits_{S_i}\left[-e_{y,p}^i\sin\phi - e_{x,p}^i\cos\phi\right]e^{\mathrm{j}kr'\cos\psi}, \tag{F.24}$$

and $e_{y,p}^i$, $e_{x,p}^i$ denote the modal electric field components (along the $\mathcal{O}x$ and $\mathcal{O}y$ axis, restively) of the p^{th} mode in the aperture i.

As a final remark, it is pointed out that one can easily verify that the far field expressions (F.21) and (F.22) are identical to those obtained by means of the spectral technique (F.5) and (F.6), respectively.

Bibliography

[1] Y.I. Abramovich, N.K. Spencer, and A.Y. Gorokhov. Identifiability and manifold ambiguity in DOA estimation for nonuniform linear antenna arrays. In *Proceedings of the ICASSP '99 Conference*, volume 5, pages 2845–2848, Mar. 1999.

[2] E. Anderson, Z. Bai, C. Bischof, S. Blackford, J. Demmel, J. Dongarra, J. Du Croz, A. Greenbaum, S. Hammarling, A. McKenney, and D. Sorensen. *LAPACK User's Guide*. SIAM, Philadelphia, third edition, 1999.

[3] M. Andreasen. Linear arrays with variable interelement spacings. *IEEE Transactions on Antennas and Propagation*, 10(2):137–143, Mar. 1962.

[4] P. Arcioni. Fast evaluation of modal coupling coefficients of waveguide step discontinuities. *IEEE Microwave and Guided Wave Letters*, 6(6):232–234, Jun. 1996.

[5] P. Arcioni, M. Bressan, G. Conciauro, and L. Perregrini. Wideband modeling of arbitrarily shaped E-plane waveguide components by the boundary integral-resonant mode expansion method. *IEEE Transactions on Microwave Theory and Techniques*, 44(11):2083–2092, Nov. 1996.

[6] R. Arora and N. Krisnamacharyulu. Synthesis of unequally spaced arrays using dynamic programming. *IEEE Transactions on Antennas and Propagation*, 16(5):593–595, Sep. 1968.

[7] T.A. Axness, R.V. Coffman, B.A. Kopp, and K.W. O'Haver. Shared aperture technology development. *Johns Hopkins APL Technical Digest*, 17:285–294, 1996.

[8] M. Bailey and C. Bostian. Mutual coupling in a finite planar array of circular apertures. *IEEE Transactions on Antennas and Propagation*, 22(2):178–184, Mar. 1974.

[9] M.C. Bailey. Technique for extension of small antenna array mutual-coupling data to larger antenna arrays. Technical Paper 3603, NASA, Aug. 1996.

[10] C.A. Balanis. *Advanced Engineering Electromagnetics*. John Wiley & Sons Inc., New York, second edition, 1989.

[11] C.A. Balanis. *Antenna Theory: Analysis and Design*. John Wiley & Sons Inc., New York, second edition, 1997.

[12] H. Baudrand, J.-W.Tao, and J. Atechian. Study of radiating properties of open-ended rectangular waveguides. *IEEE Transactions on Antennas and Propagation*, 36(8):1071–1077, Aug. 1988.

[13] A. K. Bhattacharyya. A modular approach for probe-fed and capacitively coupled multilayered patch arrays. *IEEE Transactions on Antennas and Propagation*, 45:193–202, Feb. 1997.

[14] T.S. Bird. Mode coupling in a planar circular waveguide array. *IEE Journal on Microwaves, Optics and Acoustics*, 3:172–180, Sep. 1979.

[15] T.S. Bird. Mutual coupling in finite coplanar rectangular waveguide array. *Electronics Letters*, 23(10):1199–1201, Nov. 1987.

[16] T.S. Bird. Analysis of mutual coupling in finite arrays of different-sized rectangular waveguides. *IEEE Transactions on Antennas and Propagation*, 38(2):166–172, 1990.

[17] T.S. Bird and D.G. Batemann. Mutual coupling between rotated horns in a ground plane. *IEEE Transactions on Antennas and Propagation*, 42(7):1000–1006, 1994.

[18] D. Bodnar and D. Paris. New variational principle in electromagnetics. *IEEE Transactions on Antennas and Propagation*, 18(2):216–223, Mar. 1970.

[19] M. Bozzi, G. Conciauro, and L. Perregrini. On the evaluation of modal coupling coefficients by contour integrals. *IEEE Transactions on Microwave Theory and Techniques*, 50(7):1853–1855, Jul. 2002.

[20] M. G. Bray, D. H. Werner, D. W. Boeringer, and D. W. Machuga. Optimization of thinned aperiodic linear phased arrays using genetic algorithms to reduce grating lobes during scanning. *IEEE Transactions on Antennas and Propagation*, 50(12):1732–1742, Dec. 2002.

[21] E. Brookner, editor. *Practical phased-array antenna systems*. Artech House, Boston, 1991.

[22] A. Camps, A. Cardama, and D. Infantes. Synthesis of large low-redundancy linear arrays. *IEEE Transactions on Antennas and Propagation*, 49(12):1881–1883, Dec. 2002.

[23] Byong Kun Chang, Xinyu Ma, and H. B. Sequeira. Minimax-maxmini algorithm: a new approach to optimization of the thinned antenna arrays. In *Antennas and Propagation Society International Symposium*, volume 1, pages 514–517, 1994.

[24] J.-C. Cheng, N. I. Dib, and L. P. B. Katehi. Theoretical modeling of cavity-backed patch antennas using a hybrid technique. *IEEE Transactions on Antennas and Propagation*, 43:1003–1008, Sep. 1995.

[25] S. Cogollos, S. Marini, P. Soto, H. Esteban, J. V. Morro, V. E. Boria, and B. Gimeno. Modal computation of arbitrary waveguides composed of linear, circular and elliptical arcs. *IEEE Transactions on Microwave Theory and Techniques*, 51(12):2378–2390, Dec. 2003.

[26] R.E. Collin. *Field Theory of Guided Waves*. The IEEE Press Series on Electromagnetic Wave Theory. IEEE Press, Piscataway, 1991.

[27] C.I. Coman, I.E. Lager, and L.P. Ligthart. Educational software tool for the analysis of flanged, waveguide end antennas. In *Proceedings of the 32nd European Microwave Conference*, volume 1, pages 251–254, Milano, 2002.

[28] C.I. Coman, I.E. Lager, and L.P. Ligthart. Shared aperture sparse array antenna for wide band applications. In *Proceedings of the 33rd European Microwave Conference*, volume 1, pages 515–518, Munich, 2003.

[29] C.I. Coman, I.E. Lager, and L.P. Ligthart. The design of a matching circuit for dielectric-filled open-ended waveguide antenna. In *Proceedings of the First European Radar Conference, EURAD 2004*, volume 1, pages 73–76, Amsterdam, 2004.

[30] C.I. Coman, I.E. Lager, and L.P. Ligthart. Optimization of linear sparse array antennas consisting of electromagnetically coupled apertures. In *Proceedings of the First European Radar Conference, EURAD 2004*, volume 1, pages 301–304, Amsterdam, 2004.

[31] C.I. Coman, I.E. Lager, and L.P. Ligthart. Sparse array antenna - a neural network approach. In *Proceedings of the International Symposium on Antennas and Propagation, ISAP 2004*, volume 2, pages 1221–1224, 2004.

[32] C.I. Coman, I.E. Lager, and L.P. Ligthart. A deterministic solution to the problem of interleaving multiple sparse array antennas. In *Proceedings of the Second European Radar Conference, EURAD 2005*, volume 1, Paris, 2005.

[33] C.I. Coman, I.E. Lager, and L.P. Ligthart. The design of shared aperture antennas consisting of differently sized elements. *IEEE Transactions on Antennas and Propagation*, Feb. 2006. In Press.

[34] G. Conciauro, P. Arcioni, M. Bressan, and L. Perregrini. Wideband modeling of arbitrarily shaped H-plane waveguide components by the boundary integral-resonant mode expansion method. *IEEE Transactions on Microwave Theory and Techniques*, 44(7):1057–1066, Jul. 1996.

[35] G. Conciauro, M. Bressan, and C. Zuffada. Waveguide modes via an integral equation leading to a linear matrix eigenvalue problem. *IEEE Transactions on Microwave Theory and Techniques*, MTT-32(11):1495–1504, Nov. 1984.

[36] G. Conciauro, M. Guglielmi, and R. Sorrentino. *Advanced Modal Analysis*. John Wiley and Sons Ltd., Chichester, England, 2000.

[37] Rogers Corporation Advanced Circuit Materials Division. High frequency laminates literature index. *http://www.rogerscorporation.com*, Jul. 2005.

[38] W. Croswell, R. Rudduck, and D.Hatcher. The admittance of a rectangular waveguide radiating into a dielectric slab. *IEEE Transactions on Antennas and Propagation*, 15(5):627–633, Sep. 1967.

[39] W. Croswell, W. Taylor, C. Swift, and C.Cockrell. The input admittance of a rectangular waveguide-fed aperture under an inhomogeneous plasma: Theory and experiment. *IEEE Transactions on Antennas and Propagation*, 16(4):475–487, Jul. 1968.

[40] M. A. González de Aza, J. A. Encinar, and J. Zapata. Radiation pattern computation of cavity-backed and probe-fed stacked microstrip patch arrays. *IEEE Transactions on Antennas and Propagation*, 48:502–509, Apr. 2000.

[41] M. A. González de Aza, J. A. Encinar, J. Zapata, and M. Lambea. Full wave analysis of cavity-backed and probe-fed microstrip patch arrays by a hybrid mode-matching, generalized scattering matrix and finite-element method. *IEEE Transactions on Antennas and Propagation*, 46:234–242, Feb. 1998.

[42] M. A. González de Aza, J. Zapata, and J. A. Encinar. Broadband cavity-backed and capacitively probe-fed microstrip patch arrays. *IEEE Transactions on Antennas and Propagation*, 48:784–789, May 2000.

[43] C.L. Dolph. A current distribution for broadside arrays which optimizes the relationship between beam width and sidelobe level. *Proc. IRE*, 34:335–348, Jun. 1946.

[44] R.F. Follett and J.P. Donohoe. A wideband, high-resolution, low probability of detection FFT beamformer. *IEEE Jour. on Oceanic Engineering*, 19:175–182, Apr. 1994.

[45] N. Fourikis. *Advanced Array Systems, Applications and RF Technologies*. Signal Processing and its Applications. Academic Press, London, 2000.

[46] Shivey D. G. and Stutzman W. L. Wide band array with variable element sizes. *IEE Proc. Part H: Microwave, Optical Antennas*, 137:238–241, Aug. 1990.

[47] J. Galejs. Admittance of a waveguide radiating into a stratified plasma. *IEEE Transactions on Antennas and Propagation*, 13(1):64–70, Jan. 1965.

[48] B. S. Garbow, J. M. Boyle, J. J. Dougarde, and C. B. Moler. *Matrix eigensystem routines - EISPACK guide extension*. Number 51 in Lecture Notes in Computer Science. Springer-Verlag, 1977.

[49] R. Garg, P. Bhartia, Bahl, and I. A. Ittipiboon. *Microstrip Antenna Design Handbook*. Artech House, Boston, 2001.

[50] G. G. Gentili, F. Perez-Martinez, M. Salazar-Palma, and L. Garcia-Castillo. Analysis of single and stacked microstrip patch antennas residing in a cavity by a Green's function technique. In *Proceedings of the Antennas and Propagation Society International Symposium*, volume 2, pages 944–947, 1994.

[51] P.J. Gibson. The Vivaldi Aerial. In *Proceedings of the 9th European Microwave Conference*, pages 101–105, 1979.

[52] A. Gustafsson, R. Malmqvist, L. Pettersson, L-G. Huss, M. Alfredson, S. Lindström, I. Ferrer, P. Grahn, S. Leijon, C. Samuelsson, T. Nilsson, A. Pohl, A. Ouacha, B. Carlegrim, S. Hagelin, and R. Erickson. A very thin and compact smart skin X-band digital beamforming antenna. In *Proceedings of the First European Radar Conference, EURAD 2004*, volume 1, pages 313–316, Amsterdam, 2004.

[53] M. Hajian, D.P. Tran, and L.P. Ligthart. Design of a wideband miniature dielectric-filled waveguide antenna for collision-avoidance radar. *IEEE Antennas and Propagation Magazine*, 42(1):34–40, Feb. 2000.

[54] R. C. Hansen. Fundamental limitations in antennas. *Proc. IEEE*, 69(2), 1981.

[55] R. C. Hansen. *Phased array antennas*. John Wiley & Sons Inc., New York, 1998.

[56] R.F. Harrington. *Time Harmonic Electromagnetic Field*. McGraw-Hill Book Company Inc., New York, 1961.

[57] R.F. Harrington and J.R. Mautz. A generalized network formulation for the aperture problems. *IEEE Transactions on Antennas and Propagation*, AP-24:870–873, Nov. 1976.

[58] R. L. Haupt. Thinned array using genetic algorithms. *IEEE Transactions on Antennas and Propagation*, 42(7):993–999, Jul. 1994.

[59] C. Hemmi, R.T. Dover, F. German, and A. Vespa. Multifunctional wide-band array design. *IEEE Transactions on Antennas and Propagation*, AP-47(3):425–431, Mar. 1999.

[60] H. Holter, T.H. Chio, and D.H. Schaubert. Experimental results of 144-element dual-polarized endfire tapered-slot phased arrays. *IEEE Transactions on Antennas and Propagation*, 48(11):1707–1718, Nov. 2000.

[61] H. Holter and H. Steyskal. On the size requirement for finie phased-arrays models. *IEEE Transactions on Antennas and Propagation*, 50(6):636–840, Jun. 2002.

[62] L.-G. Huss, R. Gunnarsson A. Pohl, A. Ouacha, and A. Gustafsson. Array antenna module for an X-band smart skin radar receiver. In *Proceedings of the Nordic Antenna Symposium, Antenn03*, volume 1, pages 273–278, 2003.

[63] The Institute of Electrical and Electronics Engineers. IEEE standard definitions of terms for antennas. IEEE Std 145-1993, Mar. 1993.

[64] A. Ishimaru. Theory of unequally-spaced arrays. *IEEE Transactions on Antennas and Propagation*, 10(6):691–702, Nov. 1962.

[65] R. Janaswamy and D.H. Schaubert. Analysis of the tapered slot antenna. *IEEE Transactions on Antennas and Propagation*, AP-35(9):1058–1065, Sept. 1987.

[66] J.-M. Jin and J. L. Volakis. A hybrid finite element method for scattering and radiation by microstrip path antennas and arrays residing in a cavity. *IEEE Transactions on Antennas and Propagation*, 39:1598–1604, Nov. 1991.

[67] M. A. Khayat, J. T. Williams, D. R. Jackson, and S. A. Long. Mutual coupling between reduced surface-wave microstrip antennas. *IEEE Transactions on Antennas and Propagation*, 48:1581–1593, Oct. 2000.

[68] Y. Kim and D.L. Jaggard. The fractal random array. *Proceedings IEEE*, 74(9):1278–1280, 1986.

[69] L. E. Kopilovich. On perfect binary arrays. *Electronics Letters*, 24(9):566–567, Apr. 1988.

[70] L. E. Kopilovich and L. G. Sodin. Two-dimensional aperiodic antenna arrays with a low side-lobe level. *IEE Procceding Part H*, 138(3):233–237, Jun. 1991.

[71] D. G. Kurup, M. Himdi, and A. Rydberg. Synthesis of uniform amplitude unequally spaced antenna arrays using the differential evolution algorithm. *IEEE Transactions on Antennas and Propagation*, 51(9):2210–2217, Sep. 2003.

[72] J.C. Lagarias, J.A. Reeds, M.H. Wright, and P.E. Wright. Convergence properties of the Nelder–Mead Simplex method in low dimensions. *SIAM Journal on Optimization*, 9(1):112–147, 1998.

[73] I.E. Lager, C.I. Coman, and A.T. de Hoop. WGEMLab – a simulation platform for the analysis of rectangular waveguide aperture radiation. In *Proceedings of the CEFC 2002*, pages 251–254, Perugia, 2002.

[74] I.E. Lager, C.I. Coman, and A.T. de Hoop. WGEMLab - a simulation platform for the analysis of rectangular waveguide aperture radiation. *IEEE Transactions on Magnetics*, 39(3):1697–1700, May 2003.

[75] I.E. Lager, C.I. Coman, and L.P. Ligthart. The modelling of 'local details' in the field distribution and their impact on the global economy of the solution. In *Proceedings of the Progress in Electromagnetics Research Symposium – PIERS 2004*, pages 33–36, 2004.

[76] J. J. Lee and R. S. Chu. Aperture matching of a dielectric loaded circular waveguide element array. *IEEE Transactions on Antennas and Propagation*, 37(3):395–399, Mar. 1989.

[77] D. G. Leeper. Thinned aperiodic antenna arrays with improved peak sidelobe level control. U.S. Patent 4 071 848, Jan. 1978.

[78] D.G. Leeper. Isophoric arrays - massively thinned phased arrays with well-controlled sidelobes. *IEEE Transactions on Antennas and Propagation*, 47(12):1825–1835, Dec. 1999.

[79] L. Lewin. *Advanced Theory of Waveguides*. MIT Radiation Laboratory Series. Iliffe & Sons, London, 1951.

[80] L. P. Ligthart. *Antenna Design and Characterization Based on the Elementary Antenna Concept*. PhD thesis, Delft University of Technology, Pijnacker, Dec. 1985.

[81] Y. Lo. A mathematical theory of antenna arrays with randomly spaced elements. *IEEE Transactions on Antennas and Propagation*, 12(3):257–268, May 1964.

[82] Y. Lo and S. Lee. A study of space-tapered arrays. *IEEE Transactions on Antennas and Propagation*, 14(1):22–30, Jan. 1966.

[83] H. Loui, J. P. Weem, and Z. Popovic. A dual-band dual-polarized nested Vivaldi slot array with multilevel ground plane. *IEEE Transactions on Antennas and Propagation*, 51(9):2168–2176, Sep. 2003.

[84] H. Loui, J.P. Weem, and Z. Popovic. A dual-band dual-polarized nested Vivaldi slot array withh multilevel groung plane. *IEEE Transactions on Antennas and Propagation*, 51(9):2168–2175, Sep. 2003.

[85] A.E.H. Love. The integration of the equations of propagation of electric waves. *Phil. Trans. Roy. Soc. London, Ser. A*, 197:1–45, 1901.

[86] R. MacPhie and A. Zaghloul. Radiation from a rectangular waveguide with infinite flange – exact solution by the correlation matrix method. *IEEE Transactions on Antennas and Propagation*, 28(4):497–503, Jul. 1980.

[87] R. H. MacPhie. Thinned coincident arrays for the direct measurement of the principal solution in radio astronomy. *IEEE Transactions on Antennas and Propagation*, 51(4):788–793, Apr. 2003.

[88] R. Mailloux. First-order solutions for mutual coupling between waveguides which propagate two orthogonal modes. *IEEE Transactions on Antennas and Propagation*, 17(6):740–746, Nov. 1969.

[89] R. Mailloux. Radiation and near-field coupling between two collinear open-ended waveguides. *IEEE Transactions on Antennas and Propagation*, 17(1):49–55, Jan. 1969.

[90] N. Marcuvitz. *Waveguide Handbook*. MIT Radiation Laboratory Series. McGraw-Hill, New York, 1951.

[91] N. Marcuvitz. *Waveguide Handbook*. IEE Electromagnetic Waves Series 21. Peter Peregrinus Ltd., London, 1986.

[92] J.R. Mautz and R.F. Harrington. Transmission from a rectangular waveguide into half space through a rectangular aperture (computer program descriptions). *IEEE Transactions on Microwave Theory and Techniques*, 26(1):44–45, Jan. 1978.

[93] C. A. Meijer. Simulated annealing in the design of thinned arrays having low sidelobe levels. In *Proceedings of the South African Symposium on Communications and Signal Processing, COMSIG '98.*, pages 361–366, 1998.

[94] C. Metz, L. C. Stange, A.F. Jacob, and E. Lissel. Performance of thinned antenna arrays using nonlinear processing in DBF radar applications. In *Proceedings of the IEEE MTT-S International Microwave Symposium*, volume 1, pages 275–278, 2001.

[95] A. Moffet. Minimum-redundancy linear arrays. *IEEE Transactions on Antennas and Propagation*, 16(2):172–175, Mar. 1968.

[96] M. Mongiardo and T. Rozzi. Singular integral equation analysis of flange-mounted rectangular waveguide radiators. *IEEE Transactions on Antennas and Propagation*, 41(5):556–565, May 1993.

[97] M. Mongiardo, L. Tarricone, and C. Tomassoni. A comparison of numerical methods for the full-wave analysis of flanged mounted rectangular apertures. *International Journal of Numerical Analysis & Modeling*, (13):21–35, 2000.

[98] S.A.W. Moore and A.R. Moore. Dual frequency multi-function radar antenna research. In *Proceedings of the 10th International Conference on Antenna and Propagation, 14-17 April 1997*, pages 1.522–1.526. IEE, Apr. 1997.

[99] F.J.S. Moreira and J.R. Bergmann. Asymptotic approximations for the mutual coupling in finite arrays of rectangular waveguides. volume 2, pages 776–779. Proceedings of the 8$^{\text{th}}$ International Conference on Antennas and Propagation, 1993.

[100] A. Moumen. *Analysis and Synthesis of Compact Feeds for Large Multiple-Beam Reflector Antennas*. PhD thesis, Delft University of Technology, Delft, Mar. 2001.

[101] V. Murino, A. Trucco, and C. S. Regazzoni. Synthesis of unequally spaced arrays by simulated annealing. *IEEE Transactions on Signal Processing*, 44(1):119–122, Jan. 1996.

[102] V. Murino, A. Trucco, and A Tesei. Beam pattern formulation and analysis for wide-band beamforming systems using sparse array antenna. *Signal Processing*, 56:177–183, Jan. 1997.

[103] Boon Poh Ng, Meng Hwa Er, and Chichung Kot. A flexible array synthesis method using quadratic programming. *IEEE Transactions on Antennas and Propagation*, 41(11):1541–1550, Nov. 1993.

[104] F. L. Ng. Tabulation of methods for the numerical solution of the hollow waveguide problem. *IEEE Transactions on Microwave Theory and Techniques*, MTT-22(3):322–329, Mar. 1974.

[105] I. Nicolaescu, P. van Genderen, and J. Zijderveld. Archimedean spiral antenna used for stepped frequency radar - footprint measurements. In *Proceedings of the Antenna Measurement Techniques Association Conference, AMTA 2002*, pages 555–560, Nov. 2002.

[106] T. Numazaki, S. Mano, T. Katagi, and M. Mizusawa. An improved thinning method for density tapering of planar array antennas. *IEEE Transactions on Antennas and Propagation*, 35(9):1066–1070, Sep. 1987.

[107] A.J. Pafitt and T.S. Bird. Computation of aperture antenna mutual coupling using FDTD and Kirchoff field transformation. *Electronics Letters*, 34(12):1167–1168, Jun. 1998.

[108] P.D. Patel and M.C. Bailey. Effects of high-order mode coupling in dielectric covered finite array of dissimilar rectangular waveguides. *IEEE Transactions on Antennas and Propagation*, 45(12):1749–1757, Dec. 1997.

[109] J.S. Petko and D.H. Werner. Progressive evolution of fractal random arrays by generator mitosis. In *Proceedings of the IEEE Antennas and Propagation Society Symposium*, volume 3, pages 2305–2308, 2004.

[110] J.S. Petko and D.H. Werner. The autopolyploidy enhanced evolution of large-N fractal-random arrays. In *Proceedings of the IEEE International Radar Conference*, volume 1, pages 922–926, 2005.

[111] D. M. Pozar. *Microwave engineering*. John Wiley & Sons, third edition, 2005.

[112] D.M. Pozar and S. D. Targonski. A shared-aperture dual-band dual-polarized microstrip array. *IEEE Transactions on Antennas and Propagation*, 49(2):150–157, Feb. 2001.

[113] R. Redlich. Iterative least-squares synthesis of nonuniformly spaced linear arrays. *IEEE Transactions on Antennas and Propagation*, 21(1):106–108, Jan. 1973.

[114] M. J. Rossouw, J. Joubert, and D. A. McNamara. Thinned arrays using a modified minimum redundancy synthesis technique. *Electronics Letters*, 33(10):826–827, May 1997.

[115] G. Ruggerini. Numerical representation for finite arrays of rectangular waveguide apertures. In *Proceedings of the 8^{th} International Conference on Antennas and Propagation*, volume 2, pages 772–775, 1993.

[116] M.N.O. Sadiku. *Numerical Techniques in Electromagnetics*. CRC Press LLC, Boca Raton, 2001.

[117] E.D. Sharp. A triangular arrangement of planar-array elements that reduces the number needed. *IRE Transactions on Antennas and Propagation*, pages 126–129, Mar. 1961.

[118] D.G. Shively and W.L. Stutzman. Wideband arrays with variable element sizes. *IEE Proceedings Microwaves, Antennas and Propagation*, 137:238–240, Aug. 1990.

[119] M. Simeoni, C.I. Coman, and I.E. Lager. Patch end-launchers – a family of compact colinear coaxial-to-rectangular waveguide transitions. *IEEE Transactions on Microwave Theory and Techniques*. Accepted for publication.

[120] M. Simeoni, C.I. Coman, and I.E. Lager. Compact collinear end-launcher for rectangular waveguides. In *Proceedings of the IEEE MTT-S International Symposium, IMS 2005*, 2005.

[121] M. I. Skolnik, J. W. Sherman, and F. C. Ogg. Statistically designed density-tapered arrays. *IEEE Transactions on Antennas and Propagation*, 12(4):408–417, Jul. 1964.

[122] L.C. Stange, C. Metz, E. Lissel, and A.F. Jacob. Multiplicatively processed antenna arrays for DBF radar applications. *IEE Proceedings Microwaves, Antennas and Propagation*, 149(2):106–112, Apr. 2002.

[123] B. D. Steinberg. The peak sidelobe of the phased array having randomly located elements. *IEEE Transactions on Antennas and Propagation*, 20(2):129–136, Mar. 1972.

[124] B. D. Steinberg. *Principles of Aperture and Array System Design*. Wiley, 1976.

[125] B.G. Steinberg and H.M. Subbaram. *Microwave Imaging Techniques*. Wiley & Sons Inc., New York, 1991.

[126] S. D. Targonski, R. B. Waterhouse, and D. M. Pozar. Design of wideband aperture-stacked patch microstrip antennas. *IEEE Transactions on Antennas and Propagation*, 46:1245–1251, Sep. 1998.

[127] V. Teodoridis, T. Sphicopoulos, and F. E. Gardiol. The reflection from an open-ended rectangular waveguide terminated by a layered dielectric medium. *IEEE Transactions on Microwave Theory and Techniques*, 33(5):359–366, May. 1985.

[128] M. Tian. *Characterization of Miniature Dielectric-filled Open-ended Waveguide Antenna*. PhD thesis, Delft University of Technology, Delft, Oct. 1995.

[129] M. Tian, M. Hajian, D. P. Tran, and L. P. Ligthart. Air-gap technique for matching the aperture of miniature waveguide antennas. In *Proceedings of the Instrumentation and Measurement Technology Conference, 1993. IMTC/93*, pages 197–201, 1993.

[130] D. P. Tran, M. Hajian, M. Tian, and L.P. Ligthart. The E-plane stepped microstrip like antenna. In *Proceedings of the International Conference on Antennas and Propagation, ICAP '95*, pages 513–516, 1995.

[131] D. P. Tran, M. Tian, and L. P. Ligthart. Antenna element miniaturization and the use of airgap matching techniques. In *Proceedings of the Antennas and Propagation Society International Symposium*, volume 1, pages 286–287, Jun. 1994.

[132] D. P. Tran, M. Tian, and L. P. Ligthart. Theory and practice of a novel miniature radiator: the microstrip- like antenna. In *Proceedings of the 7^{th} Mediterranean Electrotechnical Conference*, pages 422–426, 1994.

[133] H.L. Van Trees. *Optimum Array Processing*, volume 4 of *Detection, Estimation, and Modulation Theory*. John Wiley & Sons, Inc., New York, 2002.

[134] A. Trucco. Thinning and weighting of large planar arrays by simulated annealing. *IEEE Transactions on Ultrasonics, Ferroelectrics and Frequency Control*, 46(2):347–355, Mar. 1999.

[135] A. Trucco. Synthesizing wide-band sparse arrays by simulated annealing. In *Proceedings of the MTS/IEEE Conference and Exhibition, OCEANS 2001*, volume 2, pages 989–994, Nov. 2001.

[136] C.-Y. Tseng and L.J. Griffiths. A simple algorithm to achieve desired patterns for arbitrary arrays. *IEEE Transactions on Signal Processing*, 40(11):2737–2746, Nov. 1992.

[137] H. Unz. Linear arrays with arbitrarily distributed elements. *IEEE Transactions on Antennas and Propagation*, AP-8:222–223, Mar. 1960.

[138] Fan Wang, V. Balakrishnan, P. Y. Zhou, J. J. Chen, R. Yang, and C. Frank. Optimal array pattern synthesis using semidefinite programming. *IEEE Transactions on Signal Processing*, 51(5):1172–1183, May 2003.

[139] R.J. Weber. *Introduction to Microwave Circuits. Radio Frequency and Design Applications*. IEEE Press, Piscataway, 2001.

[140] T. Weiland. Time domain electromagnetic field computation with finite difference methods. *International Journal of Numerical Modelling: Electronic Networks, Devices and Fields*, 9:295–319, Jul. 1996.

[141] D.H. Werner, M.A. Gingrich, and P.L. Werner. A self-similar fractal radiation pattern synthesis technique for reconfigurable multiband arrays. *IEEE Transactions on Antennas and Propagation*, 51(7):1486–1498, Jul. 2003.

[142] D.H. Werner, R.L. Haupt, and P.L. Werner. Fractal antenna engineering: the theory and design of fractal antenna arrays. *IEEE Antennas and Propagation Magazine*, 41(5):37–58, Oct. 1999.

[143] D.H. Werner, W. Kuhirun, and P.L. Werner. The Peano-Gosper fractal array. *IEEE Transactions on Antennas and Propagation*, 51(8):2063–2072, Aug. 2003.

[144] H. A. Wheeler. Fundamental limitations of small antennas. *Proc. IRE*, pages 1479–1488, Dec. 1947.

[145] H. A. Wheeler. Small antennas. *IEEE Transactions on Antennas and Propagation*, 23(4):462–469, Jul. 1975.

[146] H. A. Wheeler. The wide-band matching area for a small antenna. *IEEE Transactions on Antennas and Propagation*, AP-31(2):364–367, Mar. 1983.

[147] R. E. Willey. Space tapering of linear and planar arrays. *IEEE Transactions on Antennas and Propagation*, 10(4):369–377, Jul. 1962.

[148] K.T. Wong and M.D. Zoltowski. Sparse array aperture extension with dual-size spatial invariance for ESPRIT-based direction finding. In *Proceedings of the IEEE 39th Midwest symposium on Circuits and Systems*, volume 2, pages 691–694, Aug. 1996.

[149] T. Y. Yun, C. Wang, P. Zepeda, C. T. Rodenbeck, M. R. Coutant, M. Li, and K. Chang. A 10- to 21-GHz, low-cost, multifrequency, and full-duplex phased- array antenna system. *IEEE Transactions on Antennas and Propagation*, 50(5):641–650, May 2002.

[150] P. Y. Zhou, M. A. Ingram, and D. P. Anderson. Synthesis of minimax sidelobes for arbitrary arrays. *IEEE Transactions on Antennas and Propagation*, 46(11):1759–1760, Nov. 1998.

Summary

A novel solution for conceiving wide band (multi-band) array antennas is presented. The solution is based on the concept of interleaving sparse, sub-arrays operating at separate frequencies. Sparse array antennas offer two major advantages, namely: they have non-uniformly distributed elements, with possibly large distances between elements (this providing the necessary space for interleaving different sub-arrays), and they do not require the amplitude tapering of the elements for controlling the array radiation pattern.

In the first part of the thesis, the theoretical formulation of the electromagnetic problem is presented. Variants of the Mode Matching Method (MMM) have been developed for the full wave investigation of the elementary radiators and of the array configurations. The second part of the thesis is dedicated to the analysis and the design of elementary antennas, sparse array antennas and shared apertures consisting of interleaved sparse sub-arrays. Moreover, the impact of the technological aspects on the antenna performance are discussed and the measurements validating the simulated results are presented.

In the formulation of the numerical electromagnetic analysis method a special attention is given to the problem of computing the modes of uniform waveguide segments with arbitrary cross-section by means of the Boundary Integral - Resonant Mode Expansion (BI-RME). Numerous mathematical aspects related to the calculation of the BI-RME modes are presented. The problem of selecting the modes in the BI-RME method is extended and an analytical solution is proposed for the optimum rotation angle that should be used in the case of processing quasi-degenerate modes. It is also demonstrated that the BI-RME modes are quasi-orthogonal and that the orthogonality of these modes can be improved by increasing the number of canonical modes used in the series representation of the Green's function. The software implementations of the MMM/ BI-RME analysis is accurately investigated by solving a large number of test cases. Furthermore, the problem of evaluating the mutual coupling effect in arbitrary arrays consisting of differently sized, rectangular apertures is addressed. The analysis is done by means of the MMM, as well. The software implementation of this MMM variant is validated by studying different test configurations and observing specific aspects related to the electromagnetic field and to the scattering parameters

of the aperture antennas. A solution for the fast evaluation of the mutual coupling effect is proposed. This fast technique is based on a polynomial interpolation of the coupling admittances between the modes used for representing the field on the aperture antennas. The conducted numerical tests point to the conclusion that the modal techniques are the most appropriated full wave methods for the analysis of waveguide (like) antennas.

The developed modal analysis tools are subsequently used in the design of elementary antennas. A number of time efficient design procedures are presented in connection to two antenna topologies: the dielectric filled waveguide antennas with an air gap matching circuit and the cavity-backed, stacked-patch and probe fed antennas. In relation to the cavity-backed, stacked-patch antennas it is noted that the systematical design methodology adopted in this work has provided antenna models with bandwidths of around 10%. The numerical simulations are validated by comparisons with measurements performed on physical models. Technological aspects are meticulously investigated and some practical solutions are proposed in the context of simplifying the manufacturing process and reducing the fabrication cost.

The study of sparse array antenna is initiated by an exhaustive investigation of the design methods available in the literature. Particular aspects of the sparse array configurations are investigated by numerical and experimental studies. These studies concentrated on two relevant aspects, namely, the estimation of the matching properties of the individual radiators functioning in non-periodic, finite array environments, and the evaluation of the radiation properties of the sparse array antenna, while also accounting for the effect of the mutual coupling. The sparse techniques are also used for generating synthetic aperture radar imagines from ground penetrating radar measurements, this solution reducing significantly the required volume of acquisition data and the computing times. Another important finding is that the mutual coupling is not correlated in sparse array configuration and, therefore, the coupling effect has a reduced influence (compared to uniform arrays) on the performance of individual radiators while electronically scanning the antenna beam. This remark can be useful in designing array antennas characterized by wide angle impedance matching (WAIM) properties.

For implementing the concept of shared aperture based on sparse array antennas one has to deal with two design stages: one of these is dedicated to the design of different sparse sub-arrays operating in isolated mode and the other one focuses on the interleaving procedure that will allow for deploying the sparse architectures on a common aperture. Contrary to the thinning techniques, the topic of interleaving sparse sub-arrays is seldom encountered in the literature. The main goal of this design step is to preserve the sparsity properties of the sub-arrays (especially in the sense of avoiding the generation of high side lobes), while preventing the overlapping of elementary radiators. Three techniques are proposed in this thesis for solving the problem of interleaving sparse configurations. The novel shared aperture concept is experimentally demonstrated by manufacturing and measuring an antenna

consisting of two interleaved sparse sub-arrays. One of these sub-arrays operates in the frequency range from 8 GHz to 8.5 GHz (relative bandwidth of 7%) and the other one is properly matched to the feeding line in the band from 8.5 GHz to 9.5 GHz (relative bandwidth of 10%), the total bandwidth of the shared aperture being around 17%. The measured radiation patterns of the shared aperture antenna are in a good agreement with the calculated ones obtained by means of the full wave MMM software routines developed during this Ph.D. research.

Samenvatting

In deze thesis wordt een nieuwe oplossing gepresenteerd voor ontvangende breedband (multi-band) antenne stelsels. Deze oplossing is gebaseerd op het concept van het door-elkaar-heen-plaatsen van antennes van het stelsel die op gescheiden frequenties functioneren. Dergelijke stelsels met verspreidde antenne groepering (zgn. sparse array antennas) hebben twee enorme voordelen: ze hebben ongelijkmatig verdeelde antenne-elementen met mogelijke grote afstanden tussen de antenne-elementen (dit levert de vereiste ruimte voor het door-elkaar-heen-plaatsen van antennes van het substelsel), en laten amplitude tapering van de elementen toe om het stralingspatroon te kunnen beheersen.

In het eerste deel van de thesis is de theoretische formulering van het elektromagnetische probleem gepresenteerd. Varianten van de "Mode Matching Method" (MMM) zijn ontwikkeld ten behoeve van het volledig golf onderzoek van elementaire stralers en van de configuratie van het antennestelsel. Het tweede deel van de thesis is gewijd aan de analyse en het ontwerp van elementaire antennes, sparse array antennes en gedeelde aperturen bestaande uit substelsels die door elkaar zijn geplaatst. Tenslotte zijn de invloeden van de technische aspecten op de prestatie van de antennes aan de orde gesteld en is het resultaat van de metingen vergeleken met de resultaten van de simulaties.

Bij het opstellen van de numerieke elektromagnetische analysemethode is in het bijzonder gekeken naar het probleem van het berekenen van modi van uniforme golfpijp segmenten met willekeurige doorsneden door middel van de zgn. "Boundary Integral - Resonant Mode Expansion" (BI-RME) methode. Numerieke rekenkundige aspecten die een relatie hebben met de BI-RME berekeningen worden gepresenteerd. Het probleem bij het kiezen van de modi in de BI-RME methode is onderzocht en er wordt een analytische oplossing voorgesteld voor de optimale rotatiehoek die zou moeten worden gebruikt bij het verwerken van quasi-gedegenereerde modi. Ook wordt gedemonstreerd dat de BI-RME modi quasi-orthogonaal zijn en dat de orthogonaliteit van deze modi kan worden verbeterd door het vergroten van het aantal canonieke modi die worden gebruikt in de reeksen welke de Greense functie vertegenwoordigen. De software implementatie van de MMM/ BI-RME analyse is nauwkeurig onderzocht door middel van het

oplossen van een groot aantal test vraagstukken. Tevens wordt het probleem onderzocht dat optreedt bij het vergelijken van wederzijdse koppeling in willekeurige antenne stelsels bestaande uit rechthoekige aperturen van verschillend formaat. De analyse is ook uitgevoerd door middel van de MMM. De software implementatie van deze MMM is gevalideerd door het bestuderen van verschillende test configuraties en het observeren van specifieke aspecten gerelateerd aan het elektromagnetische veld en van de verstrooiingparameters van de apertuur antennes. Een oplossing voor snelle vergelijking van het wederzijdse koppeleffect wordt beschreven. Deze snelle techniek is gebaseerd op interpolatie met polynomen van de koppeling admittanties tussen de modi die worden gebruikt om het veld van apertuur antennes te presenteren. Uit de numerieke tests, gepresenteerd in het eerste deel van de thesis, wordt geconcludeerd dat de modale technieken de meest geschikte "full-wave" methodes zijn voor de analyse van golfpijp antennes.

Het ontwikkelde modale analyse gereedschap is vervolgens gebruikt bij het ontwerp van de antenne-elementen. Een aantal tijdefficiënte ontwerpprocedures wordt gepresenteerd in relatie met twee antenne types: de diëlektrisch gevulde golfpijp antennes met een luchtspleet aanpassingscircuit en de zgn. cavity-backed, stacked-patch and probe-fed antennes. Met betrekking tot de cavity-backed, stacked-patch antennes moet worden geconcludeerd dat de systematische ontwerpmethode, toegepast in dit onderzoek, heeft geleid tot antennemodellen met een bandbreedte van rond de 10%. De numerieke simulaties zijn gevalideerd door vergelijking met metingen uitgevoerd op fysieke modellen. Technische aspecten zijn zorgvuldig onderzocht en enkele praktische oplossingen zijn gegeven in de context van vereenvoudiging van het productieproces en verminderen van de productiekosten.

Het onderzoek naar sparse array antennas is voorafgegaan door een uitputtend literatuuronderzoek naar ontwerpmethoden. Specifieke aspecten van de sparse array configuratie zijn onderzocht door numerieke studies en experimenten. Deze onderzoeken zijn toegespitst op twee relevante aspecten, te weten: de schatting van de overeenkomstige eigenschappen van individuele stralers die functioneren in een niet-periodieke, eindige omgeving met meerder antennes in een stelsel en de beoordeling van de stralingseigenschappen van de sparse array antennas, waarbij de koppelingseffecten zijn meegewogen. Spreidings technieken worden ook gebruikt om synthetische apertuur radarbeelden te genereren van grondpenetrerende radarmetingen; dit resultaat reduceert de data-acquisitie en berekeningstijd significant. Een andere belangrijke uitkomst is dat het koppelingseffect een beperkte invloed (in vergelijking met uniforme stelsels) heeft op de prestatie van individuele stralers tijdens het elektronisch scannen van de antenna bundel. Dit heeft zijn nut bij het ontwerpen van antennestelsels met karakteristieke zgn. "wide angle impedance matching" (WAIM) eigenschappen.

Bij de implementatie van het concept van een gedeelde apertuur gebaseerd op sparse array antennes moet rekening worden gehouden met twee ontwerpfases: de ene is gericht op het ontwerpen van verschillende

substelsels met verspreidde antenne groeperingen die gescheiden van elkaar functioneren en de andere focust op de zgn. "interleaving" (het tussen elkaar verweven van substelsels) procedure dat de mogelijkheid biedt om de ontwerp techniek van verspreiden toe te passen op een zelfde apertuur. In tegenstelling tot de techniek voor het terugbrengen van het aantal antennes in een stelsel komt het onderwerp betreffende het interleaving met verspreidde antenne groepering nauwelijks in de literatuur voor. Het belangrijkste doel van deze ontwerpstap is het behouden van de verspreiding eigenschappen van het substelsel (vooral in de zin van het voorkomen van hoge zijlobben), terwijl het overlappen van elementaire stralers wordt voorkomen. Drie technieken worden in deze thesis beschreven die gericht zijn op het oplossen van het probleem van interleaving stelsels met verspreidde antenne groepering. Het nieuwe concept van gedeelde apertuur is experimenteel gedemonstreerd door het maken van en meten aan een antenna bestaande uit twee interleaved substelsels. Een van deze substelsels functioneert binnen het frequentiebereik van 8 GHz tot 8.5 GHz met een relatieve bandbreedte van 7% en de andere is passend in het bereik van 8.5 GHz tot 9.5 GHz (relatieve bandbreedte van 10%). De totale bandbreedte van de gedeelde apertuur ligt rond 17%. De gemeten stralingspatronen van de gedeelde apertuur komen in voldoende mate overeen met de berekeningen waarbij gebruik is gemaakt van "full-wave" MMM softwareroutines die tijdens dit promotieonderzoek zijn ontwikkeld.

Acknowledgements

After having all the theoretical and technical ideas exposed it is my pleasure, in this section, to express my gratitude to the peoples and to the institutions which have contributed directly or indirectly to the successful completion of my Ph.D. program.

First of all, I am grateful to my "promotor" Prof. Leo Ligthart for entrusting me with the responsibility of a Ph.D. project and for providing me with such a generous subject as the study of interleaved sparse array antennas. Without imposing me tight research boundaries he was always present at the key points in my work. Looking back at the past four years I have noticed that most of the achievements presented in this thesis were triggered by observation coming from his side. I also want to acknowledge the significant effort that Prof. Leo Ligthart and especially his wife Ine Ligthart put in connection with my quest for having my family with me during this Ph.D. stage.

I thank Dr. Ioan Lager, my "daily supervisor" and my roommate during the past four years, for his valuable guidance in the field of computational electromagnetic and for sharing with me his knowledge in writing scientific documents. I am indebted to him for introducing me to LaTeX and for proofreading this dissertation. I would also want to thank him for advising me in many non-technical problems related to my staying in The Netherlands.

I am indebted to Prof. Piet van Genderen for his concrete and effective implication in the initiation of my Ph.D. stage with Delft University of Technology (TU Delft). I also thank him for reviewing this thesis and for his worthwhile remarks and suggestions.

I would like to express my gratitude to Prof. Ştefan Demeter for encouraging me to apply to this Ph.D. position with Delft University of Technology and for reviewing my application. I thank you Prof. Gheorghe Iubu for pointing out the possibility to join the International Research Centre for Telecommunications-transmission and Radar (IRCTR) at TU Delft, at a key moment when this opening seemed to be closed.

The doctoral stage was financially supported by the Ministry of Defence in The Netherlands. This support is greatly acknowledged. I also want to

thank Ministry of National Defence in Romania in general for giving me the permission to undertake this Ph.D. project. In particular, I am indebted to Dr. Ştefan Cantaragiu for his constant support of my position as Ph.D. student at TU Delft.

I am very gratefully to Mostafa Hajian for being an outstanding colleague and a very enthusiastic teammate. There were many scientific problems and social ones that I could openly discuss with him. He was the one who kept my interest for antennas at a high level.

I am especially indebted to Prof. Ioan Nicolaescu for his continuous support and deep understanding of the problems that I had faced during the period of his stage at IRCTR, and not only. I have always appreciated very much his valuable advice and the warm relation between our families.

I would like to thank all colleagues at IRCTR for creating such an enjoyable working environment. This had a direct impact on the quality of the research work which is presented in this dissertation. In manufacturing the experimental models presented in this thesis I have received technical assistance from several peoples, whom I wish to thank. I particularly enjoyed the help of Paul Hakkaart in getting the antennas assembled and the support of Pascal Aubry and Johan Zijderveld during the measurement campaign in the anechoic chamber.

I am indebted to the secretariat and administrative staff of IRCTR for the helpful assistance provided during my Ph.D. research. I would like to thank Mia van der Voort, for arranging all the formalities required by the commence of the doctoral stage and for helping me with visa related aspects. I also want to thank Laura Bauman for taking care of the official formalities related to my Ph.D. work.

Aside from the work many peoples in Delft helped me and my family to have a normal social life. Here my thanks go to all the Romanian friends who I met in The Netherlands. Particularly, I am indebted to Florin, Remus, Cornel and their families for the pleasant moments that we have spent together. At this point, I would also like to thank the members of the student handball club Torius in Delft for accepting me in their team and for giving me the possibility to experience the student life at TU Delft. Especially, I am indebted to Martijn Arets for the invaluable friendship that he showed to me and to my family over the years that we spent in The Netherlands and for the translation of the summary and the propositions at a moment when the printing deadline was approaching.

I would like to thank my parents and my sister Adina for supporting and encouraging me in all my pursuits, even from faraway. My very special thanks go to my wife Valentina for his constant loving support and deeply understanding of my decision to undertake this Ph.D. program in The Netherlands. I want to thank her for tacking the responsibility to be a single parent in the difficult moments encountered during this project. I am deeply indebted to my sons, Radu and Tudor, for their patience and

understanding on the many occasions when I did not arrived home on time. They are my constant source of power for tackling the challenges that life offers.

Cristian I. Coman

Delft, December 2005

About the author

Cristian Ioan Coman was born in Tîrnăveni, Romania, on March 14, 1972. In 1986 he entered the military environment by tacking his secondary education at the military high school "Mihai Viteazul", in Alba Iulia. He received the baccalaureate diploma from this military school in 1990. Subsequently, he became a student of the Military Technical Academy, in Bucharest, in the speciality of radio electronics for anti-aircraft missiles and artillery. He graduated in 1996 with a thesis on radio proximity fuses for a man portable, surface to air missile and received his license diploma in Electronic Engineering.

Since 1996, he has been with the Military Equipment and Technologies Research Agency (METRA), in Bucharest, as a research engineer in the Sensors and Simulation Division. Within METRA he has done research on antennas, microwave devices, radar signal processing and security systems. During the period 1996- 2001, he was contributing to the prototyping of the gap filler radar called START-1M and in the development of the radar and the tactical command post associated to a short range air defence system.

In 2001, he started as a Ph.D. student with the International Research Centre for Telecommunications-transmission and Radar (IRCTR) at Delft University of Technology, in The Netherlands. This educational stage was initiated in the frame work of the NATO Partnership for Peace programme, as a result of the intense cooperation between the Romanian Ministry of National Defence and the Ministry of Defence in The Netherlands. At IRCTR he has done research on numerical electromagnetism, sparse array antennas and shared aperture antennas, some of the relevant results of these studies being presented in this Ph.D. dissertation.